Citation: Rajarajan, M. (1999). Computer Modelling of Compact Photonics Devices for Optical Communications. (Unpublished Doctoral thesis, City, University of London)

Computer Modelling of Compact Photonics Devices for Optical Communications

By

Muttukrishnan Rajarajan

A thesis submitted to City University in fulfilment of the requirement
for the Degree of Doctor of Philosophy

City University

Measurement and Instrumentation Centre
Department of Electrical, Electronic and Information Engineering
Northampton Square, London EC1V 0HB, UK.

April 1999

This thesis is dedicated to my parents
and my wife

Table of Contents

Chapter 1: General Introduction

Chapter 2 : The finite element method

Chapter 3 : Coupled mode devices

Chapter 4 : Optical polarizers

Chapter 5: Multimode Interference Devices

Chapter 6: Laser-fibre-coupling

Chapter 7: Discussions and suggestions for future work

List of Tables

List of Figures

Acknowledgements

First and foremost, the author would like to acknowledge sincerely his supervisors: Dr. B.M.A. Rahman and Prof. K.T.V. Grattan for their advice and guidance throughout this research work. Particularly to Dr. B.M.A. Rahman who has been very helpful and so kind as to provide valuable discussions, at any time and on every matter.

The author is also pleased to acknowledge the financial support from the Overseas Research Studentship (ORS) for this research work.

Also, the author would like to extend his appreciation to all the secretarial staff in the department of electrical electronic and information engineering. My special thanks goes to my colleagues who created a pleasant and unforgettable atmosphere in the laboratory during the years of working with the Photonics Modelling Group, City University.

Last but not the least, the author would like to express his deep gratitude to his caring parents and wife for their encouragement and support throughout this important study.

Declaration

I grant powers of discretion to the University Librarian to allow this thesis to be copied in whole or in part without further reference to the author. This permission covers only single copies made for study purposes, subject to normal conditions of acknowledgements.

Abstract

This thesis discusses several important applications of directional coupler-based and multimode interference coupler-based devices. The numerical analysis in this study has been carried out by using the powerful and versatile finite element method (FEM). This method has been proved to be the most accurate numerical methods to date for the analysis of optical waveguides. In this study the vector **H**-field formulation is used along with the penalty function term to eliminate the spurious solutions.

Using the finite element method the accurate propagation constants of all the modes and the field profiles can be calculated. However, the finite element method cannot calculate the power transfer efficiency directly, hence the Least Squares Boundary Residual method (LSBR) is used with the FEM for this purpose. The LSBR method is rigorously convergent, satisfying the boundary conditions in the least squares sense over the discontinuity interface. The error minimisation in this approach is global rather than sampled as in the point matching method. Using this method the transmission coefficients of all the modes and the reflection coefficients of the fundamental mode can be determined once the transmission coefficients of all the modes are calculated, and the power transfer from the input to the coupler section and at the output ports can be evaluated.

In this work, to show the advantages of the finite element approach an optical polarizer with metal clad directional coupler has been designed and analyzed. The modal loss is also calculated for the TM polarised mode and a Multiple Quantum Well based optical polarizer with two-dimensional confinement is studied. Its equivalent index has been calculated by using the finite element and the results are compared with the analytical results. A large section of this thesis is devoted to the study of multimode interference based devices. An interesting and useful comparison is made on their operating properties such as the crosstalk, device length, polarization dependence and fabrication tolerance of the multimode and the directional coupler-based devices. Finally, the spot size expander approach for improved laser-to-fibre coupling is discussed. In this study initially a taper-based approach is discussed with the simulated values for the coupling loss and reflection coefficients, following which a novel approach using a synchronous directional coupler-based mode expander is studied. Some multiguide directional coupler-based spot size expanders are also discussed and finally a new approach using multimode interference-based compact devices is presented, which is technologically more promising, due to the fascinating properties of the multimode based devices. This is an interesting exciting area in the field of photonic engineering.

This thesis, starting with a small introductory chapter on optical communication will take the reader in a step-by-step approach to understand the principles and properties of the optical devices that are important for the design of all optical systems. Most of the applications that are presented in this thesis are of great interest to the optical community and I hope the reader will enjoy the contents of this thesis.

Symbols and Abbreviations

ATM	Asynchronous Transfer Mode
BPM	Beam Propagation Method
CE	Cosine Exponential
EIM	Effective Index Method
ENM	Equivalent Network Method
FDM	Finite Difference Method
FEM	Finite Element Method
HDTV	High Definition Television
ISDN	Integrated Services Digital Network
IBCN	Integrated Broadband Communication Network
LSBR	Least Squares Boundary Residual
LAN	Local Area Network
MAN	Metropolitan Area Network
MHG	Modified Hermite Gauss
MHGE	Modified Hermite Gauss Exponential
MMM	Mode Matching Method
MMI	Multimode Interference
MQW	Multiple Quantum Well
OI	Overlap Integral
OIC	Optical Integrated Circuit
SSE	Spot Size Expanders

SMHG	Simple Modified Hermite Gauss
TE	Transverse electric
TM	Transverse Magnetic
WKB	Wentzel Kramers Brillouin
WAN	Wide Area Network
VM	Variational Method
α	Penalty parameter
β	Propagation constant
δ	Weighting function
λ_0	Wavelength in vacuum
λ_g	Bandgap Wavelength
π	PI$\approx$3.142
ε	Permittivity
μ	Permeability
k	Wave number
L_C	Coupling length
n_c	Refractive index of cladding
n_g	Refractive index of the guide

Chapter 1

General Introduction

1.0 Introduction

This chapter sketches the history and future of telecommunications with particular emphasis on integrated optic devices and their applications in optical communications, which is the core of the work described in the present thesis.

1.1 Brief history of telecommunications

Telecommunications is a rapidly growing economic sector. People want to talk to family and friends away from home, companies want to do business with partners far away, and we generally like being amused by stories that reach us from elsewhere. The oldest telecommunications event mentioned in the literature are the fires, lit on a series of successive mountains, by the ancient Greeks to herald the fall of Troy. Other examples of primitive telecommunications include the smoke signals, employed by the American Indians, and drum signals employed by numerous African peoples. The desire to communicate at a distance more quickly led to the development of semaphore systems and later the electrical telegraph (Morse), the first of the modern era of telecommunications systems. They were followed quickly by the telephone (Bell), radio telegraphy (Marconi), radio and television broadcasting, telex, mobile telephony and data transmission. Telegraphy over land began in 1767 with Edfeworth's development of the semaphore, a pole with rotable arms. A more primitive system for visual telegraphy had been suggested in 1684 by Robert Hooke, but had not been tried out in practice. The semaphore was first employed in France, where the need for faster communication was felt after the revolution of 1789, when France was threatened by the allied forces of Britain, Prussia, Austria, and Spain.

In 1794 the French engineer Claude Chappe completed an optical telegraph connection between Paris and Lille (230 km). It consisted of 22 semaphores over which a message could be transmitted with less than two minutes delay. Signalling rates were low; in the order of 10 to 20 signals per minute. Telegraphy networks were further extended in the following decades. In France the network ultimately covered a distance of 4800 km with 566 stations.

From these primitive beginnings, today we have a world-wide telephone network that in principle allows us to speak to any other telephone subscriber anywhere in the world, at any time, and that can also be used to transmit written information by means of facsimile, and to transmit data via Integrated Services Digital Network (ISDN) lines using computer modems. More and more people and institutions are connected to the world wide computer network *the internet*, over which they send each other email, work on each other's computers, and exchange data more easily than exchanging floppy disks.

The world market for telecommunications equipment is greater than that for consumer electronics and microelectronic components together; in the information sector it is only exceeded in size by the computer market. Telecommunications equipment and services together make up more than half of the total information market, and they will soon exceed the market volume of the automobile industry to form the greatest market segment in the industrialised world.

It is interesting to note that the development of modern telecommunications began with optical communications. By the middle of the 19th century optical telegraphy had developed as far as it could; however, and the torch was taken over by electrical telegraphy, which is less dependent on weather conditions and allows for higher signalling rates. In 1845 Morse established the first intercity telegraphy connection (Washington-Baltimore). His system was based on an electromagnet which was driven by the signalling current allowing for a higher signalling rate than that permitted by optical telegraphy or earlier experiments with electrical telegraphy.

Looking to the future, in 2010 it is likely that the private subscriber will still be an important customer of the telecommunications companies. In addition to his telephone set, which is equipped with a video display, he has a terminal which gives him access to services such as electronic banking, tele-shopping and many other low-priced information services. Next to his terminal he has a small colour printer which is suitable for making hard copies and can also receive facsimile. His old-fashioned television set has been replaced by a flat screen HDTV (High-Definition Television) set which is also suitable for inspection of electronic mail. All equipment is provided with an optical plug which is combined with the power supply plug and can be used everywhere in the house. The thermostat and the central heating apparatus communicate via the local in-house network ; other equipment such as the oven and an electronic door lock can be remotely controlled with a multi-purpose wireless controller. Bandwidth problems have disappeared; the capacity of the network is more than sufficient for the actual service package.

The use of the network by the professional user has increased considerably since the introduction of the ISDN. In addition to voice telephony, transfer of many kinds of data from simple electronic mail to documents with high-quality graphics has become the most important application. Video-conferencing has also gained some popularity. The (single) in-house network is intimately coupled to the public telephone network so that communication both inside and outside the building is equally easy. An important difference with earlier networks is the world-wide standardisation of communication protocols. All sorts of equipment can communicate without difficulty over the network and the wrong installation of equipment is reserved only to very intelligent people.

Automobiles, as well as ships and aeroplanes have been equipped with an electronic navigation system. Using this system the on-board computer faultlessly guides the driver to the required destination, and avoids road-blocks and other stagnations, which are reported to the board computer by a mobile datalink. Car-drivers have taken their share in the spread of telecommunication services. The car telephone, which became popular in the 1980s, will be a standard equipment in every car by 2010.

Digital transmission and a sophisticated cellular structure of the mobile network guarantee fast access to the network even if traffic stagnation occurs and many drivers call at the same time. Personal portable telephone sets and mini-terminals, which can be used over a large part of the world, have become wide-spread.

The role of satellite communication has shifted from fixed communication links to more specific applications such as broadcast services to mobile users and thinly populated regions and communication with ships and aeroplanes. Furthermore, geostationary satellites connect low-orbit satellites to the communications network via free-space laser beams, and provide a diversion path if a terrestrial connection is broken.

The quality of the weather forecast has been greatly improved on the basis of data provided by a large number of remote sensing satellites. Satellite data are transmitted to the network via a geostationary communications satellite. Ship movements, sea surface pollution, crop development and the state of the forests are also observed by satellite. Image data are processed in special centres and directly available to the interested user via the network. Behind the wall sockets of the network, an invisible revolution has taken place. Each subscriber can attach as many terminals to his network port as he desires, without the need to ask permission and wait until the change has been affected. The local networks of different buildings can be coupled via the public network in such a way that two colleagues 2000 km apart communicate just as easily as if they were working in the same building. It is not necessary to reserve a hired line for this, the connection is realised within a few milliseconds when it is needed. The only place where the user sees the difference between this type of connection and the permanent one is when the monthly bill arrives!

Achievements in the field of computer techniques and automation are presently being integrated into a telecommunication environment by the rapid spread of data networks (Local Area Networks, Metropolitan Area Networks, and Wide Area Networks) and such techniques as distributed processing.

To achieve this vision of the future it may therefore be expected that in the next few years microelectronic technology will become more and more telecommunications driven. This is already seen in III-V semiconductor technology, where the shift from AlGaAs to InGaAsP is fully attributable to the fact that optical fibres perform best at wavelengths of 1.3 and 1.55μm.

A similar development is seen in optical communications technology. In order to integrate more and more services into the network function, the channels have to be as transparent as possible and the form in which data are transmitted has to be as universal as possible. These requirements have stimulated the development of broadband digital channels and switches. Important steps on the road to a completely transparent digital broadband network are the introduction of the ISDN, the development of an Integrated Broadband Communication Network (IBCN), and the development of Asynchronous Transfer Mode (ATM) switching and routing techniques.

Optical communications links offer the bandwidth which is required for this development. It can be concluded from this that a fixed part of the network will be all-optical. Short in-house networks may be cabled with multimode fibres which provide easy connections combined with Gigabit transmission capacity on short distances. The other networks will be, or are already, cabled with monomode fibres which provide a virtually unlimited transmission capacity. Electronic switches will become potential bottlenecks in these networks: with optical switches Gigabit data streams may be switched as easily as electronic mail. The development of optical connectors and small switching matrices which are suitable for mass application still has a long way to go, however, so that the switches will probably be the last parts of the network to become optical.

1.2 Guided wave optical devices

The more immediate future of optical communications systems is clear: there is now little doubt that guided wave optical devices will have an increasing impact on electrical engineering in the coming years. Primarily, this is because of the sustained development of both semiconductor laser and the optical fibre. These two major developments have revolutionised the telecommunications industry, and they are making considerable advances in a variety of other new and exciting application areas.

Optical fibre acts as a propagation medium for guided optical waves. The most important fibre type is single-mode optical fibre, which can support guided waves over extremely long distances (thousands of kilometres) with low loss and low signal dispersion. Single-mode fibre is generally formed from silica glasses, which are arranged in a cylindrical geometry with a core region of high refractive index surrounded by a lower-index cladding layer (A W Snyder and J D Love 1983).

The overall diameter of a single-mode fibre is comparable to that of human hair. However, the light actually travels almost entirely in the much smaller core region (which is normally 8-10μm) and is guided within this region by a phenomenon known as the *total internal reflection*. This can occur when light is incident on an interface between two lossless dielectric media with different refractive indices. The physics of this is discussed extensively in several texts (A W Snyder and J D Love 1983).

In the last two decades the optical fibre has finally allowed the use of light as a carrier of information, and this application has given rise to a new area of engineering known as the *photonic engineering*. The optical field normally oscillates at a high frequency ($\approx 10^{15}$ Hz) and hence acts as a high-frequency carrier. Due to its low dispersion characteristics, the optical fibre allows information to be transferred at a high data rates. Optical fibre offers an increase in channel capacity by a factor of 10^4-10^5 and very low attenuation to its competitor microwave guide, but coupled with a considerable reduction in cost, size and weight. Because of the low cost of silica, the optical fibre will replace the copper cables in all applications involving transfer of low-power signals.

The semiconductor laser is a small, efficient light source, where the technology required to fabricate a semiconductor laser is now well-developed. Its optical output can be very intense-beams of powers from milliwatts to Watts now routinely available and it can be directly modulated at very high speeds, typically upto the Terahertz range. The semiconductor laser is also a guided wave device, and is usually configured to emit light from a small stripe. However, the spot size of the laser is only 1-2 μm whereas the spot size of the fibre is around 8-10μm. Thus an intermediate section is required to expand the laser field, to achieve good coupling and this is explained in more detail in chapter 6.

Furthermore, the semiconductor laser can emit light of the wavelength at which Silica fibre shows minimum dispersion and minimum propagation loss, near $\lambda=1.3$ and 1.55 μm respectively. With careful design, the output can also consist of very nearly a single optical frequency, an important advantage for communications, since it reduces the effects of dispersion.

Tunable lasers for use in wavelength-division multiplexed communication systems, surface-emitting lasers for optical processor applications and high-power laser arrays are also the subject of an intense development effort. The latter can generate quite staggering amounts of power in watts, continuous wave (cw) form from a tiny chip, and may well pose a challenge to large gas lasers in the future. Recent advances include the use of semiconductor lasers as in-line amplifiers and repeaters in optical fibre systems, and the development of semiconductor laser-pumped optical fibre lasers. Together with photodiodes, which are light-detecting devices fabricated in semiconductor materials, optical fibre and semiconductor lasers form the key elements of optoelectronics. Today, there are several guided wave devices which can be used to design complete guided wave circuits.

Even though there are several devices present at the moment, it is hard to predict which of them will be the most successful in the long run with cost a most important factor, coupled to their performance. Today a major challenge in research laboratories throughout the world is the demonstration of various optical integrated circuits (OICs) to replace the electronic integrated circuits (EICs), and also to perform special functions particularly suited to optics. The major advantages of OICs are low-loss couplers, compact, lower power consumption, increased bandwidth, improved optical alignment and the possibility of expanded frequency (wavelength) division multiplexing (FDM). The major disadvantage is the increased cost in fabrication technology. Integrated optical devices such as lasers, couplers, modulators and filters are increasingly becoming popular and the possibility of all optical systems seems to be very promising.

1.3 Optical communications technology

After the development of electrical telegraphy, interest in optical signal transmission faded, but did not completely disappear. In 1880, for example, Bell experimented with a photophone based on photo-sensitive selenium cells in which speech was transmitted using the modulated light wave. The development of the first laser by Maiman in 1960 gave a new impetus to optical communications research. Initially experiments were carried out with free space beam propagation and suffered from the same problem which hampered early optical communications, namely, great susceptibility to adverse weather conditions.

Today's optical fibre communications system was invented in the Harlow laboratories of STL back in the 1960s, where a team of visionary engineers pursued the dream of long distance communications using light. Initially various techniques for guided optical communication were explored including the use of reflective pipes, concatenated lens systems, thin film waveguides, and single mode optical fibres. Although short glass fibres had already been used as simple light pipes, it was Charles Kao and George Hockham in 1966 (Kao and Hockham, 1966) who first directed serious attention to the use of optical fibres for long distance communication. That visionary publication showed that an optical fibre waveguide had the potential to provide long distance communication with large bandwidths, despite the prohibitively high loss of the best fibre available at the time. Their work in Harlow addressed most of the issues later found to be crucial and this was done with remarkable foresight. They showed that the high loss of early samples was not fundamental, and could be reduced sufficiently to make optical fibre a far more practical solution than other competing approaches such as long haul microwave waveguide. The dedication and commitment of Kao and his colleagues eventually overcame the early opposition to the idea of optical fibre communication.

The first transmission systems had very short range, e.g. in 1967 high fibre loss limited the first video transmission system to only 20 metres. However the immunity of optical fibre to electromagnetic interference made even this a useful step forward.

In 1977 the Harlow laboratory developed and installed the first practical fibre trunk transmission system using multiple remotely powered generators. This field demonstration system was installed along a 9km route between Hitchin and Stevenage in the UK operated at 140 Mbits/s, used multimode fibre and 850nm semiconductor lasers. The world's first deep water undersea optical cable trial was demonstrated by Nortel at Loch Fyn, Scotland in 1980, which led in turn to installation of the UK-Belgium link, the world's first commercial undersea fibre system in 1986, followed by TAT-8, the worlds first transoceanic optical fibre system which entered service across the Atlantic in 1988.

The main problem in employing glass fibres was the high level of attenuation. Even the purest glasses exhibited attenuation in excess of 1000 dB/km, so that unamplified propagation was limited to some tens of metres. Kao and Hockam predicted that the attenuation could be reduced to below 20dB/km. Their prophecy was already fulfilled in 1970 when Kapron, Keck, and Maurer reported a (monomode) quartz fibre with 20dB loss per kilometer. Within fifteen years fibre losses had been reduced below 0.2dB/km, close to the theoretical limit. Until the mid-1980s optical communications systems were based on multimode fibres. Due to the non-linearity and noise problems in channels containing lasers in combination with multi-mode fibres, optical communications moved to became almost completely digital in nature.

The rapidly growing market for multimode fibre links formed a base for increased investments in fibre fabrication and connector technology. By the end of the seventies, the technology had been developed so far that monomode fibre links, which offered a much greater transmission capacity, became feasible. In monomode fibres, the transmission performance is limited by the fundamental material absorption and dispersion properties of quartz and have minimum dispersion at 1.30μm and minimum loss at 1.55μm. These wavelengths cannot be generated by the AlGaAs semiconductor laser, which is limited to the wavelength range of 0.78-0.87μm. In the first half of the 1980s, the direction of optical communications research shifted, therefore, to the quartenary InGaAsP semiconductor system on InP substrate. Employing this system, the wavelength range from 0.9-1.65μm, which includes the optimal wavelengths 1.3 and 1.55μm, can be encompassed by an appropriate choice of the material composition. From 1984 growth in the use of monomode fibre technology outstripped that of multimode fibres at an unexpectedly rapid rate. The installation rate in the longer trunks is expected to drop soon; in the United States it has already dropped because the old network has almost been replaced. Monomode fibre is now seen to penetrate rapidly the short-distance network to the local exchanges. The main reason for this development is the increasing demand for bandwidth on communication trunks, as in monomode fibres can transport even higher bit rates over more than one hundred kilometres without amplification, so that transmission between cities is feasible without repeaters, in most parts of Europe.

The next step towards a completely integrated digital communication network will be the extension of the fibre network to the home, and this will increase the optical communication market by at least one order of magnitude. As has been seen before, however, history does not always take the straight line from one point to another. The road from present digital optical transmission to an integrated digital network may very well go along the path of analogue optical transmission. If the digital transmission scheme of modern optical links is applied in the new distribution network, all subscribers will have to be equipped with fast digital decoders. This requires enormous investments over a short period. This problem can be eliminated by employing a subcarrier modulation technique, in which a composite electrical signal, containing the full desired spectrum of video and FM-channels, is intensity-modulated onto an optical carrier. After detection, this signal can be directly applied to conventional receivers. The high quality of the latest available lasers, coupled with the monomode fibres, meets the required signal-to-noise ratio and the linearity required from these modulation schemes. If component costs can be sufficiently reduced, 'fibre-to-the-home' may become reality for many subscribers in the early part of the next millennium.

A major issue on the road to technical integration of the cable-television network and the public telephone network is formed by the ownership and the exploitation of the networks and government regulations. In many countries the cable-television networks and the public telephone network are operated by different companies and government monopoly regulations may limit the involvement of telephone network supplies in 'entertainment' delivery.

1.4 Integrated Optics

The name *integrated optics* was coined by Miller (Miller, 1969) in an issue of the *Bell Systems Technical Journal* containing several contributions on planar optical waveguides. Previously, integrated optics was known as the planar optics; research was focused on single components and the possibility of integration of all those components on a single chip seem to be out of reach. The laser was the only component which passed beyond the R & D stage of such an integrated concept.

Initially planar technology was hampered by the fact that the optical communications was based on multimode fibres, and it was difficult to couple light from a multimode fibre to a monomode device as most of the power was lost in the process. Research on components other than lasers were promising at that stage but was conducted at a low profile.

In the second decade of the subject (1980-1990), laser technology was the first planar-optics activity to become big business, mainly because of its application in compact disk players. In this decade the breakthrough in the field of monomode fibres opened the door for a telecommunications - driven acceleration of integrated - optics research. In addition to the development sophisticated long-wavelength telecommunication lasers, a variety of planar components and a few integrated circuits (coupling and switching matrices) were reported by several groups.

The real flavour of progress in integrated optics is in its third decade (1990-2000). The main driving force behind integrated-optics research is its potential to avoid most of the connection costs which occur in optical circuits built from fibre-pigtailed components, and to reduce the large volume occupied by these circuits (Koch and Koren, 1990).

Monolithic integration of a chip with sources and detectors is only possible in III-V semiconductor materials, mainly the quartenary alloy InGaAsP (or InGaAlAs) on InP substrates, because it is the only material system which allows the generation and detection of light at wavelengths of 1.3 and 1.55μm, where the waveguide properties are optimal. Therefore the InP based quartenary semiconductors are the most promising materials for monolithic integration. The development of monolithically integrated optical chips, which is presently growing out of its infancy, will probably take another decade to reach the low-cost commercial production stage. The introduction of fibres in the local network will require a similar period. Large-scale application of optical chips may, therefore, begin around the turn of the century.

1.5 Theory of optical waveguides

All the integrated optical devices studied on this thesis are based on optical waveguides. In this section, some theoretical background on the subject of waveguiding is presented; both passive components such as directional couplers, power splitters, tapers, optical filters, and (de-) multiplexers, and active components such as lasers, modulators and polarisation controllers are presented, based on optical waveguide structures. More detailed accounts of waveguiding theory and technology have been given in several texts e.g. by Tamir (Tamir (Ed), 1979).

Propagation of light through a waveguide is an electromagnetic phenomenon, and is described by Maxwell's equations. In 1865, James Clerk Maxwell published his famous paper " A Dynamic Theory of the Electromagnetic Field ", in which he laid down the familiar eponymous equation. Maxwell did not use vector notation, and his equations number a total of twenty. Today, in vector notation, Maxwell's equations are denoted by

$$\nabla \cdot \mathbf{D} = \rho \qquad \text{(Gauss' law)} \qquad (1.1)$$

$$\nabla \times \mathbf{E} = -\frac{\partial \mathbf{B}}{\partial t} \qquad \text{(Faraday's law)} \qquad (1.2)$$

$$\nabla \cdot \mathbf{B} = 0 \qquad (1.3)$$

$$\nabla \times \mathbf{H} = \frac{\partial \mathbf{D}}{\partial t} + \mathbf{J} \quad \text{(Ampere's law)} \tag{1.4}$$

where

$\mathbf{E}$ = electric field intensity (volts/meter)

$\mathbf{D}$ = electric flux density (coulombs/meter^2)

$\mathbf{H}$ = magnetic field intensity (amperes/meter)

$\mathbf{B}$ = magnetic flux density (webers/meter^2)

$\mathbf{J}$ = electric current density (amperes/meter^2)

ρ = electric charge density (couloumbs/meter^3)

Besides these, Maxwell's original equations also include Ohm's law, the equation of conservation of charge, and the relations $\mathbf{D}=\varepsilon\mathbf{E}$, $\mathbf{B}=\mu\mathbf{H}$ and $\mathbf{J}$ and, ρ are the current and charge densities.

For most optical materials (such as dielectrics and semiconductors), μ is a constant equal to the permeability of vacuum, $\mu_0 \equiv 4\pi x10^{-7}$ F/m. Likewise, when a source-free ($\rho=0$), homogeneous ($\nabla \cdot \varepsilon = 0$) medium is assumed, (1.1) implies $\nabla \cdot \mathbf{E} = 0$. In the absence of currents (1.2) and (1.4) can be combined to form

$$\nabla^2 \mathbf{E} = -\varepsilon\mu_0 \frac{\partial^2 \mathbf{E}}{\partial t^2} \tag{1.5}$$

and there exists an identical equation for **H.** By substitution, it is seen that the plane waves

$$\mathbf{E}(r,t)=\mathbf{E}_0 e^{j(\omega t-\mathbf{k} \bullet \mathbf{r})} \tag{1.6a}$$

$$\mathbf{H}(r,t)=\mathbf{H}_0 e^{j(\omega t-\mathbf{k} \bullet \mathbf{r})} \tag{1.6b}$$

are solutions to the wave equation (1.5) when $\frac{|k|}{\omega} = \sqrt{\varepsilon\mu_0} = \frac{n}{c}$, with $n = \sqrt{\frac{\varepsilon}{\varepsilon_0}}$ the refractive index of the medium; where ε_0 is the permittivity of the vacuum and *k* is the wavevector. A lossy (e.g. absorbing) medium may be described as having a complex refractive index. Where **E** and **H** are perpendicular to each other and to wave vector **k**, the wavelength of the plane waves described by (1.6) is $\lambda = \frac{2\pi}{k} (= \frac{\lambda_0}{n}, \text{where} \lambda_0 = \frac{2\pi}{k_0}$ the wavelength in vacuum).

1.6 Waveguiding

In a *z*-invariant structure, i.e. one with a refractive index distribution $n = n(x,y)$, solutions of the wave equation can be found of the form

$$\mathbf{E}(x,y,z) = \mathbf{E}_m(x,y)\, e^{-j\beta_m z} \tag{1.7a}$$

$$\mathbf{H}(x,y,z) = \mathbf{H}_m(x,y)\, e^{-j\beta_m z} \tag{1.7b}$$

These equations describe a two-dimensional field distribution in the *x-y* transverse plane, propagating in the *z* (or longitudinal) direction unmodified, with a longitudinal wavenumber, β_m for the mode, *m*. Such a modal field distribution is called a *mode*, and the wavenumber β_m is called the *propagation constant* of the mode, where the subscripts *m* is used to distinguish different solutions. An *effective refractive index* can be associated with the structure for each mode *m*, by writing $n_{eff,m} = \beta_m / k_0$.

1.7 Boundary conditions

For a waveguide with arbitrary dielectric distribution, the satisfying of the boundary conditions at these interfaces is necessary. If there are two dielectric media 1 and 2, with a unit vector $\bar{n}$ normal to the medium 1 as shown in Fig. 1.1, in the absence of any surface currents (J=0) and surface charges (ρ=0), the following boundary conditions apply:

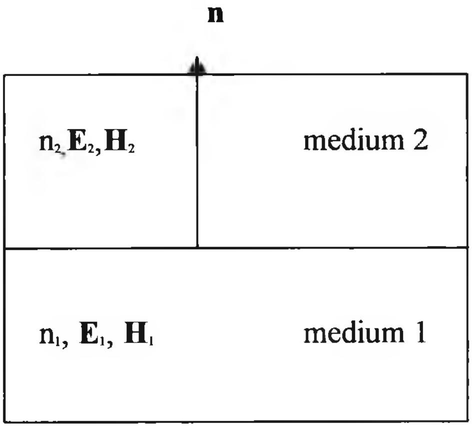

Fig. 1.1 Boundary between two media of refractive indices n_1 and n_2 where **n**, is the unit vector normal to the interface

(i) The tangential component of the magnetic field must be continuous

$$\bar{n} \times (\mathbf{H}_1 - \mathbf{H}_2) = 0 \quad (1.8)$$

(ii) The tangential component of the electric field must be continuous

$$\bar{n} \times (\mathbf{E}_1 - \mathbf{E}_2) = 0 \quad (1.9)$$

(iii) The normal component of the magnetic flux density must be continuous

$$\bar{n} \cdot (\mathbf{B}_1 - \mathbf{B}_2) = 0 \quad (1.10)$$

(iv) The normal component of the electric flux must be continuous

$$\bar{n} \cdot (\mathbf{D}_1 - \mathbf{D}_2) = 0 \quad (1.11)$$

The necessary boundary condition on any electric conducting boundaries is

$$\mathbf{n} \times \mathbf{E} = 0 \text{ or } \mathbf{n} \bullet \mathbf{H} = 0 \quad (1.12)$$

and when one of the two media becomes a perfect megnetic conductor, an useful approach to improve modal field symmetry, a magnetic wall boundary condition is imposed as

$$\mathbf{n} \times \mathbf{H} = 0 \text{ or } \mathbf{n} \bullet \mathbf{E} = 0 \tag{1.13}$$

The above boundary condition will ensure the continuity of the normal component of the megnetic field at the boundary.

1.8 Two-dimensional waveguides

The planar, or slab waveguide consists of a core layer sandwiched between the cladding and the substrate layer. Since in the planar waveguides the light is confined in one dimension only the Maxwell's equations (1.1-1.4) have to be modified to their scalar form for the case of TE and TM polarisations. By considering the light confinement in the *y*-direction, the partial derivative along the *x*-direction can be assumed to be $\frac{\partial}{\partial x} = 0$.

Then to obtain the TM modes where, the magnetic field in the propagation direction, H_z is zero, by using Maxwell's curl equations (1.2 and 1.4) the only dominant components are E_y, E_z and H_x which are expressed as :

$$E_y = -\frac{\beta}{\omega\varepsilon_0} H_x \tag{1.14}$$

$$E_x = -\frac{1}{j\omega\varepsilon} \frac{\partial H_x}{\partial y} \tag{1.15}$$

$$H_x = -\frac{\beta}{\omega\mu} E_y - \frac{1}{j\omega\mu} \frac{\partial E_z}{\partial y} \tag{1.16}$$

similarly for the TE case the logitudinal component of the electric field is zero, i.e. (E_z = 0). So by choosing Maxwell's curl equations (1.2 and 1.4) the dominant field components are H_y, H_Z and E_X which are given as :

$$H_y = \frac{\beta}{\omega\mu} E_x \tag{1.17}$$

$$H_z = \frac{1}{j\omega\mu} \frac{\partial E_x}{\partial y} \tag{1.18}$$

and

$$E_x = \frac{\beta}{\omega\varepsilon} H_y + \frac{1}{j\omega\varepsilon} \frac{\partial H_z}{\partial y} \tag{1.19}$$

where β and ω are the phase constant, and angular frequency respectively and ε and μ are the permittivity and the permeability respectively.

By combining the equations (1.14-1.16) and (1.17-1.19) for the TM and the TE modes, the scalar wave equations for the isotropic, three-layer, planar optical waveguide can be obtained, which can be expressed as (Koshiba, 1992a) :

$$\frac{\partial^2 \Phi}{\partial y^2} + (k_o^2 n^2 - \beta^2)\Phi = 0 \tag{1.20}$$

where, k_0 is the wavenumber and Φ is the dominant field component for each polarisation i.e. E_x for the TE mode and H_x for the TM mode.

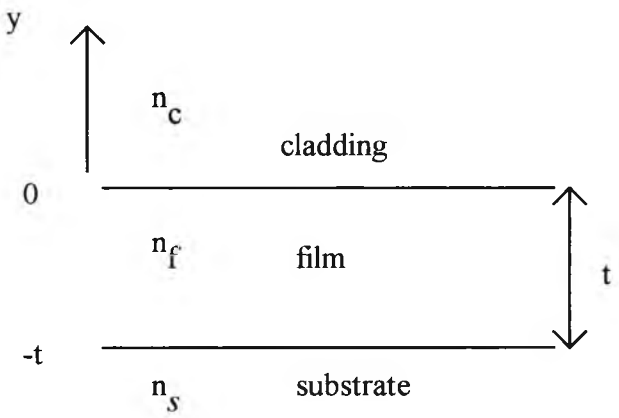

Fig. 1.2 Three-layer planar optical waveguide

In a three-layer planar waveguide, as shown in Fig. 1.2, provided that $n_c < n_g < n_f$ a guided mode satisfies the condition, $k_o n_s \leq \beta \leq k_o n_f$, where n_f, n_s, and n_c are the refractive indices of the core, the substrate and the cladding of the guide, respectively. Then the solution to the wave equation can be expressed as (Koshiba, 1992a) :

$$\Phi = \begin{cases} A_c \exp(-\alpha_c y) & 0 \leq y \\ A_f \cos(k_f y) + B_f \sin(k_f y) & -t \leq y \leq 0 \\ A_s \exp[\alpha_s (y+t)] & y \leq -t \end{cases} \tag{1.21}$$

where A_c, A_f, A_s and B_f are arbitrary

constants and α_c, α_s and k_f, can be defined by :

$$\alpha_c = \sqrt{\beta^2 - k_0^2 n_c^2} \tag{1.22}$$

$$\alpha_s = \sqrt{\beta^2 - k_o^2 n_s^2} \tag{1.23}$$

$$\kappa_f = \sqrt{k_0^2 n_f^2 - \beta^2} \tag{1.24}$$

By applying the boundary conditions for continuity of the tangential components of the electric and magnetic fields (1.12 and 1.13), which are E_X and H_Z for the TE mode and

E_y and E_Z for the TM mode, the phase shift relations can be obtained, which may be expressed as (Koshiba, 1992a) :

$$\Phi_s = \tan^{-1}(m_s\alpha_s / m_f k_f) \qquad (1.25)$$

$$\Phi_c = \tan^{-1}(m_c\alpha_c / m_f k_f) \qquad (1.26)$$

where m_c, and m_s and m_f can be defined by (Koshiba, 1992a) :

$$m_c = m_s = m_f = 1 \qquad (1.27)$$

for the TE mode and,

$$m_c = 1/n_c, \quad m_s = 1/n_s, \quad m_f = 1/n_f \qquad (1.28)$$

for the TM mode.

Then, the condition for the existence of a guided mode is the total phase shift in the y direction during one cycle and it must be an integral multiple of 2π. This can be expressed by the transcendental, or eigenvalue equation as (Koshiba, 1992a ; Tamir 1990) :

$$k_f t - \Phi_c - \Phi_s - q\pi = 0 \qquad (1.29)$$

where q=0,1,2, ...

The formation of discrete modes in a two dimensional waveguide can be explained by using the diagram below :

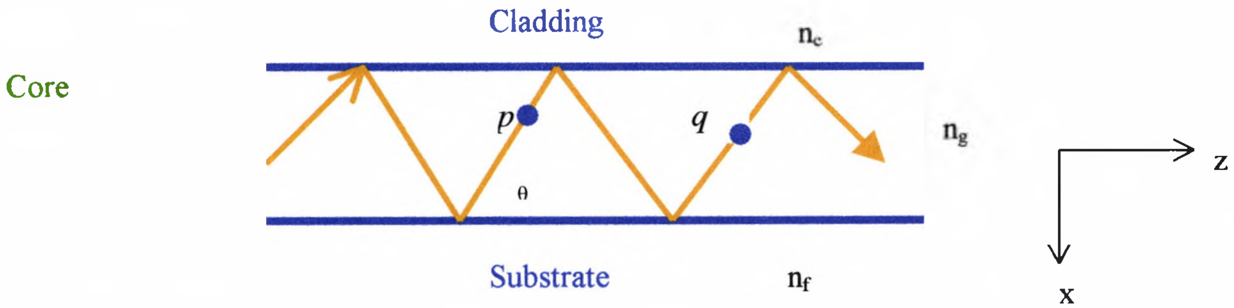

Fig. 1.3 Two dimensional structure showing the total internal reflection

The ray of light in the material of refractive index, n_g, incident on the interface with one of the outer layers, with a refractive index n_c will be partially reflected. If $n_c < n_g$ and the angle of incidence θ is smaller than the critical angle, θ_c, for total internal reflection, given by

$$\theta_c = \cos^{-1}\frac{n_c}{n_g} \tag{1.30}$$

the reflection coefficient will be 1, and the light will be confined to the central layer of the structure, propagating back and forth between the two interfaces. A ray of light confined in such a structure will only interfere constructively with itself when the total phase in one round trip e.g. from p to q in Fig.1.3 , is an integer multiple of 2π, under which condition the light distribution is described as *self-maintaining*.

The actual light distribution of a mode can be found by viewing it as a superposition of an upward and a downward travelling plane wave :

$$\mathbf{E}(x,z)=E_0(a_1 e^{-jk_x x} + a_2 e^{+jk_x x})\, e^{-j\beta z} \tag{1.31}$$

where $k_x^2 + \beta^2 = k_x^2 + k_z^2 = k^2 = (n_1 k_0)^2$. The coefficients a_1 and a_2 are equal for a symmetric structure. Because $(e^{-jk_x} + e^{+jk_x x}) = 2\cos k_x x$, the field in the central (guiding) layer has a cosine-like shape.

1.9 End-to-end coupling of two waveguides

When two waveguides are coupled face-to-face it is called the *butt-coupling*. The modal fields, $\mathbf{H}_m$ in the second waveguide that are excited by the field $\mathbf{H}^{inc}$ emerging from the first waveguide can be decomposed as

$$\mathbf{H}^{\mathrm{inc}}(x,y,z)=\sum_m b_m \cdot \mathbf{H}_m(x,y)\, e^{-j\beta_m z} \tag{1.32}$$

in which b_m is called the *excitation coefficient* for mode, *m*. Because of the orthogonality of the modes (i.e. $\int \mathbf{H}_\mathrm{m}\mathbf{H}_\mathrm{n}^* \cdot d\Omega = 0$ for $m \neq n$), it can be shown that

$$b_m = \frac{\int \mathbf{H}^{\mathrm{inc.}} \cdot \mathbf{H}_\mathrm{m}^* \cdot d\Omega}{\int \mathbf{H}_\mathrm{m}^* \cdot \mathbf{H}_\mathrm{m}^* \cdot d\Omega} \tag{1.33}$$

The numerator of the right hand side of Eq. (1.33) is called the *overlap integral* of fields $\mathbf{H}^{\mathrm{inc}}$ and $\mathbf{H}_\mathrm{m}$. It can be used to calculate the coupling loss occurring at the end-to-end coupling between, for example, a straight and curved waveguide, as well as the optimal lateral offset needed to compensate for the outward shift of the mode profile in the curved waveguide.

1.10 Waveguide Loss

In this section the most important waveguide loss mechanisms are reviewed. With the use of new etching/descuming fabrication process, ridge waveguides have been fabricated on InP with losses below 1dB/cm for TE polarisation, for effective index contrasts up to 0.03. (Spikemen,1993). The ridge sidewall plays a negligible part as far as the scattering loss is concerned. High losses for TM have been observed (10-20 dB/cm), the explanation for which may lie in the large and laterally extended non-dominant field component of the TM mode of these waveguides.

In an optical waveguide, a number of mechanisms may contribute to the loss of part of the guided light. Interaction of light and matter may cause *absorption* or *scattering*, and imperfect guiding can give rise to leakage. Absorption results from imperfect material transparency in which the optical power is converted into other forms of energy. Scattering and leakage remove optical power from guided modes, converting it into radiation.

If the sources of losses are evenly distributed along the waveguide, then the total input power, P, decreases exponentially with propagation distance, z, given by

$$P(z)= P_0\, e^{-\alpha z} \tag{1.34}$$

in which α is the power attenuation coefficient.

1.11 Solutions of optical waveguide problems

In order to understand the propagation characteristics of optical waveguides, the famous Maxwell's equations have to be satisfied with necessary boundary conditions. However, this is not an easy task, because the arbitrarily-shaped dielectric waveguides, in many cases, also happened to be arbitrarily inhomogeneous and/or arbitrarily anisotropic (Saad, 1985). Solutions to these problems can be achieved by using numerical techniques. However, there are several analytical approximations available which can be used to solve one-dimensional problems. They use methods such as the Ray Approximation Method (RAM), (Qiao and Wang, 1992), and the Wentzel, Kramers, Brillouin (WKB) method (Srivatsava *et al.* 1987). On the other hand the numerical methods for solving optical waveguides differ in several respects. Firstly, some methods are aimed at directly solving the equations

$$\nabla \times \mathbf{E} = -\frac{\partial \mathbf{B}}{\partial t} \tag{1.35}$$

$$\nabla \times \mathbf{H} = \frac{\partial \mathbf{D}}{\partial t} \tag{1.36}$$

or their equivalent integral forms, or any of their special-case reduced forms, but the majority of methods aim at transforming such differential or integral equations, through various mathematical modelling processes. This could lead into a system of linear equations solvable by the standard matrix techniques. Secondly, the method may approximate the field over each of the dielectric layers of the waveguide, either at discrete points, employing finite differences, or by an expansion valid over the entire layer, such as in the point-matching method. Thirdly, the methods differ in the way they deal with the infinite extent of the waveguide cross section. For example, the point-matching and some finite-element approaches take advantage of the fact that the field decays in the radial direction away from the guide, while some other finite-element approaches impose various kinds of boundary conditions at some optimised distances, far enough from the guide.

1.11.1 Approximate methods based on separation of variables

There are few waveguide structures that can be analysed exactly by the method of separation of variables. However, the idea of converting a two-dimensional problem into a one-dimensional problem is so appealing that considerable effort has been attracted to developing methods based on approximating rigorously non-separable fields by using separable fields. The major problem with these methods is the limit of the accuracy of the solutions. The most commonly used methods are the Marcatilli Method (MM), and the Effective Index Method (EIM) for rectangular structures.

1.11.1.1 The method of Marcatili and its perturbation correction

Marcatili (1969) approximated the field in a homogeneous rectangular core waveguide with the fields in two slab waveguides, which were obtained by extending the width and the height, respectively, of the rectangular core to infinity. This approach works well in the far-from cut-off region but gives poor results in the near cut-off region. In the scalar approximation, Kumar *et al.* (Kumar *et al.*, 1983) identified the truly separable rectangular structure for which the method of Marcatili was exact, and treated the waveguide under investigation as a perturbation of this structure. This perturbation method produces more accurate results, and has been applied to anisotropic channel waveguides (Kumar *et al.*, 1984), and strip and rib waveguides (Varshney and Kumar, 1988).

1.11.1.2 Effective Index Method

The effective-index (EI) method was first proposed by Knox and Toulis (Knox and Toulis, 1970) with a view to improving Marcatili's earlier results (Marcatili, 1969) for the fundamental mode of a simple rectangular core waveguide. The basic principle of the effective index method involves the replacement of the rectangular structure by an equivalent slab with an effective refractive index obtained from another slab. As only the solutions for slab waveguides are required, this method is significantly more efficient than those methods that solve the rectangular structure directly.

The first theoretical study of the method was given by Peng and Oliner (Peng and Oliner, 1981), who pointed out that, in the case of analysing composite rectangular waveguides, the effective index method was, in fact, the lowest-order version of the mode-matching method, which they developed.

In spite of its popularity, the effective-index method does not give satisfactory results in the near cutoff region (Marcatili, 1969). To improve the accuracy, Chiang (Chiang, 1989) proposed the dual effective-index method, which required a linear combination of two solutions corresponding to two different ways of applying the effective-index method to the waveguide. Kim *et al.* (Kim *et al.*, 1993) proposed a modified effective-index method, in addition to the similar method proposed by Cheng and Lin (Cheng and Lin, 1990), which are no better than the method of Marcatili in the scalar approximation (Chiang, 1992). Recently Chiang proposed an effective-index method with a built-in perturbation correction. This method is more accurate than other methods given by (Marcatili, 1969) and (Kumar *et al.*, 1983) with the same degree of simplicity and efficiency. Kumar *et al.* in their scalar approximation derived the rectangular structure for which the effective index method was exact. Kumar's findings were used by Chiang (Chiang, 1996) to derive asymptotic error expressions for the method and clarified quantitatively many of the long-observed properties of the method.

1.11.2 Fully numerical method or approximate method

The choice between a fully numerical method or an approximate method depends on the accuracy that is required in any particular situation. In general, for the planar structures, the EI method gives satisfactory results which are accurate enough for the characterisation of most of the devices. However, for the accurate characterisation of two dimensional structures a fully numerical method, such as the finite-element or finite-difference method is more accurate. However, the numerical methods also suffer from certain built in errors, where such errors are caused especially in the finite difference method near the cut-off, due to discretisation problem associated with the slowly decaying field. So generally if the accuracy of the method is satisfactory by an approximate method for a particular problem it is better to use that. The continuing improvement in computer power will make computational efficiency less of an issue in the future than it has been. This trend will favour the implementation of fully numerical methods, but a consideration of the effort required for software development may still favour the use of approximate methods for low-budget projects.

The selection of a numerical scheme is dominated by several factors, and so to find the 'best method' the following steps have to be considered :

(a) the shape of the region R; in particular if it is curved or, polygonal and concave or non-convex.

(b) the method should be realised with a computer program which

  (i) should be suitable for the automatic solution of a wide range of geometry's.

  (ii) virtually has to be written specially for each region R.

(c) whether the field distribution as well as the cut-off frequency is required.

(d) whether the dominant mode or a number of the low eigenvalues are required.

(e) the requirement of accuracy for eigenvalues, e.g. is the asymptotic convergence a 2:1 improvement in accuracy, requiring twice or more the computing time.

(f) whether the selected method can handle near cut-off frequencies and the degree of accuracy achievable.

(g) if the selected scheme is accurate for both the linear and non-linear models.

(h) the computational time and the memory requirement.

1.11.2.1 The variational method

The variational principle may be used to analyse waveguides by finding a closed-form, approximate solution to the given problem. Initially a closed-form field solution is assumed, with unknown parameters which can be chosen to match the assumed field to the actual field solution in the optimum way. Then a functional, which is based on the scalar wave equation and which is stationary for the solutions to the waveguide problem, may be used. By substituting the assumed field into the functional and knowing that the functional is stationary at the actual solution, the values of the unknown parameters which will yield a best-fit approximation may be determined. This information may also be used to determine the propagation constant of the propagating mode solution. The values of the unknown parameters of the assumed field are calculated by solving a set of simultaneous equations, not by a search method. Hence this method is computationally more efficient.

In variational method the accuracy of the method depends on a judicious choice of the trial field (Mishra, 1985). There are several trial fields employed in optical waveguide problems, which are the cosine-exponential function (CE), the modified Hermite-Gauss function (MHG), a simple modified Hermite-Gauss function (SMHG) and a modified Hermite-Gauss exponential function (MHGE). The choice was made to resemble the fields encountered in practice, but in each case the trial field will be adjusted by adjusting a variational parameter to maximise the propagation constant β, without changing the functional form of the trial function.

The finite element and the finite difference methods are based on the variational formulation.

There are different forms of variational formulation for finite element methods. The scalar form of the FEM is used for solving homogeneous waveguide problems. This scalar form may be inadequate in hybrid mode situation, inhomogeneous or anisotropic problems. A finite element formulation using the axial components of the fields has been used to solve many waveguide problems (Mabaya, 1981). However, for a guide with arbitrary dielectric distribution, the satisfying boundary conditions in this method can be quite difficult. Another disadvantage is that it uses the axial components, which are the least important components of the six-vector field. In 1956 Berk (Berk, 1956) derived some important vector variational formulations in the form of a Rayleigh quotient for loss-free anisotropic microwave waveguides and resonators. Later Morishita and Kumagai (Morishita and Kumagai, 1977) derived a vector variational formulation. By contrast, a vector field was applied by English and Young (English and Young, 1971). In this vector **E** field formulation it involved more Dirichlet (rather than Neuman) boundary conditions. But for this formulation, the natural boundary condition **n** x **E** =0 is necessary on the conducting boundaries, it is an added difficulty to implement that boundary condition on an arbitrarily shaped guided wall. The **H**-field formulation is more advantageous than the other formulations because in this formulation the natural boundary condition is that of the electric wall. So that for arbitrary conducting guide walls it can be left free. This formulation can also handle the anisotropic problems, which are important for many active and passive integrated optics structures. As the natural boundary condition for **H**-formulation is the electric wall we need not force any boundary condition. However, if the structure is symmetrical than boundary can be forced to reduce the computational cost.

1.11.2.2 The boundary-matching method

There are several ways to eliminate matching the fields at discrete points, and hence choosing these points. Wang and Vassallo (Wang and Vassallo, 1989) proposed a method for the analysis of an arbitrarily shaped optical fibre, in which both the boundary and the field are expanded in circular harmonics and a set of ordinary differential equations for the radial components in the expansion for the field is generated. Solving this set of equations in an annular region leads to a matrix equation. In this method, the fields in the core and the exterior region are expanded in series of circular harmonics as in the point-matching method, but the field along the boundary is expanded in a Fourier series. In the method proposed by Miyamoto (Miyamoto, 1991) for the analysis of a three-layer elliptical-core waveguide, the fields in different regions are expanded in series of circular harmonics and matched at the boundaries in the least-squares sense.

1.11.2.3 The mode-matching method

The Mode Matching Method (MMM) is very similar to the boundary-matching method. Here the field is expanded in the local regions of the waveguide in terms of the normal modes of those regions. This method which is also known as the Equivalent Network Method (ENM), is an approximate analysis used for the determination of the propagation characteristics of an open dielectric waveguide.

The waveguide cross section is varied in terms of its constituent parts or building blocks, which are usually portions of uniform dielectric layered structures interfaced by the dielectric step discontinuities. The fields in the various regions are then expanded in terms of transverse modal expansions over each region, thus resulting in a microwave equivalent circuit representation of the waveguide.

1.11.2.4 The Spectral Index Method

The spectral index method is a semi-numerical method in which the Maxwell's equation is expressed in terms of Fourier series and Fourier transforms. This method is mainly used to solve the rib waveguide problems (Kendal *et al.*, 1989; Stern *et al.*, 1990). This method is also used to analyse strip loaded directional coupler (Burke, 1990). Recently Pola *et al.*, (Pola *et al.*, 1996) have used this method to analyse multiple core coupled rib waveguides.

The speed and accuracy of the method lie in its use of a Fourier transform to generate a spectral index for the region below the rib. The problem reduces to a 1-dimensional problem, where the refractive indices of the layer below the rib are represented by their corresponding spectral indices. The spectral index solution requires three steps :

(i) a Fourier transform in the transverse horizontal direction below the rib and (ii) a Fourier series in terms of sine and cosine functions inside the rib, together with (iii) a technique for linking the two solutions via a transfer relationship and obtain transcendental equation. By solving these transcendental equations the propagation constant can be determined. The presence of the strong dielectric discontinuity at the rib region can be dealt with by using an effective rib width and an effective outer slab width. While in the Fourier transform for the region below the rib evanescent regions are expressed by imaginary spectral indices. However, the problem with this method is that in Fourier series expansion of a discontinuous function in continuous basis functions the 'Gibbs phenomenon' occurs. Therefore the series converges slowly and exhibits oscillation near the discontinuity when truncated after a finite number of terms (Subdo, 1992).

1.11.2.5 The Beam Propagation Method

The Beam Propagation Method (BPM) solutions for optical waveguides can be made to generate such mode-related properties such as propagation constants, relative mode powers, and group delays with high precision and considerable flexibility. This method which was originally introduced by Feit and Fleck (Feit and Fleck, 1980) to optical waveguide problems solve the Helmholtz or the parabolic wave equations and a system of coupled ordinary differential equations, for each dielectric layer, is obtained. By suitable matrix transformations, the above system is uncoupled and the equations can be solved analytically. Further application of boundary conditions at waveguide discontinuities leads to matrix equation, from which the eigenvalues can be calculated.

When applied to uniform waveguides, the BPM consists of calculating the field in the paraxial approximation as it propagates down the waveguide, and performing the Fourier transform of a correction function relating the evolved field and the incident field to yield the mode spectrum. The advantage of BPM compared to FEM is that BPM can be used to analyse non uniform waveguides. The BPM has been limited in the past to solve the scalar-wave equation, but significant progress has been made to extend the method to solve the vector-wave equation (W.P. Huang, 1992).

For the analysis of uniform structures, however, this method is not as efficient as the FDM or the FEM. Because the discretization in both the transverse plane and the longitudinal axis are required for which FDM or the FEM is more accurate.

1.11.2.6 The finite difference method

The finite difference method (FDM) is one of the oldest and easy to implement numerical technique to solve optical waveguide problems. The finite-difference method, like the finite element method, demands the division of the waveguide cross-section into a small sub region, and therefore, is suitable for modelling inhomogeneous media and complicated boundaries. Although the FDM is potentially applicable to anisotropic wave-guides, the implementations so far have been mainly limited to isotropic media.

In this method the electric component of the optical field is taken as a matrix of discrete values throughout a box large enough to contain the waveguide and the adjacent regions where the field strength is significant. It is assumed that the field at the boundary is zero. The scalar wave equation becomes a difference equation, with the partial derivatives approximated by the differences between adjacent field points. Given a guess of electric field within the box and an estimation of propagation constant, an iterative procedure can be used to establish the propagation constant of the mode after each iteration, and convergence of this value is the criterion for sufficient accuracy.

Because of the discontinuities in refractive index at the interfaces between different layers and air, two alternative methods of assigning refractive index values to matrix points have been used.

In the first case the mesh is chosen so that the points lie on the interfaces where they are assigned to have a refractive index equal to an average of the adjacent points. In the second case, the matrix points are arranged to straddle the boundaries. The mesh size will also determine the accuracy of the field and the propagation constant because the larger the mesh size, the less valid is the approximation of a difference equation to the wave equation. The size of the box within which the computations are performed is also important. If the box is too large the convergence will be very slow; if it is too small the assumption of zero field at the boundaries of the box may be invalidated.

The only disadvantage of the FDM over FEM is that irregular meshing cannot be easily implemented. So in analysing structures which are large with interesting properties in certain smaller regions the accuracy of the solutions will depend on the mesh. Even though the recent super computers can handle very large mesh sizes the computational time is reasonably high.

1.11.2.7 The Finite Element Method

In order to optimise the performance of microwave and optical devices a good knowledge of their propagation characteristics and field distribution is essential. The Finite Element Method (FEM) has become one of the most accurate and versatile numerical tool in the analysis of optical waveguides. The FEM is also used widely in other areas of engineering. Particularly in the analysis of complicated structures, thermal, fluid flow, semiconductor, and electromagnetic problems. This method can handle waveguides with arbitrary shape, arbitrary refractive index profile, and anisotropy.

Finite element formulations can be done by the variational or the Galerkin method. Variational approach is more appropriate when only one global parameter is required. In the FEM, the primary dependent variables are replaced by a system of discretized variables over the domain of consideration. In this method initially the waveguide cross section will be divided into patch work of triangular sections called '*elements*'. Using many such elements complex structures with arbitrary index profiles can be accurately approximated.

The simplest triangular element assumes a linear interpolation between the vertices of the triangle. By expressing the fields in terms of the nodal values and with the assumed shape functions, the resulting field components are continuous over the whole domain. By applying the variational principle (Davies, 1989) to the functional of the system, the problem reduces to a standard eigenvalue equation, with vector x of nodal variables, $Ax-\lambda Bx=0$. This equation can be solved by one of the standard subroutines available and hence the eigenvalues and eigenvectors can be obtained.

In 1956 Berk (Berk, 1956) presented a number of vector variational formulations in the form of Rayleigh quotient for loss-free anisotropic waveguides and resonators in terms of the **E** field and **H** field or the combination of both. However, for the **E** field formulation, the natural boundary condition is that of a magnetic wall, which cannot be left free for an electric wall boundary. As the necessary boundary condition **n** x **E** =0 must be imposed on any conducting boundaries, it is very difficult to implement this boundary condition on arbitrarily shaped guide walls. The other disadvantage of the **E**-field formulation is that a special care should be taken to preserve the continuity condition of the transverse components of the fields. For many purposes, a vector **H**-field formulation (Rahman and Davies, 1988) has the advantage over all the others. In this formulation the natural boundary condition is the electric wall, so that for an arbitrary conducting guide walls it can be left free. In this formulation, the chosen field is continuous at the dielectric interfaces, and so it is very convenient for the finite element solution of dielectric waveguide problems.

This formulation can be used for general anisotropic problems, which are important for many active and passive waveguide structures. However, in vector **H**-field formulation the most serious early problem arised due to the presence of the spurious or non physical modes (Rahman and Davies, 1984). In the conventional FEM, the associated Euler equation is consistent with the two Maxwell curl equations but does not imply $\nabla \cdot \mathbf{B}=0$. This causes the system to be 'under-determined' or excessively flexible, which in turn is believed to be responsible for the spurious modes. Spurious modes can be identified from their dispersion curve (Rahman and Davies, 1984), since the non physical field distributions usually vary in an unreasonable, sometimes random fashion over the guide cross section. In the full vector formulation from the values of $\nabla \cdot \mathbf{B}$ the spurious modes can be identified. The spurious solutions can be eliminated if the condition $\nabla \cdot \mathbf{H} = 0$ is somehow forced. The penalty function method introduced by Rahman and Davies (Rahman and Davies, 1984) introduces a penalty term in the variational formulation. A scheme for the elimination of spurious modes involve so-called *'edge-elements'* has been proposed by Bossavit and Mayergoyz in 1989 (Bossavit and Mayergoyz, 1989). In this approach, the tangential field components between elements are forced to be continuous. The spurious modes can also be eliminated by the $\mathbf{H_t}$ formulation (Koshiba *et al.*, 1985), where H_z component is eliminated by using the divergence condition.

In the finite element method often it is required to calculate the fields at infinity near the cutoff and it is important to consider an extended boundary near the cutoff. One conventional technique is to shift the virtual boundary wall recursively to satisfy a maximum field strength at that wall. However, the infinite elements introduced by Rahman and Davies (1984) is the most powerful technique to deal with waveguide problems near cutoff. The full vector (**E** or **H**) formulation appears to be still the most convenient for practical large scale problems since, although it uses three rather than the minimum of two components to describe the fields, the resultant matrix problem can be solved using standard software packages.

The FEM is comparatively more accurate than the finite difference method for most of the guided wave device characterisation. Although computationally the FDM is easy to implement the computational time increases exponentially with accuracy. Apart from that the FDM cannot handle problems with arbitrary shaped boundaries and index profiles. FDM cannot be used for cases where irregular meshing is desired, whereas in FEM irregular mesh can be used, which increases the accuracy of the results.

1.12 Aims and objectives of the thesis

So far the background information to this research work has been illustrated and important topics related to this research have been covered. The main objectives of this thesis are outlined below :

(1) To study the characteristics of optical polarizers based on different techniques, starting with a metal clad optical polarizer. In this study the TE/TM polarizer is designed such that $L_{cTE} = 2*L_{cTM}$ where L_{cTE} and L_{cTM} are the coupling lengths of the Transverse Electric (TE) and Transverse Magnetic (TM) modes respectively, and the power transfer characteristics of a metal clad polarizer are shown. The importance of the modal loss is also studied and the power transfer curve is shown for the loss case. Following that, a Multiple Quantum Well (MQW) based polarizer is studied, this being the first time such an approach is considered for the design of optical polarizers.

(2) In a study of the important properties of multimode interference-based devices (MMI), initially a planar 3dB coupler is analyzed. The propagation constants and the coupling lengths of all the modes present in the multimode section are calculated and the excited coefficients for two different mesh sizes are obtained to show the accuracy of the finite element method. Next a more realistic structure with a two dimensional confinement is investigated and a comparison is made on the basis of some important operating properties of both the directional coupler and the MMI. This is the first time properties such as cross talk, polarization dependence and device length have been rigorously compared for both the devices.

(3) To investigate the properties of spot size expanders based on directional couplers (DC) and multimode interference devices (MMI). The coupling lengths, L_C , for both the MMI and the DC are obtained from the first and the second mode propagation constants. In this section, some of the previously published work is considered initially and the topic is extended to the study of reflection coefficients in spot size expanders. The modal excitation coefficients are calculated and the power transfer efficiency is

determined. Direct laser-to-fibre coupling efficiency is compared with the results obtained using an intermediate directional coupler section. A three-guide and five-guide directional coupler based spot size expanders coupling efficiency is also studied. In the three guide case initially a planar structure is investigated. The idea of MMI based spot size expanders is also illustrated for the first time in this work.

The power transfer efficiency using simple analytic equations are compared with that of the Least Squares Boundary Residual (LSBR) solutions.

1.13 Structure of the thesis

This section gives an outline of the thesis. The author has used the powerful and versatile finite element method in combination with the Least Squares boundary Residual method to study some of the relevant and topical properties of optical waveguides for use in a range of situations.

Initially to give a flavour to the topic studied in this research work, an introduction section is given with some historical background to the topic. Chapter 1 also explains the need to use the numerical techniques and covers the basis of some semi-analytical and most of the important numerical techniques. The subsequent chapters give an introduction to the basic theory followed by the analysis and presentation of results.

Thus Chapter 2 starts with a brief introduction section which extends to give a historical background to the finite element method. The uses and advantages of using the finite element method are discussed, followed by consideration of the detailed formulation of the finite element method for optical guided wave problems. A small section is contributed on the penalty function method, which is used to avoid the spurious or non physical modes. Finally the use of the infinite elements to analyze optical fields at infinite regions is also included in this chapter.

Chapter 3 discusses some of the important theory and the operating principles of directional coupler and the Multimode Interference-based devices considered in this work.

Chapters 4,5, and 6 describe the analysis of the results of various types of important optical waveguide problems. The results obtained using the finite element and the Least Squares boundary Residual methods are compared with the results obtained using simple techniques, such as the overlap integral (OI) method.

Chapter 4 describes the design of optical polarizers using directional couplers. Two different approaches are presented here, one using metal clad on one of the branches of the directional coupler and the other using a directional coupler with one guide made of MQW. In the first approach using the metal-clad based directional coupler the modal propagation constants and the field values are obtained for the super structure. The excited coefficients of the supermodes are calculated and the power transfer at various axial (*z*) locations are calculated. The modal loss is an important parameter which is excluded in most of the waveguide analysis. In this study the modal loss is included and the power transfer characteristics for both the polarisations is plotted. In the MQW based polarizer the equivalent index of the MQW region for the 2-dimensional structure is evaluated using the finite element method and a comparison is made with the analytical results which is valid only for 1-dimensional structures.

Chapter 5 is dedicated to the study of multimode interference based devices (MMI). In this chapter initially a planar 3-dB coupler based on MMI is studied to show the validity of our method. In this study the accuracy of the results is varified by changing the mesh values, and the theory of *'restricted resonance'* is also verified. Next a two dimensional structure is simulated to get a more accurate design. In the 2-dimensional study the excited coefficients of the dominant modes are calculated by using the LSBR and the simple overlap integral methods. It is shown that the results obtained using the

LSBR method is more accurate compared to the one using overlap integral. The reflection coefficient is also calculated for this structure. Important design properties such as crosstalk, excess loss and imbalance are also calculated for those 3dB coupler. The fabrication tolerances of the MMI devices are demonstrated by changing the MMI width, as is its polarization property, for the 3 dB coupler.

Secondly, a 1X4 way power splitter is studied, from which it can be shown that the MMI can be used as a multiplexer.

Thirdly, a MMI based duplexer is characterised. Initially a planar duplexer structure is simulate, its operating principle is studied, and it is shown that at a particular axial location the two wavelengths 1.55μm and 0.98μm emerge from the two output ports of the MMI.

Finally a comparison is made between the directional coupler and the MMI. Some of the important properties such as the device length, cross talk, polarization dependence, and fabrication tolerance are studied. This is the first time such a rigorous comparison is made between the MMI and DC.

Chapter 6 deals with spot size expanders which is currently an industrially demanding area of research, as laser-to-fibre coupling is an important issue as far as photonics technology is concerned.

Initially some of previously published results are reproduced and a comparison is made on different structures, where the reflection coefficients are also calculated for these designs, which is an important factor and frequently neglected by many research workers.

Next, in chapter 6, a new design using synchronous directional couplers is studied. It is shown in this study by using an intermediate directional couper section the laser field from the input guide can be transferred to a lower guide of larger dimension so that a bigger spot size can be obtained. This idea of using directional couplers is further extended to the case of three-guide and five-guide couplers. Initially a planar three guide structure is studied, where the power coupling efficiency is obtained using the LSBR method and this results is compared with that of the simple analytical results. Next a 2-dimensional three guide structure is simulated, and finally a five guide structure is studied to show that the five guide structure eventhough has a larger spot size suffers from tight fabrication tolerances.

Finally in this chapter conclusions from this research work are analysed and discussed in detail. Some suggestions are also been made for some future work on this area. The list of references are given in the final part of this thesis, together with publications by the author relevant to the work.

1.14 Summary

In this chapter a brief introduction is given to the field of optical communications, and some of the advantages and the problems that are faced are also discussed. Several numerical methods are discussed with their comparative advantages and disadvantages, and finally the structure of this thesis is sketched. With the knowledge of the basic concepts to the subject and to the numerical methods, in Chapter 2 the finite element method is explained in more detail which will be used as the numerical tool in this research work.

Chapter 2

The finite element method

2.1 Introduction

Most waveguiding problems can be described by the differential equations and subsequently may be solved by using the variational principles. In general due to the complexity of problem geometry encountered in practice, it is often difficult if not impossible to find a solution to these equations in a closed form that will satisfy given boundary conditions, and numerical methods have to be used.

The development of increasingly sophisticated integrated optical and microwave devices has created a strong need for accurate analysis of arbitrary structures. The finite-element method (FEM) is probably by far the most powerful method for dealing with optical waveguides that cannot be treated by analytical techniques. This method is used to determine the propagation constants of the modes in dielectric waveguides.

The FEM formulations are usually established via a variational (Davies, 1989) or a Galerkin (Berk, 1956) approach. In the FEM, the region of concern is subdivided into a patchwork of a number of subregions called '*elements*'. These elements each can be of various shapes, such as triangles or rectangles or even have curved sides and they can be of various sizes, to suit the device to be represented. Using many elements, any cross-section with a complex boundary and various refractive index profiles can be accurately approximated. Each element can also have a different loss or gain factor, different anisotropy or different nonlinearity, so a wide range of practical waveguides can be considered.

2.2 Historical background

The research on the application of the finite-element method to the electromagnetic-wave engineering has been made in the early 1960s (Ahmed, 1968). However, the application of the FEM to the electromagnetic problems became active since the early 1970s. Today the FEM is considered to be one of the most powerful numerical techniques to analyse optical waveguide problems from the microwave to optical wavelength regions. However, one of the earlier difficulty in applying the finite-element method to such electromagnetic waveguide problems is the appearance of the so-called 'spurious', non-physical solutions. The approach to suppress these spurious solutions has earlier been demonstrated by Rahman and Davies (Rahman and Davies, 1984). The ways to avoid these spurious modes have also been studied extensively (Hayata, 1986).

2.3 The range of applications

Electromagnetic problems can be classified into the following groups :

1. One-, two-, and three-dimensional problems
2. linear and nonlinear problems
3. bounded and unbounded field problems
4. homogeneous and inhomogeneous problems
5. forward and inverse problems
6. steady and unsteady problems
7. scalar and vector problems
8. isotropic and anisotropic problems

The waveguide problem discussed in this chapter belongs to the categories of eigenvalue and of steady state nature. Because the problem region is the waveguide cross section, the waveguide problem can be regarded as the one- or two- dimensional problem. In this chapter the emphasis is on the **H**-field formulation since it forms the basis of the numerical analysis presented here. In this formulation each field component H_x, H_y, and H_z is separately represented by a function continuous over the whole transverse domain. This is particularly convenient for guides with permittivity discontinuities where continuity of **H**-field components is automatically satisfied.

2.4 Elementary ideas of the finite-element method

In the FEM, instead of differential equations (governing equations) for the system under investigation, corresponding functionals (variational expressions) to which a variational principle is applied are set up, where the region of interest is divided into the so-called *'elements'*; an equivalent discretized model for each element is constructed; and then all the element contributions to the system are assembled. In other words, the finite-element method can be considered a subclass of the Ritz-Galerkin method, in which piecewise defined polynomial functions are used for trial functions and infinite degrees of freedom of the system are discretized or replaced by a finite number of unknown parameters. In classic analytical procedures without subdivision processes, the system is modelled using analytical functions defined over the whole region of interest, and therefore these procedures generally are applicable only to simple geometry's and materials. Of the various forms of discretization possible, one of the simplest is the finite-difference method, and its original versions use a regular mesh, i.e. a rectangular grid with nodes at the intersections of orthogonal straight lines. However, a regular grid is not suitable for curved boundaries or interfaces, because they intersect gridlines obliquely at points other than the nodes. Moreover, a regular grid is not suitable for problems with very steep variations of fields. The FEM is somewhat similar to the finite difference method, however in the FEM, the field region is subdivided into elements; that is, into subregions. Elements can have various shapes and sizes, such as triangles and rectangles, allowing the use of an irregular grid. Therefore, the FEM is suitable for problems with steep variations of fields. Furthermore, this approach can be easily adapted to inhomogeneous and anistropic problems, and it is possible to systematically increase the accuracy of solutions obtained as necessary. Furthermore, the FEM scheme can be established not only by the variational method but by the Galerkin method, which is a weighted residual method. Therefore, the FEM may be applicable to problems where a variational principle does not exist or cannot be identified and certainly will become more widespread in the near future.

2.5 Steps involved in the FEM analysis

- discretization of the region of interest into a number of subregions or elements. The finer the discretization, the more accurate the solution.
- derive the functionals to which the variational principle is applied for the elements.
- assemble all the element contributions.
- solve the system of equations that is obtained.

In classic analytic procedures, without subdivision processes, the system is modelled over the whole region using analytic functions, hence these approaches are only suitable for planar or -one dimensional structures.

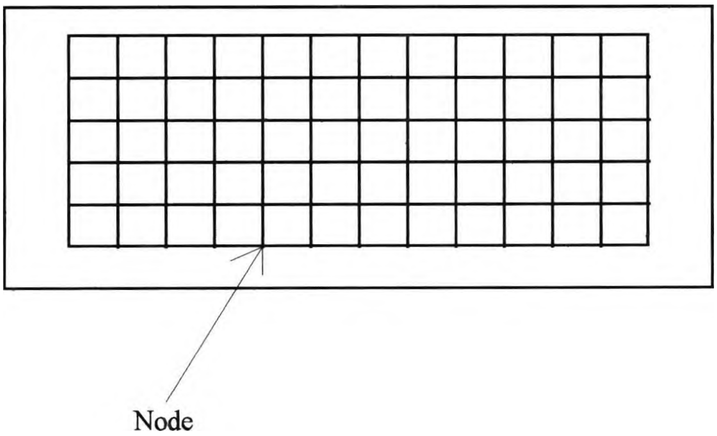

Fig. 2.1 Regular grid

An important part of the FEM is as described above, the discretization of the region of interest, into elements. One of the simplest forms of discretization is to use a regular grid as shown in Fig. 2.1 (Finite difference method). A regular grid consists of rectangular grid in which the intersection of the orthogonal straight lines are termed the 'nodes'. However, a regular grid is not suitable for curved boundaries or interfaces, because they intersect grid lines obliquely at points other than the nodes. Also the regular grid is not suitable when the area of interest is only a small region surrounded by a larger area.

From experience, some general rules for the discretization process have been established :

- when the field is suspected to have step variations at a point it is recommended to use more divisions (finer mesh) around this point.
- the elements should not have very obtuse or acute angles.
- the elements should not be intersected by physical boundaries or interfaces.
- if a domain is symmetrical, the mesh should follow the same type of symmetry.

In Fig. 2.2 it is clearly shown, how the different regions of the waveguide (cladding, core and substrate) can be divided into different numbers of elements. Nevertheless, in order to get accurate results, it is necessary to use a much finer mesh.

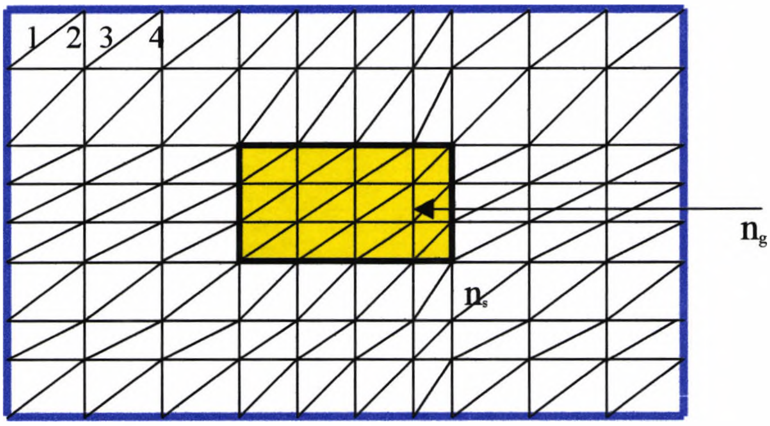

Fig. 2.2 10 x 8 mesh. The first few elements are numbered.

In Fig. 2.2 the numbers 1,2 signify the triangular elements, and n_g and n_s are the refractive indices of the guide and the substrate respectively.

The elements shown here are triangular shape and this is quite common for the FEM as it is easier to represent an arbitrary cross section with a set of triangles rather than rectangles. In the analysis of 2-D waveguides the triangles can be of first, second or even higher order, depending on the allowable field variation within the triangles.

2.6 Different types of elements

Each of the discretized subdivision of a whole domain is called an 'element'. There are various elements available in FEM to discretize a continuous domain. They are

(i) line elements (one-dimensional)

  (a) first order

    - (b) second order
    - (c) or higher order

- (ii) triangular elements (two-dimensional)
    - (a) first order
    - (b) second order
    - (c) or higher order

- (iii) rectangular elements (two dimensional)
    - (a) first order
    - (b) second order
    - (c) or higher order

- (iv) tetrahedral elements (three dimensional)
    - (a) first order
    - (b) second order
    - (c) or higher order

- (v) ring elements (one dimensional)
    - (a) first order
    - (b) second order
    - (c) or higher order

The unknown function ϕ within each element is defined in terms of ϕ_i as

$$\phi = \sum_{i=1}^{m} N_i \phi_i \tag{2.1}$$

where ϕ_i is the ith nodal parameter and N_i is the ith shape function for the *m* nodes in each element.

In the FEM analysis of electromagnetic problems the use of triangular elements of first, or second order is very common. In the application of the first order elements, nodes occur at the vertices of the triangle, while for second order triangles, nodes are also defined at the middle of the edges of the triangle. The second order triangular elements are computationally costly. In this research work the first order triangular elements are used.

It should be noted that since adjacent elements, have common nodes, the numbering of the nodes should be done in such a way so that common nodes are assigned the same number.

2.6.1 Triangular elements

Figure 2.3 below show the fist and the second order triangular elements which are very common in the finite element analysis.

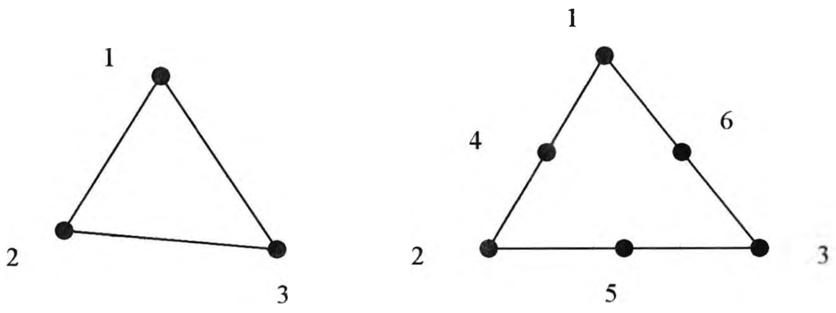

Fig. 2.3 (a) first-order (b) second order triangular elements

In two-dimensional analysis of FEM the area co-ordinates L_1, L_2, L_3 are introduced. The relation equation between the area co-ordinates and Cartesian co-ordinates is given by

$$\begin{bmatrix} 1 \\ x \\ y \end{bmatrix} = \begin{bmatrix} 1 & 1 & 1 \\ x_1 & x_2 & x_3 \\ y_1 & y_2 & y_3 \end{bmatrix} \begin{bmatrix} L_1 \\ L_2 \\ L_3 \end{bmatrix} \tag{2.2}$$

or

$$\begin{bmatrix} L_1 \\ L_2 \\ L_3 \end{bmatrix} = \begin{bmatrix} 1 & 1 & 1 \\ x_1 & x_2 & x_3 \\ y_1 & y_2 & y_3 \end{bmatrix}^{-1} \begin{bmatrix} 1 \\ x \\ y \end{bmatrix} = -\frac{1}{2A_e} \begin{bmatrix} a_1 \, b_1 \, c_1 \\ a_2 \, b_2 \, c_2 \\ a_3 \, b_3 \, c_3 \end{bmatrix} \begin{bmatrix} 1 \\ x \\ y \end{bmatrix} \tag{2.3}$$

where x_k, y_k are the Cartesian co-ordinates of the vertex k (k=1,2,3) of the triangle, and the area of the element, A_e, and the coefficient a_k, b_k, and c_k are given by

$$2\,A_e = \begin{bmatrix} 1 & 1 & 1 \\ x_1 & x_2 & x_3 \\ y_1 & y_2 & y_3 \end{bmatrix} \tag{2.4}$$

$$a_k = x_l\,y_m - x_m\,y_l \tag{2.5a}$$

$$b_k = y_l - y_m \tag{2.5b}$$

$$c_k = x_m - x_l \tag{2.5c}$$

Here the subscripts *k*, *l*, *m* always progress module 3 *i.e.*, cylindrically around the three vertices of the triangle.

Defining the local co-ordinates ξ, η as

$$L_1 = \xi \tag{2.6a}$$

$$L_2 = \eta \tag{2.6b}$$

$$L_3 = 1-L_1-L_2 = 1-\xi-\eta \tag{2.6c}$$

the transformation relation for differentiation is given by

$$\begin{bmatrix} \dfrac{\partial}{\partial \xi} \\ \dfrac{\partial}{\partial \eta} \end{bmatrix} = [J] \begin{bmatrix} \dfrac{\partial}{\partial x} \\ \dfrac{\partial}{\partial y} \end{bmatrix} \tag{2.7}$$

with

$$[J] = \begin{bmatrix} x_1 - x_3 & y_1 - y_3 \\ x_2 - x_3 & y_2 - y_3 \end{bmatrix} \tag{2.8}$$

or

$$\begin{bmatrix} \dfrac{\partial}{\partial x} \\ \dfrac{\partial}{\partial y} \end{bmatrix} = [J]^{-1} \begin{bmatrix} \dfrac{\partial}{\partial \xi} \\ \dfrac{\partial}{\partial \eta} \end{bmatrix} \tag{2.9}$$

$$[J]^{-1} = \frac{1}{2A_e} \begin{bmatrix} b_1 & b_2 \\ c_1 & c_2 \end{bmatrix} \tag{2.10}$$

The transformation relation for integration is given by

$$\iint_e f(x,y)\, dx.dy = 2A_e \int_0^1 \int_0^{1-\xi} f(\xi,\eta).d\xi.d\eta \tag{2.11}$$

from Eq. (2.6)and (2.11) we can write differentiation and integration formulas as

$$\frac{\partial f}{\partial x}=\frac{1}{2A}(b_i\frac{\partial f}{\partial L_1}+b_2\frac{\partial f}{\partial L_2}+b_3\frac{\partial f}{\partial L_3}) \tag{2.12}$$

$$\frac{\partial f}{\partial y}=\frac{1}{2A_e}(c_1\frac{\partial f}{\partial L_1}+c_2\frac{\partial f}{\partial L_2}+c_3\frac{\partial f}{\partial L_3}) \tag{2.13}$$

$$\begin{aligned}\iint_e L_1^k L_2^l L_3^m .dx.dy &= 2A_e\int_0^1\int_0^{1-\xi} \xi^k[\eta^l(1-\xi-\eta)^m .d\eta].d\xi \\ &= 2A_e\frac{k!\,l!\,m!}{(k+l+m+2)!}\end{aligned} \tag{2.14}$$

2.7 Application to waveguide problems

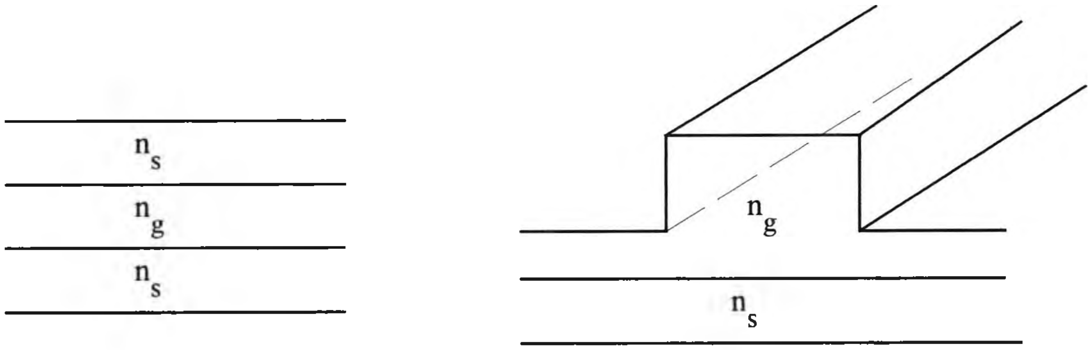

Fig. 2.4 (a) Planar waveguide (b) Two dimensional structure

The waveguide analysis can be classified into two types

(a) one- dimensional, and

(b) two- dimensional.

Fig. 2.4 (a) shows a simple planar waveguide which can be solved as a simple one dimensional problem. Fig. 2.4 (b) an arbitrarily shaped waveguide which should be treated as a two dimensional problem. However, the analysis method to consider depends on the eigenmode property in a waveguide. Which will lead to either a scalar or a vector analysis. From the above discussion the following classifications can be made :

(i) scalar wave analysis by the one- dimensional, FEM

(iii) scalar wave analysis by the two dimensional FEM.

(iv) vector wave analysis by the two dimensional FEM.

From the above three classes the vector approach is more accurate and versatile for two dimensional analysis. For the one dimensional cases the scalar approach is sufficient. However, to handle hybrid mode situation and for polarisation study a rigorous two-dimensional vector model is needed.

The problem with the vector solution is that the spurious solutions appear. These can be eliminated by either using the H_t (Hernandez-Figueroa *et al.*, 1994) formulation or the penalty function (Rahman and Davies, 1984) in the variational formulation.

2.8 Variational formulations

The use of a variational principle in the formulation of a finite element analysis, has the advantage that it allows a particular analysis (and the computer program), to be generalised to solve any problem of the same mathematical nature. This approach has been extensively applied to a wide variety of electromagnetic field problems, in particular to the problem of wave propagation along arbitrary shaped waveguides, with anisotropic material.

There are many different types of variational formulation of waveguide problems which have been developed and shown for different types of propagating problems.

(i) *Scalar field formulation*: - This method has been applied to problems of electromagnetic wave propagation in homogeneous, isotropic media, where a single potential or single field has been applied. However, it is inadequate to handle inhomogeneous problems, where the guided modes are inherently hybrid. It is also not suitable for anisotrpic problems.

(ii) *H_t formulation* (vector): - Most of the formulations are restricted to structures without modal loss or gain. However, in the $\mathbf{H}_t$ formulation in order to yield a vector solution the transverse magnetic field components are used. And the advantage of this formulation is that it does not yield spurious solutions. However it is computationally expensive as it needs a complex eigenvalue solver.

(iii) *Full vector field formulation* : - There are two types, **E**-field and **H**-field. It is usually applied to problems, where the waveguide has anisotropic or spatial variations. The vector **E**-field formulation was first applied by English and Young (English and Young, 1971), unfortunately in this formulation the natural boundary condition is a magnetic wall, so for the electric wall situation it needs to be specifically implemented, and for a waveguide having arbitrary electric wall boundary it is quite difficult to impose such a required boundary condition. Another disadvantage of this formulation is that, it also needs an additional integral to impose continuity of the fields at dielectric interfaces.

By comparison, the **H**-field vector formulation has its natural boundary condition as that of an electric wall, so for metallic waveguide we do not require to impose the boundary conditions. Another advantage is that, at the dielectric interfaces, the fields are continuous so we do not need to impose any additional boundary conditions. This formulation has the ability to solve a problem with arbitrary anisotropic materials. The work of this thesis uses this type of formulation and so it will be described in detail in the following sections.

(iv) *Mixed field formulation* : - It covers all types of problems but it has the disadvantage that it is very complicated since six components are needed to be considered.

2.8.1 Vector H-field formulation

The vector H-field formulation can be written as

$$\omega_o^2 = \frac{\int (\nabla \times \mathbf{H})^* . \hat{\varepsilon}^{-1} . (\nabla \times \mathbf{H}) d\Omega}{\int \mathbf{H}^* \cdot \hat{\mu} \cdot \mathbf{H} \cdot d\Omega} \qquad (2.15)$$

The derivation of the above equation can be found in Appendix *A*.

Since the **E**-field is not continuous across the dielectric interfaces, the **H**-field formulation is considered in this work.

Where $\hat{\varepsilon}$ and $\hat{\mu}$ can be general anisotropic permittivity and permeability tensors of the loss-free medium respectively. Anisotropy can include gyrotropic media, to give non-reciprocal components. As the natural boundary condition is that of an electric wall, we need not force any boundary condition on conducting guide walls. But for regularly shaped guides, and at the symmetric walls (if applicable), we can enforce the boundary conditions to reduce the problem size.

However, the above formulation gives non physical spurious solutions (Mabaya, 1981), because the divergence condition $\nabla \bullet \mathbf{H}=0$ is not satisfied. Hence there are alternative approaches developed by Rahman and Davies (Rahman and Davies 1984) to include a penalty term in the above equation. There are other methods as well to eliminate the spurious solutions. Variational formulation using transverse field components solved by the Rayleigh-Ritz method or method of moments do not have spurious solutions. But these formulations are not valid for general anisotropic materials, the functionals are not self adjoint, and because of the additional differentiation involved with them, these are not very suitable for implementation in the FEM. However, the non appearance of the spurious or non physical solutions may be attributed to the divergence free basis functions.

2.9 Numerical solutions

In order to calculate the field at nodal points the variational formulation must be minimised to form a linear algebraic equation.

By using many elements, it is possible to approximate any continum with a complex boundary and with an arbitrary index distribution to such a degree that an accurate analysis can be carried out. The field functions H_x, H_y, and H_z are defined by a set of algebraic polynomials (first order polynomials for first order elements) over each element. By expressing these fields in terms of nodal values, the resulting field can be continuous over the whole region of interest. The extremum functional from the variational formulation is minimised with respect to the nodal values of the field components. This minimisation will generate a set of linear algebraic eigenvalue equations which can be expressed in matrix notation as

$$Ax - \lambda Bx=0 \tag{2.16}$$

The solution of this equation is an approximate solution to the original waveguide problem. Where $\boldsymbol{A}$ is a complex Hermitian matrix and $\boldsymbol{B}$ is a real symmetric matrix, and the eigenvectors x represent the unknown field components at the nodal points for different modes with λ as their corresponding eigenvalues. In general the matrices $\boldsymbol{A}$ and $\boldsymbol{B}$ are quite sparse. By using the sparcity the complex Hermitian matrix can be transformed into a real symmetric matrix. The resulting solutions include not only the possible propagating modes, but also a number of other solutions that have no physical existence. These solutions which are called the 'spurious solutions' will be discussed in the next section.

2.10 Spurious solutions

The scalar variational formulation (Silvester, 1991) is limited to certain waveguides only. For general inhomogeneous and general anisotropic problems it is not suitable. Hence the vector variational formulation is needed. However, these vector variational formulations suffer from the non-physical or spurious solutions.

There are a number of methods that can be used to detect these spurious solutions. One way that it can be done is to examine the field. Spurious solutions are characterised by the inconsistency and the random fashion that the field varies.

Mathematically, the underlying idea is that for physical (true) solutions, the eigenvector obeys the condition **∇.H**=0. Thus by calculating the **∇.H** for each eigenvector, it is possible to identify the spurious solutions from the physical ones. Although **∇.H** may never be exactly zero, but the values of **∇.H** can be divided into two groups; one with high values (spurious) and one with low values (physical).

Nevertheless, the objective is to determine or atleast suppress these solutions, not just find a way to detect their presence.

Among the various methods that were developed, Rahman and Davies (Rahman and Davies, 1984), developed the so-called penalty function method. This consists of the addition of a term in the variational formulation which now becomes

$$\omega_0^2 = \frac{\int (\nabla \times \mathbf{H})^* . \hat{\varepsilon}^{-1} . (\nabla \times \mathbf{H}) d\Omega + (\frac{\alpha}{\varepsilon})(\nabla \cdot \mathbf{H})^* (\nabla \cdot \mathbf{H}) d\Omega}{\int \mathbf{H}^* \cdot \hat{\mu} \cdot \mathbf{H} \cdot d\Omega} \qquad (2.17)$$

where α is the dimensionless penalty number. This equation has the desired additional Euler equation **∇.B**=0, in precisely the manner that terms are added (Berks, 1956) to give desired boundary conditions. Larger the value of the penalty number heavier the corresponding constraint imposed on the Euler equation. One advantage of using the penalty term is that it does not increase the matrix order, and the additional computational time is negligible.

2.11 Mathematical formulation of FEM

In section 2.9 it has been stated that the variational formulation can be approximated in terms of an eigenvalue equation of the form

$$Ax - \lambda Bx = 0$$

The eigenvalue λ and the eigenvector {x}, will give k_0^2, and the three **H**-field components H_x, H_y, and H_z respectively. It has already been discussed in section 2.1, the waveguide has to be divided into a number of triangles and for each triangle, the variational formulation must be applied. To simplify the process the numerator and the denominator will be treated separately.

The numerator can be written as :

$$x^T \cdot Ax = \int (\nabla \times H)^* \cdot \hat{\varepsilon}^{-1} (\nabla \times H) \cdot d\Omega \qquad (2.18)$$

and the denominator as :

$$x^T \cdot B \cdot x = \int H^* \cdot \hat{\mu} \cdot H \cdot d\Omega \qquad (2.19)$$

Then the functional

$$J = \int (\nabla \times H)^* \hat{\varepsilon}^{-1} \cdot (\nabla \times H) \cdot d\Omega - k_0^2 \int H^* \cdot \hat{\mu} \cdot H \cdot d\Omega \qquad (2.20)$$

can be written as

$$J = x^T \cdot A \cdot x - \lambda \cdot x^T \cdot B \cdot x \tag{2.21}$$

In order to find a stationary solution, we need that

$$\frac{\partial J}{\partial x} = 0 \tag{2.22}$$

and this minimisation leads to the eigenvalue equation

$$Ax - \lambda Bx = 0$$

To start the analysis, we need to consider a typical element as shown in Figure 2.5.

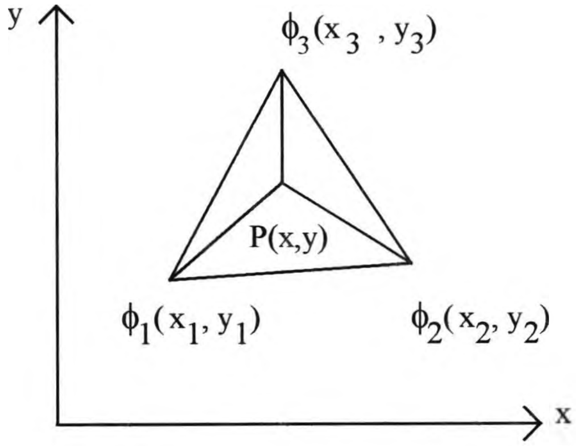

Fig. 2.5 Schematic of a typical element

In order to approximate the field over each element, we need to consider a continuous function that is allowed to vary in a linear manner over the element region i.e. the true variation of the field is approximated by a jewel-faceted approximation.

The way that the function varies is constrained by the fact that at the nodal points, the function should take values equal to the nodal values ϕ_1, ϕ_2, and ϕ_3. Therefore the functions have to be expressed interms of its nodal values. This function is called the '*shape function*'.

2.11.1 Shape function

Within the triangle, the field value can be adequately modelled by the expression

$$\phi = a + bx + cy \tag{2.23}$$

where *a*, *b*, *c* are constants. These constants can be represented in terms of the co-ordinates of the nodes. The nodal values of ϕ can be expressed as :

$$\phi_1 = a + bx_1 + cy_1 \tag{2.24a}$$

$$\phi_2 = a + bx_2 + cy_2 \tag{2.24b}$$

$$\phi_3 = a + bx_3 + cy_3 \tag{2.24c}$$

solving the above system of equations, we can determine a, b, c in terms of ϕ_i, x_i, and y_i, i=1,2,3.

$$a = \frac{\phi_1(x_2y_3 - x_3y_2) + \phi_2(x_3y_1 - x_1y_3) + \phi_3(x_1y_2 - x_2y_1)}{2A} \tag{2.25a}$$

$$b = \frac{\phi_1(y_2 - y_3) + \phi_2(y_3 - y_1) + \phi_3(y_1 - y_2)}{2A} \tag{2.25b}$$

$$c=\frac{\phi_1(x_3-x_2)+\phi_2(x_1-x_3)+\phi_3(x_2-x_1)}{2A} \tag{2.25c}$$

where A denotes the area of the triangle.

Substituting the values back in equation (2.23) we get

$$\phi(x,y)=N_1\,\phi_1+N_2\,\phi_2+N_3\,\phi_3 \tag{2.26}$$

or

$$\phi(x,y)=[N]\,\{\phi\} \tag{2.27}$$

where

$$N_1=\frac{x_2y_3-x_3y_2}{2A}+\frac{y_2-y_3}{2A}x+\frac{x_3-x_2}{2A}y \tag{2.28a}$$

$$N_2=\frac{x_3y_1-x_1y_3}{2A}+\frac{y_3-y_1}{2A}x+\frac{x_1-x_3}{2A}y \tag{2.28b}$$

$$N_3=\frac{x_1y_2-x_2y_1}{2A}+\frac{y_1-y_2}{2A}x+\frac{x_2-x_1}{2A}y \tag{2.28c}$$

N_1, N_2, and N_3 can be written as

$$N_1=a_1+a_2x+a_3y \tag{2.29a}$$

$$N_2=a_4+a_5x+a_6y \tag{2.29b}$$

$$N_3=a_7+a_8x+a_9y \tag{2.29c}$$

with a_i, i=1,2,3,4,5,6,7,8,9 being the corresponding terms in (2.29a, 2.29b and 2.29c), which can easily be calculated from the nodal coordinates.

A very useful property that N_1, N_2, and N_3 have is that

$$N_1 + N_2 + N_3 = 1 \tag{2.30}$$

This is because, if we consider for example N_i, we can identify it as being twice the area of the triangle $P\phi_3\phi_2$ divided by two times the area of the whole triangle (Fig. 2.5). The same is true for N_2 and N_3 for the triangles $P\phi_3\phi_1$ and $P\phi_1\phi_2$ respectively. Hence, the sum of N_1, N_2 and N_3 is unity.

2.11.2 Matrix formation

Using (2.26) the **H**-field components H_x, H_y, H_z can be expressed as

$$H_x\,(x,y) = N_1\,H_{x1} + N_2\,H_{x2} + N_3\,H_{x3} \tag{2.31a}$$

$$H_y\,(x,y) = N_1\,H_{y1} + N_2\,H_{y2} + N_3\,H_{y3} \tag{2.31b}$$

$$H_z\,(x,y) = N_1\,H_{z1} + N_2\,H_{z2} + N_3\,H_{z3} \tag{2.31c}$$

The above equations can be represented by the matrix form as

$$H = \begin{bmatrix} H_x \\ H_y \\ H_z \end{bmatrix} = \begin{bmatrix} N_1 & 0 & 0 & N_2 & 0 & 0 & N_3 & 0 & 0 \\ 0 & N_1 & 0 & 0 & N_2 & 0 & 0 & N_3 & 0 \\ 0 & 0 & N_1 & 0 & 0 & N_2 & 0 & 0 & N_3 \end{bmatrix} \begin{bmatrix} H_{x1} \\ H_{y1} \\ H_{z1} \\ H_{x2} \\ H_{y2} \\ H_{z2} \\ H_{x3} \\ H_{y3} \\ H_{z3} \end{bmatrix} \tag{2.32}$$

or it can be written as H= [N] {H}

Where [N] is the 3 X 9 matrix shown above and {H} is a 9 X 1 column vector, representing the components of the field.

Further, we can write

$$\nabla \times H = [Q] \cdot H \tag{2.33}$$

where

$$[Q]=\begin{bmatrix} 0 & -\frac{\partial N_1}{\partial z} & \frac{\partial N_1}{\partial y} & 0 & -\frac{\partial N_2}{\partial z} & \frac{\partial N_2}{\partial y} & 0 & -\frac{\partial N_3}{\partial z} & \frac{\partial N_3}{\partial y} \\ \frac{\partial N_1}{\partial z} & 0 & -\frac{\partial N_1}{\partial x} & \frac{\partial N_2}{\partial z} & 0 & -\frac{\partial N_2}{\partial x} & \frac{\partial N_3}{\partial z} & 0 & -\frac{\partial N_3}{\partial x} \\ -\frac{\partial N_1}{\partial y} & \frac{\partial N_1}{\partial x} & 0 & -\frac{\partial N_2}{\partial y} & \frac{\partial N_2}{\partial x} & 0 & -\frac{\partial N_3}{\partial y} & \frac{\partial N_3}{\partial x} & 0 \end{bmatrix} \tag{2.34}$$

After evaluating the partial derivatives, the Q matrix becomes :

$$[Q]=\begin{bmatrix} 0 & j\beta N_1 & a_3 & 0 & j\beta N_2 & a_6 & 0 & j\beta N_3 & a_9 \\ -j\beta N_1 & 0 & -a_2 & -j\beta N_2 & 0 & -a_5 & -j\beta N_3 & 0 & -a_8 \\ -a_3 & a_2 & 0 & -a_6 & a_5 & 0 & -a_9 & a_8 & 0 \end{bmatrix} \tag{2.35}$$

Similarly from Equation 2.19, the components of the B_e matrix can now be calculated. Since μ is a scalar quantity, it can be taken outside the integral.

Therefore

$$x^T \cdot B \cdot x = \mu \int H^* \cdot H \cdot d\Omega \tag{2.36}$$

and the element global matrix is given by

$$B_e = \int_{\Delta} [N]^* \cdot [N] \cdot d\Omega \tag{2.37}$$

as H = [N] {H}

The solution of the above expression gives a 9 X 9 matrix. The integration is carried out by using the integration expression

$$\int_{\Delta} N_1^p \cdot N_2^q \cdot N_3^r \cdot d\Omega = \frac{(p!q!r!)}{(p+q+r+2)} \cdot 2A \tag{2.38}$$

This way the coefficients of the B_e matrix can be calculated and they are

$$B_e = \begin{bmatrix} \frac{A}{6} & 0 & 0 & \frac{A}{12} & 0 & 0 & \frac{A}{12} & 0 & 0 \\ 0 & \frac{A}{6} & 0 & 0 & \frac{A}{12} & 0 & 0 & \frac{A}{12} & 0 \\ 0 & 0 & \frac{A}{6} & 0 & 0 & \frac{A}{12} & 0 & 0 & \frac{A}{12} \\ \frac{A}{12} & 0 & 0 & \frac{A}{6} & 0 & 0 & \frac{A}{12} & 0 & 0 \\ 0 & \frac{A}{12} & 0 & 0 & \frac{A}{6} & 0 & 0 & \frac{A}{12} & 0 \\ 0 & 0 & \frac{A}{12} & 0 & 0 & \frac{A}{6} & 0 & 0 & \frac{A}{12} \\ \frac{A}{12} & 0 & 0 & \frac{A}{12} & 0 & 0 & \frac{A}{6} & 0 & 0 \\ 0 & \frac{A}{12} & 0 & 0 & \frac{A}{12} & 0 & 0 & \frac{A}{6} & 0 \\ 0 & 0 & \frac{A}{12} & 0 & 0 & \frac{A}{12} & 0 & 0 & \frac{A}{6} \end{bmatrix} \tag{2.39}$$

A is the area of each element (triangle)

similarly the coefficients of the A_e matrix can be calculated.

From Eq. 2.18

$$x^T \cdot A \cdot x = \int (\nabla \times H)^* \cdot \hat{\varepsilon}^{-1} \cdot (\nabla \times H) \cdot d\Omega \tag{2.40}$$

where H = [N] {H} and

$$\nabla \times H = [Q] \cdot \{H\} \tag{2.41}$$

Therefore substituting (2.41) into (2.40) gives

$$x^T \cdot A \cdot x = \int \{H\}^* \cdot [Q]^* \cdot \hat{\varepsilon}^{-1} \cdot [Q]\{H\} . d\Omega \tag{2.42}$$

Simplifying (2.42) the element matrix A_e can be evaluated as

$$A_e = \int_\Delta [Q]^* \cdot \hat{\varepsilon}^{-1} \cdot [Q] \cdot d\Omega \tag{2.43}$$

For isotropic case ε is scalar and hence it can be taken out of the integration.

$[Q]^*$ is a 9 X 3 matrix and [Q] is a 3 X 9 matrix therefore the result is a 9 X 9 matrix. However, for the anisotropic case we need to include the tensor in the analysis

The first thing that needs to be done is to find the inverse matrix of ε. The way that the inverse matrix is calculated is shown in Appendix B.

Now the A_e matrix equation can be written as

$$A_e = \int_\Delta [Q]^* \cdot [P] \cdot [Q] d\Omega \tag{2.44}$$

$[Q]^*$ is a 9x3 matrix,

[P] is a 3x3 matrix and

[q] is 3x9 matrix.

Using simple algebra, the multiplication is carried out in two steps, first the product [P] [Q] is evaluated and the result is multiplied with $[Q]^*$

To illustrate the way that the elements of the matrix are determined the A_{e11} element will be considered.

After carrying out the multiplication's, the first row first column element of the matrix inside the integral is

$$-j\beta N_1 \cdot (P_{22}(-j\beta N_1) - P_{23}\, a_3) - a_3 \cdot (P_{32}(-j\beta N_1) - P_{33}\, a_3) \qquad (2.45)$$

Hence the A_{e11} element, will be given from

$$A_{e11} = \int \; -j\beta N_1 \cdot (P_{22}(-j\beta N_1) - P_{23}\, a_3) - a_3 \cdot (P_{32}(-j\beta N_1) - P_{33}\, a_3) d\Omega \qquad (2.46)$$

Rearranging terms gives

$$A_{e11} = P_{22}\beta^2 \int N_1^2\, d\Omega + a_3 j\beta P_{23} \int N_1\, d\Omega + a_3 j\beta P_{32} \int N_1\, d\Omega + a_3^2 P_{33} \int d\Omega \qquad (2.47)$$

Using again the integration formula given in Eq. 2.38, the integrals can be evaluated.

$$\int N_1^2\, d\Omega = \frac{A}{6} \qquad (2.48a)$$

$$\int N_1\, d\Omega = \frac{A}{3} \qquad (2.48b)$$

$$\int d\Omega = A \qquad (2.48c)$$

where A is the element (triangle) area.

Therefore, the A_{e11} element is given from the equation

$$A_{e11} = P_{22}\beta^2 \frac{A}{6} + P_{23}\, a_3\, j\beta \frac{A}{3} + P_{32}\, a_3\, j\beta \frac{A}{3} + P_{33}\, a_3^2\, A \tag{2.49}$$

But as P_{23} and P_{32} for the lossless waveguides, A_{e11} will be a real quantity.

Similarly, the equations for the other elements of the A_e matrix can be derived.

2.12 Analysis of infinite region

Because most of the dielectric waveguides are in general unbounded, some proper account must be made about the infinite regions. There are various methods developed to handle this situation. The most popular ones are

(i) A method using artificial boundaries
(ii) A method using exterior finite elements
(iii) A method using the conformal mapping technique
(iv) The method using infinite elements at the boundaries
(v) A method combining the FEM and the analytical method.

The method in (i) using the artificial boundaries is the most simplest approach for both the scalar and vector analysis. In this technique the artificial boundary can be shifted to satisfy a given criterion for the maximum field strength at that boundary. This is done by an iterative process.

The other method known as the infinite elements developed by Rahman and Davies (Rahman and Davies, 1984) can handle the situation when the field decays infinitely in the transverse direction. This extension of the problem domain is particularly important when dealing with problems near the cutoff, as the field decays slowly and there is a significant field of importance is arbitrarily large. The standard approach is to set an artificial boundary walls enclosing the guide at a particular distance where the field is small. In this case, care has to be taken to avoid the influence of the position of this artificial walls and at the same time it is sufficiently close to limit the necessary number of finite elements.

Boundary elements have been used by Yeh *et al.* (1979), considering an exponential decay outside the guide core. But in their method, because of nonconfirmity of the two co-ordinate systems, the fields used were not continuous. Bettes (1977) has used infinite elements with a Cartesian co-ordinate system, using an exponential decay and Lagrange multipliers, for fluid flow problems.

An infinite element is a finite element that indeed extends to infinity, and shape functions for such an element should be realistic to represent the fields and should be square integrable over an infinite-element area, to satisfy the radiation condition. For an infinite element extending towards infinity in the x-direction, we can assume exponential decay in x and conventional shape function dependence in the y-direction. It can be expressed as

$$N_i\,(x,y) = f_i\,(y)\exp\,(-x/L) \qquad (2.50)$$

where L is a decay length. Similarly, we can have infinite elements extending towards the y-direction by considering exponential decay in y. Similarly, by assuming exponential decay in both x and y, we can consider a rectangular or quadrant element extending towards infinity in both x- and y- directions. Integration of these shape functions or their derivatives over the infinite elements are finite, and can be simply carried out combining all of these elements along with the conventional finite element, we can represent any open-type waveguide cross-sectional domain very conveniently, with each field component being continuous over the whole infinite domain.

Chapter 3

Coupled mode devices

This chapter describes the properties of a directional coupler and also its special form which is known as a 'multimode interference (MMI) coupler'. Such MMI couplers are becoming very popular due to their good performance and the excellent reproducibility of their characteristics.

3.1 Introduction

Coupled mode devices are important in the design of compact photonic systems. Directional couplers play a major role in the design of such systems. Directional couplers and power MMI couplers, belong to a class of passive devices in which power exchanges between two modes which are in close proximity to each other. A directional coupler consists of a pair of waveguides placed parallel to each other so that the evanescent field of one penetrates into the other and optical power couples into the propagating mode of the latter waveguide. In Fig. 3.1 the length of the coupler at which the maximum power transfer occurs is referred to as the coupling length, L_C, which depends on the structure, the refractive indices of the constituent waveguides and the intervening isolation region. Beyond the coupling length, the light then couples back to the incident guide, and so the power transfer process is periodic along the axial distance. This coupling phenomenon is shown in the Figure 3.1, below

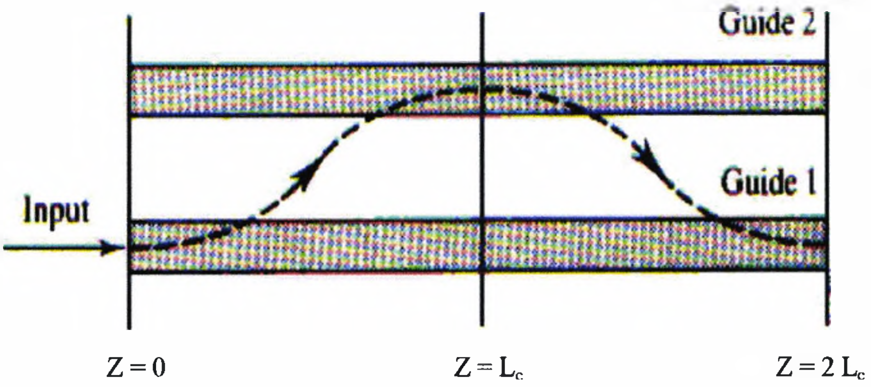

Fig. 3.1 Schematic of a directional coupler

If the input to guide 1 is at $z = 0$ then the complete power transfer to guide 2 occurs at $z = L_c$. The power can again couple back to guide 1 and at $z=2L_c$ most of the power is in guide 1. If a directional coupler is phase matched then most of the power can be coupled from one waveguide to the other.

Since work began in integrated optics, it has been evident that elements capable of switching light from one channel guide to another would play an essential role. The realization of directional coupler as a light switch was demonstrated by Somekh *et al.*, in 1974 (Somekh *et al.*, 1974). An optical directional coupler was realized in $LiNbO_3$ by a diffussion technique using titanium. The switch uses an original electrode configuration and it was called 'Cobra' (Commutateur optique binare rapide). Directional coupler based electrooptic switches (Kogelnik and Schmidt, 1976), tunable optical waveguide filters (Alferness and Schmidt, 1978), and Ti diffused lithium niobate switches and modulators (Alferness *et al.*, 1979) have been demonstrated. These directional couplers are also used in a variety of integrated optical devices, such as power dividers (Donnelly, 1986), input-output couplers, modulators (Wongcharoen *et al.*, 1997), filters (Wongcharoen *et al.*, 1996), switches (Meshulach and Ruschin, 1994), polarises (Albrecht *et al.*, 1990, Li and Deck, 1994, Liao *et al.*, 1996), and spot size expanders (Buss *et al.*, 1994) for example.

The coupling length is a very sensitive parameter and it varies exponentially with the separation between the guides. The coupling length as a function of the separation between the guides is shown in Fig. 3.2.

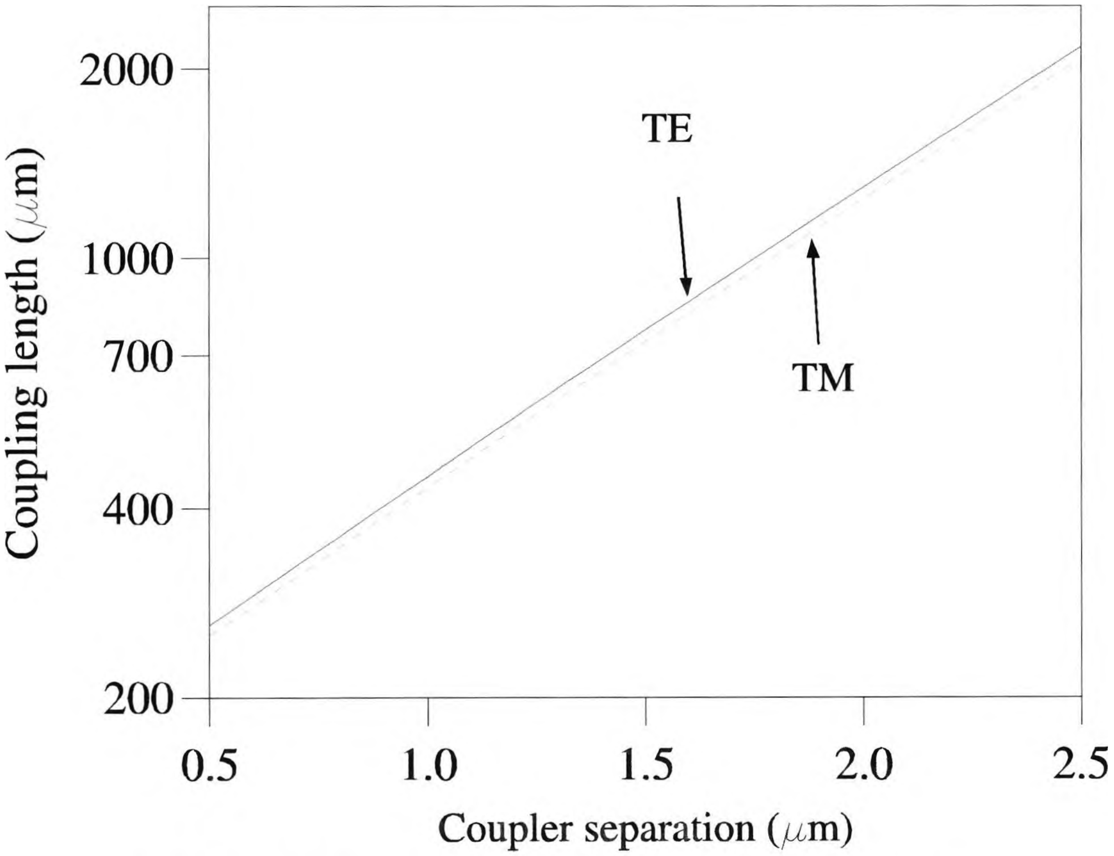

Fig. 3.2 Coupling length as a function of the guide separation, S

In Figure 3.2 the coupling length is plotted in a semi-log scale so that it can be represented as a straight line. However, when the separation between the guides are considerable the coupling length can be reasonably long. This leads to a tight tolerance on the separation requirements for the fabrication process particularly for weakly coupled guides. In order to obtain good control of the power coupling, the only practical way this can be achieved is to include a tuning or trimming facility. However, this complicates the component design and restricts the material choice.

Another type of coupler known as the *two-mode interference couplers* (Chung *et al.*, 1989), which is a special type of directional coupler with zero gap can be produced. These are less sensitive devices than their directional coupler counterpart. The width of such a device will be that of the two access waveguides. This type of structure could be called a two-mode interference coupler (similar to strongly coupled directional couplers) when it can support two modes.

The cross-talk problem in optical waveguide is a major design issue. When light is launched into an input waveguide, ideally all the power should emerge from one of the two output guides. However, it is generally observed that a small amount of power is emerges from the other guide, causing undesirable cross-talk. This has been attributed to the absorption loss (Marcuse, 1972), and the non-optimum coupling length (Alferness, 1982). Wilson and Reinhart (1980) have mentioned that cross-talk is zero in the coupling region only to the first approximation, due to the field overlap of the coupling waveguides.

Next, the prospects of three-guide directional couplers are discussed (Buus *et al.*, 1993). The operation of a multiguide (more than two) coupler can be more complicated than that of a two-guide coupler, because of the higher number of modes which can exist in this type of structure. If the individual guide is single moded, the number of possible guided normal (also called super) modes of a multiguide coupler is generally equal to the number of guides in the coupler.

The operating principle of a three-guide directional couplers is illustrated, in Figure 3.3, shows a waveguide with three high index regions. The refractive index of the guide, was given by n_g=3.3, and it was surrounded by a cladding of index 3.17 (Buus *et al.*, 1993). The thickness of the two outer guides was set to be 0.225μm and that of the centre guide was 0.26μm. the separation, *s*, between them was considered to be 1.80μm. This structure can support three guided super modes with their field profiles as shown in Figures 3.4(a)-(c). Figure 3.4a shows the dominant H_y field profile of the first or the fundamental TE_0 mode. The three high index regions can be identified by the three peaks of the modal field profile. Figure 3.4b shows the H_y field profile of the second mode, TE_1, which is an antisymmetric mode of the structure, and Figure 3.4c shows the third mode, TE_2, which is symmetric.

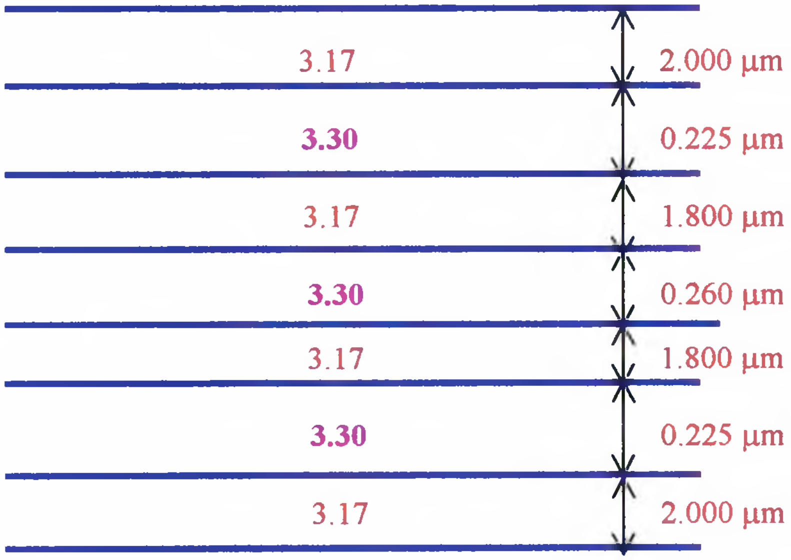

Fig. 3.3 Schematic of the three-core directional coupler

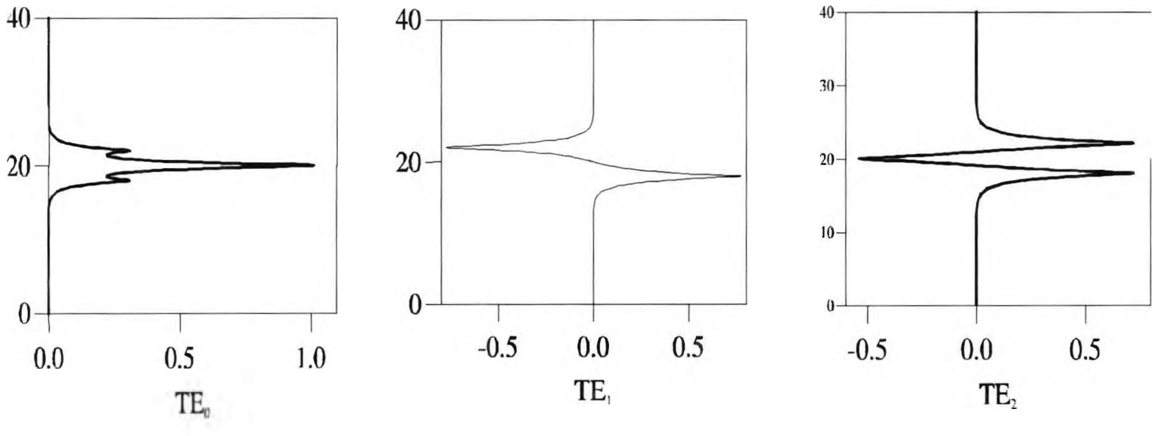

Fig. 3.4 (a) The field profiles of (a) TE_0 mode (b) TE_1 mode and (c) TE_2 mode

Initially these multi-core three guide couplers have been used as spot size converters (Buus *et al.*, 1994). Recently, the nonlinear three guide couplers have been shown as good switching devices at low powers (Buah *et al.*, 1997).

Most of the analysis of this type of coupled structure has been based on coupled-mode approaches (Hardy and Streifer, 1985). Further techniques which have been used by other workers include the effective index method (Donnelly, 1983), the finite difference method (Bierwirth *et al.*, 1986), the spectral index method (Berry and Burke, 1995) and the beam propagation method (Van Roey, 1981). However, as the range of optical waveguides and coupled waveguiding structures becomes more intricate, so the need for computer analysis becomes greater and more demanding, to understand the structure more fully. The finite element method has become a powerful tool in many branches of engineering due to its flexibility and versatility (Zienkiewicz *Ed*, 1994 and Silvester and Ferrari, 1991 This method is capable of calculating the propagation constants and the field profiles.

3.2 The finite element and the least squares boundary residual methods

The finite element method (FEM) is considered to be more accurate to obtain modal solution than the other available techniques (Rahman and Davies, 1984) due to its distinct properties, which have been explained in Chapter 2. The FEM can be applied to arbitrary shaped guides in which the refractive indices, nonlinearities and anisotropies can have arbitrary profiles.

The power transfer efficiency between two guides can be calculated in either of two ways :

(i) from the individual modes of the isolated guides

(ii) from the supermodes of the coupled structures

In this work the second approach is discussed, with the requirement that the accurate eigenvalues and eigenvectors can be obtained.

Since the FEM is capable of calculating the modal propagation constants of the coupled super structures, this approach is used where possible. To find the power coupling efficiency, the coupled mode or the simple overlap techniques can be used. An alternative and a powerful tool to analyse coupled structures is the use of the least squares boundary residual method. The advantage of this method, compared to other available techniques, is that it can calculate the reflection coefficients of the modes, and also it enforces the satisfaction of the field continuity more rigorously at the interfaces.

3.2.1 Implementation of the finite element and the Least Squares Boundary Residual methods to coupled mode devices

In this section some of the important computational aspects relating to the calculation of the eigenvalues and eigenvectors will be presented. In addition, the LSBR technique is also presented which is used to calculate the excitation coefficients at the discontinuity interfaces. In this section the implementation of the FEM discussed in Chapter 2 using computer codes, will be illustrated with the help of a flow chart.

The steps involved in the calculation of the eigenvalues and eigenvectors depend on various factors such as the guide dimensions, mesh size, penalty term etc. These data values are entered through a data file **BLOCKDATA**. In order to analyse a two dimensional problem, the x and y co-ordinates of all the nodes and the relationship between the node identifiers and node numbers for all element has to be defined and entered for an arbitrary two dimensional problem. The critical steps involved in an optical waveguide analysis are shown in the flowchart in Fig. 3.5

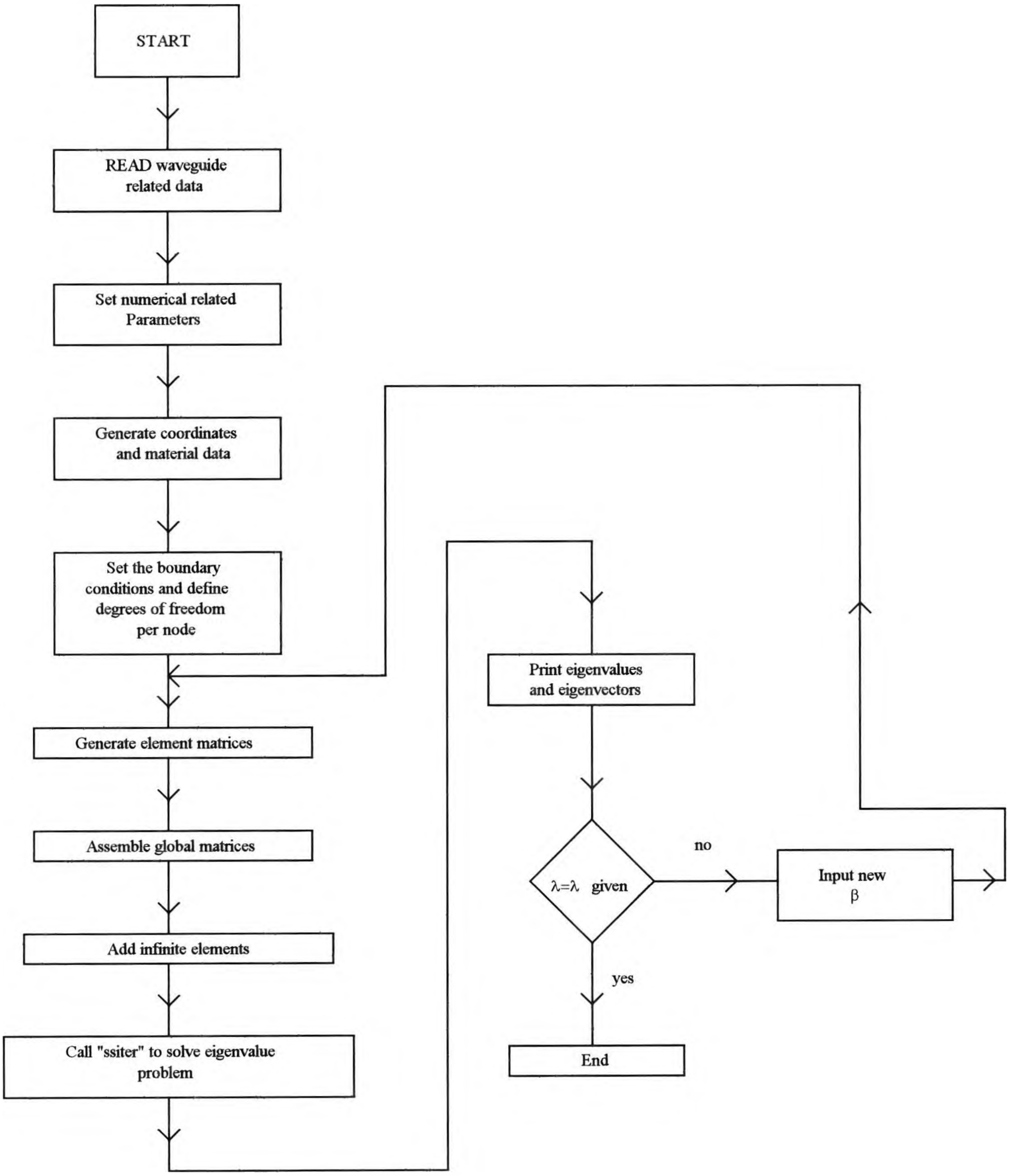

Fig. 3.5 Flowchart showing the optical waveguide analysis

Initially all the waveguide parameters are read from the block data, and the associated numerical parameters are also read from the input data file. Next the co-ordinates and the material data are calculated, depending on the given mesh where normally an irregular meshing is used in most of our analysis. Then the boundary conditions have to be defined. If the required boundary condition is the same as the natural boundary condition, then the boundary can be left free. However, for symmetric structures if a boundary can be imposed it is to be preferred so that a one-fold or two-fold symmetry can also be exploited. The implementation of boundary conditions also reduces the matrix size and by applying the boundary conditions at the time of assembling the matrices, more storage space can be saved. Even though for two-fold symmetry the matrix order reduces to one-fourth, the major drawback is that the given waveguide must be solved four times for different possible ODD/EVEN symmetric combinations, if all the modes are required. The CPU time will reduce depending on the matrix solver. This two-fold symmetry allows the usage of a higher mesh divisions, hence giving more accurate answers.

The degrees of freedom can be different for different formulations. In the present full vector form the degrees of freedom is three, since it has H_x, H_y and H_z fields for the x ,y and z components of the **H** field respectively. It is normally preferred to calculate the rough propagation constants using the scalar formulation, as this is free from spurious solutions. The resulting data can be consequently used as input for the two dimensional study, where the CPU time required for the scalar finite element is very small compared to that for the vector formulation.

In analysing MMI-based devices, it is better to use the planar approximation first to get an estimate of the number of modes present in the MMI section. This could be used to give a better estimation for the complete analysis of its two dimensional counterpart.

The infinite element subroutine is normally added when dealing with problems which operate near cutoff as in this situation field decays very slowly outside the core region.

3.2.2 Use of finite element output data

In most of the coupled devices the calculation of just the propagation constants and field values is not of much interest. Hence a further technique has had to be developed to calculate the power transfer from the input to the intermediate or output sections. This can be done by using the coupled mode (Hardy and Streifer 1989) or simple overlap integral techniques (Soldano and Pennings, 1995).

However, it has been shown in this study that the LSBR method is an accurate and versatile numerical tool to calculate the power transfer between the coupled waveguides. The LSBR method uses the propagation constants and the field values generated by the finite element and is used to calculate the transmission and the reflection coefficients at the discontinuity interfaces. The LSBR method matches the continuity of the tangential components of the electric and magnetic fields in the least squares sense over the discontinuity interface by including many modes to yield the general scattering matrix.

In the next section a brief account of the use of the LSBR method is presented. The application of the LSBR method is presented in Chapters 4, 5 and 6 with particular emphasis in Chapter 5.

3.2.3 Analysis of optical waveguide discontinuities

The main aim of using the LSBR method is to calculate the coefficients of the transmitted and the reflected modes at the discontinuity interfaces. This approach is more rigorous than the point-matching method because the error integral is evaluated over the discontinuity interface, rather than just field matching at some specific points.

Most of the devices analysed in this work consists of an input, an intermediate and output sections. In order to calculate the power transfer from the input to the output section it is vital to calculate the excited modal coefficients at the discontinuity interfaces. To do so the LSBR method is the most powerful and versatile numerical tool. Most of the other theoretical methods considered so far ignores the radiated or reflected modes or apply only under the assumption of slight discontinuity.

The problem considered here consists of an abrupt discontinuity, in the transverse plane $z = 0$, between two uniform waveguides with arbitrary cross-sections. The input guide is normally taken as a single mode guide.

The LSBR method was introduced as an alternative to point-matching and simple overlap integral methods, satisfying boundary conditions in the usual least-squares sense over the interface. The LSBR method is rigorously convergent, and the error minimisation being global rather than sampled, and the method has the flexibility of introducing an electric/magnetic weighting factor to balance electric and magnetic field continuity errors.

The LSBR method can be illustrated using the Fig.3.6 below

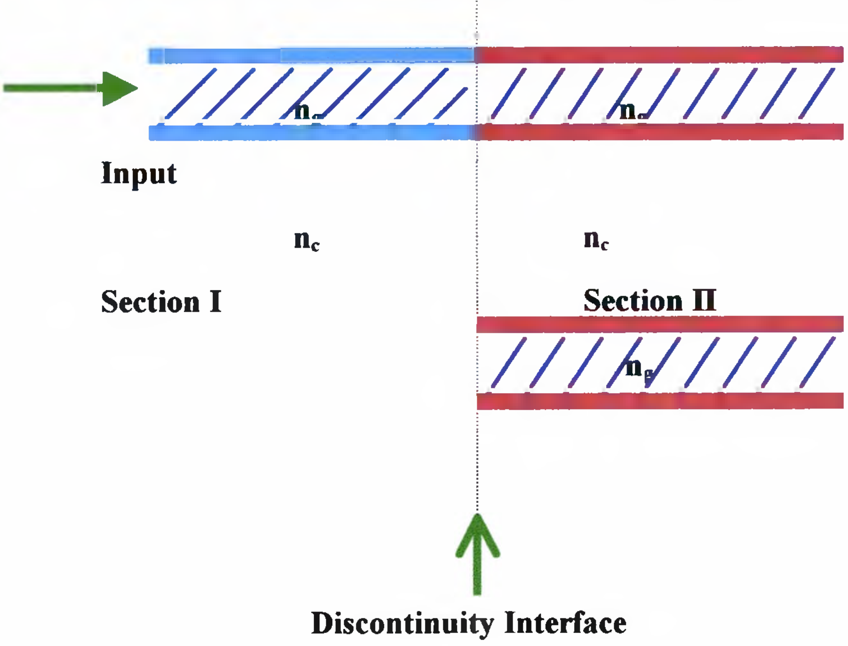

Fig. 3.6 Discontinuity representation for LSBR

It may be assumed that the junction is excited by an incident wave of one mode from side *I*, when the transverse components of the electric and magnetic fields are E_t^i and H_t^i. Some of the incident wave is reflected back into side *I*. At the discontinuity plane, there will be several modes to satisfy the boundary conditions. These can be guided or radiated modes in side *I* and side *II*. The transverse components of the total electromagnetic fields E_t^{II} and H_t^{II} in side *II* at the discontinuity plane can be expressed in terms of the eigenmodes in side *I* and side *II* respectively, as follows :

$$E_t^I = E_t^i + \sum_{i=1}^{\infty} a_i E_{ti}^I \tag{3.1}$$

$$E_t^{II} = \sum_{i=1}^{\infty} b_i E_{ti}^{II} \tag{3.2}$$

$$H_t^I = H_t^i - \sum_{i=1}^{\infty} a_i H_{ti}^I \tag{3.3}$$

$$H_t^{II} = \sum_{i=1}^{\infty} b_i H_{ti}^{II} \tag{3.4}$$

At the discontinuity plane, many modes are generated to satisfy the boundary conditions. They may be propagating, radiating, or evanescent, and a_i are the amplitudes of the different ith modes (modal field profiles E_{ti}^{I}, H_{ti}^{I}) E_i^{I}, H_i^{I} reflected from the junction in side I and b_i are the amplitudes of the ith modes transmitted in side II, with their modal electric and magnetic field profiles, E_{ti}^{II}. H_{ti}^{II} , respectively.

The LSBR method looks for a stationary solution to satisfy the continuity conditions of the tangential fields in a least squares sense by minimising error functional J, where

$$J = \int \left|E_t^I - E_t^{II}\right|^2 + \delta . Z_0^2 \left|H_t^I - H_t^{II}\right|^2 d\Omega \tag{3.5}$$

where Z_0 is the free-space wave impedance and δ is a dimensionless weighting factor. To obtain the approximate numerical solution to the problem, the infinite series expansions of Eq. 3.1-3.4, including all the relevant propagating modes plus as many radiating and/or evanescent modes as is convenient. The minimum criterion of Eq. 3.5 reduces to the following linear equation :

$$\mathbf{C}x = v \tag{3.6}$$

Here $\mathbf{C}$ is square matrix generated from the eigenvectors and v is an array due to the incident mode. The solution of this equation gives the vector in $\{x\}$ consisting the required modal coefficients a_i and b_i of the reflected and the transmitted modes. These constitute one column of the scattering matrix, corresponding to the chosen incident mode. Vector $\{x\}$ is made up of all the unknown modal amplitudes. The elements of $\mathbf{C}$ and v are given by

$$C_{ij} = \langle E_{ti}, E_{tj} \rangle + \delta Z_0^2 \langle H_{ti}, H_{tj} \rangle \tag{3.7a}$$

$$v_i = \langle E_t^i, E_{ti} \rangle + \delta Z_o^2 \langle H_t^i, H_{ti} \rangle \tag{3.7b}$$

where $i,j=1,\dots,N$ and N is the total number of modes in sides I and II and the vectors E_t and H_t are made up of all the corresponding modal fields in both sides.

Inner products involved in the above expression are defined as

$$\langle x_1, x_2 \rangle = \int x_1 \cdot x_2^* \cdot ds \tag{3.8}$$

where x_1 and x_2 are two field vectors, x_2^* is the complex conjugate of x_2 and integration is carried over the waveguide cross-section.

3.3 Principle and theory of Multimode Interference Devices (MMI)

Multimode couplers are important elements of optical networks, having an excellent fabrication tolerance compared to their directional coupler counterpart. Their operation is principally based on the 'self imaging' phenomenon (Ulrich and Kamiya, 1978, Bryngdahl, 1973). This section describes the principle and the theory of these devices with particular emphasis on duplexers and power splitters.

In all optical communication system the couplers play an important role as optical power divider or combiner. A directional coupler may be formed by bringing two planar guides close together. The optical power will be able to 'tunnel' from one waveguide to the other, the fabrication of power transferred depending strongly on the distance of the waveguides and the confinement of the fields in the cores. Therefore the tolerance requirements of the directional coupler are extremely strict and both the lithographic line width and the etch depth must be very well controlled.

An alternative approach is to use a multimode interference coupler (Jenkins *et al.*, 1994, Soldano *et al.*, 1995) in which the parallel input guides are separated by a multimode section. As long as the separation between the input guides is considerable, there will be no overlap of the input field. The coupling in these devices takes place as a result of the self-imaging of the input field being reproduced at the output. The self-imaging mechanism in the multi-mode section is almost independent of the etching depth, making the MMI a very fabrication-tolerant component. The self-imaging phenomenon is a property of a multimode waveguide which result from a constructive interference of the waveguide modes which are excited by the object. Each mode propagates along the guide with its own characteristics phase velocity, and therefore, the modes soon become dephased. An image plane is determined then by the condition that the accumulated phase differences between any two excited modes are multiples of 2π. Under that condition, the superposition of the modal fields in the image plane is the object plane, and a self-image is formed.

However, the phase differences mentioned cannot all simultaneously be made exact multiples of 2π. Consequently, the self-images show aberrations and a reduced contrast, and they have limited resolution. Knowledge of the resulting image quality is essential for possible applications of self-imaging waveguides in integrated optics or in connection with optical fibres.

An MMI device essentially consists of three parts; a wide multimode section, a single or set of input waveguides and a single or set of output waveguides. It is usually desirable if the input and output optical waveguides support only one mode (Berry and Burke, 1995). By selecting the correct configuration for the output waveguides and their position along the multimode section, a so called 'self-image' or 'multiple-image' can be coupled into the output.

Figures 3.7 (a)-(c) shows schematic diagrams of three different MMI couplers.

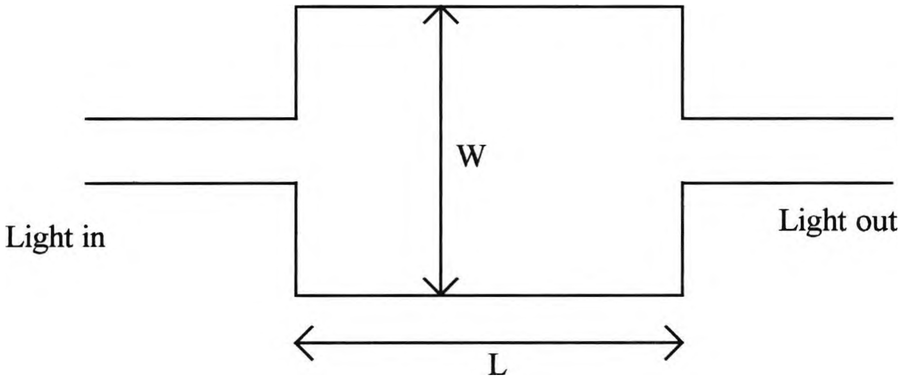

Fig. 3.7 (a) A 1-to-1 way self-imaging waveguide

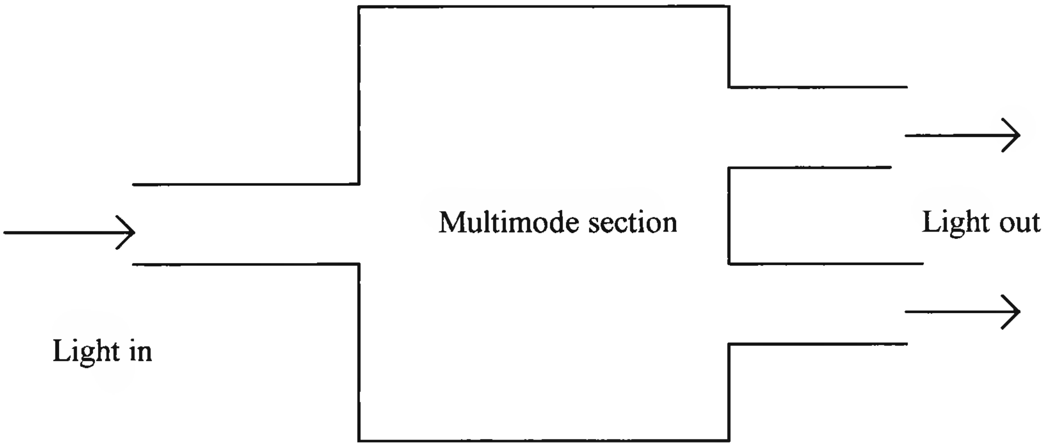

Fig. 3.7 (b) A symmetric 3 dB power splitter

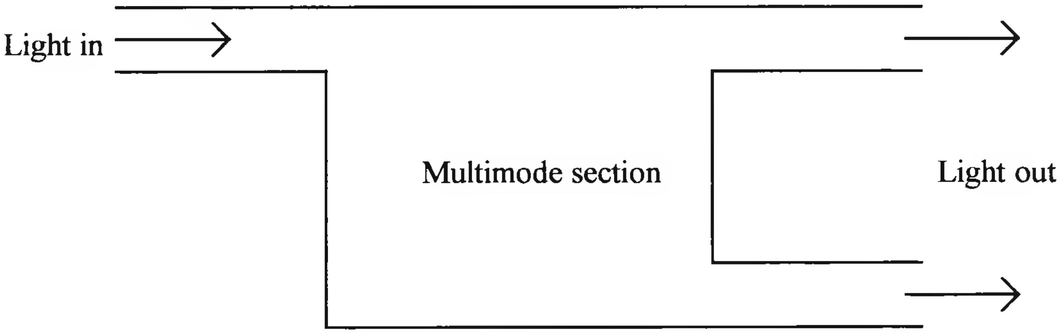

Fig. 3.7 (c) An asymetrically fed 1-to-2 way power splitter MMI waveguide

The first structure is a 1-1 way self-imaging MMI waveguide (such a structure operates using only symmetric modes, often referred to as '*restricted resonance*' (Besse *et al.*, 1994). In these restricted interference devices, the access waveguides are positioned in order not to excite modes 2, 5, 8, ... of the multimode section; this design permits the realisation of short couplers. The second two structures shown in Figure 3.7b and 3.7c are symmetric 3 dB power splitters (Spikeman *et al.*, 1994, Kim *et al.*, 1997) and an asymmetric 1-to-2 way power splitter (Besse *et al.*, 1996). These structures are of practical importance as optical splitters and/or re-routers.

The beat length , L_π of the MMI coupler may be calculated from the two lowest order modes as given by (Soldano *et al.*, 1995)

$$L_\pi = \frac{\pi}{\beta_0 - \beta_1} \tag{3.9}$$

The quadrature modal spacing can be calculated by using the simple relationship below (Soldano *et al.*, 1995) :

$$(\beta_0 - \beta_v) = \frac{v(v+2)\pi}{3L_\pi} \tag{3.10}$$

where v=0,1,2,3,..... (m-1) and m is the number of modes.

3.3.1 The properties of MMI section

Several important properties of MMI sections can be summarised below :

- An MMI section with length $6L_\pi$ reproduces the input field (self-imaging)
- An MMI section with length $3L_\pi$ inverts the input field.
- MMI sections with lengths $3*1/2\ L_\pi$ and $9*L_\pi$ divide the input power equally between a direct and a $\pm 90^0$ phase shifted inverse image.

These properties are periodic along the axial direction L with a period of $6L_\pi$. The three cases are depicted symbolically in Fig. 3.8.

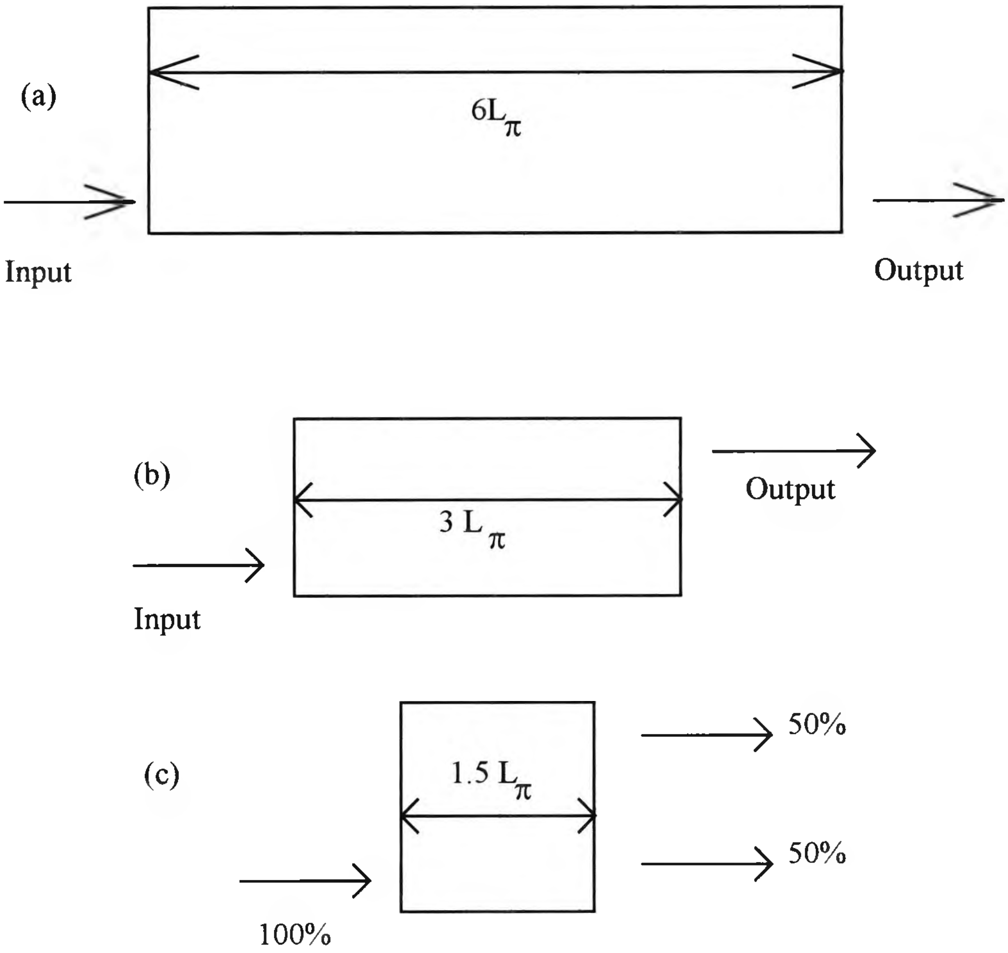

Fig. 3.8 Elementary operation of *3L* MMI- couplers in (a) the bar state (b) the cross state and (c) the 3 dB states

Couplers with section lengths as indicated above will be denoted as 3*L* MMI couplers, because their length equals three times that required in the TMI regime. The advantage of 3L MMI-couplers over TMI couplers is that the coupling properties are no longer dependent on the shape of the input field. There is thus freedom in choosing the width, the curvature and the position of the input waveguides, and the positions may be chosen so that the coupling between the guides can be eliminated.

3.3.2 Performance of MMI couplers

For N-way splitters (Thoen *et al.*, 1997), the relevant quantities for describing the performance are the excess loss and the balance between the outputs. For cross couplers, the important properties are the cross talk and the excess loss.

The excess loss of a splitter may be defined as (Spikeman *et al.*, 1993)

$$\text{Loss [dB]} \equiv -10\log_{10}\sum_{n}^{N}\frac{P_n}{P_{ref}} \tag{3.11}$$

where N is the total number of output ports, P_n the power measured at the output *n*, and P_{ref} is a reference power at the input. The balance between outputs *m* and *n* is defined as (Spikeman *et al.*, 1993)

$$\text{Balance}_{m,n}\text{ [dB]} = -10\log_{10}\frac{P_m}{P_n} \tag{3.12}$$

For a 2 x 2 cross coupler, the excess loss is defined as (Spikeman *et al.*, 1993)

$$\text{Loss [dB]} = -10\log_{10}\frac{P_c}{P_{ref}} \tag{3.13}$$

and the cross talk is defined as (Spikeman *et al.*, 1993)

$$\text{Crosstalk [dB]} = -10\log_{10}\frac{P_b}{P_c} \tag{3.14}$$

with P_b and P_c being the corresponding powers emerging from the bar and the cross output guides. Thus, an MMI is characterised by the power transmitted to all its outputs, relative to the power transmitted by a straight reference waveguide.

In an ideal *N*-way splitter, *N* perfect images, each carrying a fraction 1/N of the input power, will be projected onto the output waveguides, so the loss Eq.3.11 will be 0 dB, as will the balances Eq. 3.12. Due to the finite image resolution in physical MMI splitters, some loss will be incurred. When the dimensions of the MMI coupler deviate from the design dimensions, e.g., due to fabrication variations, the images will be slightly out of focus, leading to additional losses. To a first order approximation the loss will increase equally for all outputs, and as a result the balance will stay good over an appreciable range of variations.

What was said above about the loss in splitters also holds for cross couplers. As far as crosstalk is concerned, it should be absent in ideal cross couplers, because all the power would be imaged onto the cross output with infinite accuracy. For physical cross couplers, however, the finite accuracy with which the mode spectrum is constructed will not leave the region in front of the bar output absolutely dark, so there will be some crosstalk, which can be used. Besides, the power loss in the out-of-focus image, projected onto the cross output, will be coupled into the bar output, thereby rapidly increasing the crosstalk.

3.4 Summary

In this chapter the properties of directional couplers were first discussed. The importance of the finite element method for the calculation of accurate propagation constants and modal field values were explained in detail. The Least Squares Boundary Residual method, used to calculate the excited modal coefficients, was discussed next. The importance of the MMI based devices with their basic principles and properties such as crosstalk, excess loss and imbalance were explained in detail.

In the following chapters results will be presented for the directional coupler and MMI based devices as discussed in this chapter by using the numerical methods explained in Chapter 2.

Chapter 4

Optical polarizers

*Metal-clad directional coupler-based polarizer with two-dimensional modal confinement has been designed and its performance has been rigorously computed by using the accurate vector **H-field** finite element method, after taking into consideration the polarization-dependent coupling lengths, phase mismatchings and losses due to metal-cladding of the system involved. For the first time numerical analysis of a Multiple Quantum Well based polarizer is discussed. The equivalent refractive indices were calculated by using both the finite element and analytical expressions, and a rigorous comparison is made.*

4.1 Introduction

Since the single mode fibre cannot maintain the polarization state of the incoming signal the knowledge of the polarization state in a photonic device is essential. TE/TM polarization beam splitters are being increasingly considered for use in optical communications and signal processing systems, especially as essential components for the realisation of integrated-optical circuits for optical sensor and communications applications (Albert *et al.*, 1994). Passive optical waveguides which support only quasi-Transverse Electric (TE) or Transverse Magnetic (TM) optical modes constitute the easiest means of fabricating such guided wave polarizers. There is a number of different possible approaches by which an integrated circuit, incorporating polarization control can be achieved. The others being by using an anisotropic overlay (Uehera *et al.*, 1974) and a short section of a proton-exchanged waveguide (Suchoski *et al.*, 1974). Integrated optic TE/TM mode splitters have also been demonstrated on silicon (De Ridder *et al.*, 1993). One of the simplest concepts is to use a metal-clad layer on the top of one guide (Sun and Yip, 1994 and Saini and Sharma, 1995 and Tseng *et al.*, 1997). A Mach-Zehnder interferometer-based polarizer has been developed by Soldano *et al.* (1994) where, in this work, the metal-clad method is considered for rigorous numerical simulation to study its design parameters because it offers high-differential TE/TM mode attenuation. Optical polarizers without metal layers have also been demonstrated (Vander Tol *et al.* 1997). TE/TM mode splitter using directional coupling between hetrogeneous waveguides in $LiNbO_3$ has been demonstrated (Maruyama *et al.*, 1995).

The influence of the metal cladding on the coupling can be analysed by the use of several analytical approaches (such as the perturbation and equivalent methods) and numerical methods. There are advantages and disadvantages in the employment of both the techniques. The analytical methods are only accurate for planar structures but they may be inadequate, especially for practical waveguides with two or three dimensional optical structures. The analytical or semi-analytical solutions are also inaccurate, at times, due to the use of certain approximations which are necessary to make such solutions possible. However, the numerical scheme, on the other hand, can handle two-and three-dimensional problems more effectively and with the ever reducing computational costs, it becomes an effective and versatile approach for the design and development of modern complex optical components.

Metal-clad polarizers have been studied by using the perturbation method and the beam propagation method (Sun and Yip, 1994). However in this study, the vector **H**-field-based finite element technique has been used to consider several polarization-dependent optical parameters, including the effect of a thin metal overlayer on the device. A rigorous Least Squares Boundary Residual (LSBR) -based approach has also been employed to find the supermode coefficients for the two polarizations, as this approach is accurate even when the guides are non identical and/or strongly coupled. Modal losses for the supermodes are also considered in the present simulation to study the device performance in detail.

4.2 Theory of metal-clad polarizers

In a metal clad polarizer, the TM wave "*sees*" the metal whereas the TE mode is not much affected by the presence of the metal layer. As the modal profiles and the propagation constants of the TM wave experience the presence of the metal, the coupling lengths associated with these two coupled modes for the TM polarized wave are different than that of TE polarized wave. Thus if a relationship between the coupling lengths, L_{cTE} and L_{cTM}, for the TE and TM polarizations, respectively, can be established such that the device length, L, is given by

$$L = m * L_{cTM} = n * L_{cTE} \tag{4.1}$$

where m and n are integers (one of them being even and the other one odd), then the two polarized waves will emerge from two different output waveguides.

It has been shown earlier that for practical waveguide characterization, an understanding of the modal loss/gain nature of the waveguides is also important (Saini and Sharma, 1995 and Themistos *et al.*, 1995). However, the metal layer has been more frequently approximated as a planar layer and often the loss/gain characteristics due to the lossy metal layer have not been considered for polarizer design incorporating a two dimensional structure. However, to consider the modal loss in practical optical waveguide devices, the vector solution in terms of the transverse magnetic field vector ($\mathbf{H}_t$ formulation) (Abid *et al.*, 1993 and Lu and Fernandez, 1994) is important. In this approach, even though the size of the original global matrices is reduced, the computing time required is high compared to that for the **H**-formulation, as in the $\mathbf{H}_t$ formulation it is required to solve a complex eigenvalue equation.

Alternatively, the perturbation approach can be applied along with the vector **H**-field formulation, where all three magnetic field components are taken into account for the estimation of the modal loss/gain characteristics of optical waveguides (Themistos *et al.*, 1995). The advantage of the use of the **H**-field formulation with the perturbation technique is that numerically it is faster and it can be used for waveguides where the loss is not very large. For most of the practical guided-wave devices, this can be considered as a sufficiently accurate and an efficient approach.

From the modal amplitudes, field profiles and propagation constants of the excited modes, the evolution of the optical power along the axial direction can be calculated. By utilising the above numerical techniques, the percentage of power in each of the guides for the TE and TM polarizations, with and without loss, can be analysed and an optimised metal-clad polarizer design has been developed, along with several other possible designs, with their advantages and disadvantages discussed.

4.2.1 Loss/Gain analysis

Most of the available optoelectronic devices such as optical amplifiers, metal-clad TE/TM polarization splitters and semiconductor lasers have materials with complex refractive indices. Where complex refractive index could introduce a modal loss or gain depending on the sign of real and imaginary terms. The majority of the methods used to analyse optical waveguides ignore this important parameter. In this thesis it is shown that the gain/loss factors make a considerable effect on its performance and its accurate estimation is vital for the accurate design of optical guided wave devices. The metal-clad TE-TM polarizers demonstrated by Soldano *et al.*, (1994) are important components in many optical communication applications, such as polarization shift keying and polarization diversity multiplexing. These devices are based on the control of the absorption performance of the device.

These advances in lightwave technology during the last decade have encouraged the researchers in this field to develop techniques to calculate the gain/loss parameter in the optoelectronic devices. The waveguide problem can be solved analytically if the problem is a one-dimensional planar waveguide. However, most of the practical optoelectronic devices show two -dimensional confinements and hence an efficient numerical method is necessary. In this section the numerical approach to handle such a situation using the finite element method in conduction with the perturbation technique is discussed in detail. In the commonly used finite element formulation, such as the $\mathbf{E}_Z/\mathbf{H}_Z$ and **H**-field formulations the modal loss/gain is frequently neglected. The FEM to yield a vector solution in terms of the transverse magnetic field vector (H_t formulation) has been reported by several authors (Hayata *et al.*, 1986, Abid *et al.*, 1993, and Lu and Fernandez, 1994) and in this formulation the modal loss can be calculated directly from the solution of the complex eigenvalue equation and does not yield spurious solutions.

Earlier perturbation techniques have been applied to the analysis of modal loss/gain (Hayata *et al.*, 1986, and Themistos *et al.*, 1995) of optical waveguides. In this work the perturbation method is applied to the vector **H**-field formulation, where all the three magnetic field components are taken into account for the estimation of the gain/loss characteristics of different types of optical waveguides. This full vector approach is quite satisfactory for waveguides with small modal loss/gain and can be easily applied when the solution for a loss free waveguide is available.

4.2.2 The perturbation technique

The perturbation technique involves finding new result from those of another solution whose modal fields perturbate slightly from the original solution. For example, fibres that are slightly anisotropic, absorptive and elliptical, as well as being composite waveguides consisting of two or more well-separated fibres, can be considered as the perturbations of the basic circular fibre type with an isotropic refractive - index profile (Snyder and Love, 1991).

By taking advantage of the smallness of perturbation, the approximation technique can be used to derive accurate expressions for the modes of the perturbed fibre in terms of the known modes of the unperturbed fibre.

Perturbation formulae can be derived by use of two methods:

(i) By using the Taylor series expansion in terms of the small perturbation parameter.

(ii) Directly from the variational approach.

The perturbation technique which is applied to find the modal loss/gain approximates the phase constant, β and the **E** and **H** field profiles with perturbed values $\hat{\beta}$, $\hat{E}$ and $\hat{H}$, which are the solutions to the loss-free optical waveguide problem. The gain/loss of the dielectric medium is given by the imaginary part, n', of the complex refractive index, $\bar{n}$.

The attenuation constant, α, in a dielectric medium, arising due to dielectric losses can be expressed as (Pantic and Mittra, 1986) :

$$\alpha = \frac{P_d}{2P_o} \tag{4.2}$$

where P_d is the power dissipated in the dielectric material and P_0 is the time-averaged power flow.

Over a cross section Ω of a dielectric optical waveguide, with any number of subregions, Ω s, incorporating gain or loss, expressed as complex dielectric constant, ε_s', for each subregion, the perturbation method can be applied by evaluating the attenuation constant for the whole guide, in terms of the electromagnetic fields as (Pantic and Mittra, 1986) :

$$\alpha = \frac{\omega \sum_{s} \varepsilon \frac{\varepsilon_{s}^{'}}{\varepsilon_{s}} \cdot \int_{\Omega_s} |E_0|^2 . d\Omega}{2 \operatorname{Re} \int_{\Omega} (E_o \times H_o^{*}) \cdot \hat{z} \cdot d\Omega} \qquad (4.3)$$

where ω is the angular frequency, $\hat{z}$ is the unit vector along the z-axis, $\mathbf{H_0}$ and $\mathbf{E_0}$ are the unperturbed electric and magnetic field vectors for the loss-less conditions respectively and $\varepsilon_s^{'}$ and ε_s are the imaginary and the real parts of the loss tangent of each sub-region.

The perturbation Eq. 4.3, is based on the assumption that the unperturbed magnetic, H_0 and electric, E_0 field components remain unchanged in the presence of loss and that the value of the loss tangent is very small *i.e.* $\varepsilon_s^{'} << \varepsilon_s$.

4.2.3 Finite element method with perturbation

The perturbation method, described in the previous section, can be used in conjunction with the FEM, to determine the loss/gain characteristics of an optical waveguide. As was shown in Section 2.9, a loss-free optical waveguide problem can be formulated to be a standard eigenvalue problem (2.24), where the eigenvalue corresponds to the square of the free space wavenumber, k_0^2, and the eigenvectors to the magnetic field profile, **H** (x,y). By assuming that the above eigenvalue of the discretised model of the loss-free optical waveguide is perturbed by a small amount in the presence of a small loss, this can be directly substituted in a discretized form of the perturbation Eq. 4.3 in order to estimate the attenuation constant.

In an earlier work, discretized perturbation equations have been developed (Themistos *et al.*, 1995) based on the scalar formulation for the TE and TM modes and the full vector **H**-field formulation, to determine the attenuation characteristics of the optical waveguide problem.

4.2.3.1 Full vector FEM with perturbations

The use of the scalar approximation of the FEM with the perturbation technique provides a quite accurate and time efficient computational tool for the determination of the propagation characteristics in simple optical waveguide structures where the optical fields can be described as predominantly TE or TM. For a more accurate representation of the electromagnetic field, in optical waveguides a vector formulation is required, where all the field components are taken into account. Therefore, a perturbation formula has been developed, which has been used in conjunction with the full vector **H**-field formulation, for the estimation of the gain/loss properties of several optical waveguide structures, with small gain or loss. In the above approach, the contribution of all the three magnetic field components is considered in the calculation of the attenuation constant, α. By using Maxwell's equations to express the electric field, **E**, in terms of the magnetic field components, H_x, H_y, and H_z, the perturbation formula (4.3) can be written as :

$$\alpha=\frac{\frac{1}{\omega}\sum_{e}\frac{\varepsilon_e'}{\varepsilon_e^2}\iint_{\Delta}\left\{\left(\beta H_y-j\frac{\partial H_z}{\partial y}\right)^2+\left(j\frac{\partial H_z}{\partial x}-\beta H_x\right)^2+\left(j\frac{\partial H_x}{\partial y}-j\frac{\partial H_y}{\partial x}\right)^2\right\}\cdot dxdy}{\frac{2}{\omega}\sum_{e}\frac{1}{\varepsilon_e}\iint_{\Delta}\left\{\left(\beta H_y H_y+\beta H_x H_x-\frac{\partial H_z}{\partial y}H_y-\frac{\partial H_z}{\partial x}H_x\right)\right\}dxdy} \tag{4.4}$$

By using the above formula the attenuation coefficient can be calculated.

4.3. Results of the analysis

The schematic of the structure considered in this study is shown in Figure 4.1, it consisting of two identical InGaAsP/InP -based parallel rib waveguides, but with a metal cladding on one of the ribs (guide *a*). The refractive indices of the guide and the substrate are 3.39

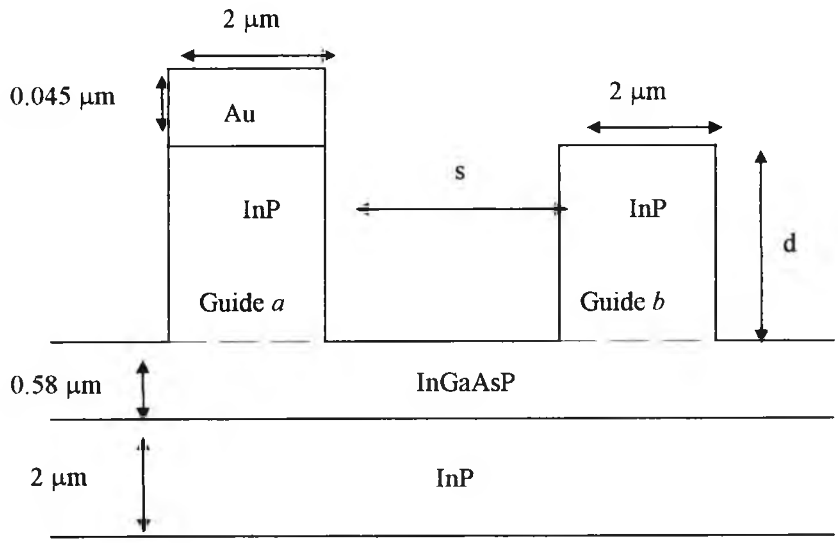

Fig. 4.1 Schematic of the metal-clad directional coupler-based polarizer

and 3.17 respectively at an operating wavelength of 1.55μm calculated by using Broberg *et al.* (1984). The complex refractive index of gold (Au) was taken as n_{au}= 0.18-j10.2 (Soldano *et al.*, 1995). The rib width was 2μm and the rib height, *d*, was varied to obtain an optimized design and also to show the effect of the metal layer on the TM mode. Here, *s* is the separation between the two guides. For the TE case, although the two guides are nonidentical their propagation properties do not, however, suffer from the presence of the metal layer. The propagation constants of the isolated guides are almost identical. Figure 4.2a shows the H_y field profile for the even TE supermode.

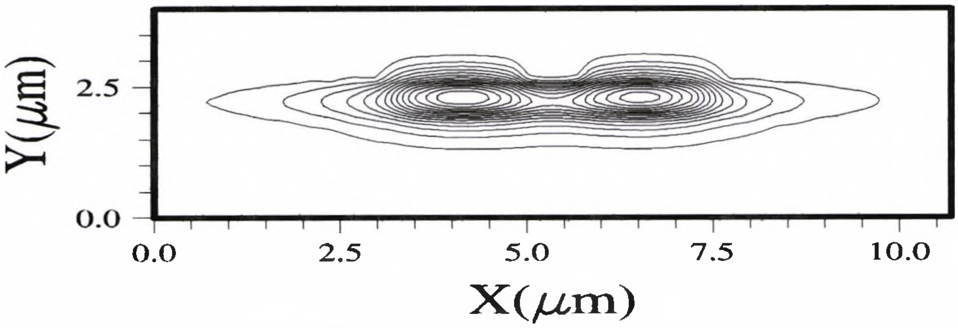

Fig. 4.2a H_y field profile for the TE even supermode

It can be seen that the guides are coupled and the even supermode power is equally distributed in both the guides, where the propagation constant of the even mode is slightly higher than those of the two isolated guides. Figure 4.2b shows the H_y field profile for the TE odd supermode,

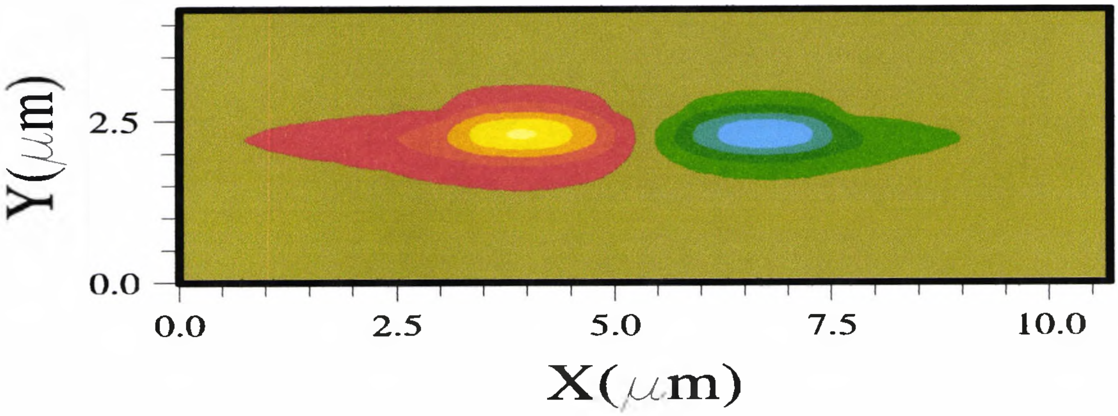

Fig. 4.2b H_y field profile for the TE odd supermode

and in this case the field is anti-symmetric and again the optical power nearly equally distributed between the guides. The propagation constant of the odd mode is slightly smaller than that of the two isolated guide modes. Although the two TE supermodes, shown in Figs. 4.2a and 4.2b, are almost symmetric or antisymmetric, however, a very slight imbalance can be noticed by observing the slightly higher power density in guide *a* for the odd supermode. On the other hand, the TM modes will be affected considerably by the presence of the metal cladding on top of one of the waveguides. This metal cladding can support a surface plasmon mode, which is the first TM mode, where this TM_0 mode was also identified for this structure. However, its propagation constant was much larger than that of the first TM mode of guide *b* (without the metal layer) and they will not interact to form coupled supermodes. The second TM mode in guide *a* has a propagation constant closer to that of the first TM mode in guide *b*, and interacts to form two coupled supermodes of the structure. However, for the TM polarized waves, the propagation constant of guide *b* is not identical to that of guide *a*. When the separations between the guide is large, both the propagation constant and the field profile of the TM even-like supermode are almost the same as those of the guide *b* and that of the TM odd-like supermode is similar to that of the isolated guide *a*. The H_X field profiles for the TM supermodes are shown in Figures 4.3a and 4.3b, where the power imbalance of the supermodes between both the guides is visible.

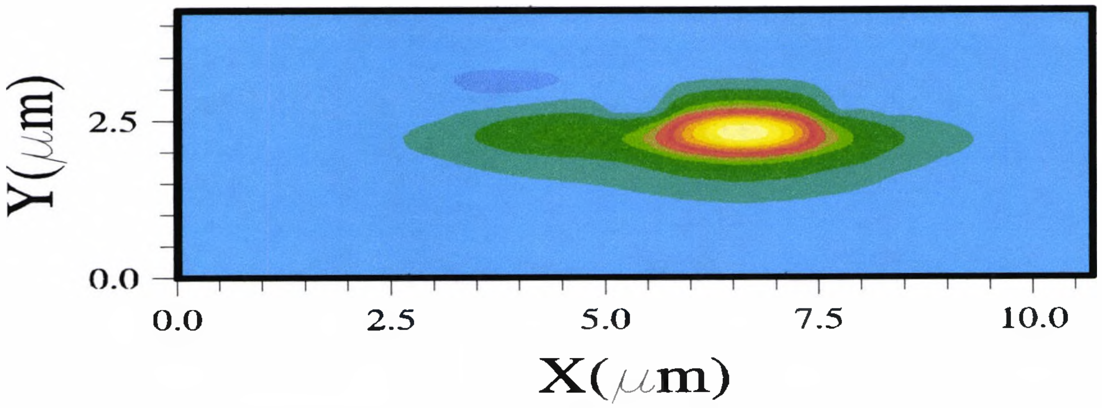

Fig. 4.3a H_X field profile for the TM even supermode

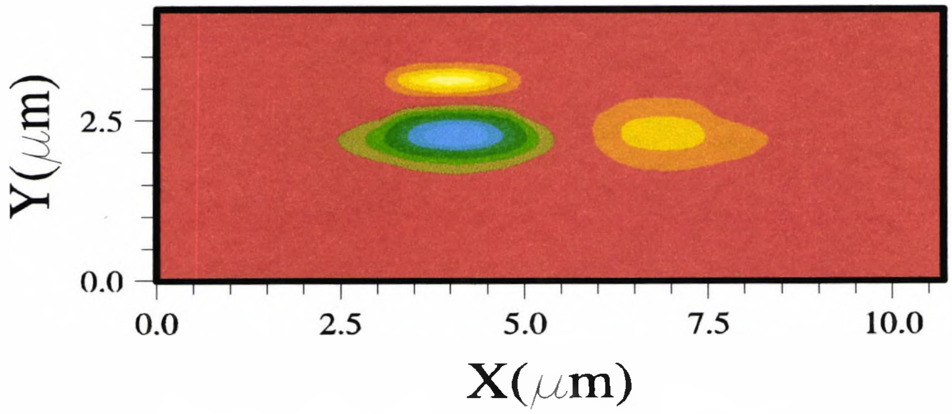

Fig.4.3b H_x field profile for the TM odd supermode

It can be seen in Figure 4.3a that there is more power in guide *b* than in guide *a*. It can also be seen that the presence of the metal layer is quite visible from the field distribution in the case of the odd mode. Fig. 4.3b shows the odd mode. It can be noticed from Fig. 4.3b that the metal clad is present on the left side of the directional coupler.

Figure 4.4 illustrates the coupling length as a function of the separation between the waveguides, *S*, for the TE and TM polarizations.

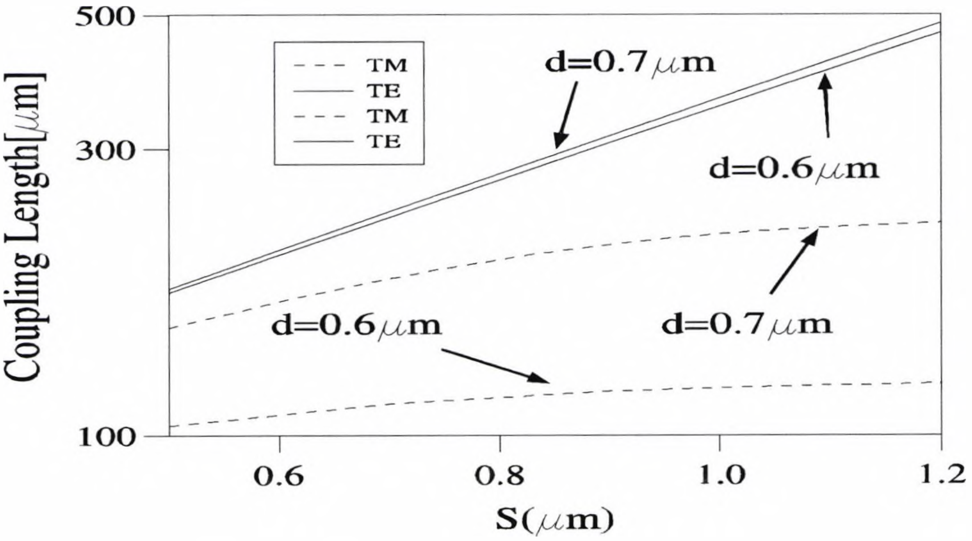

Fig. 4.4 Variation of the coupling length, L_c with the separation between the guides, *S*.

The variation of the coupling lengths with waveguide separation increases exponentially and in a semi-log scale it is shown as a linear line to illustrate the behaviour of the TE mode which is the typical nature expected for coupled identical waveguides. When the value of *s* is decreased, the modes are strongly coupled and the value of the propagation constant of the even mode increases, that of the propagation constant of the odd mode decreases and hence the coupling length L_c decreases. In this design, although the guides are non-identical due to the presence of a metal cladding on the top of one rib, the TE supermodes are, however, not affected by the metal layer and therefore the modal solutions are not influenced by the presence of the metal and the L_c variation with *S* relationship is almost linear. The effect of the rib height (*d*) on the value of L_C is also very small. However, the TM modes, on the other hand, see the metal and hence are influenced strongly by the presence of the metal layer. The modal solutions for TM polarization are slightly more sensitive than for the TE polarization. This is visible from the L_C relationship for the TM polarization (dashed) in Figure 4.4, and in this case the coupling length initially increases linearly (in a log-scale plot) with *s*, but, however, asymptotically reaches a constant value at higher values of separation. The effect is more prominent for lower values of *d*, as when the metal layer is closer to the waveguide core and it can be observed that the TE and the TM curves are further apart. The use of 10000 linear elements provides an accurate estimate of the coupling lengths for both the polarizations.

In this study the main objective was to design a polarizer such that the device length, *L*, was an integer odd or even multiple of the coupling length for the TE and the TM modes as given by Eq. 4.1, and the effect of rib height, or the proximity of the metal layer the guide core has also been investigated. Three different rib heights were considered. When *d*, the rib height, was 0.7μm the TM mode was affected considerably by the presence of the metal. Here three times the coupling length of the TE mode was found to be equal to four times that of the TM when the waveguide separation s was 0.75μm and in this case the device length was 762μm. However, when the metal layer was shifted further away from the guiding core, (d was increased) the effect of the metal layer was less and hence the TE and TM coupling curves were seen to be very close to each other, but this has not been plotted here as the overall device length will become too large. On the other hand, when the rib height is reduced to 0.6μm, the effect of the metal layer increases and it is possible to obtain twice the coupling length for the TM polarization to be equal to the coupling length of the TE polarization at a coupler separation (s) of 0.7μm. In this case, the device length was 233μm. Thus by choosing d=0.6μm a shorter device length can be obtained, which is an important factor in designing compact photonic integrated circuits. However, as the modal loss per unit length for an isolated metal clad guide for the TM polarization will increase, the total loss for the TM modes also needs to be investigated.

Figure 4.5 shows the loss characteristics as a function of the rib height, d, for the TE and the TM polarizations. As can be seen from this figure, the TE mode suffers minimum modal loss due to the presence of the metal and this value reduces with the rib height (d). However, on the other hand, the second and third transverse magnetic modes, TM_0 and TM_1 respectively suffer significant modal loss. The first TM mode (TM_0) is the surface plasmon mode, confined only near the metal layer and hence experiencing a high attenuation, and it is not affected by the change of rib height. However the TM_1 mode, predominantly is confined in guide a, and losses are due to the field extending towards the metal layer, where the modal loss reduces as the rib height is increased.

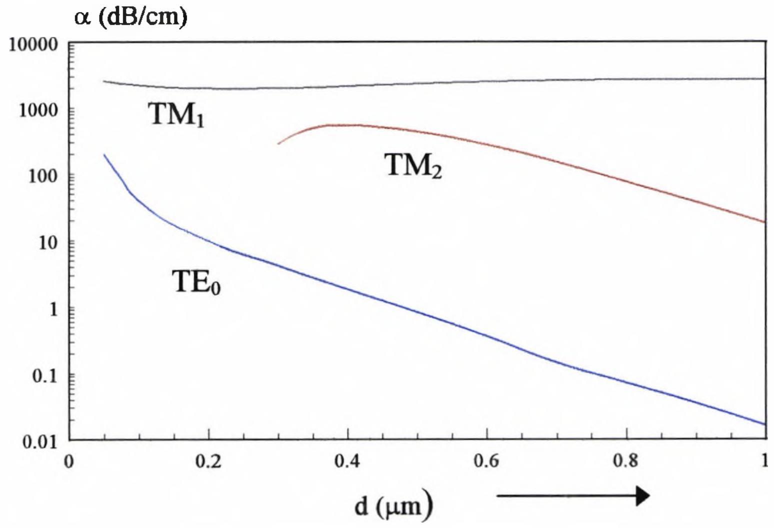

Fig. 4.5 Modal loss as a function of the rib height for the TE and the TM isolated modes

From Figure 4.5 it can be seen that the values of the loss decay exponentially with the rib height (*d*) for the modes confined in the rib cores.

Once the modal propagation constants (β_e and β_o) and the field profiles ($\mathbf{H}_e$ and $\mathbf{H}_o$) of the superstructure are computed by using the FEM, then the LSBR method is applied to find the excited modal coefficients (b_e and b_o). The modal coefficients are then used to find the evolution of the composite field along the axial direction. By taking the phase of the even mode (β_e) as a common factor out of the sum and assuming a time dependence, given by $\exp(j\omega t)$ and implicit hereafter, the field profile $\mathbf{H}(x,y,z)$ can be written as :

$$\mathbf{H}(x,y,z)=b_e\mathbf{H}_e(x,y)+b_o\mathbf{H}_o(x,y)e^{-j\Delta\beta z} \tag{4.5}$$

where $\Delta\beta = \beta_e-\beta_o$ and similarly the field profile can be written for the $\mathbf{E}(x,y,z)$ field.

Since the rib height of 0.6μm gives the smallest device length, it was first considered as the basis of a calculation of the power transfer efficiencies. In Figures 4.6a and 4.6b the composite fields are plotted at *z*=0_+μm, just at the beginning of the directional coupler section, and at *z* = L_{cTE} = 233μm for the TE polarizations, where L_{cTE} is the coupling length of the TE polarization. In this case, the exited modal

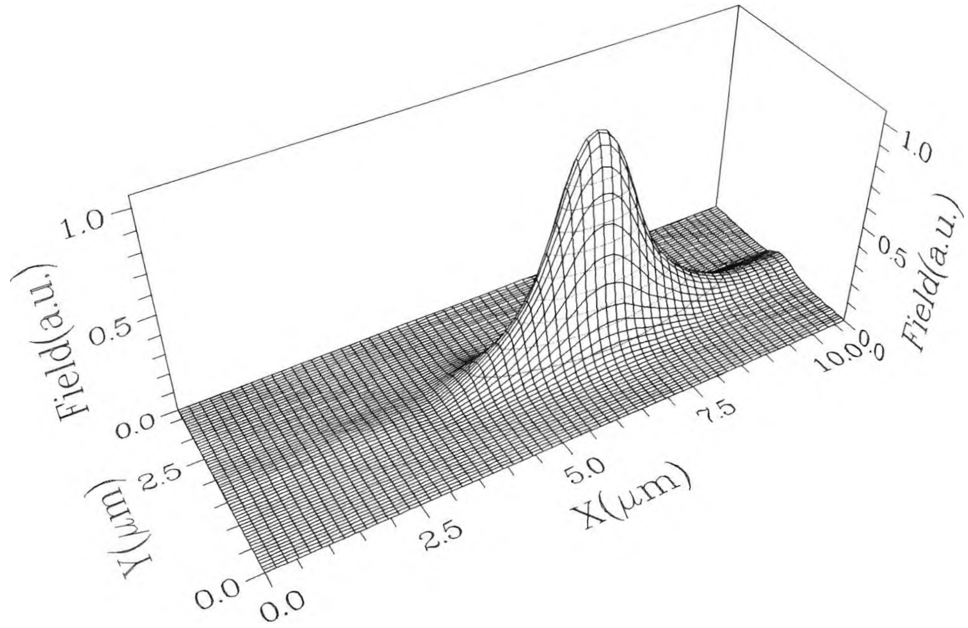

Fig. 4.6a Composite field profile at *z*=0_+ for TE the polarization

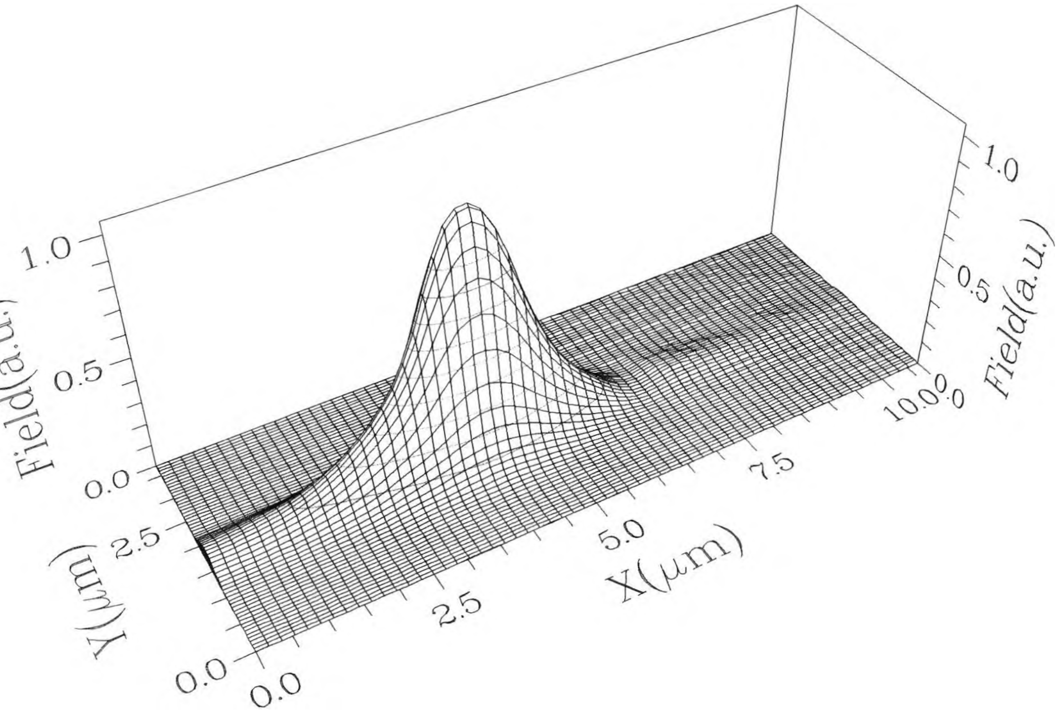

Fig. 4.6b Composite field profile at *Z*=233μm for the TE polarization

coefficients for the first and the second mode are nearly identical for the TE polarization and calculated to be 0.748 and 0.659 respectively, which means they carried 56% and 43% of the power respectively. Since both the supermodes were also nearly symmetrical or antisymmetrical, the addition of the supermodes (with their appropriate coefficients) produces an overall field similar to the input field profile and from Figure 4.6a it can be seen that most of the input power is coupled to guide *b* at the discontinuity interface. However, due to the π phase reversal at L_C, nearly all the power is transferred from guide *b* to guide *a* due to the near complete cancellation of the modal field profiles in guide *b* and their addition in guide *a*.

Similarly after the TM supermode profiles were calculated, as shown earlier in Figure 4.3, the LSBR method was used to find the coefficients of the TM supermodes generated at the beginning of the directional coupler section. However, in this case, the excited modal coefficients of the two supermodes were determined to be 0.981 and

0.176 respectively, which means they carry 96% and 0.03% of the power, respectively. It should be noticed that the two supermode profiles were also highly unbalanced.

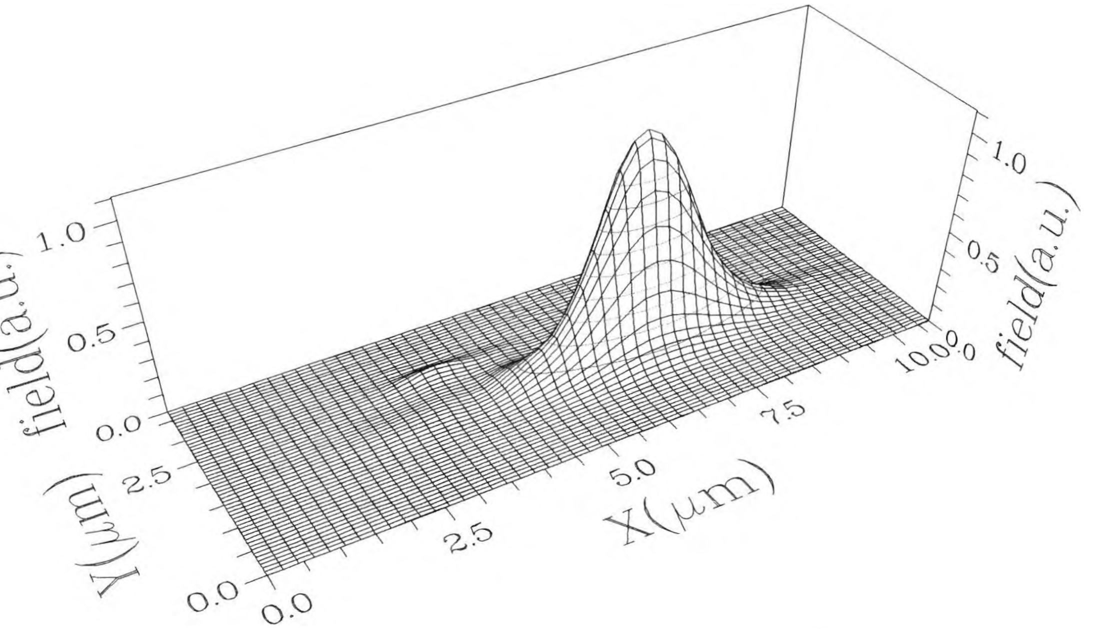

Fig. 4.7a Composite field profile at z=0_+ for the TM polarized wave

Although the supermode coefficients are unequal, however the fields at the beginning of the directional coupler section will be quite similar to the input field, at z=0_+ as shown in Figure 4.7a, as the necessary boundary conditions are the continuity of the tangential electric and magnetic fields.

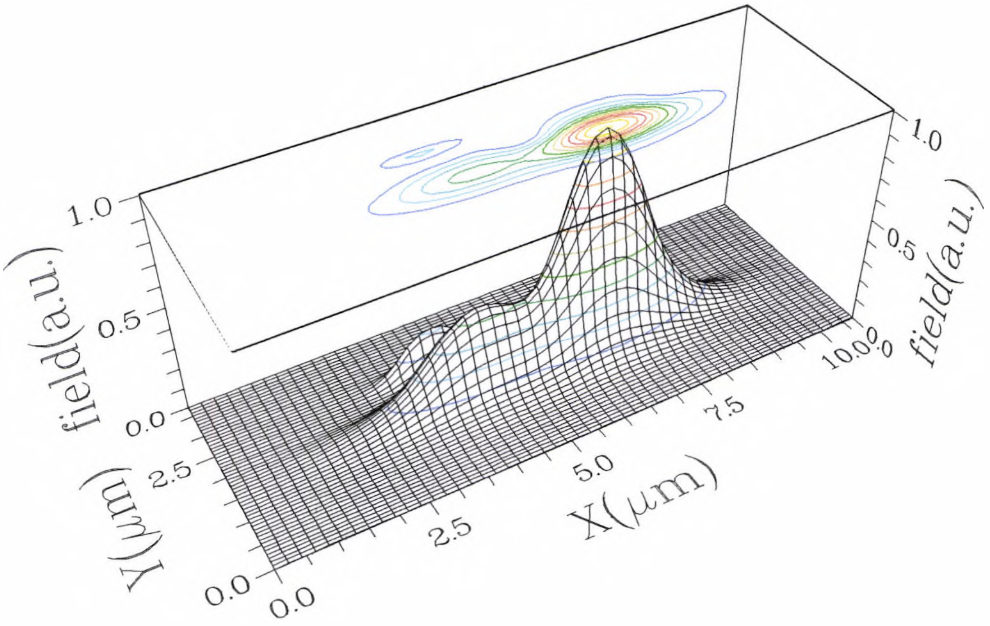

Fig. 4.7b Composite field profile at z=114μm for the TM polarized wave

The presence of a small field in the metal layer is visible in Fig. 4.7b. However, the composite field in Figure 4.7b shows that at the coupling length L_{cTM} (z=114μm) power is coupled from guide *b* to guide *a* but at a level which is significantly lower. This is due to the incomplete cancellation of the modal fields. In Figure 4.7b the presence of optical energy in the metal layer is also clearly visible. Figure 4.8 shows the evolution of power sharing by the two waveguides along the coupler length.

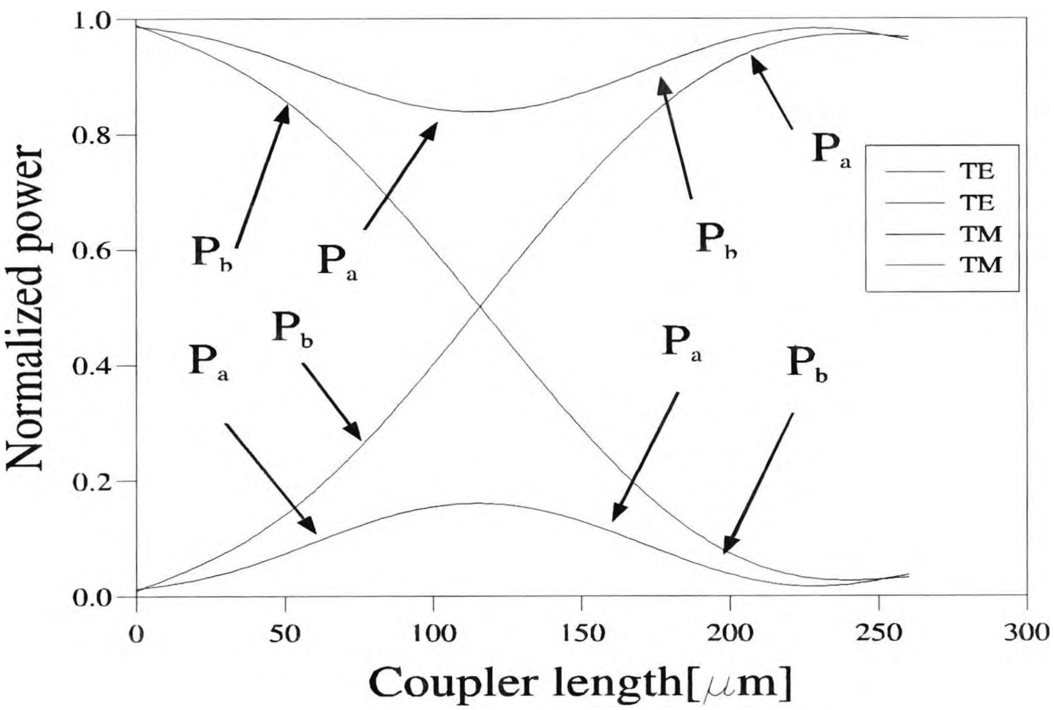

Fig. 4.8 Power coupling between the waveguides along the axial direction

It can be observed that for the TE polarization, at $z=0_{+}\mu\text{m}$, 99% of the power was coupled to guide *b* and nearly zero power to guide *a*. Along the coupler length, TE polarized power is coupled to guide *a* from guide *b* and at a distance, $L=L_{cTE}$ = 233μm, most of the power has been transferred to guide *a*. The device length was adjusted such that one coupling length of TE was equal to twice that of TM. For the TM mode at $z=233\mu m$, guide *b* has almost 100% power but guide *a* has nearly 0%. However, at one coupling length, for the TM case only, a fraction of total power couples to guide *a,* due to the lack of phase matching between the TM modes and while the maximum power transfer efficiency is only 16%, even this power couples back to guide *b* at twice the coupling length. Thus at $z=L_{cTM}$=114μm, 84% of the power was in guide *b* and 16% was in guide *a,* and at approximately 230 μm, which is twice the coupling length, most of the TM power will emerge out of guide *b* whereas the TE power will come out of guide *a*. This indicates the operating principle of a directional coupler-based TE/TM mode splitter.

4.3.1 Calculation of modal loss

It is important to estimate the attenuation constants of the supermodes, rather than just the isolated modes. The attenuation constants for the TE and the TM supermodes were calculated for the superstructure which is shown in Fig.4.9.

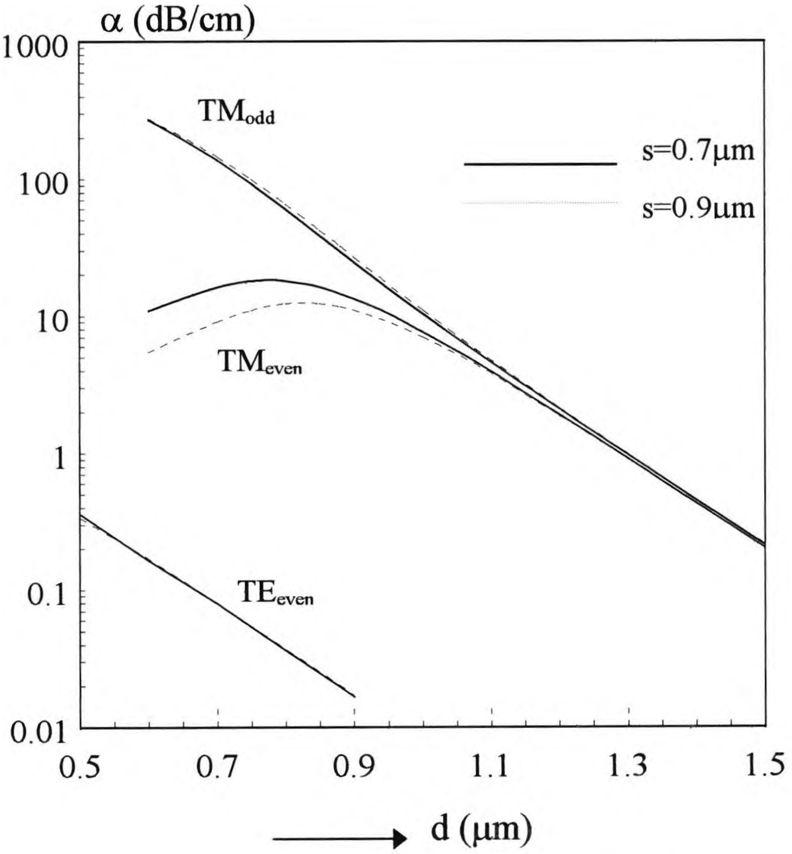

Fig. 4.9 Modal loss characteristics for the two TM supermodes

Although it can be observed that the loss constants for TM supermodes were higher than those for TE polarizations, however, some distinct features can be observed, when compared to the isolated modes. These attenuation constants are calculated for a coupler separation of 0.7μm and 0.9μm for varying rib height, *d*. When *d* is higher, the metal layer is far away from the guide core, the loss is less and also since the perturbation due to the presence of this layer is smaller, the two isolated guides are nearly phase matched, and the two supermode power profiles are equally divided into two waveguides, with their loss coefficients similarly decreasing. At a lower *d* value, the loss coefficient is higher, as the metal layer is near to the guide core *a*, but however, for the TM odd mode this is much higher than for the TM even supermode, since in the former case the optical power is mostly confined in guide *a*, which contains the lossy metal layer. It can be seen from Figure 4.9 that for a higher value of *d*, the effect of the metal is almost identical for the odd and even modes, but however the odd mode suffers a higher loss than the even mode at lower separations. At smaller waveguide separations (*S*), the guides are strongly coupled and guide *a* will have an increased share of power for the even mode and the presence of the metal will affect the modal loss. This can be seen from Figure 4.9. It can be predicted from this figure that, at very low separations, the TM odd-like and the even-like modes would have nearly identical loss characteristics. Figure 4.10 shows the power transfer characteristics between the guides after considering the loss in the metal layer.

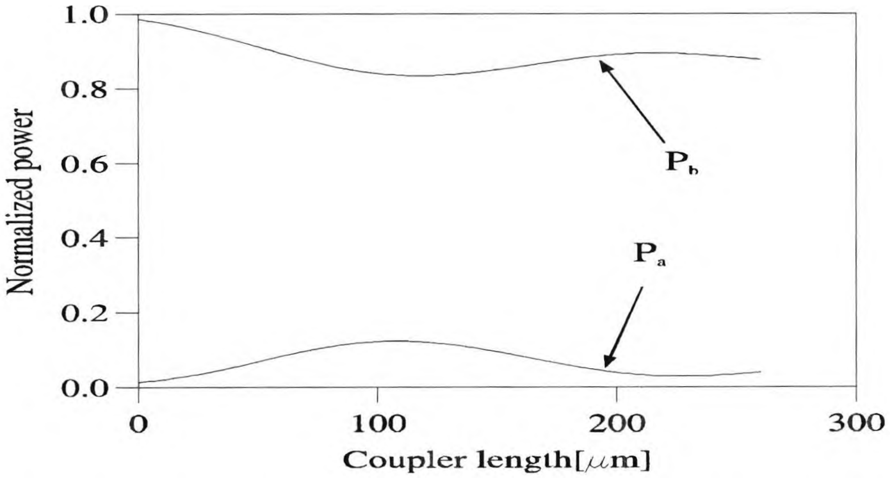

Fig. 4.10 Power coupling characteristics after considering the attenuation of the supermodes

It is obvious from this figure that the total power decay exponentially with coupler length for the TM mode, hence showing the importance of the inclusion of the modal loss in practical optical waveguide designs since the overall power available in the two waveguide ports for the two different polarizations is an important factor. It can be noted that although a larger *d* value caused a reduced modal loss per unit length, the overall device performance will be unfavourable. This is primarily due to the small difference between the TE and TM modes, and thus the *m* and *n* integers have to be larger which, coupled with larger values of *S*, will make the device longer. So the overall modal loss for the TM and TE modes can be higher. Besides that, when *d* is reduced, the propagation constants of the two TM modes are very different, and only a small amount of power can be transferred between the guides. In this case, if the TM mode is launched into guide *b*, most of the power will remain in that guide, which has a smaller loss for the TM modes, and the overall loss will be smaller.

4.4 Optical Polarizers Incorporating Multiple Quantum Wells

In this section a novel approach has been demonstrated to the design of an optical polarizer using nonidentical coupled optical waveguides with 2-D confinement. The equivalent index for the Multiple Quantum Well (MQW) region has been computed rigorously by using finite element method incorporating the vector **H**-field formulation. The power transfer characteristics of the TE and the TM polarizations have been computed by using the Least Squares Boundary Residual method.

4.4.1 Results of the analysis incorporating MQW regions

Although the simple directional coupler shows a polarization-dependent performance, however, its TE/TM extinction is not sufficient for the design of an optical polarizer. It is also known that MQW regions show a different equivalent index for two polarizations, but however, this difference of equivalent indices is also insufficient to enable the design of an optical polarizer incorporating two *identical* MQW waveguide cores. In this work, two *nonidentical* waveguides, with only one incorporating a MQW region, are used in the design of an optical polarizer.

A schematic of the directional coupler with nonidentical guides simulated in this study is shown in Figure 4.11. illustrating two guides *a* and *b* separated by a distance, *s*. In this design the top waveguide is fabricated from bulk $In_{1-x}Ga_xAs_yP_{1-y}$ material and by adjusting the molar fractions, the refractive index of the top guide can be made 3.3141 for both the TE and TM polarizations. On the other hand, the lower waveguide, being a MQW region, sees an equivalent index for the TE and the TM polarizations of 3.3141 and 3.3013 respectively (Rahman *et al.*, 1993).

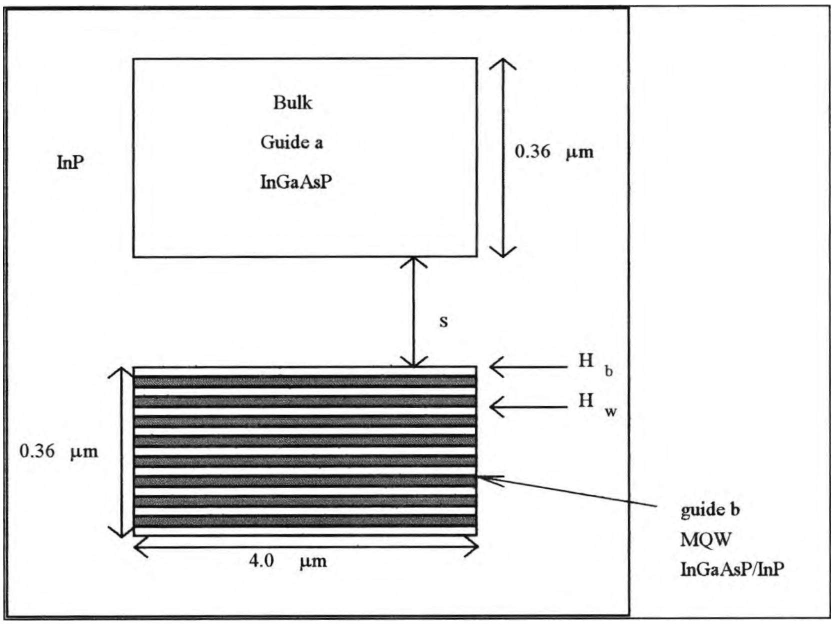

Fig. 4.11 A schematic of the directional coupler with non identical guides

To do so, the vector **H**-field based finite element method (FEM) is used to find an accurate modal solution for coupled optical waveguide structures. However, due to the many layers involved in the MQW region, the concept of using the equivalent index for the MQW can be an acceptable approach to reduce computational costs. Since equivalent index concept has thus far been derived (Alman *et al.*, 1992) or numerically verified (Rahman *et al.*, 1993) for planar structures, in this work, a similar concept is rigorously tested for a 2-dimensional structure, using the vector **H**-field FE formulation.

In this work the lower guide, *b*, is a MQW guide comprising nine periods. Initially a single waveguide incorporating a InGaAsP well and a InP barrier layer completely covered by a InP region is considered for characterization. The thickness of the well (H_w) and of the barrier (H_b) are 20nm and the corresponding refractive indices of n_w and n_b were 3.4636 and 3.17174 respectively. The width of the waveguide was taken as 4μm at an operating wavelength of 1.52μm. For computational efficiency, a two-fold symmetry (thus using only one-quarter of the structure) has been considered. By using a total of 4800 first order elements, by representing the actual MQW region exactly, the effective index, ($n_e=\beta/k_0$) and the propagation constant for the waveguide was calculated to be 3.20804 for the quasi-TE and 3.19955 for the quasi-TM polarized fundamental modes. To proceed, the entire MQW region is replaced by a homogeneous region with its equivalent index, calculated by using the equations below (Alman *et al.*, 1992)

$$n_{TE}^{"\,2} = \frac{n_W^2 H_w + n_b^2 H_b}{H_w + H_b} \tag{4.6a}$$

$$\frac{1}{(n_{TM}^{"})^2} = \frac{\dfrac{H_W}{n_w^2} + \dfrac{H_b}{n_b^2}}{H_w + H_b} \tag{4.6b}$$

and previously these equations were verified numerically for planar waveguides (Rahman *et al.*, 1993).

In this example, following these equations, the values of the equivalent index for the TE and TM polarizations were calculated as 3.3201 and 3.3080 respectively. When these values were used to replace the MQW region, the modal solutions generated by the FEM yielded effective indices (n_e) 3.21067 for the TE polarization and 3.20175 for the TM polarization, which clearly shows an overestimate for both the polarizations. Next, the equivalent indices for the two polarizations are adjusted to obtain the same modal solutions as were obtained for the true MQW structure and the correct effective index values were found to be 3.3141 and 3.3013 respectively (Rahman *et al.*, 1993). The variations of the equivalent indices with the well thickness, H_w, for the TE and TM polarizations, using the Eq.4.3, are shown by the solid lines in Fig. 4.12.

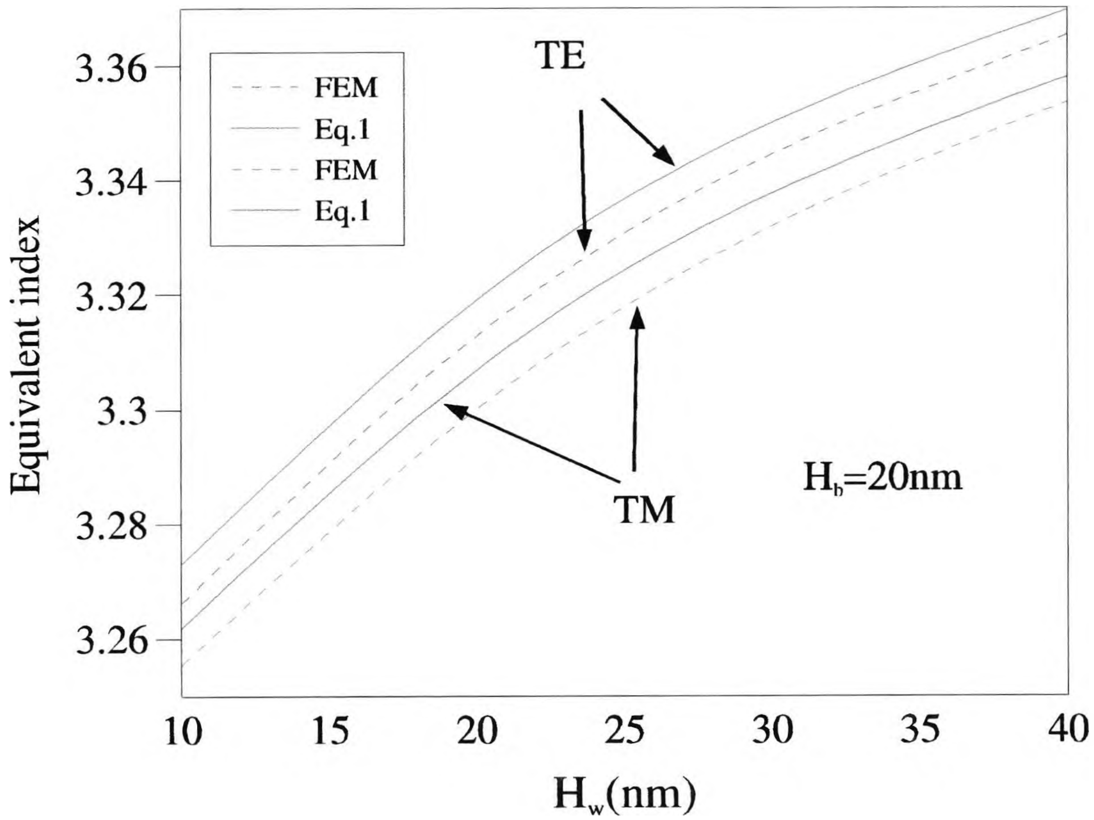

Fig. 4.12 Variation of the equivalent indices with well thickness H_w for the TE and TM polarizations

On the other hand, the actual equivalent index, which gives the same modal solutions for the MQW region, obtained in this work, is shown as the dashed line in Fig. 4.12.

It can be observed that the simple planar approximation used previously (Alman *et al.*, 1992) overestimates the value obtained by rigorous numerical simulation for the MQW structures with 2-dimensional confinement.

Figure 4.13 shows the variation of the coupling length with the changing separation, *S* between the guides.

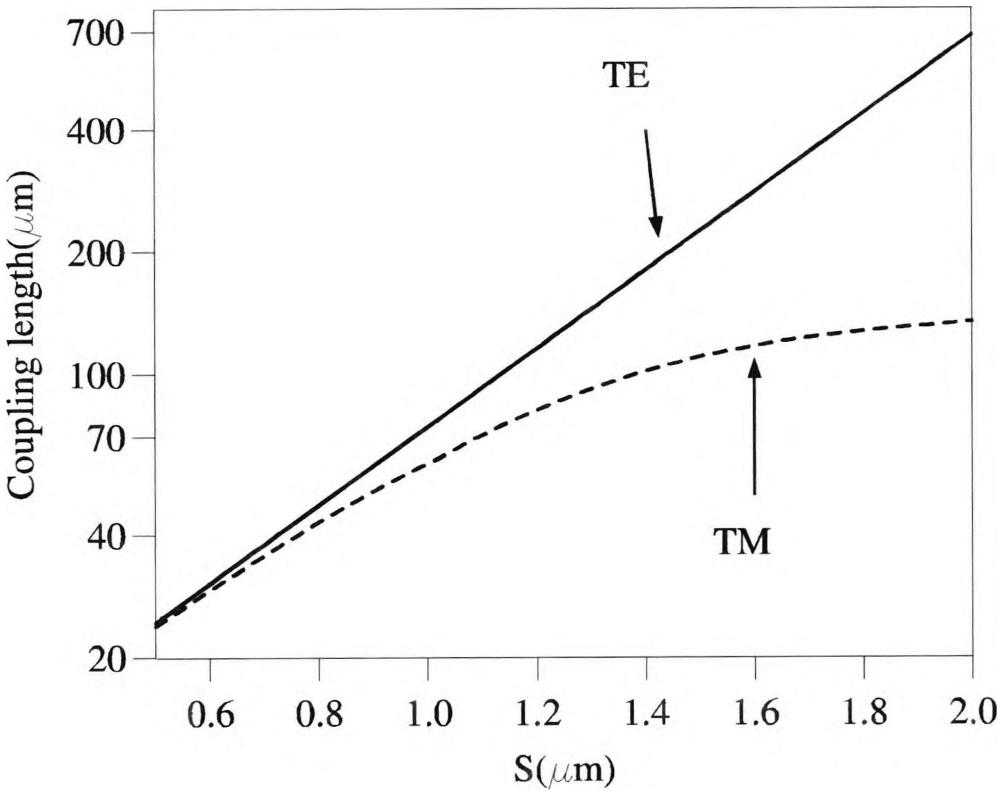

Fig. 4.13 Variation of the coupling length with the guide separation, *S*.

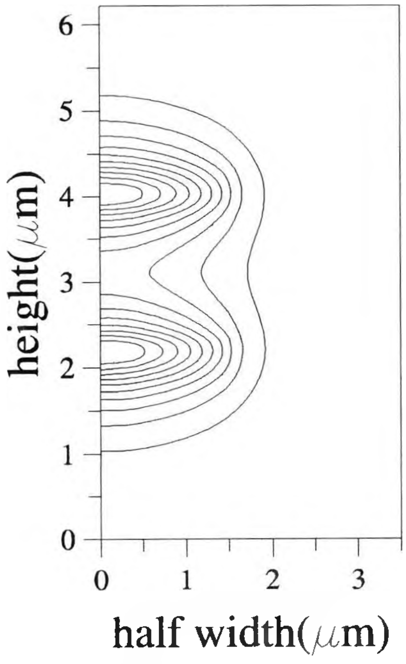

Fig. 4.14a **H_y**field profile of the TE even supermode

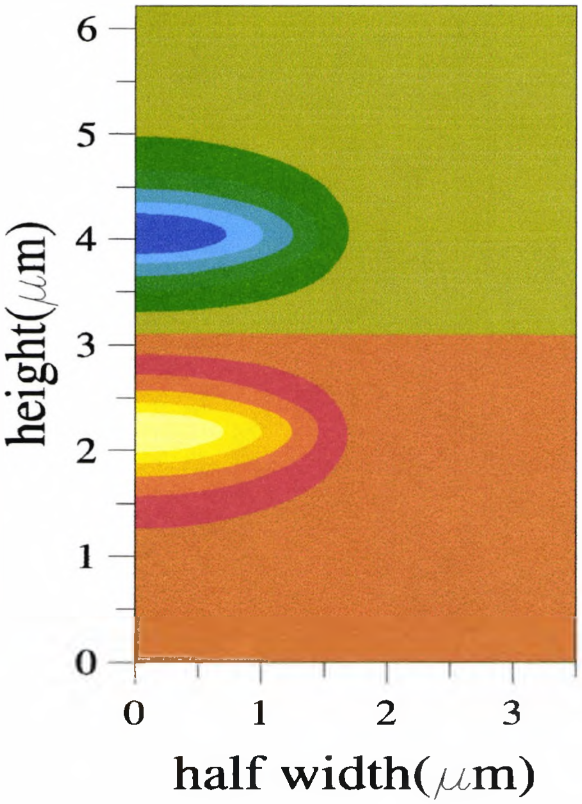

Fig. 4.14b $\mathbf{H_y}$ Field profile of the TE odd supermode

The coupling length axis is plotted in semi-log scale to reveal exponential variation (as a straight line in the semi-log plot) of the coupling length for the TE polarization (solid line) with the increasing separation. However the coupling length for the TM polarization (dashed line), initially increases exponentially with *s*, but asymptotically reaches a maximum value with the further increase of the separation. At higher separations the guides are isolated and with the waveguides being nonidentical the propagation constant difference does not change with increasing separation. Thus the coupling length remains constant. From Fig.4.13, a relationship can be derived such that two times the coupling length for the TM polarization equals the coupling length of the TE. In this case, when the separation between the waveguides was 1.495μm, the coupling length of the TM polarization was 110μm and that for the TE polarization the coupling length was 220μm. Therefore by choosing a directional coupler section of 220μm an effective TE/TM polarizer can be designed.

For the TE polarization, the waveguide parameters were designed such that the two waveguides were identical and the two supermodes were completely symmetrical or antisymmetrical. The height and width of the top guide was 4μm and 0.36μm respectively. Figures 4.15a and 4.15b shows the even and the odd supermodes for the TM polarization.

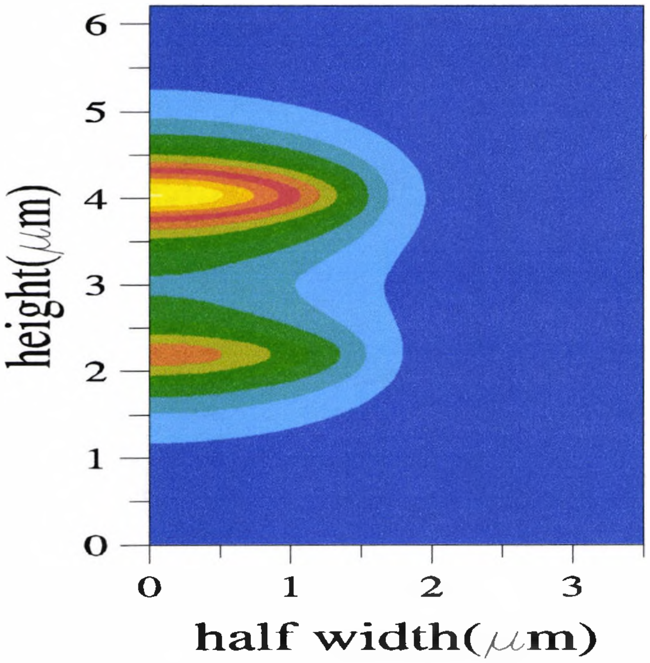

Fig.4.15a $\mathbf{H_x}$ Field profile of the TM even supermode

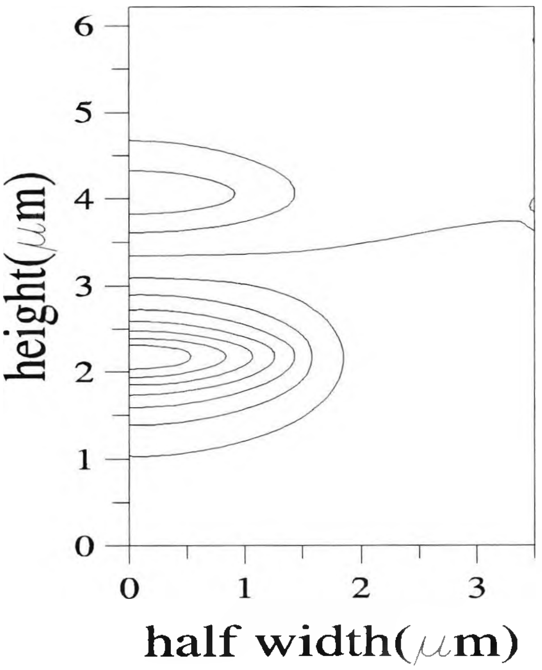

Fig.4.15b **H_x** Field profile of the TM odd supermode

It can be noticed from Fig. 4.15 *a* or *b* that most of the power is in guide *a* (upper guide) and there is little power in guide *b*, because the guides are non identical for the TM polarization.

The propagation constant of the even and the odd TE polarized modes were 13.27611 and 13.26217 respectively, which are nearly equal and hence their coupling length is larger than the TM mode. The propagation constants of the even and the odd TM polarized modes were calculated as 13.25705 and 13.22857 respectively.

Next, using the field profiles and the propagation constants generated by using the vector **H**-field finite element method, the LSBR approach can be used to calculate the excited modal coefficients and from these parameters the composite field profiles at various *z* locations. Eq. 4.5 can be used to calculate the composite field profiles. It is assumed that the power is launched into the top waveguide, *a*, at the beginning of the directional coupler section. Figure 4.16 shows the composite field profile at $z=0_+\mu m$.

The excited coefficients of the TE polarized modes are 0.74485 and 0.66716 for the even and the odd modes respectively. However, for the TM polarized wave the values are not equal and the even and the odd mode values were computed as 0.93246 and 0.35914 respectively. It can be noticed from this figure that most of the power is in guide *a*.

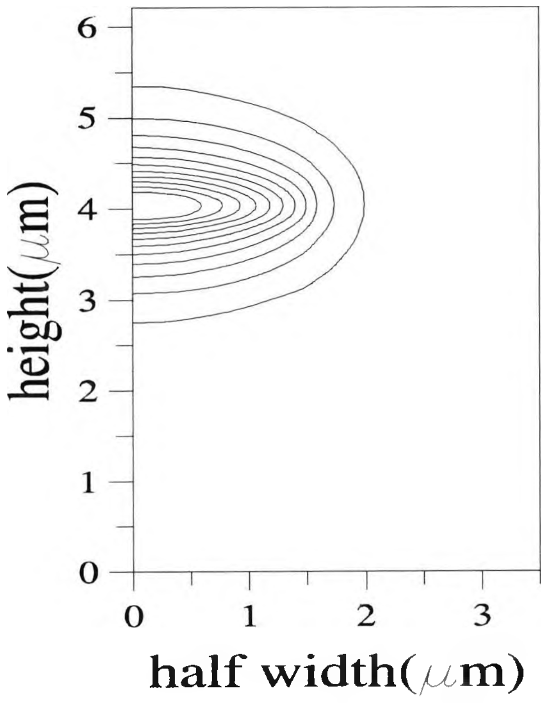

Fig. 4.16 Composite field profile at $z=0_+$ for TM polarization

Fig. 4.17 shows the composite field profile at one coupling length for the TM polarization.

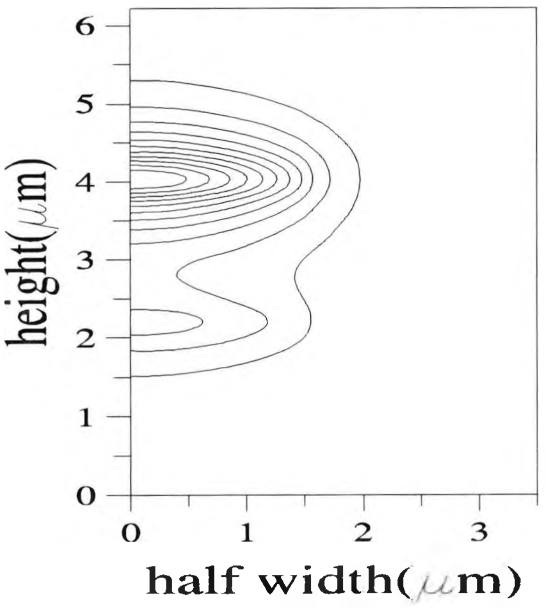

Fig. 4.17 composite field profile at one coupling length, L_{cTM}

It can be noticed from this figure that only a fraction of the input power has been transferred to the adjacent lower guide at one coupling length. As the power in the supermodes is not equally distributed for both the even and the odd supermodes there is incomplete power transfer at the coupling length for the TM case due to lack of phase matching between the guides for the TM polarised waves.

Figure 4.18 shows the composite field profile at twice the TM coupling length, i.e. at 220μm.

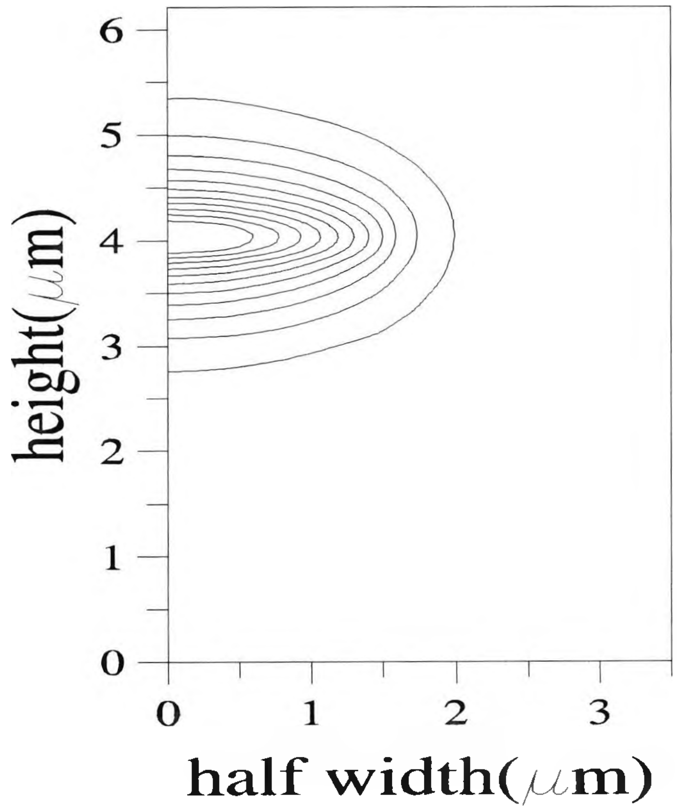

Fig.4.18 Composite field profile at $z=2*L_c$ for TM polarization

It can be seen from this figure that all of the power previously coupled to lower guide, *b*, has now been transferred back to the top guide, *a*. However, for the TE polarization, the guides are phase matched and there will be complete power transfer from guide *a* to guide *b* at its coupling length, L_{cTE}, which is 220μm .

Figure 4.19 shows the variation of the waveguide power along the axial direction for the TE and the TM polarizations.

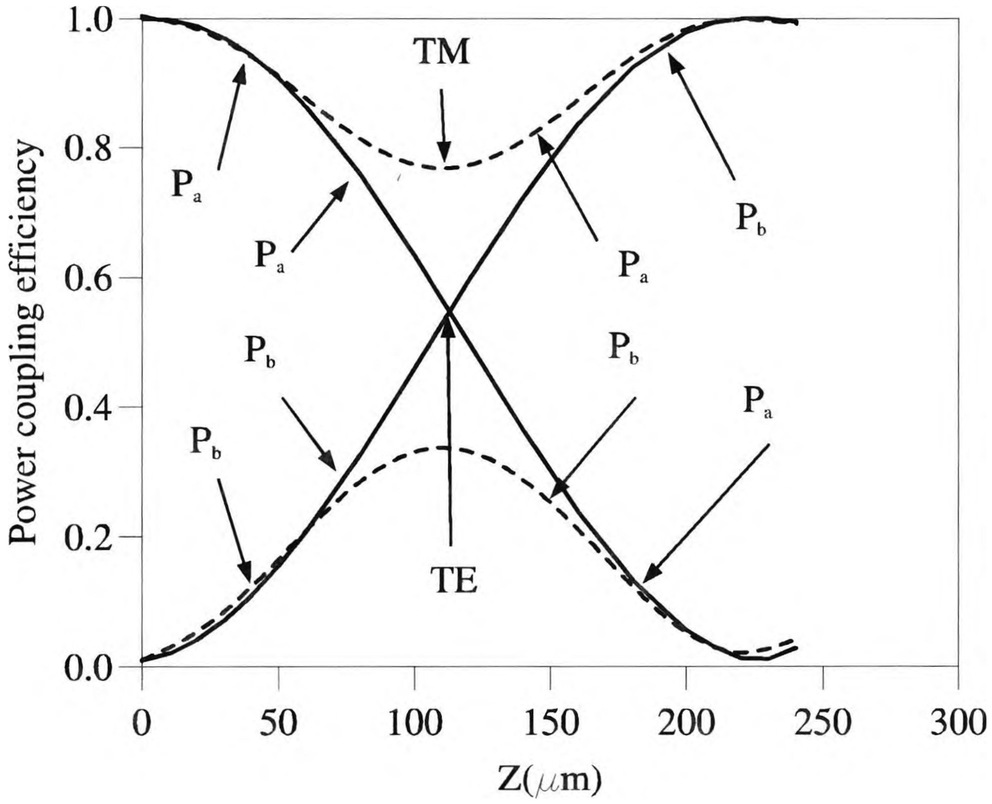

Fig. 4.19 Power transfer efficiency with the device length

As can be seen from this figure at z=0μm for both the TE and TM polarization, most of the power is in guide *a* and there is almost zero power in guide *b*. However, at z=220μm most of the TE power is in guide *b* and most of the TM power is in guide *a*. Therefore by carefully selecting the device parameters a passive TE/TM polarizer can be designed using the MQW region, without introducing surface plasmon modes, which are inherently lossy.

4.5 Summary

In this chapter a number of important properties of optical polarizers have been discussed. Two types of polarizers were considered in detail, the first being a metal clad optical polarizer. The effect of the metal layer was demonstrated by the TM supermode field profiles, and the inclusion of modal loss was also considered. The application of the FEM and the perturbation techniques for the loss calculations were also discussed. As a result, the power transfer curve was plotted for the TM case, with and without modal loss, to show the performance degradation. Following that, for the first time, a MQW based polarizer with two-dimensional confinement has been analyzed. The approximate equations to calculate the equivalent indices for the TE and the TM polarizations have shown to be inaccurate for the analysis of two-dimensional structures. In the next chapter the idea of multimode interference devices is developed with several applications.

Chapter 5

Multimode Interference Devices

In chapter 5 the interesting properties of the multimode interference (MMI)-based devices is discussed. The MMI is introduced as a 3-dB coupler, 1X4 coupler and as a duplexer. A direct comparison is made with the performance of the directional coupler to show the important properties of the MMI which has only been stated so far by most of the research workers.

5.1 Introduction

Multimode interference based 3 dB couplers have attracted attention in the field of optics in recent years due to their superior performance in light of several design criteria, such as their compact size, low crosstalk, good fabrication tolerance and stable splitting ratio (Soldano, 1995). Today such MMI-based devices are used widely as 3 dB couplers (Spiekman *et al.*, 1994), 90 degree hybrids, power splitters or combiners (Rasmussen *et al.*, 1995) or as an input section for a ring laser (Krauss, 1995) and for narrow-band arrayed filters (Soole, 1996).

The MMI-based devices thus reported have been mostly characterized by several simple approaches such as the use of the effective index and the overlap integral methods (OI). The accurate characterization of these MMI sections is important for the optimization of compact optoelectronic systems in which they can be incorporated. However, in this thesis it is shown that the rigorous analysis of MMI-based devices using the combination of the Least Squares Boundary Residual (LSBR) and the vector finite element (VFE) methods can be more accurate than using the simple overlap integral approach and would be numerically more efficient than the full vector beam propagation method (BPM). In this chapter, results obtained by using this accurate and efficient approach are presented for several practically realizable devices with two -dimensional confinement and important comparisons are made with the results obtained using one dimensional approximations. A 2 x N restricted *self-imaging*, which occurs when the number of modes excited, M, given by 0,1,3,4,6,7,.. only, has been analyzed. This restricted imaging is achieved by placing the input guides at positions $W/3$ and at $2W/3$ on the device, where W is the width of the MMI section.

5.2 Theoretical background of MMI

The MMI-based device consists of a large multimode section with an input and output access waveguides. The constructive interference between the waveguide modes causes a '*self-imaging*' phenomenon which is the basic principle of operation of MMI-based devices. Since the excited modes in the MMI section propagate with different phase velocities, they interfere with each other to form one or more interference patterns, the so-called '*self-images*' or '*multiple-images*', which are dependent on the position along the waveguide section. This reflects the basic principle of MMI operation. Ulrich and Ankles (1975) have showed the use of ray optics technique to describe the self-imaging phenomenon, followed by the work of Chang and Kuester (1981) who used a decomposition employing a Green's function technique. However, recently, Weinert *et al.* (1995) used the finite difference-based beam propagation method (BPM) and a further analysis by Berry and Burke (1995) employed the semi-analytic Discrete Spectral Index (DSI) method to show the self-imaging nature of multimode interference devices.

The intermodal coupling length, L_{cn} between the first and the higher order modes of the MMI section can be calculated by using

$$L_{cn}=\frac{\pi}{\beta_0-\beta_n} \qquad (5.1)$$

where β_0 is the propagation constant of the first fundamental mode in the MMI section in side II, as shown in Figure 5.1 and β_n is the propagation constant of the n^{th} order mode in the same section. When the device length, L, is equal to L_{c1}, defined as one coupling length, self-imaging of the input field may be obtained. A careful consideration of the positioning of the input waveguides can lead to a wider MMI device, resulting in a reduction of its potential length. This is a very attractive nature of the MMI based devices as the main purpose of the use of MMI in photonics circuit is due to their compact size. However, in order to analyze these MMI-based devices, an accurate calculation of the modal solutions of the access waveguides and the multimode waveguide section is necessary. Although the effective index (EI) method is a simple and useful technique which may be used to calculate the propagation constants for simple structures. However, for the accurate characterization of complex MMI-based devices, the numerically versatile finite element method is an ideal tool to calculate the modal field profiles, $\mathbf{H}(x,y)$, and their propagation constants, β.

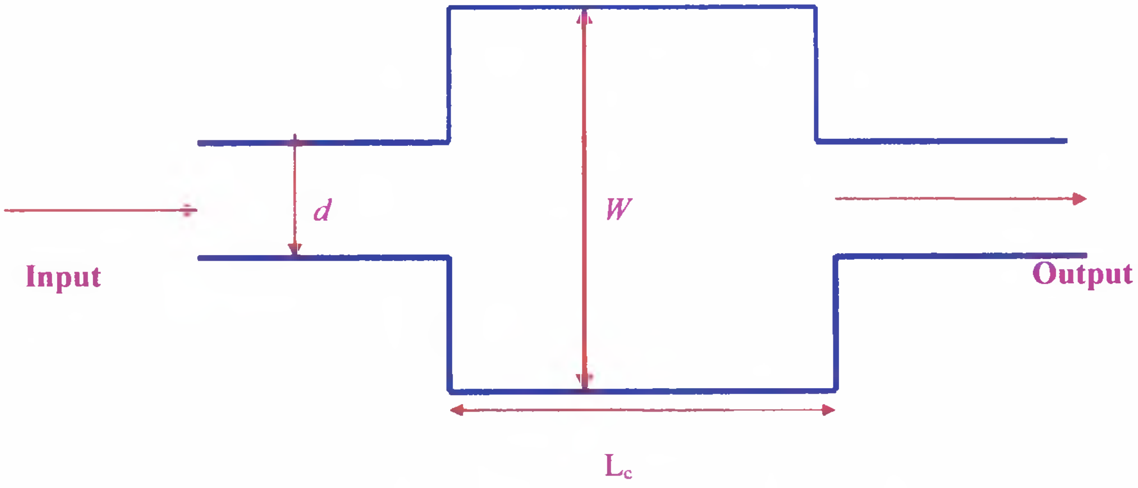

Fig 5.1 Schematic diagram of a 2-D MMI coupler

In using the numerical approach presented in this thesis, an arbitrary incident field is decomposed into the guided modes of the MMI section and propagated along the length of the MMI. To calculate the power carried by these modes, it is vital to be able to calculate excited coefficients of the modes in the MMI section due to the incident mode via the access waveguide. The LSBR method is used to calculate the transmitted and the reflected coefficients of the modes.

In order to calculate the power output of the MMI device, the evolution of the optical field along the MMI can be calculated as a superposition of all the guided mode field distributions. By taking the phase of the fundamental mode (β_0) as a common factor out of the sum and assuming a time dependence, given by $exp(j\omega t)$ and implicit hereafter, the field profile $\mathbf{H}(x,y,z)$ can be written as

$$\mathbf{H}(x,y,z) = \sum_{i=0}^{M-1} b_i \cdot \mathbf{H}_i(x,y) e^{-j(\beta_0 - \beta_i)z} \tag{5.2}$$

and similarly for the $\mathbf{E}(x,y,z)$ field. Here M is the total number of modes considered in the MMI section and b_i are the coefficients of each mode generated at the start of the MMI section and guided along the MMI guide.

5.3 The Simulation used and Results obtained

Initially, to show the validity and usefulness of the numerical method developed a planar one dimensional structure was simulated. Two structures were considered. One with a corner fed input guide and the second one was simulated with a centre fed access waveguides.

5.3.1 The structure simulated

Figure 5.2 shows the schematic diagram of the MMI structure used in this simulation.

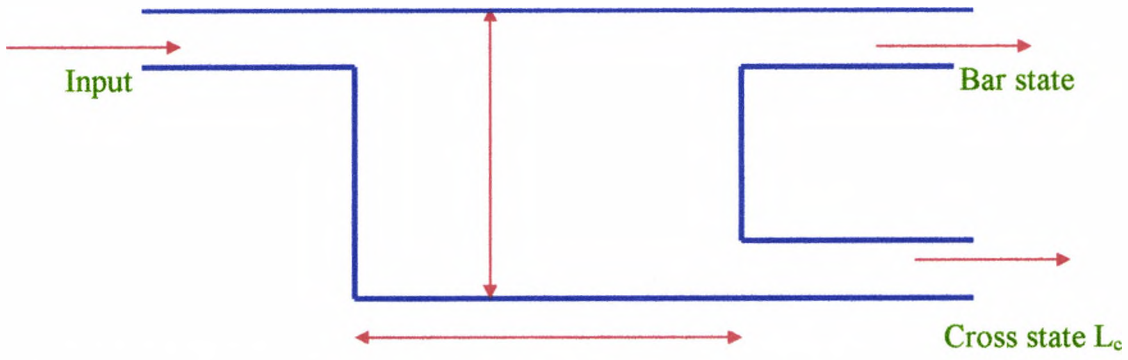

Fig.5.2 Schematic diagram of the corner fed multimode interference coupler

For all the MMI coupler simulations assumed the width of the multimode section is assumed as W_{MMI} and the width of the access waveguides were taken as 2.6μm. There can be multiple input and output guides for a specific device, but here only the axial dependence (*z*) power profile variation is studied. The refractive index in the guide and cladding sections are n_g=3.473 and n_S=3.420 respectively and the operating wavelength is 1.064μm (Jenkins *et al.*, 1994).

The exact imaging of the MMI devices is based on the quadratic spacing of the propagation constants, but however, it has been shown that in a practical waveguide this is only an approximation (Weinert and Agrawal, 1995). For the dielectric waveguides especially, in the case of weakly confined multimode waveguides, the eigenmode spectrum deviates from the exact quadratic spacing of the propagation constants. It can be shown that, for the structure considered in this study, the exact beat length for the 6th and the 7th modes (with respect to the first mode) will deviate by 1.8% and 3.2% from the ideal quadratic spacing approximations. This deviation from the ideally-required β spacing will show aberrations and a reduced contrast, particularly when the splitting number is large. Fig. 5.3 shows the *x-z* field profile in the MMI section using the accurate modal coefficients employing the LSBR method and accurate propagation constants using the finite element method.

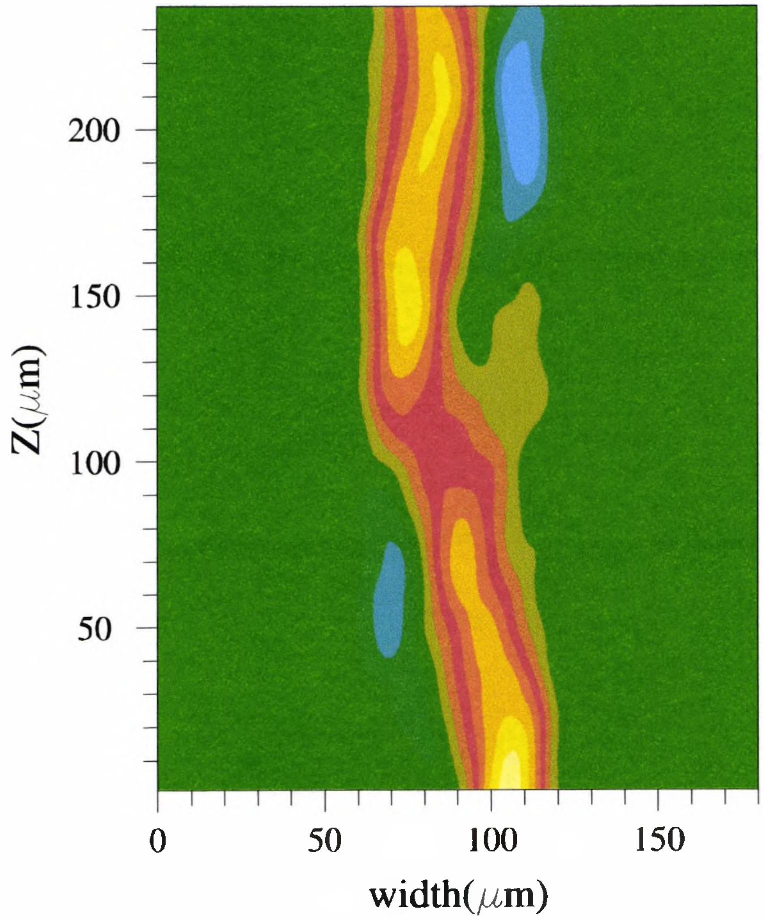

Fig. 5.3 Evolution of the light-wave propagation in the MMI

Table 5.1 shows the amplitude coefficients of the transmitted modes ($\tau_i = b_{i+1}$) in the MMI section calculated by the LSBR method, where the first coefficient, b_1 is the transmission coefficient of the first mode, TE_0, identified at τ_0. It should be stated that, although the guided modes in each section are othogonal to each other, however, the coefficients of each transmitted and reflected mode also depend on the inclusion of other modes in the simulation.

Table 5.1 shows the transmission coefficients using the LSBR and the overlap integral methods. The ninth row in the table shows that when there are eight guided modes in the MMI section and if they are excited by an incident mode from side 1 their excitation coefficients will have amplitudes which shows the contribution of the perticular mode. The square of these coefficients will give the intensity. As we go from row nine to row four we see that the value of the excitation coefficient changes slightly for the first mode in the MMI section. Similarly the second and the third mode excitation coefficients also slightly vary. If we compare the values of the modal excitation coefficients obtained by the LSBR method with that of the overlap integral method there is around 9% difference in their values. It can be noted that, although they can be accepted as an approximate solution, however, the results using the LSBR method are more accurate. The results shown in the second last raw (LSBR, M=1), when only one mode is considered in each side, and are also better than those using the OI method, due to the better balance between the electric and the magnetic fields during the error minimization by using the optimum weighting function,δ. The summation of the field intensities of the transmitted and the reflected coefficients are always less than or equal to 1.

Mode in each side	τ_0	τ_1	τ_2	τ_3	τ_4
1	0.49855	-------	-------	---------	--------
2	0.49864	0.67872	-------	---------	--------
3	0.49867	0.67877	0.49998	---------	--------
4	0.49866	0.67877	0.50000	0.18467	--------
5	0.49866	0.67877	0.50000	0.18467	0.027115
6	0.49866	0.67877	0.50000	0.18467	0.027124
7	0.49866	0.67877	0.50000	0.18467	0.027125
8	0.49866	0.67877	0.50000	0.18467	0.027125
LSBR-1	0.49855	0.67865	0.49987	0.18460	0.027116
OI	0.45491	0.61898	0.45576	0.16861	0.023567

Table 5.1 Transmission coefficients (τ_i) for the guided modes in the MMI section

It can be seen that the coefficients converge to accurate results as number of modes considered in each side of the discontinuity plane is increased. The last line of the table shows the values obtained by using the simple overlap integral (OI), and all of them are about 10% smaller than the LSBR resultsFig. 5.4 shows the variation of the transmitted modal coefficients (τ_i) with the width of the MMI section.

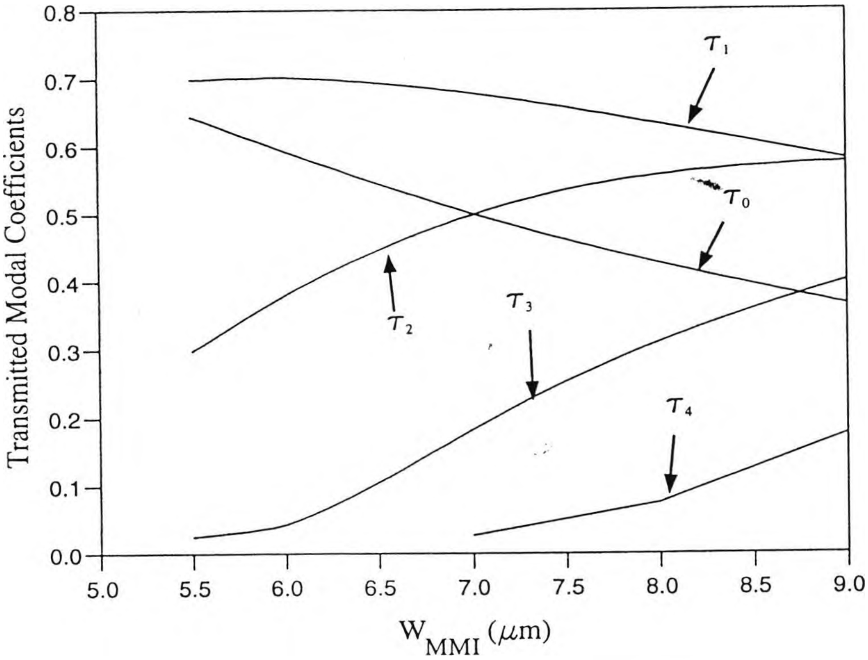

Fig. 5.4 Variation of the transmission coefficient with the width of the MMI

As this width of the MMI section, W_{MMI} is increased, more and more higher order modes are generated. It can also be seen that the coefficients of the lower order modes are decreased. Using some specific structures such as those with a particular symmetry and specific light illumination, the generation of some of these modes can be suppressed.

Thus in a real structure, at any longitudinal position (z), *all* the individual modes with significant power will never be exactly in or out-of-phase with the reference fundamental mode. So, it is not possible to obtain a perfect image. To design the optimum location for the bar or cross state, the axial dependence power in the two halves of the guides can be calculated numerically by integrating the poynting vector in these regions. Figure 5.5

shows the fraction of the power carried in the upper ($0<x<W_{MMI}/2$) and lower ($W_{MMI}/2<x<W_{MMI}$) regions with respect to the axial distance (z). A suitable termination distance can be chosen according to the device requirement.

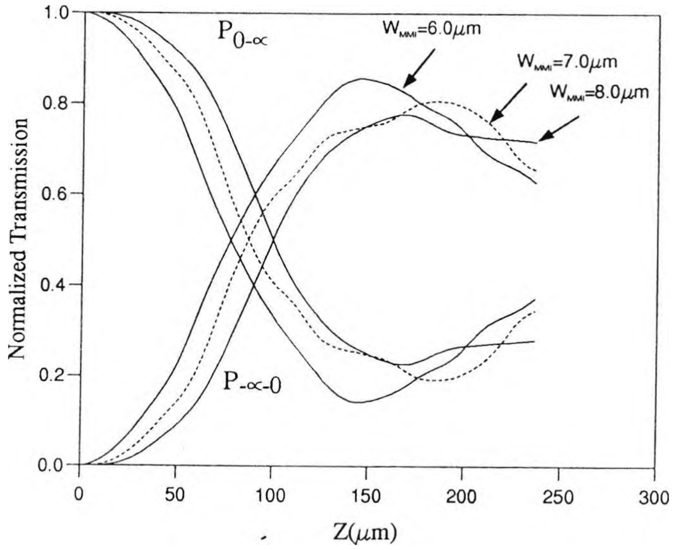

Fig. 5.5 The power fractions in two sides of the MMI section with the axial distance (z) for several different MMI widths

Next a centre-fed planar multimode interference device is considered. Fig. 5.6 shows the schematic diagram of the centre fed MMI.

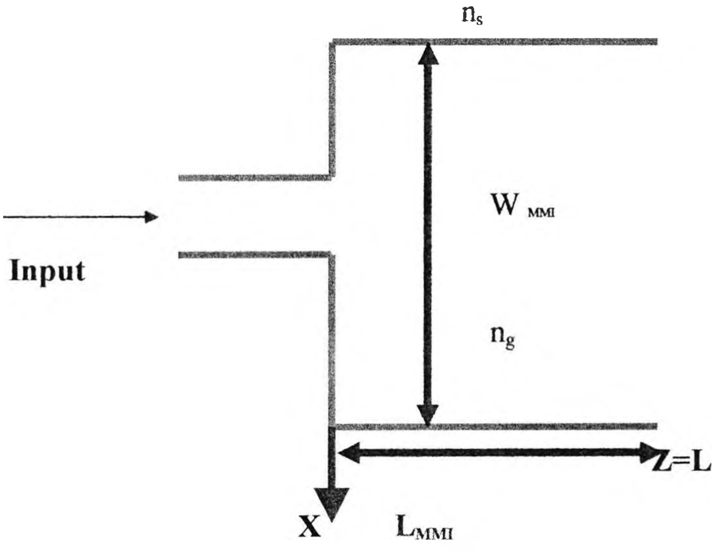

Fig. 5.6 Schematic diagram of a 1-D multimode interference (MMI) coupler

In this structure the width of the MMI is taken as W_{MMI} and the width of the center-fed access waveguide is d_1=2.6μm. For this example, only the axial dependence (z) of the field profile is studied. However there may be multiple input or output channels with their specific locations for a MMI device, depending on their applications, such an N x N splitters. The refractive index in the guide and cladding sections are n_g=3.3989 and n_s=3.1645 respectively and the operating wavelength is considered to be 1.55μm.

The weighting factor, δ, is adjusted to obtain a better balance for the error minimisation between the electric and the magnetic energy functionals. Fig. 5.7 shows the variation of the condition number (C) and the transmission coefficients (τ_0) of the fundamental mode with the weighting factor.

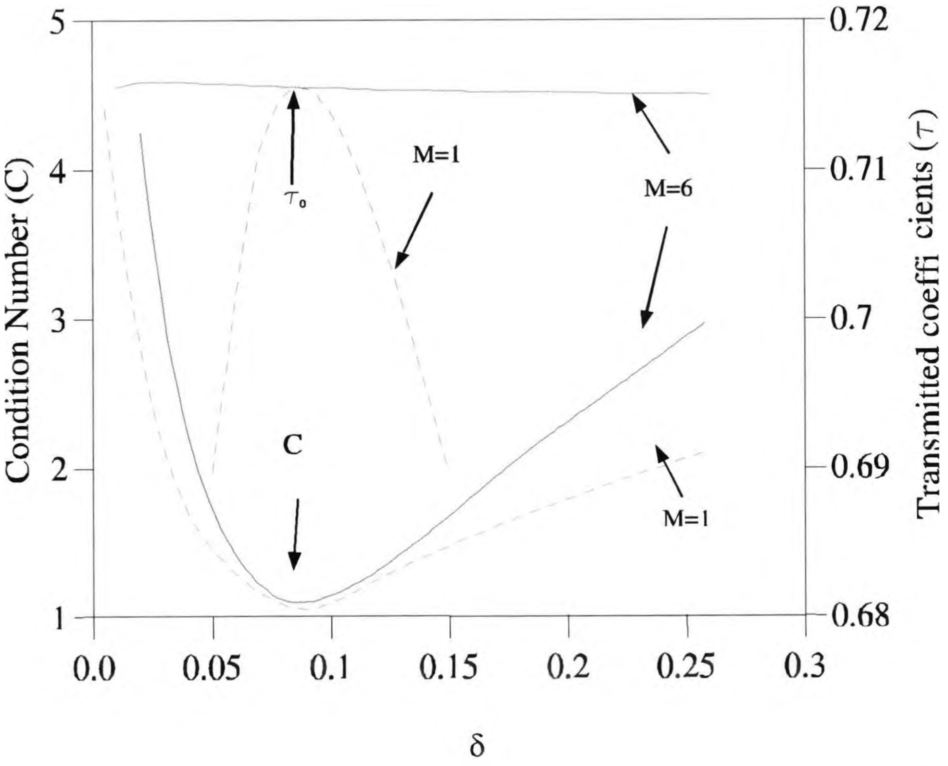

Fig. 5.7 Variation of the transmission coefficient (τ_0) and condition number (C) with the weighting factor, δ.

The singular value decomposition (SVD) is a powerful numerical technique for solving most linear least squares problems. The condition number, *C*, may be defined so that a large value of the condition number is related to the lowest residual error of the energy functional *J*, given as

$$J = \int_{\Omega} \left| E_t^I - E_t^{II} \right|^2 + \delta \cdot Z_0^2 \left| H_t^I - H_t^{II} \right|^2 d\Omega \qquad (5.3)$$

where E_t^I and E_t^{II} are tangential components of the electric field in side *I* and side *II* and H_t^I and H_t^{II} are the magnetic components in side *I* and side *II* and Z_0 is the characteristics impedance and δ is a dimensionless weighting factor.

Initially a 9μm wide multimode section was considered. It can be observed that when δ = 0.08 then the condition number is minimum, which signifies that the residual error in field continuity matching is also a minimum. This optimum value of α correlates with the inverse of the square of the effective indices, and corresponds to the correct balance between the electric and magnetic fields. It can be seen that the transmission coefficients also vary slightly with the condition number when only one mode is used (M=1) on each side of the junction (noting the highly magnified scale), but however, for M=6, the transmission coefficient value is very stable with δ. For each different example, the weighting factor δ is optimized to achieve the minimum field continuity error.

Table 5.2 shows the amplitude coefficients of the transmitted modes (τ_j) in the MMI section calculated by using the LSBR method when the width of the MMI section was 9.0 μm.

	τ_0	τ_2	τ_4	τ_8	τ_{10}	τ_{12}
M=6	0.71547	0.57499	0.36002	0.15689	0.02267	0.03230
M=1	0.71427	0.57439	0.35956	0.15669	0.02265	0.03286
OI	0.66658	0.53511	0.33433	0.14521	0.02087	0.03018
ρ	ρ_0	ρ_1	ρ_2	ρ_3	ρ_4	ρ_5
M=6	0.3143E-3	0.2206E-16	0.1421E-2	0.4926E-16	0.1999E-3	0.6986E-19

Table 5.2 Transmission coefficients (τ_i) and the reflection coefficients (ρ_i) for the guided modes in a 1-D MMI section

The amplitudes of the reflected modes into the incident waveguide are also given in Table 5.2. Due to the structural and excitation symmetry, antisymmetric odd modes will not be generated and this has been numerically tested by including them in the simulation and noting very small values of their coefficients. In the following simulations, six symmetirc even modes in the MMI section, and one guided and five radiated modes in side 1, are considered to match the field continuity at the butt-coupling interface and the results are shown in the first row (*M*=6). It should be stated that although the guided modes in each section are orthogonal to each other, the coefficients of each transmitted and reflected mode, however, also depend on the inclusion of other modes in the simulation. It can be noted from the table that the modal coefficients of the higher order modes are becoming progressively smaller or are very small. In this simulation 500 elements have been used for both the waveguide sections. The fourth line of Table 5.2 shows the values obtained by using the simple overlap integral (OI), and all of these values are about 7% smaller than the LSBR results shown in first two rows. However in both the approaches, namely, using the LSBR and the OI method, accurate vector fields generated by the finite element simulation have been used. After calculation of the modal field profiles, a further computer program is used to calculate the transmission and the reflection coefficients by using both the approaches. The last line of Table 5.2 shows the reflection coefficients. Typical CPU time required is about 2 minutes on a Sun Classic workstation. It can be noted that, although the overlap integral approach can be accepted as an approximate method, the results obtained using the LSBR method are somewhat more accurate. The results shown in the middle row (M=1), when only one mode is used in the LSBR approach, are also better than those using the simpler OI method, and these increased accuracy is only due to the better balance achieved between the electric and magnetic field components of the error function, ***J***, during the minimisation by using the optimum weighting function, δ.

Fig. 5.8 shows the variation of the transmitted modal coefficients (τ_i) with the width of the MMI section. In this case only the results using the LSBR method have been plotted. Due to the structural symmetry, the antisymmetric modes are not generated, and only the coefficients of the symmetric even modes are plotted here. As this width of the MMI section, W_{MMI}, is increased, more and more higher order modes are generated. It can also be observed that the coefficients of the lower order even modes have increased and at the same time that of the fundamental mode has decreased. By using some specific structures, such as those with a particular symmetry and specific light illumination, the generation of some of the modes can be controlled, if required.

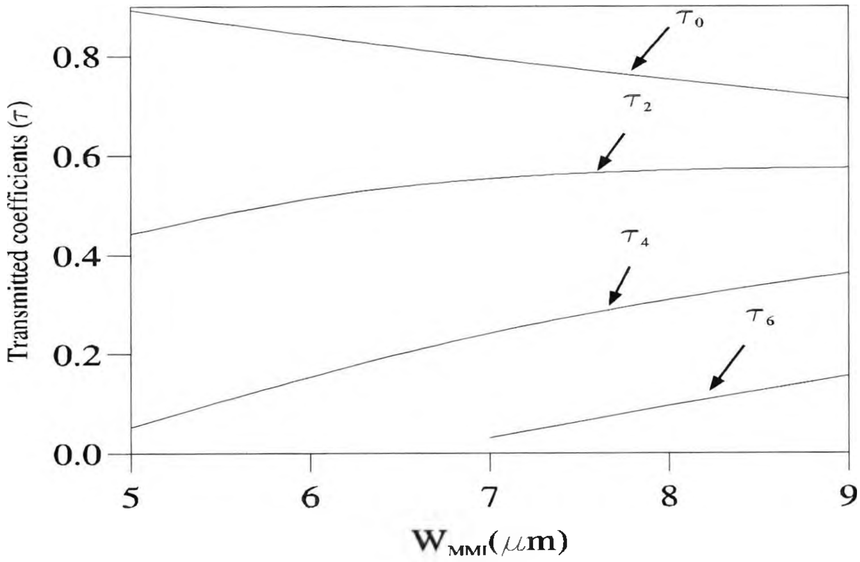

Fig. 5.8 Variation of the transmitted modal coefficients (τ_i) with the MMI width, W_{MMI}

Fig. 5.9 shows the *x-z* field profile in the MMI section using the accurate modal coefficients employing the LSBR method and accurate propagation constants and field profiles by using the finite element method. It can be observed that the propagation field profile breaks down to multiple sections and refocuses again at a further distance. In this case the width of the MMI section is 5μm. From Fig. 5.9 it can be noticed that around 40μm the input field divides into tow equal peaks. The number of power splitting sections can be increased by increasing the width of the MMI section.

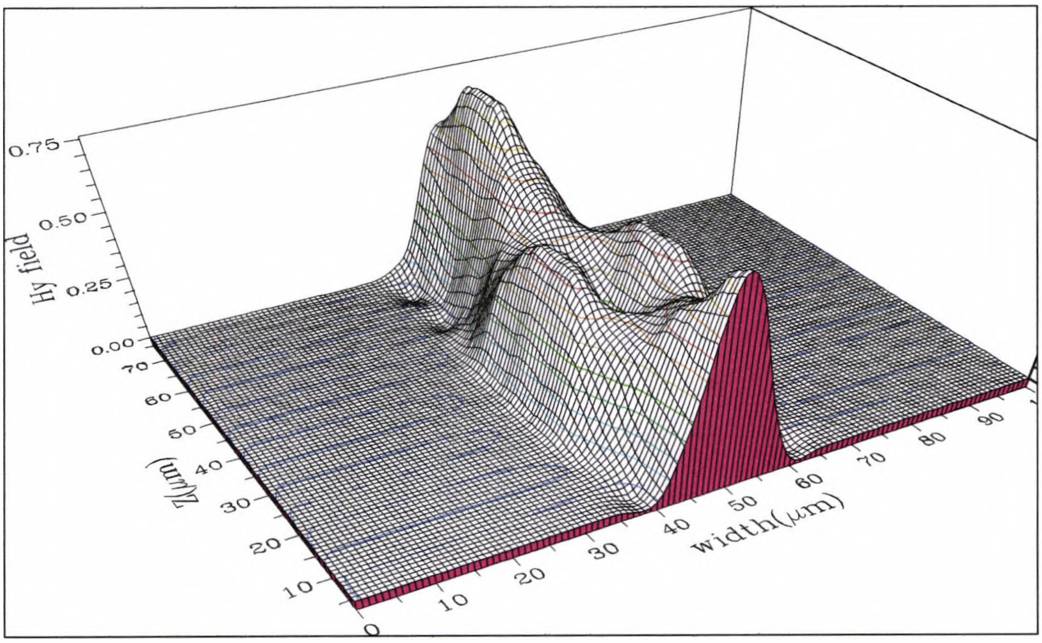

Fig. 5.9 Evolution of the light-wave propagation along the MMI section

The exact imaging of the MMI devices is based on the quadratic spacing of the propagation constants, but however, it has been shown that in a practical waveguide this is only an approximation (Weinert and Agrawal, 1995). For the dielectric waveguides especially, in the case of weakly confined multimode waveguides, the eigenmode spectrum deviates from the *exact* quadrature spacing of the propagation constants. It can be shown that, for the structure considered in this study the exact beat length for the TE_6 modes (with respect to the first mode, TE_0) will deviate by 0.3 % from the ideal quadratic spacing approximations and the deviation will increase further for the higher order modes. This deviation from the ideally required β spacing will produce aberrations and a reduced contrast, particulalry when the splitting number is large.

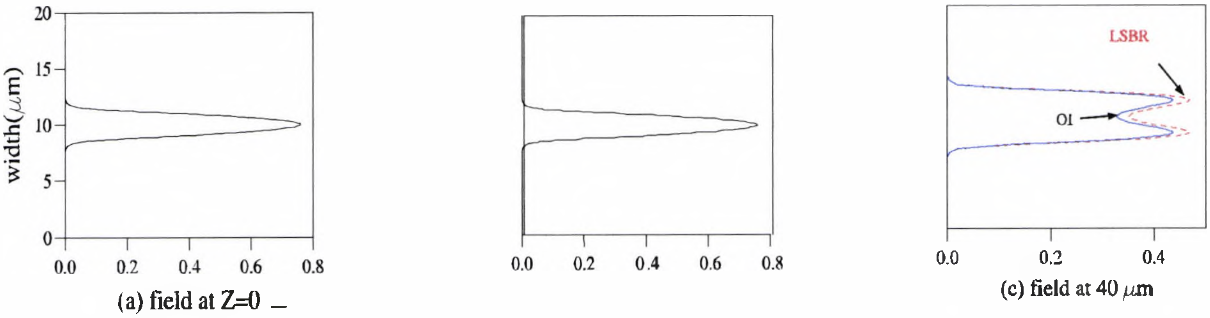

(a) field at Z=0 _

(c) field at 40 μm

Fig. 5.10 The resultant field profiles (a) in the input waveguide section at $z = 0_-$, (b) in the MMI section at $z = 0_+$, and (c) in the MMI section at $z = 40\mu m$

Fig. 5.10 shows the transverse (x) dependence of the field profiles at three axial (z) positions. Fig. 5.10(a) shows the incident field profile in the input waveguide section ($z = 0_-$), which is the fundamental TE_0 mode in that section. Fig. 5.10(b) shows the resultant field profile at the beginning ($z = 0_+$) of the MMI section which is very similar to the profile shown in Fig. 5.10(a). This resultant field profile is generated by superposition of all the excited modes in the MMI section and small ripples at the edges are visible which due to incomplete cancellation of the fields. However, as the composite field propagates through the MMI section, each mode with its own propagation constants, their relative phase difference modifies the resulatant field profile, and this profiel at $z = 40\mu m$ is shown in Fig. 5.10(c). It can be observed that the field profile calculated (solid line) by using the modal coefficients from the overlap integral approach differs from that of using LSBR method (dashed line). The resultant field profile at this position is quite distinct from the profile at the beginning of the MMI section and can be used in the design of a two-way power splitter.

5.4 MMI based 3 dB coupler

Figure 5.11 below shows the basic layout of the structure simulated in this work. The MMI-based 3 dB couplers simply consist of three major sections, which are classified as the input, MMI and the output sections.

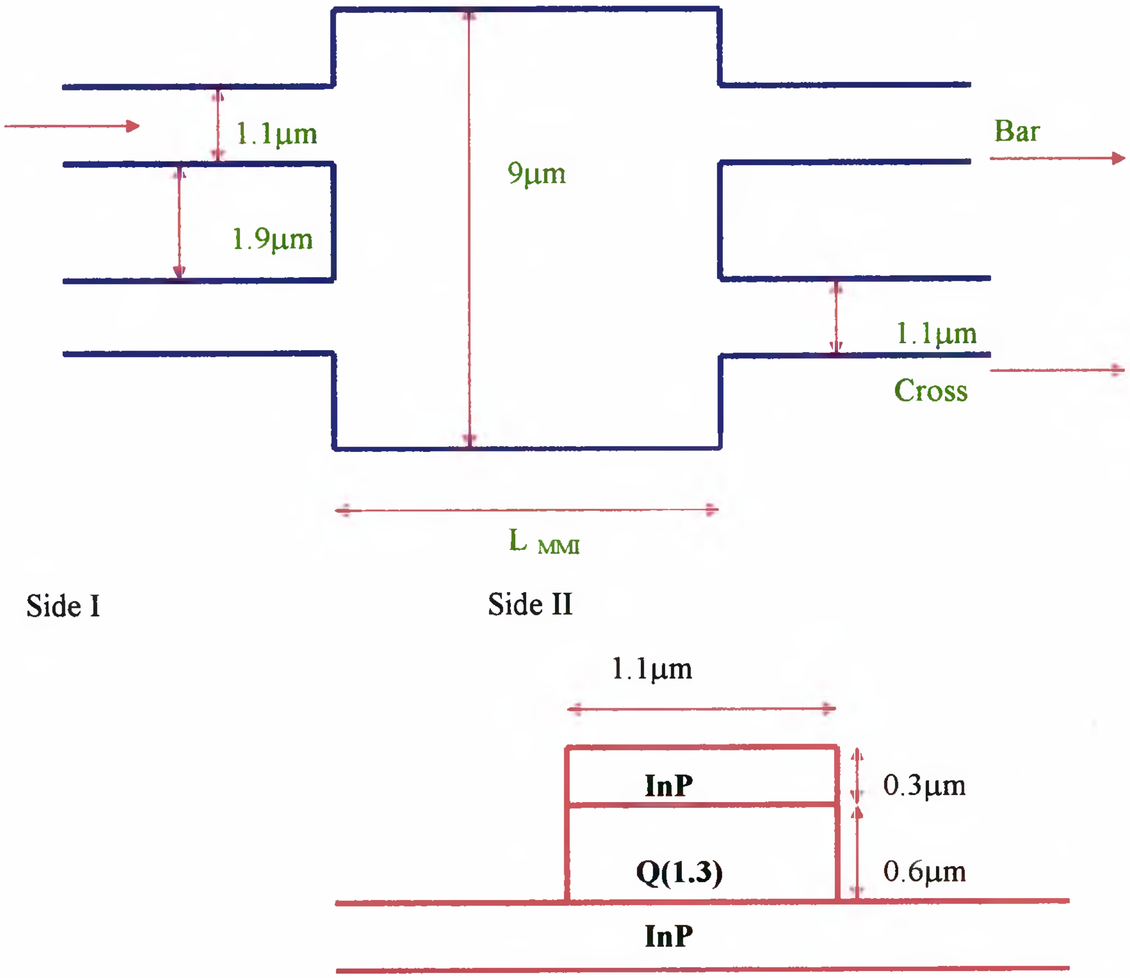

Fig. 5.11 Schematic diagram of a 2-D MMI-based 3 dB coupler and cross section of access waveguides.

The input section consists of two access guides of width 1.1μm separated by 1.9μm and connected to a multimode section of 9μm in which a large number of modes can be guided. The output configuration consists of two output waveguides with the same dimensions as the input access waveguides and are termed the *bar* and the *cross* states, depending on the position of the excitation in the input section. The guide which is directly opposite the input guide at the output is the *bar state* and the other guide at the output is termed as the *cross state.* The refractive index of InP and InGaAsP were calculated using the formula given by Broberg *et al.* (Broberg *et al.*, 1985) for a quartenary material of bandgap (λ_g) 1.3μm and an operating wavelength (λ_0) of 1.507μm.

5.4.1 Refractive index calculation of InGaAsP and InP

The InGaAsP-InP materials system is today widely used for fabrication of optoelectronic devices such as lasers and detectors. These components tend to become more complicated and include passive and active waveguides, Bragg reflectors, etc. Also, new types of integrated optics devices such as switches, modulators, and filters are made in this materials system and will be included in the integrated optoelectronic circuits of the future. Therefore, the refractive index of the material is a key parameter in their design.

It is known that the refractive index depend on light wavelength, crystal composition, lattice mismatch, doping level, carrier density, temperature, etc.

From the bandgap energy the Arsenic concentration (*y*) can be calculated by using the following two equations:

$$E_g\,(\mathrm{eV}) = 1.35-0.72y+0.12y^2 \tag{5.4}$$

$$\lambda_g\,(\mu\mathrm{m}) = 1.240/E_g(\mathrm{eV}) \tag{5.5}$$

where E_g is the bandgap energy and λ_g is the bandgap wavelength.

The Galium concentration was calculated by Nahory *et al.* (1978) using the following expression:

$$x=0.1894y/(0.4184-0.013y) \qquad (5.6)$$

These *x* and *y* relationships are only valid when the material is lattice matched to InP.

Broberg *et al.* have derived an expression to calculate the refractive index (*n*) given as

$$n=\left[1+\frac{E_d}{E_0}+\frac{E_dE^2}{E_0^3}+\frac{\eta E^4}{\pi}\ln\left(\frac{2E_0^2-E_g^2-E^2}{E_g^2-E^2}\right)\right]^{1/2} \qquad (5.7)$$

where

$$\eta=\frac{\pi E_d}{2E_0^3(E_0^2-E_g^2)} \qquad (5.8)$$

$$E_0 = 0.595x^2(1-y) + 1.626xy - 1.891y + 0.524x + 3.391 \qquad (5.9)$$

$$E_d = (12.36x-12.71)\ y + 7.54x + 3.391 \qquad (5.10)$$

$$E_g=1.240/\lambda \qquad (5.11)$$

where λ_0 is the wavelength of light in μm.

The refractive index value thus calculated for the guide was n_g=3.3988 and that of the substrate n_s=3.1708, for λ_g= 1.3μm and λ_0 = 1.507μm.

5.4.2 Description of the 3 dB coupler

Since most of the research workers consider a simplified planar approximation, in the first part of this paper a planar approximation has also been considered, where the numerical stability and convergence of the results can be easily tested. In the planar approximation, it has been assumed that an equivalent planar guide of width 9μm with refractive index same as the equivalent index of the rib section (n_e=3.3154) surrounded by air on both the sides. Table 5.3 below shows the propagation constants (β) for the first 16 modes for a mesh size of 320, the intermodal coupling length, L_{cn}, with respect to the fundamental mode, TE_0, is also shown in Table 5.3.

Mode	β(320)	L_{cn}	L_{cn}'	% Error
TE_0	13.81888	------------	---------	---------
TE_1	13.80605	244.86	---------	----------
TE_2	13.78465	91.78	91.82	0.04
TE_3	13.75464	48.90	48.97	0.14
TE_4	13.71597	30.53	30.61	0.26
TE_5	13.66850	20.89	20.99	0.48
TE_6	13.61223	15.20	15.30	0.65
TE_7	13.54692	11.55	11.66	0.94
TE_8	13.47257	9.07	9.18	1.20
TE_9	13.38891	7.31	7.42	1.48
TE_{10}	13.29587	6.01	6.12	1.80
TE_{11}	13.19317	5.02	5.14	2.33
TE_{12}	13.08018	4.25	4.37	2.74
TE_{13}	12.95774	3.65	3.77	3.18
TE_{14}	12.82463	3.16	3.28	3.65
TE_{15}	12.68058	2.76	2.88	4.67

Table 5.3 Propagation constants (β_n), coupling lengths using FEM (L_{cn}), the coupling lengths using the quadrature relationship (L_{cn}') and the coupling errors using the quadrature relationships for planar MMI structure for a series of TE modes.

It can be noticed from Table 5.3 that the quadrature relationship does not hold for the higher order modes. The recalculation of the coupling lengths using the quadrature relationships shows that the design coupling length is around 240μm.

Mode	β(320)	L_{cn}	τ (80)	τ (320)
TE_0	13.81888	------------	0.41657	0.42476
TE_1	13.80605	244.86	0.40437	0.40911
TE_2	13.78465	91.78	-----------	0.01738
TE_3	13.75464	48.90	0.39041	0.40138
TE_4	13.71597	30.53	0.36215	0.36064
TE_5	13.66850	20.89	-------------	0.02841
TE_6	13.61223	15.20	0.32876	0.34434
TE_7	13.54692	11.55	0.29077	0.29079
TE_8	13.47257	9.07	-------------	0.03612
TE_9	13.38891	7.31	-------------	0.27008
TE_{10}	13.29587	6.01	0.20616	0.20235
TE_{11}	13.19317	5.02	--------------	0.03482
TE_{12}	13.08018	4.25	0.15800	0.18260
TE_{13}	12.95774	3.65	0.12553	0.12235
TE_{14}	12.82463	3.16	------------	0.02963
TE_{15}	12.68058	2.76	0.08208	0.10492

Table 5.4 Propagation constants (β_n), coupling lengths (L_{cn}) and Tranmission coefficients (τ) for planar MMI structure for a series of TE modes.

For this particular structure, it can be observed from Table 5.4 that the excited coefficients in the MMI section for every third mode is very small (shown for the case of 320 mesh divisions), as would be expected for this type of restricted self-imaging structure. In order to show the stability of the modal coefficients, the results obtained by using 80 meshes have also been included. This clearly indicates that even at the low mesh divisions used, the values of the excited modal coefficients are reasonably stable, indicating the powerful nature of this approach, a combination of the finite element and the LSBR. From Table 5.4 it can be seen that the amplitudes of the higher order modes decreases monotonically, except every third mode coefficients which have a very small value as in this design '*restricted resonance*' was considered.

5.4.2.1 Results for the planar approximations

From the modal field profile, **H**(x), the modal coefficients, b_i, and the propagation constants, β_i, the composite field **H**(x,z) may be calculated. Although many higher order modes were generated with a significant value of the coefficient, however, with the superposition of all of them, the filed at $z=0_+$ resembles to the incident field from the input access waveguide. The field profile at $z=0_+$ is shown below in Fig. 5.12.

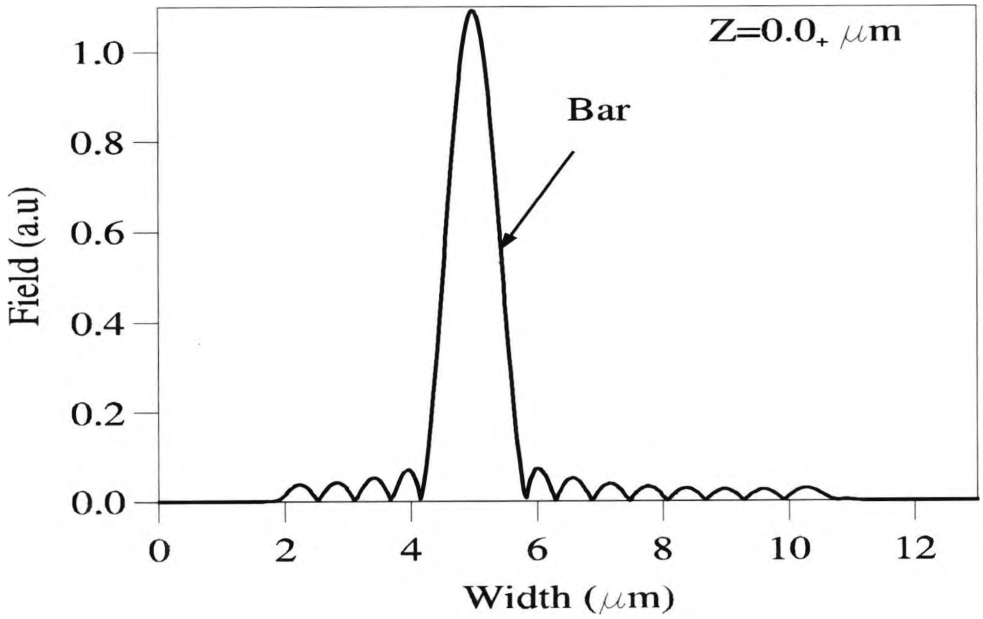

Fig. 5.12 The resultant field profile inside the MMI section at $z=0_+$ μm.

This field is very similar to the fundamental mode in the access waveguide, which is also shown by the dotted line labelled as *bar*. Small ripples are visible due to the incomplete cancellation of the fields beyond the input guide width. However, interference of the modal fields in the MMI section causes different images along the length of the MMI and at a position (*z*) nearly 120μm along the guide, the input power divides equally into the bar and the cross states.

Figure 5.13 shows the field profile at half the coupling length, $L_C/2 \approx 120\mu m$. It can be seen from this figure that the power division into the *bar* and the *cross* output states are as discussed earlier.

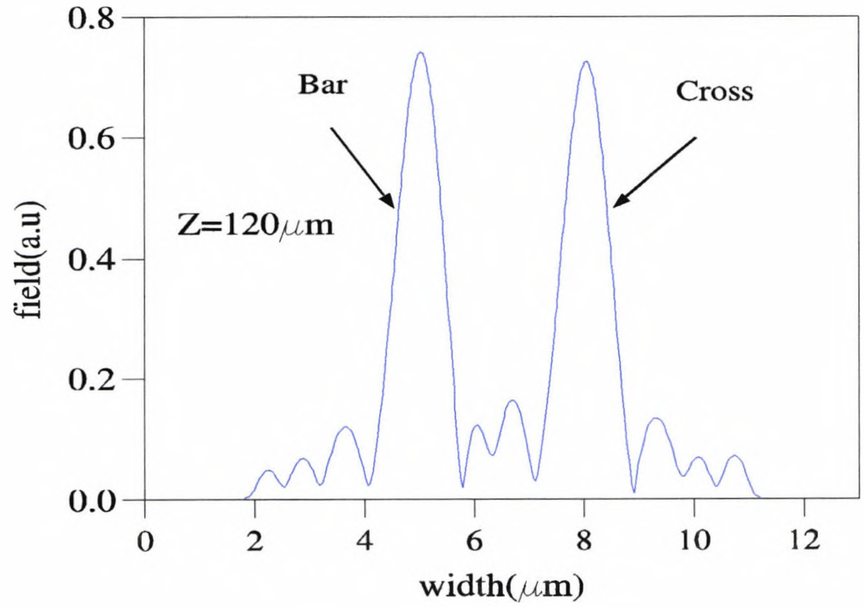

Fig. 5.13 The resultant field at *z*=120μm

In this case, L_c is the coupling length calculated from the first two modes of side *II* in structure Fig. 5.11

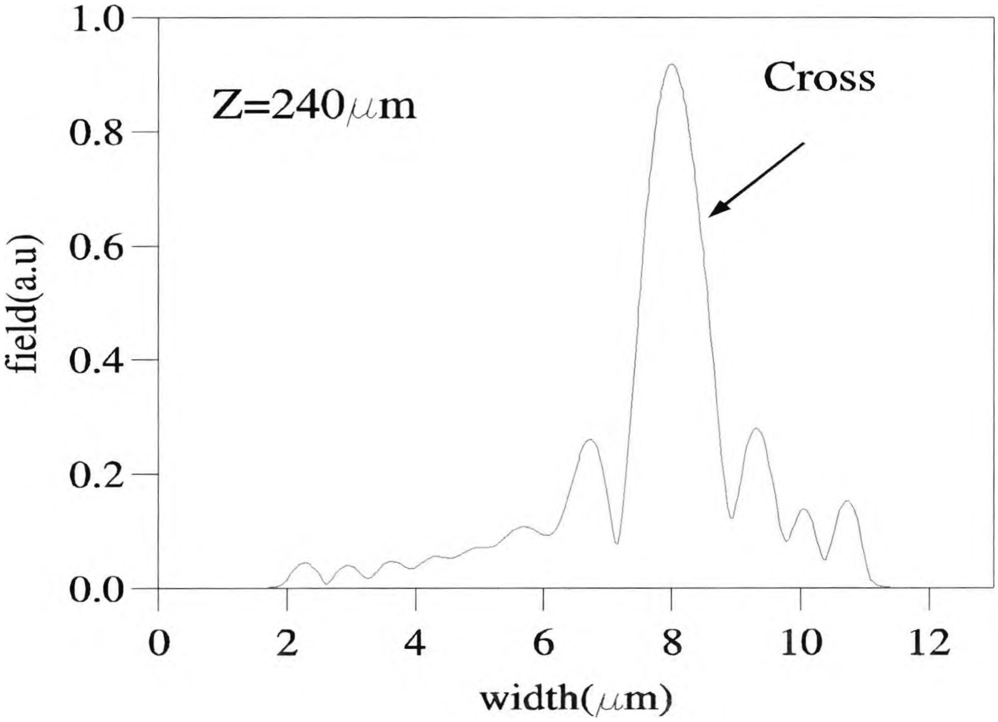

Fig 5.14 The resultant field at z=240μm

Figure 5.14 illustrates the total input field emerging from the cross state at z=240μm, a distance slightly smaller than the coupling length (L_{c1}), showing the self-imaging phenomenon of the input field.

At each longitudinal location, the composite field, $\mathbf{H}(x,z)$, may be evaluated and the LSBR method reapplied to obtain the power coupled to the two separate waveguides representing the power coupling to the *bar* or *cross* state waveguide at that location. The variations of the output power in the bar and cross states along the axial direction are shown in Fig. 5.15 below :

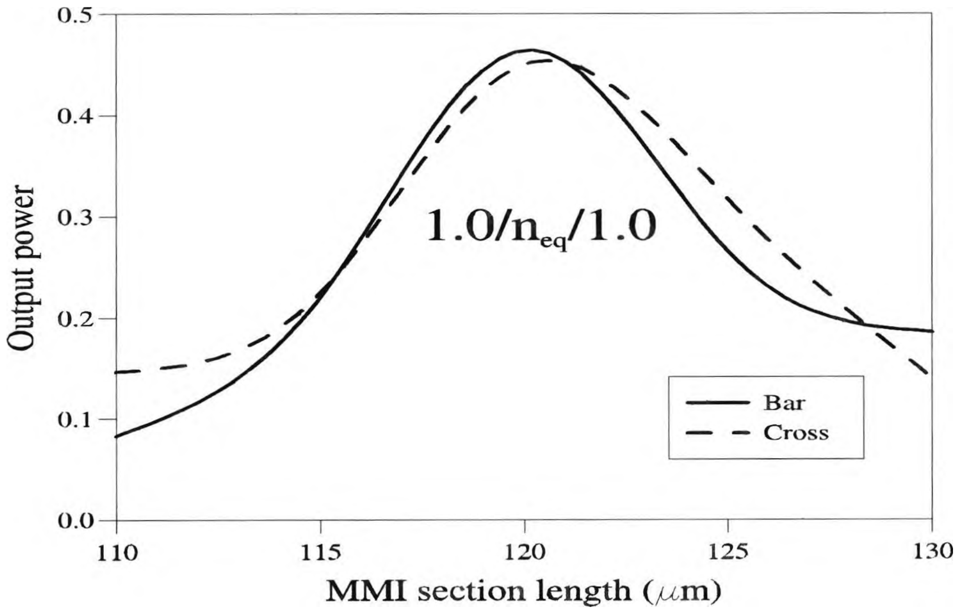

Fig. 5.15 The power coupling efficiency of the 3dB coupler for the 1-D approximation

It can be noted that the maximum power coupled to each state is at a position around 120μm±2μm, at distances slightly shorter than $L_{c1}/2$. It can be observed that there is a very good agreement between the theoretical results obtained by using the LSBR method which show a power output of around 45% in the bar and the cross states at 120μm length and the experimental results obtained by Spikeman *et al.,* (1994). This indicates that the LSBR method, which satisfies the continuity of the transverse field components at the interface, is accurate and more versatile than the other available numerical techniques, in light of such experimental results.

5.4.2.2 Use of two-dimensional confinement in the 3dB coupler design

Next, a realistic MMI section with two-dimensional confinement is studied. In this example, in a similar way to the earlier 1-D example, a single waveguide of 1.1μm width and 0.9μm height, as shown in Figure 5.11, is used as the input access guide followed by an MMI section of 9μm width, with all these guides being 0.9μm high. The output coupler configuration follows the same dimensions as the input with a separation of 1.9μm between the guides and a 0.3μm InP layer on top of the quartenary material. Such a quartenary InGaAsP material of bandgap 1.3μm was considered with an operating wavelength of 1.507μm. In this simulation 12800 first order elements were used. Table 5.5 below shows the propagation constants and the modal coefficients for the two-dimensional simulation calculated by using the vector finite element and the LSBR methods.

Modes	**β**	**L_{cn}**	**τ (LSBR)**	**τ (OI)**	**ρ (LSBR)**
H^y_{11}	13.81432	-------	0.40439	0.39439	0.80346E-2
H^y_{21}	13.80096	235.15	0.39406	0.38462	-----------
H^y_{41}	13.71718	32.34	0.37660	0.36875	-----------
H^y_{51}	13.70667	29.18	0.36347	0.35685	----------
H^y_{71}	13.59809	14.53	0.32199	0.31800	----------
H^y_{81}	13.52943	11.03	0.30831	0.30567	----------
$H^y_{10,1}$	13.36345	6.97	0.24913	0.24922	----------
$H^y_{11,1}$	13.26539	5.72	0.21894	0.22280	----------

Table 5.5 Propagation constants (β), Coupling lengths (L_c), Transmission (τ) and reflection (ρ) coefficients for the 2-D MMI structure for a series of H^y modes.

In this study TE polarization has been considered. The modal coefficients obtained by using the simple overlap integral (OI) method are also included for comparison and the excited coefficients are slightly lower than the LSBR values. It can be noticed that the overlap integral gives a slightly lower values for the lower order modes. It can also be noticed that the values of the transmitted coefficients also decrease slowly for the higher order modes. It can be seen that the values obtained by the LSBR method, which satisfies the continuity condition by minimizing the error functional, J, and using the optimum weighting factor, δ, is mathematically accurate, rigorously convergent and a powerful and versatile approach. The reflection coefficients, ρ, for the fundamental incident mode have been included as their estimation could be important for the characterization of many practical photonic devices, however, which is difficult inaccurate or impossible to determine using simple methods. As can be observed from Table 5.5, the coupling length (L_{cn}) is slightly smaller than that obtained using the equivalent planar approximation. The CPU time for each modal solution is around 14 minutes using a Sun Classic Workstation. From the modal parameters given in Table 5.5, the evolution of the filed profile **H** (x,y,z) along the axial direction can be calculated. Figure 5.16 below shows the field at the junction $z=0_+$.

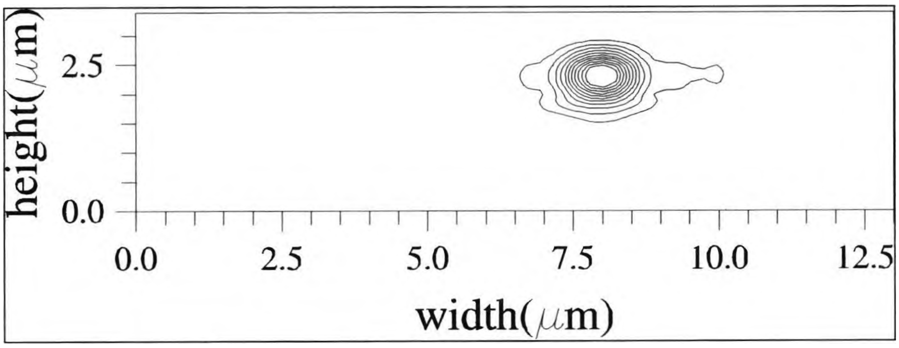

Fig. 5.16 Resultant coupled field in the MMI section at $z=0_+$ µm for a 2-D structure

Fig. 5.16 indicates clearly that at this position most of the power couples to the bar state, such as to match the incident field. In a similar way to the planar example, the small ripples beyond the input guide width are caused by incomplete cancellation from the superposition of the modal fields excited in the MMI section, beyond the input guide width.

As the field propagates in the longitudinal z direction, it divides into two equal peaks at $z=115\mu m$, as shown in Fig. 5.17. The two peaks in the figure below reveal that the total power incident via the access waveguide is divided into equal portions at half the coupling length thus indicating the possibility of an MMI based 3 dB coupler, and Figure 5.18 reveals the power emerging from the output cross state at one coupling length, L_C=230μ m, due to a 2π phase shift, compared to the field at the input, $z=0_+$. In this case it can be seen that the coupling length is slightly lower than the one for the one dimensional approximation. This shows that although the one dimensional solutions give an approximate results for more rigorous study a two-dimensional approach is necessary.

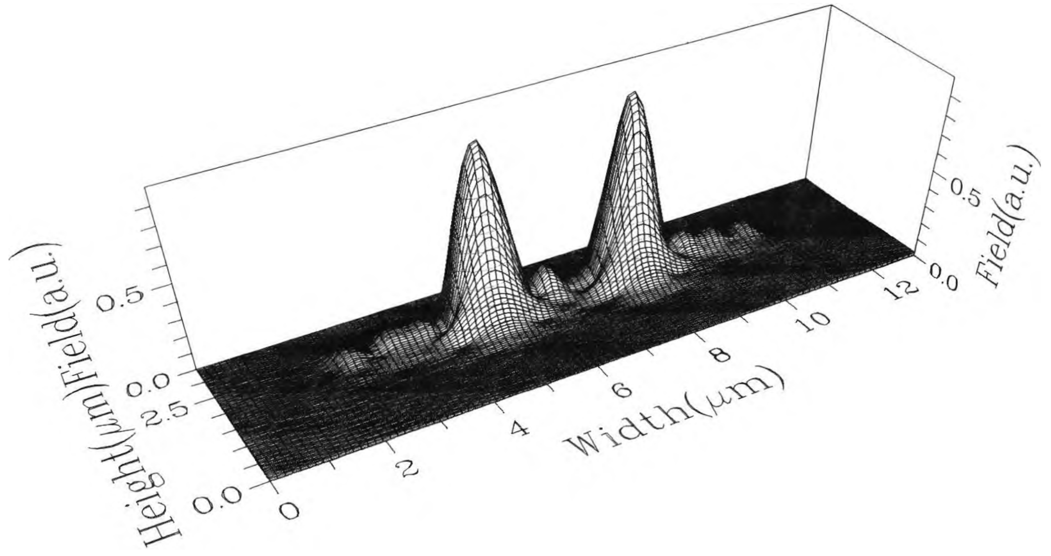

Fig. 5.17 Resultant field at z=115μm for a 3 dB coupler

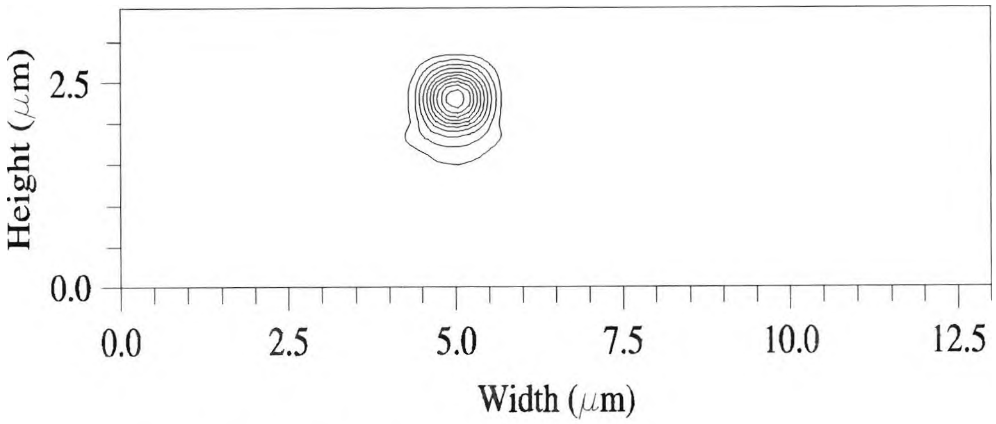

Fig. 5.18 Resultant field at z=230μm for a cross coupler

Finally the power transfers to the bar and cross states are calculated by using the composite field at each axial location (*z*) and this is shown in Figure 5.19 for the 3 dB coupler as a function of the device length.

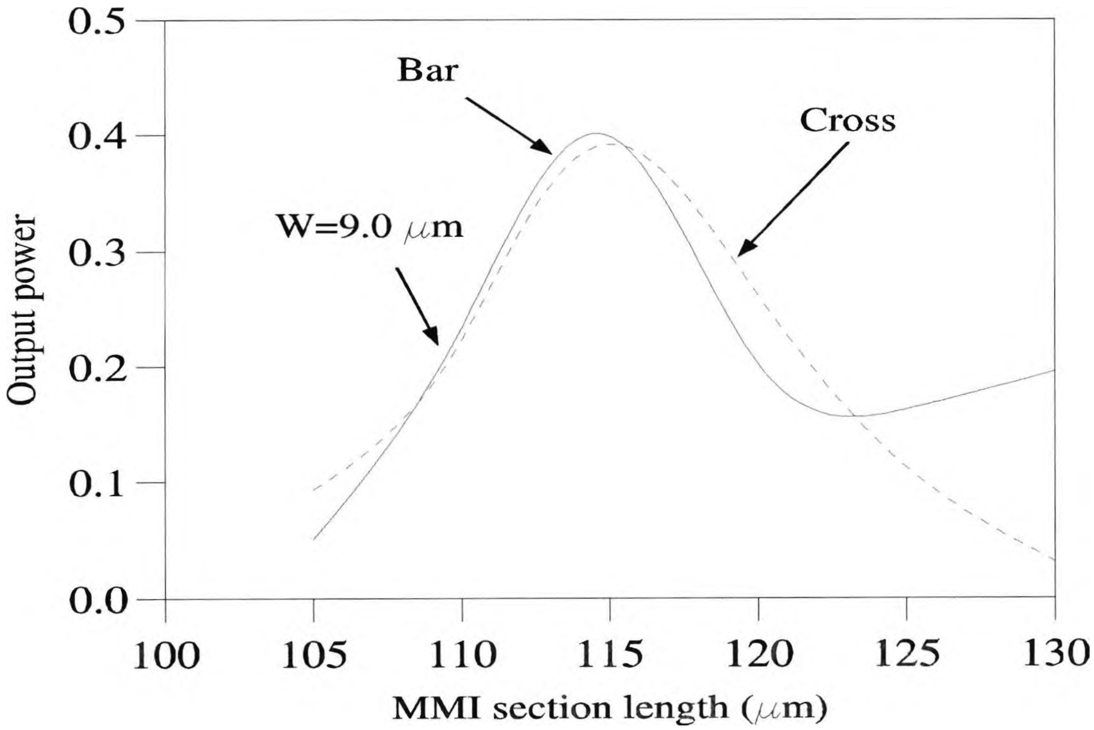

Fig. 5.19 Power transfer curve for a 3 dB coupler of 2-D Confinement

At the junction of the input access guide and the MMI section, 80% of the input power was transferred to the MMI waveguide. From Fig. 5.19 it can be observed that the cross states have 40% of the power that has been input to the MMI section, at around a length of 115μm. This compares favourably with the experimental results obtained by Spikeman *et al.* and confirms the accuracy of the results of the numerical schemes presented here. However, a slight difference between the experimental results and the results of the simulation may also be attributed to the inaccuracy in the actual structural parameters including the refractive index values used. In this study the structural symmetry has been considered and by using 12800 elements for half of the MMI waveguide section should be reasonably accurate for the subsequent calculation of the coupling lengths, and a much finer mesh, at an increased computational cost, could change the coupling length only slightly. This suggests that the numerical results presented here are highly accurate, given the structural data in the simulation.

5.5 Reduction of loss and cross talk in MMI devices

A part of the incident power may not couple to either of the two output waveguides and a reduction of this loss may be important in some photonic devices. The excess loss may be calculated from the power lost by not coupling to either of the two states, and this can be given as

$$\text{Excess loss} \equiv -10\log_{10}\frac{P_{cross}+P_{bar}}{P_{in}} \qquad (5.12)$$

where P_{in} is the input power of the MMI section and P_{cross} and P_{bar} are the power in the *cross* and the *bar* states respectively. To study the effect of the fabrication tolerance, the excess loss was calculated. The excess loss curve for the 3 dB coupler is shown in Fig. 5.20, where, at the optimum design length of 115μm, the excess loss is a minimum, corresponding to a value of about 0.5dB, and remaining within a 2dB limit for a range of 10μm axial distance variation. However, if the design length, on either side, is exceeded by a larger amount, the excess loss will rise very sharply. When the device length is z = L_{c1} = 230μm most of the power will return to the cross state.

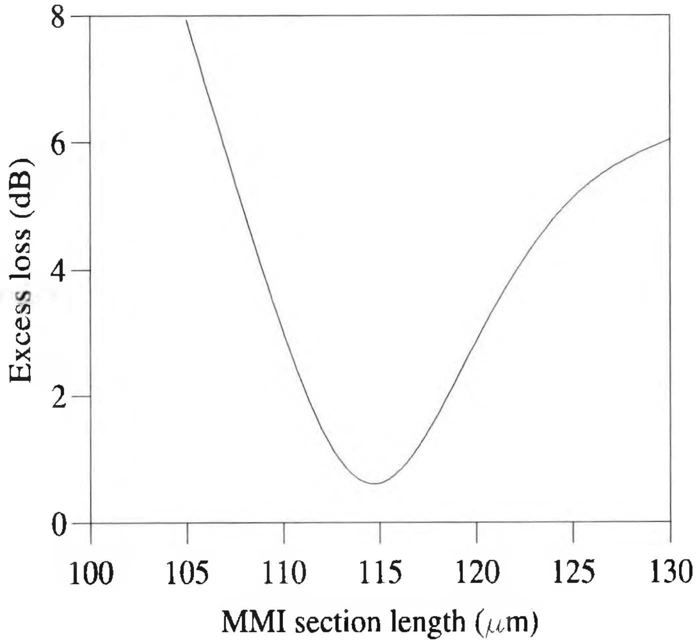

Fig 5.20 Variation of the excess loss with the axial distance for the 3dB coupler

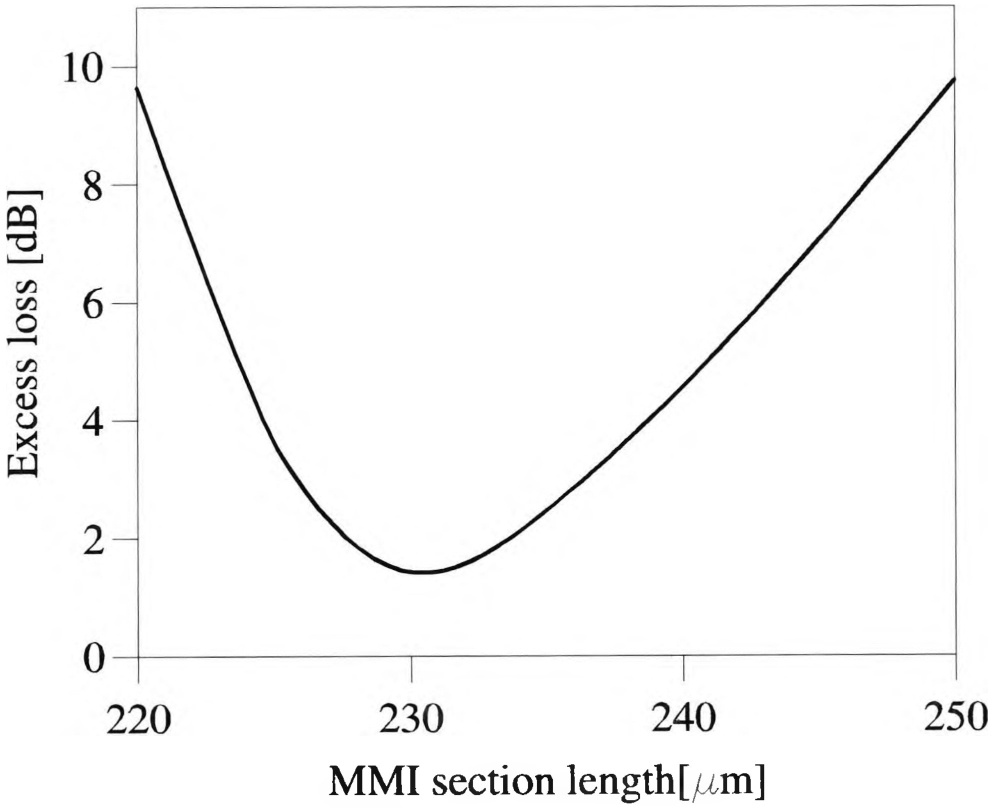

Fig. 5.21 Variation of the excess loss with the axial distance for the cross coupler

However there will also be some uncoupled power, and Figure 5.21 shows the excess loss for the cross coupler configuration. An excess loss of 1.5dB has been calculated at the optimal cross coupler length, which is three times that of the 3dB coupler.

For such a 3dB coupler, it is desirable that the power coupling to the two waveguides be identical. However, practically it may not be possible to achieve this and more importantly the effect of the fabrication tolerance may also need to be considered to do so. The power imbalance of the coupler is given as

$$\text{Imbalance [dB]} \equiv -10\log_{10}\frac{P_{bar}}{P_{cross}} \qquad (5.13)$$

where P_{bar} and P_{cross} are the power in the bar and the cross states respectively.

Figure 5.22 shows the tolerance of the axial position is around 8μm at the design length of 115μm, with a power imbalance of ±0.5dB. Around 125μm the power imbalance is about 2dB, which lies within the tolerance.

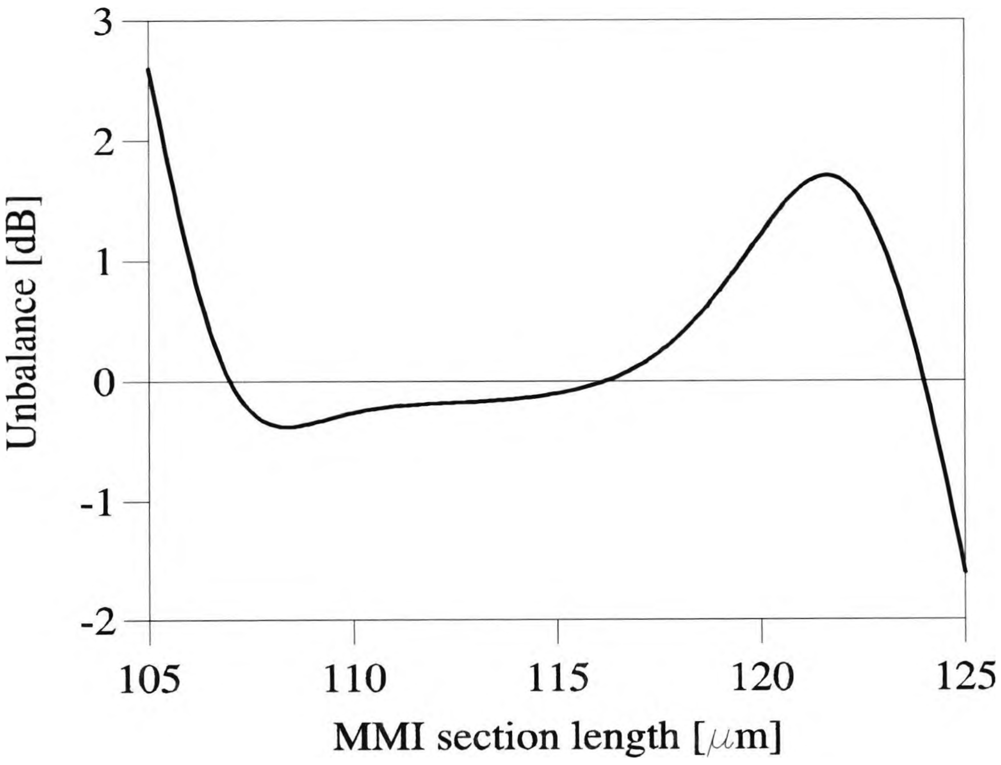

Fig. 5.22 Variation of the power unbalance with the axial distance for the 3dB coupler

Again the small deviation from the experimental results reported may be due to the selection of the guide and substrate indices, the accurate determination of which may be limited by the experimental constraints employed.

5.6 Fabrication tolerances

Next the effect of the fabrication tolerance for the MMI width is investigated. For this study the width of the multimode section was increased by 0.5μm to 9.5μm from that used in the earlier section. The modal profiles for the MMI section were calculated by using the FEM and the excited modal coefficients were calculated by using the LSBR. The composite field along the length of the multimode section was determined for the estimation of the power coupling to the two output waveguides. The power coupling efficiency of the new structure is shown in Fig. 5.23, and it can be observed that the length required for the 3dB coupler increased, since the intermodal coupling lengths were also increased.

Apart from that fact, it can be noticed that there is a higher imbalance between the bar and the cross states at the design length. This was due to the position of input and output waveguide sections as they were kept unchanged, as in the original design.

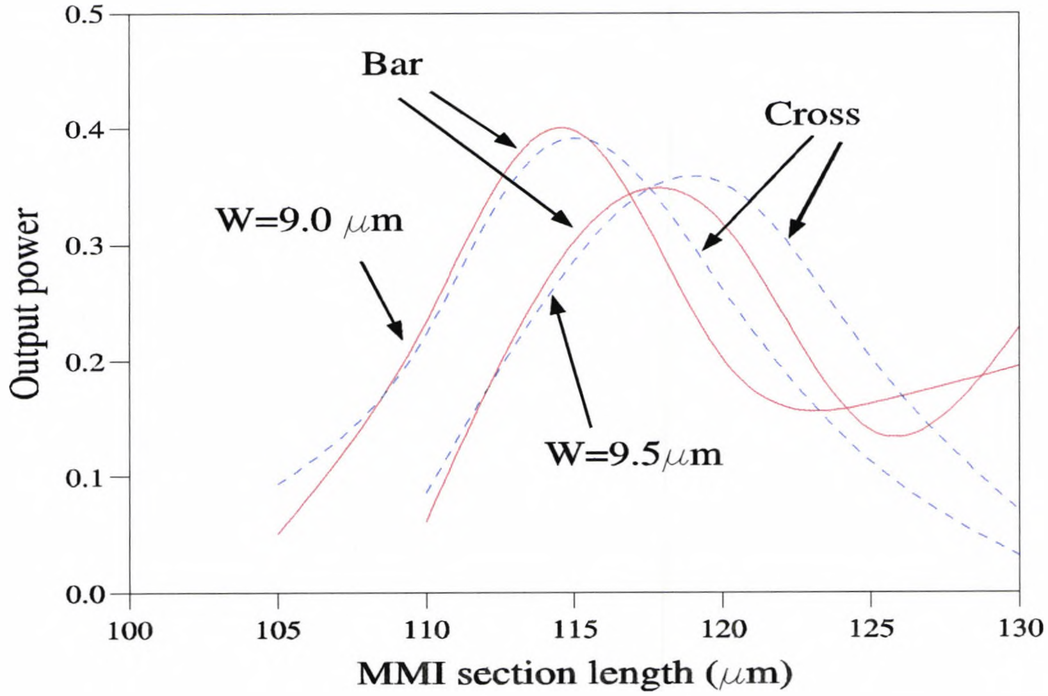

Fig. 5.23 Power transfer characteristics of the 3 dB coupler for different MMI widths.

Even though the possibility of having a tolerance of 0.5μm is unlikely in most of the fabrication processes, it has been chosen to indicate the importance of accurate design parameters for better performances.

5.7 Polarization dependence

In this section the polarization characteristics of the MMI based 3dB coupler configuration is studied. For this purpose, all the quasi-TM modes in the input, output and the MMI waveguide sections were calculated by using the vector **H**-field FEM.

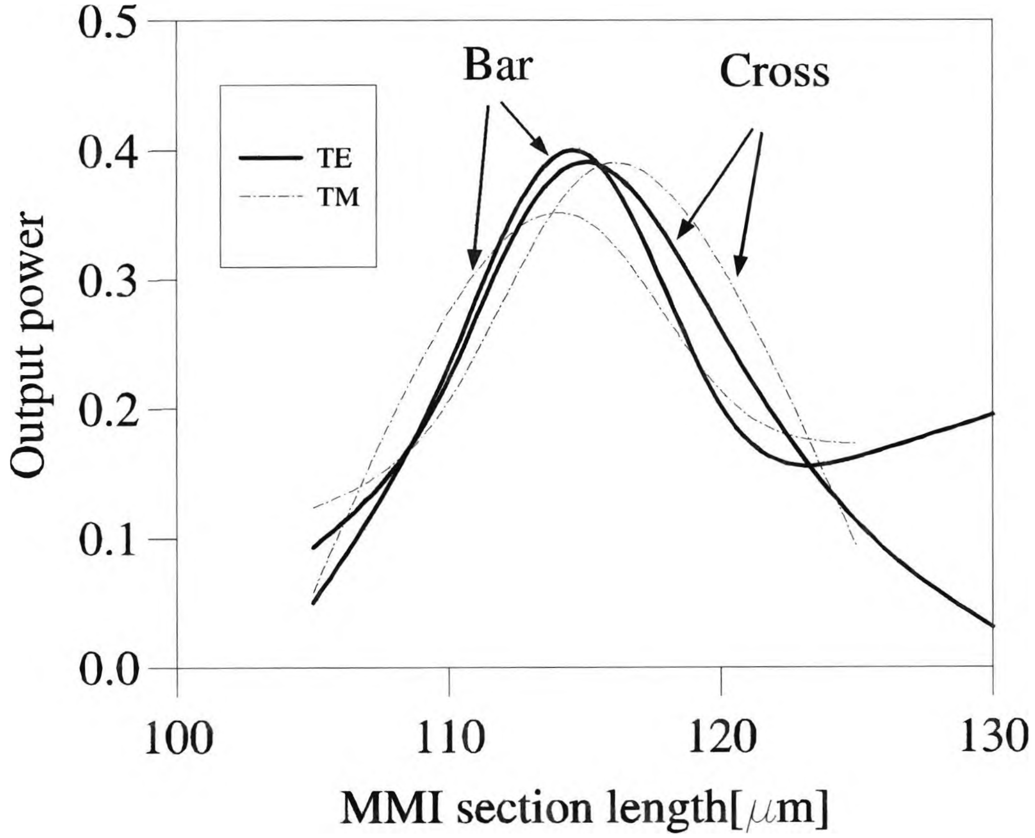

Fig. 5.24 Comparison of the power transfer curves for the TE and the TM polarizations

The intermodal coupling length between the first two modes is 233μm for TM polarization. This is around 2μm less than that determined for TE polarization. The excited modal coefficients for both the TE and the TM polarizations were almost identical. From Figure 5.24 a small polarization dependence is clearly noticeable, but this may not be much detrimental for some of the purposes for which the device may be used.

5.8 2-Dimensional simulation of a 1X4 MMI power splitter

In this section the performance of the MMI as 1x4 way power splitter is studied. This approach can be extended to 1XN way MMI based splitters which are an attractive candidate in the MMI based multiplexer designs.

Figure 5.25 below shows the top view of the multimode interference power splitter. It consists of an input access waveguide of 2.5μm centred symmetrically into a rectangular guide of width 24μm and length, *L*, and four output waveguides which are the same as the input access guides.

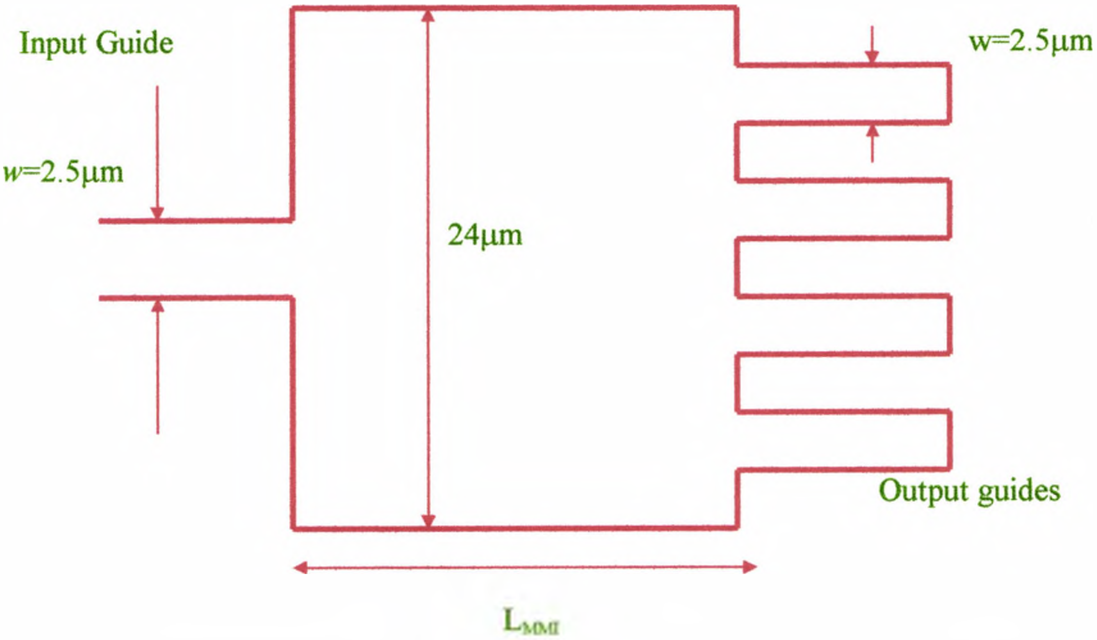

Fig. 5.25 Top view of a multimode interference power splitter (1x4)

A quartenary InGaAsP material of bandgap 1.3μm was used in this simulation. At an operating wavelength of 1.55μm, the guide and the substrate refractive indices were calculated as 3.3988 and 3.1645 respectively. The structure consists of a layer of InGaAsP 0.3μm high, surrounded by InP. There were two guided modes in the output access waveguides and 22 guided modes in the MMI section. Since the structure is symmetric only half of the structure was used. The full structure contains 22 guided modes. Due to the exploitation of the two-fold symmetry only 11 guided modes in the MMI section and 1 guided mode in the input section were considered. This reduces the computational time and gives greater flexibility in the usage of a relatively finer division. Table 5.6 below shows the propagation constants (β), the coupling lengths (L_{cn}), and the excited modal coefficients (b_i) of the 11 modes considered in the MMI section length.

Modes	β	L_{cn}	τ
H^y_{11}	13.14699	----------	0.47109
H^y_{13}	13.14127	579.62	0.46293
H^y_{15}	13.13045	193.45	0.42090
H^y_{17}	13.11419	96.66	0.37704
H^y_{19}	13.09247	57.94	0.32023
$H^y_{1\_11}$	13.06536	38.63	0.24875
$H^y_{1\_13}$	13.03253	27.52	0.09793
$H^y_{1\_15}$	12.99413	20.59	0.14536
$H^y_{1\_17}$	12.95047	16.01	0.10004
$H^y_{1\_19}$	12.90108	12.79	0.06350
$H^y_{1\_21}$	12.84783	10.51	0.03374

Table 5.6 Table showing the propagation constants (β), coupling lengths (L_{cn}) and modal coefficients (b_i) for the 11 modes in the MMI section.

At half the coupling length, where $L_c/2$=290μm the input power divides equally into the central and the lateral output guides. As there exists a structural symmetry only two equal peaks are seen in Figure. 5.26. This confirms that the MMI can be used as a 4-way (or *N*-way, where *N*>1) power splitter depending on the width and length of the MMI.

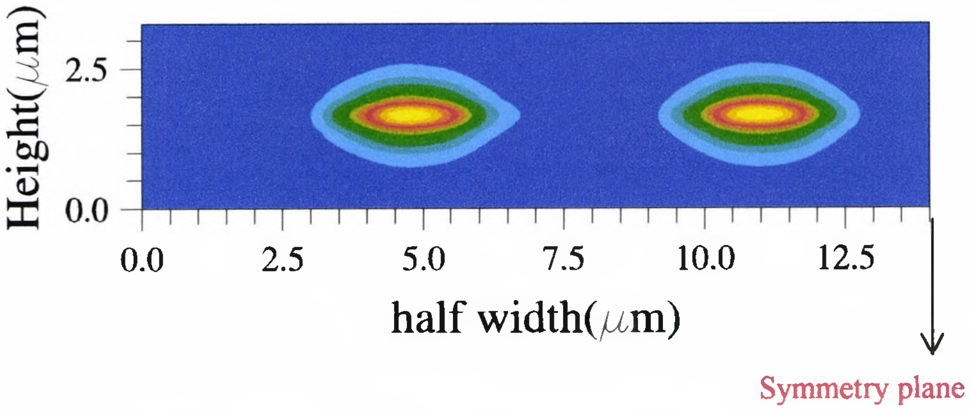

Fig. 5.26 Field profile at half the coupling length, $L_C/2$.

Figure 5.27 shows the '*self-imaging*' phenomenon of the MMI at $L_c/4$ where the field divides into 4 equal peaks. This shows that the number of self-images depends on the length of the MMI section.

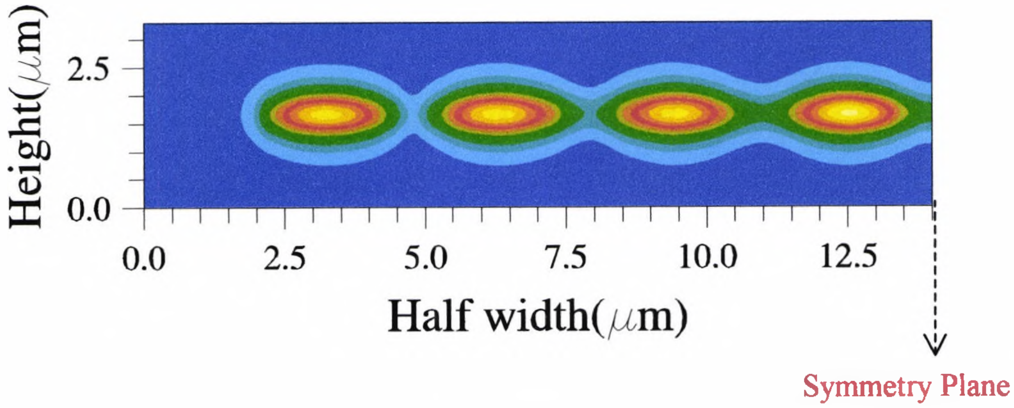

Fig. 5.27 Field profile at $L_c/4$ showing the 'self-imaging' phenomenon

The output guide supports two guided modes and the power carried by them is illustrated in Figures 5.28 *a* and *b* for the inner and outer output guides respectively. It can be observed from these figures that, the fundamental mode carries most of the input power. It can also be observed from Figures 5.28*a* and 5.28*b* that the maximum power is transferred from the MMI section to the output access guides, at half the coupling length.

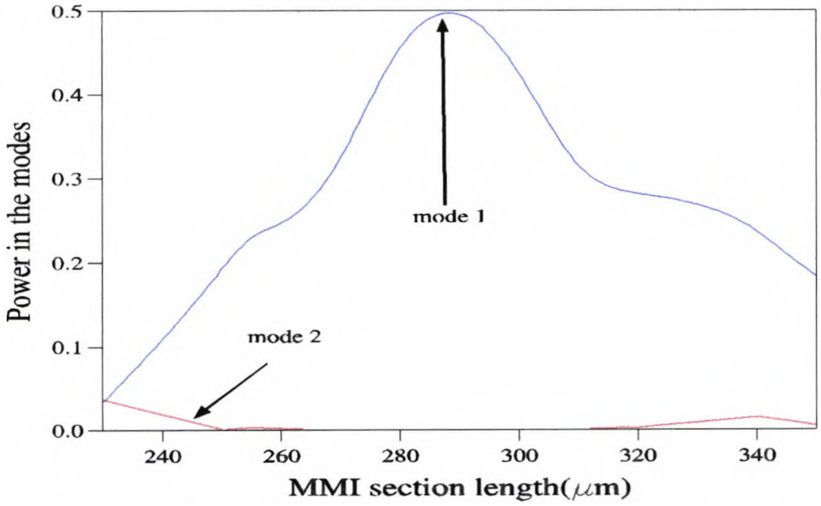

Fig. 5.28a Power coupled to the two guided modes of the output inner waveguide.

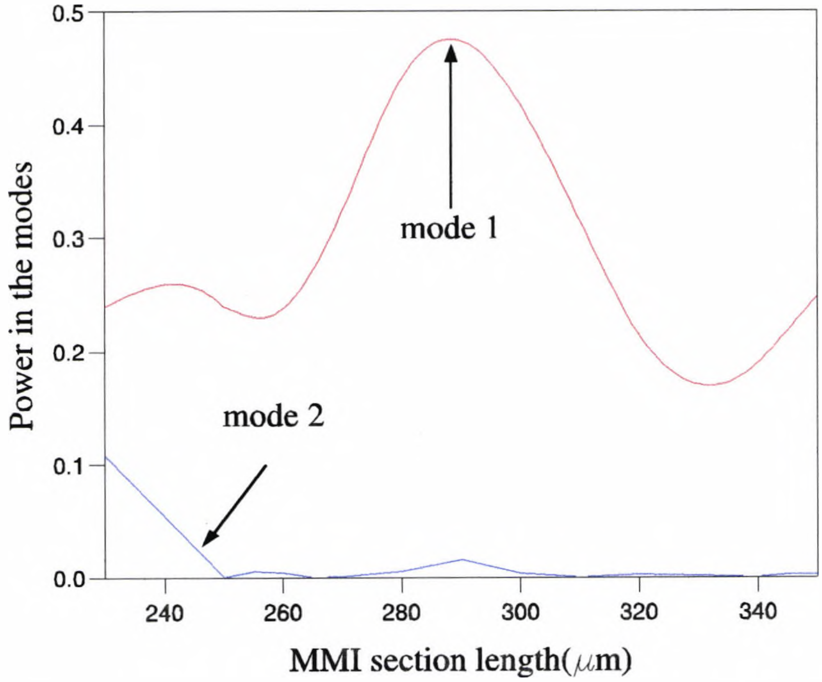

Fig. 5.28b Power coupled to the two guided modes of the output outer waveguide.

Since one of the peaks of the section will match exactly the output lateral access guide field profile, it can be observed that around 45% of the power is being transferred to the outer guides. Similarly, the central guide field overlaps with the other peak in Fig.5.28b. A part of the incident power may not couple to the two output waveguides and a reduction of this loss may be important for some practical photonic devices. This excess loss may be calculated from the power lost by not coupling to either of the two states, and this can be given as

$$\text{Excess Loss} = -10 \log_{10} \frac{P_l + P_c}{P_{in}} \tag{5.14}$$

where P_{in} is the input power to the MMI section, P_l is the power in the outer and P_c is the power in the inner output guides.

The excess loss curve for the 1x4 coupler is shown in Fig. 5.29 below:

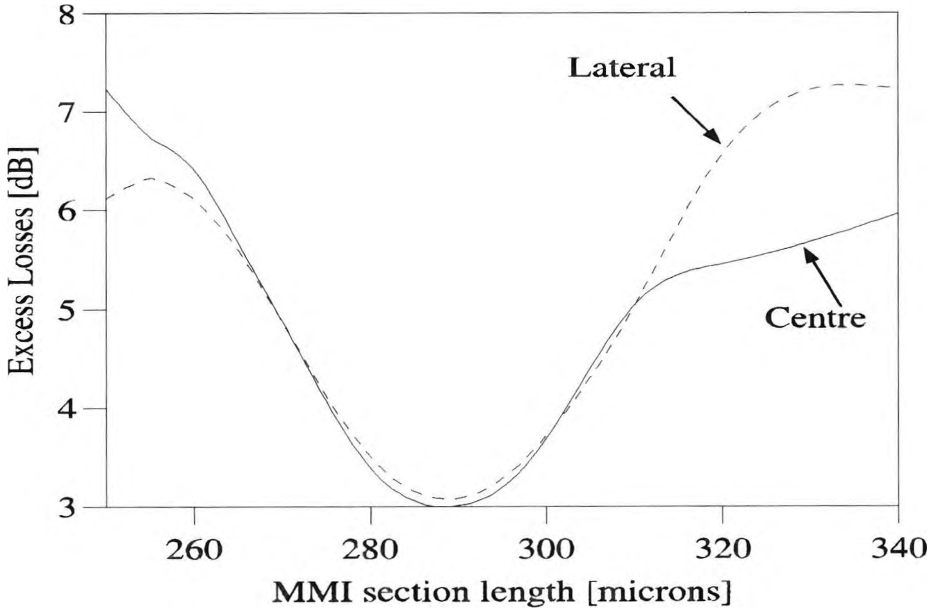

Fig. 5.29 Excess loss curve for the 1 x 4 power splitter

where, that at the optimum design length of 290μm, the excess loss is at its minimum. The study has also shown that when varying the device parameters such as the refractive index and length, these are seen to be less critical parameters. The total width of the rectangular section must be controlled to within a certain limit, which is a very important parameter for designing MMI-based devices.

Next, a MMI section with a slightly different dimension is considered. The schematic diagram of the structure is shown in Fig. 5.30 below.

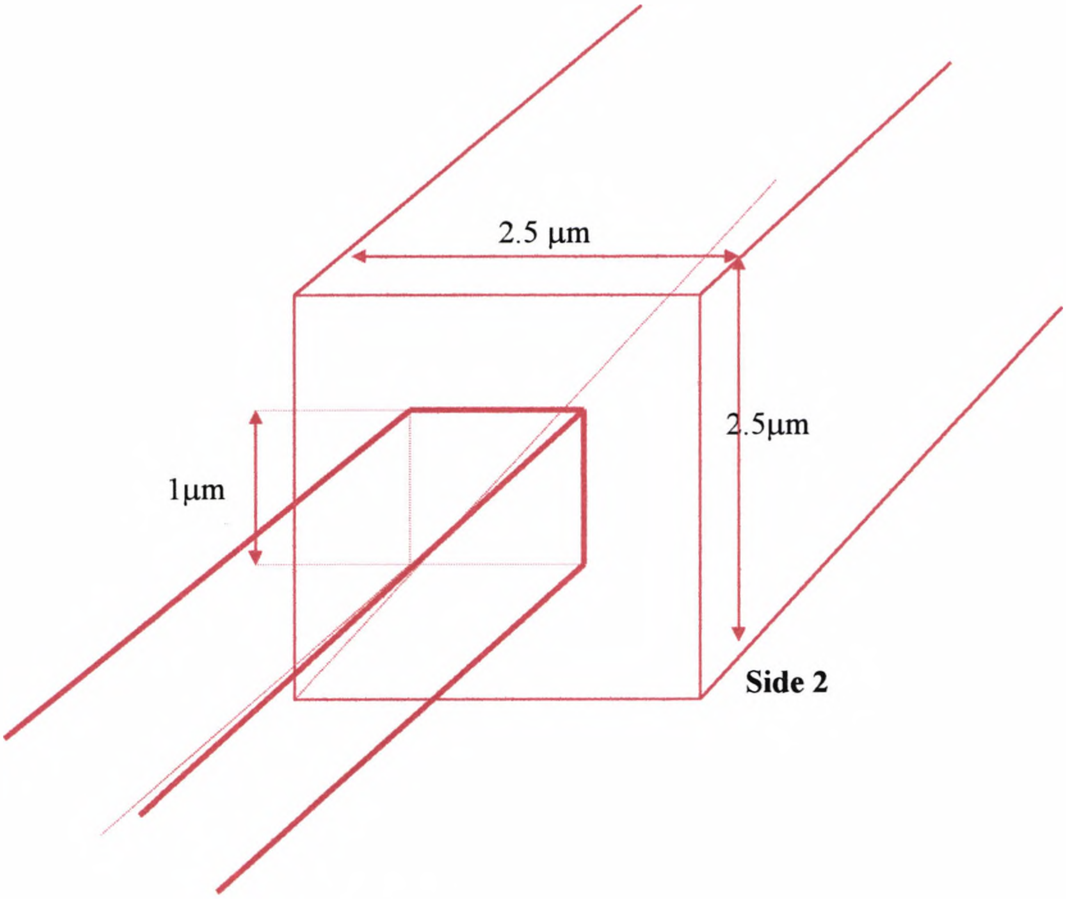

Fig.5.30 Schematic diagram of the 2-D MMI based 1x4 splitter

A single mode square waveguide with 1μm dimensions is butt-coupled to a MMI section of square cross section. The guide and cladding indices are 3.3989 and 3.1645, respectively, for both the narrow input and MMI guides and the operating wavelength was 1.55μm. In this example, it is assumed that both the waveguides are aligned at the centre, so a two-fold structural symmetry does exist. When the fundamental quasi-TE (H^y_{11}) mode is incident from side 1 (which also has got same two fold symmetry), the available total symmetry condition is exploited to reduce the computational time. In the finite element simulations and the subsequent LSBR calculations, 7200 first-order triangular elements are used for a quarter of the structure and it takes about 5 min. CPU time for each modal solution.

The dominant H_y field profile for the fundamental quasi-TE mode, H^y_{11}, in the narrow input waveguide at $z=0_-$ μm is shown in the Fig. 5.31a. The field profile at the beginning ($z=0_+$) of the MMI section is shown in Fig 5.31b. This profile is obtained by a superposition of all the four modes with their appropriate excitation coefficients. It can be observed that the resultant field profile is very close to the incident field profile shown in Fig. 5.31a, except for a slight aberration around the edges of the MMI guide-core.

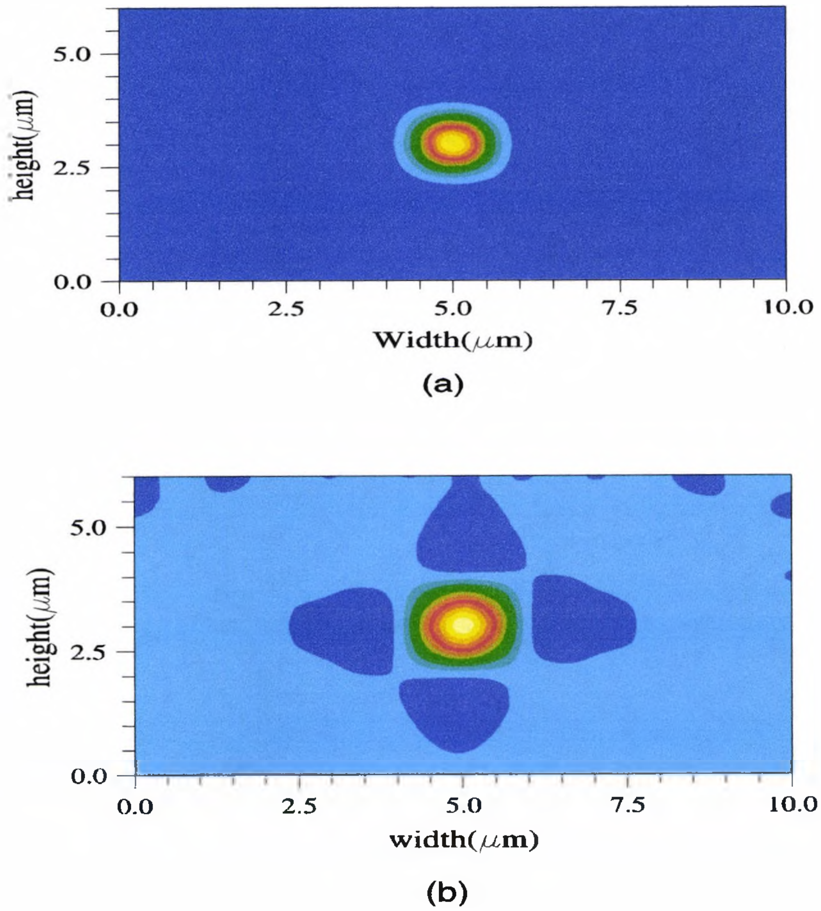

Fig. 5.31 Field profile (a) in the narrow input waveguide section ($z=0_-$) and (b) at the beginning ($z=0_+$) of the MMI section.

This combined profile is due to all the four modes generated in the MMI section and propagated through the waveguide. However, as the individual modes popagate with different propagation constants, their relative phase difference will change the overall field profile along the axial direction. The modal coefficients of the excited modes in the MMI section are shown in Table 5.7 below.

Modes	LSBR(M=4) τ	LSBR (M=1) τ	LSBR (M=4) ρ	OI τ
H^y_{11}	0.82506	0.82464	0.44141E-2	0.81508
H^y_{31}	0.39440	0.39384	--------------	0.38880
H^y_{13}	0.31430	0.31404	--------------	0.32154
H^y_{33}	0.18712	0.18696	---------------	0.19049

Table 5.7 Transmission coefficients (τ) and the reflection coefficients (ρ) for the modes in a 2-d MMI section

The width of the MMI section is $W_{MMI} = 2.5\mu m$. The amplitudes of the reflected modes into the incident waveguides are also given in the table above. More accurate results by considering four modes simultaneously (M=4) in each side for the field continuity enforcement in a least squares sense are shown in column 2 of Table 5.7. The approximate results using the overlap integral (OI) are also shown in column 5 of Table 5.7. It can be seen that results using only one mode at a time (M=1) even yields better results than the overalp integral, due to the better balance achieved between the electric and magnetic components of the error functional J during the minimization of the field continuity error.

Fig. 5.32 shows the field profile at z=9.1μm. It can be observed that at this axial position (z), the total power is equally divided into the four corner sections, and a MMI section of this length can be used as a four-way symmetrical three-dimensional power divider.

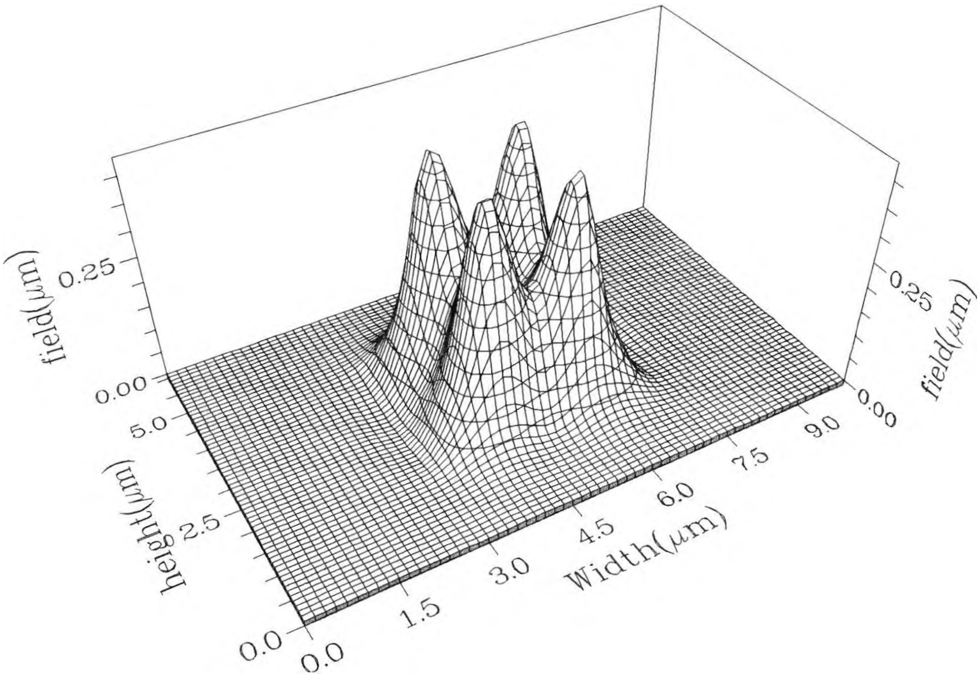

Fig. 5.32 Field profile in the MMI section at z=9.1μm

5.9 MMI based duplexer

Today's evolving telecommunication systems demand a steadily increasing share of access networks. These networks are increasingly demanding on high flexibility and reconfigurability, which requires enhanced functionality of photonic integrated circuits (PICs) for optical communications. In these optical systems, the key issue is the development of highly economic but reliable optoelectronic transreceivers. In order to set up a bi-directional link on a single fibre transmission line, a passive duplexer is required at the transceiver modules for wavelength routing. Due to the high power levels incoming and the outgoing signals, a high level of isolation is required at the routing ports. This can be achieved by using a directional coupler section. However, the device length increases as the separation between the guides increases. Duplexing can also be achieved by using a compact multimode interference (MMI) -based device. The basic function of it is to split and/or re-route the incoming light. MMI devices are increasingly becoming popular due to their excellent properties such as low-loss, high splitting ratio and their insensitivity to fabrication tolerances.

5.9.1 Theory of Duplexer

The device parameters of a MMI can be adjusted such that a simple relationship can be derived in relation to the device length, *L*, where

$$L = mL_{\pi(\lambda=1.55)} = nL_{\pi(\lambda=0.98)} \tag{5.15}$$

a duplexer may be designed where two different wavelengths will emerge as the *bar* and the *cross* states when the device length is *L*, and *m* and *n* are odd or even integers.

To analyze the performance of duplexers, e.g. in terms of crossover power, and device fabrication tolerances the finite element method in combination with the LSBR method is used.

5.9.2 Results of the 1-D duplexer simulation

Initially a one dimensional structure is simulated to study the duplexer properties. The schematic diagram of the MMI considered is shown in Fig. 5.33.

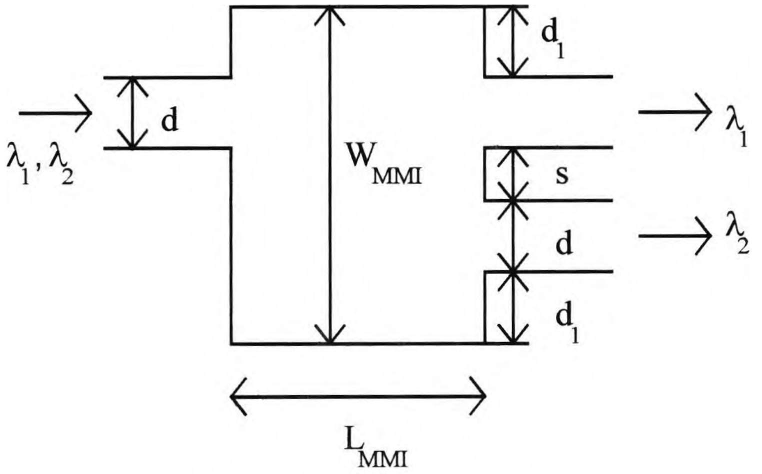

Fig. 5.33 The schematic of the 1-D duplexer

In this case the width of the single mode input section was assumed to be, *d*=0.5μm and that of the MMI section was taken as W_{MMI}. The output guides were placed at W/3 and at 2W/3 for the case of 'restricted resonance'. The output guides were of the same dimensions as the input guide. The output guide opposite the input is termed the 'bar state' and the other output guide is termed the 'cross state'. The refractive index of the guide was 1.502 and that of the substrate was 1.4982 at an operating wavelength of 980nm and at 1550nm, the waveguide index was 1.4982 and that of the substrate was 1.444. The 980nm wavelength is becoming very popular after the invention of the erbium doped amplifiers as this wavelength is used as the pump wavelength. In a InGaAsP/InP material system the binary compound InP is transparent at λ=1550nm, the wavelenth important for optical communications. The band gap can be tuned by adding Ga and As, forming quartenary compounds than can emit or absorb light at this wavelength for the fabrication of lasers and detectors. The 1550nm is very popular in the semiconductor matrial systems due to the low loss at this wavelength.

According to the self-imaging principle, an input field in a multimode waveguide is reproduced at periodic intervals along that waveguide. In the general resonance mechanism at a coupler length of $L_c = p(3L_\pi)$, a direct or mirrored image of the input field is formed if p is an even or odd integer, respectively. Now, a MMI coupler can perform separation of two wavelengths λ_1 and λ_2 if it is a bar coupler for one wavelength and a cross coupler for the other wavelength; The length (L_c) of the demutiplexing coupler has to satisfy the following relation (Paim *et al.*, 1995)

$$L_c = p(3L_\pi^{\lambda_1}) = (p+q)(3L_\pi^{\lambda_2}) \tag{5.16}$$

Where p is a natural number ($p = 1,2,3,\ldots$), q is an odd integer, and L_π^λ is the beat length at wavelength λ. From Eq.5.16, the ratio of the two beat lengths is given by $L_\pi^{\lambda_1}/L_\pi^{\lambda_2} =(p+q)/p$. So by taking the smallest even and the odd numbers, (*i.e.*, p=2, q=1) the ratio is 1.5. Therefore in Figure 5.34 the even and the odd multiples of the coupling lengths for the two different wavelenths are plotted versus the MMI width, plotted on a logarithmic scale.

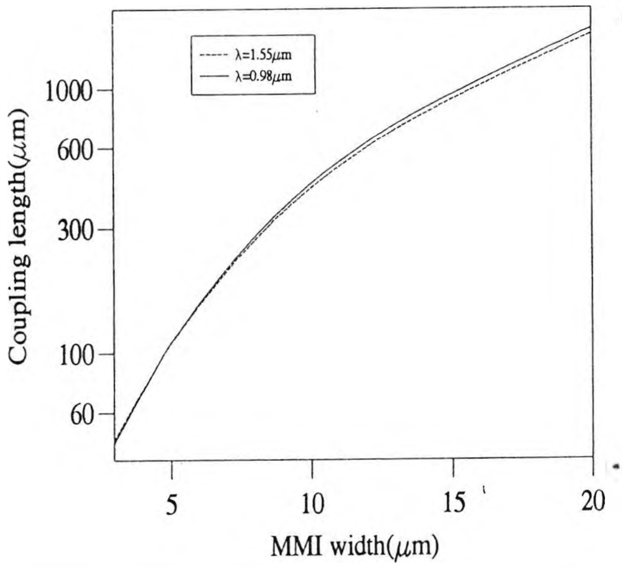

Fig. 5.34 Coupling length versus MMI width

From Fig. 5.34 it can be seen that the two wavelengths intersect at an MMI width of 4.8μm, and this value was taken for this simulation.

The effect of material dispersion is considered and in the initial stage, simple planar equivalent of the structure is considered. When the height of waveguide and MMI sections are to be 0.5μm, to achieve single mode in the vertical direction the effective index for the 1550nm and 980nm was calculated to be 1.4642 and 1.4833 respectively. Both the wavelengths were applied to the input waveguide and the composite field profiles were plotted at multiples of $L\pi$. Table 5.8 shows the propagation constants, coupling lengths, the excited coefficients and the percentage deviation from the quadrature phase relationship. From Table 5.8, L_π $(\pi/(\beta_0-\beta_1))$ for the first two modes may be calculated to be 51.94μm. It can be noticed from Table 5.8 that every third mode is not excited due to the '*restricted resonance*' and their respective coefficients are negligible. It can also be observed from Table 5.8 that the quadrature relationship does not hold for more realistic practical devices.

Figure 5.35 shows the composite field for λ=980nm at the first interface, *i.e.* at $z=0_+$. The input field (solid line) is superimposed on the dashed line to show that most of the power is in the bar state. The small ripples shows the incomplete cancellation of the field. Figure 5.36 shows the field at z=50μm, which is around a value of one coupling length. From Table 5.8 it can be seen that the quadrature error increase for the higher order modes.

Mode	β	L_c	b_i	Error %
TE_0	9.48958	——	0.58552	——
TE_1	9.42908	51.94	0.52164	
TE_2	9.32752	19.38	0.05000	0.51
TE_3	9.18373	10.27	0.44770	1.15
TE_4	8.99596	6.36	0.31586	2.00
TE_5	8.76192	4.32	0.05920	2.92
TE_6	8.47854	3.11	0.23343	4.31
TE_7	8.14187	2.33	0.12444	5.67
TE_8	7.74726	1.80	0.03471	7.69
TE_9	7.28988	1.43	0.07132	8.92

Table 5.8 Shows the propagation constants, coupling lengths, the excited coefficients and the percentage of deviation from the quadrature relationship for the 980nm wavelength

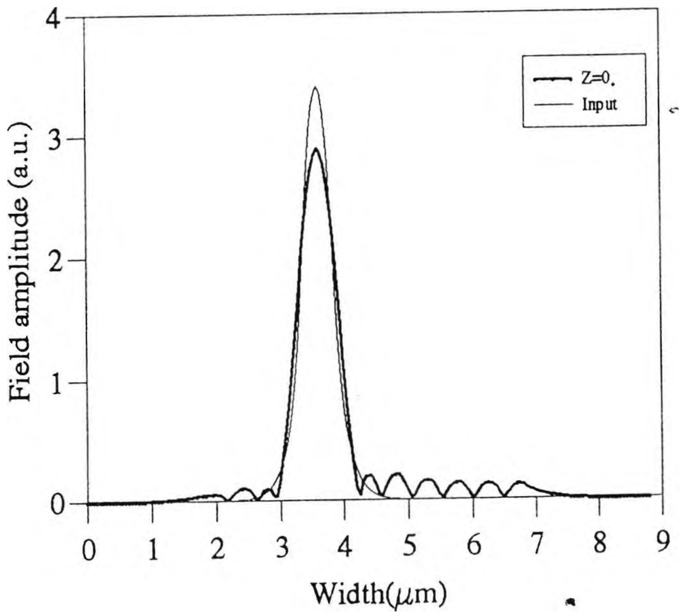

Fig. 5.35 The composite field profile at $z=0_+$ for $\lambda=980$nm

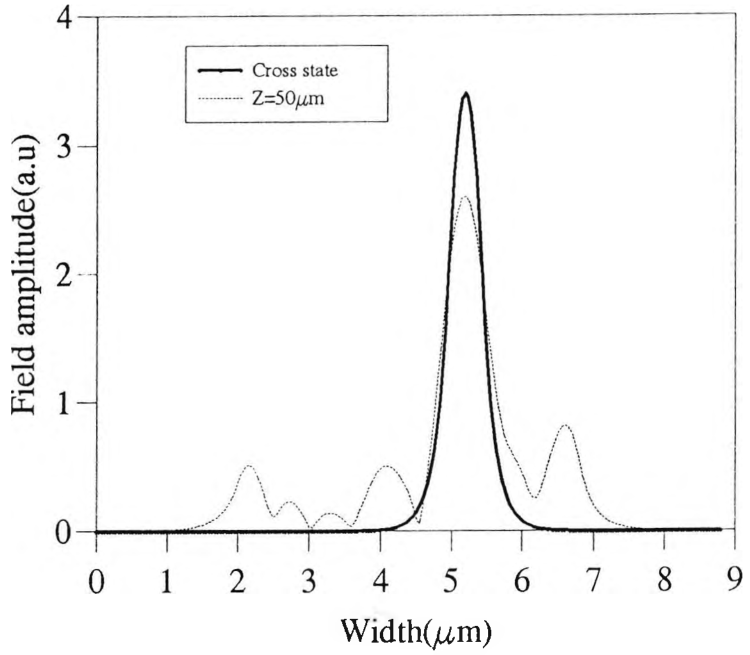

Fig. 5.36 Composite field profile at z=50μm for λ=980nm

It can be seen that at this position the input power will be coupled to the cross state of the output guide. Compared to Fig. 5.35, Fig 5.36 has developed some side lobes due to the deviation from the quadrature phasing. Fig. 5.37 shows the composite field at a value of 2Lπ(beat length). Here the total field is transferred from the cross state back to the bar state showing the '*self-imaging*' principle of the MMI.

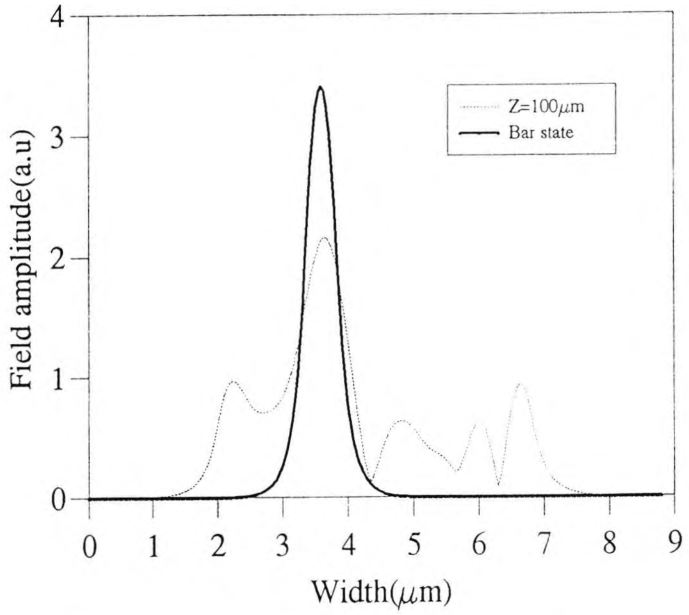

Fig. 5.37 Composite field profile at z=105μm for λ=980nm.

Fig. 5.38 shows the composite field at z=305μm which is six times the coupling length (L_π). It can be clearly observed that as the quadrature relationship does not hold exactly, and the cumulative error is increased with the multiples of L_π and this causes large side lobes.

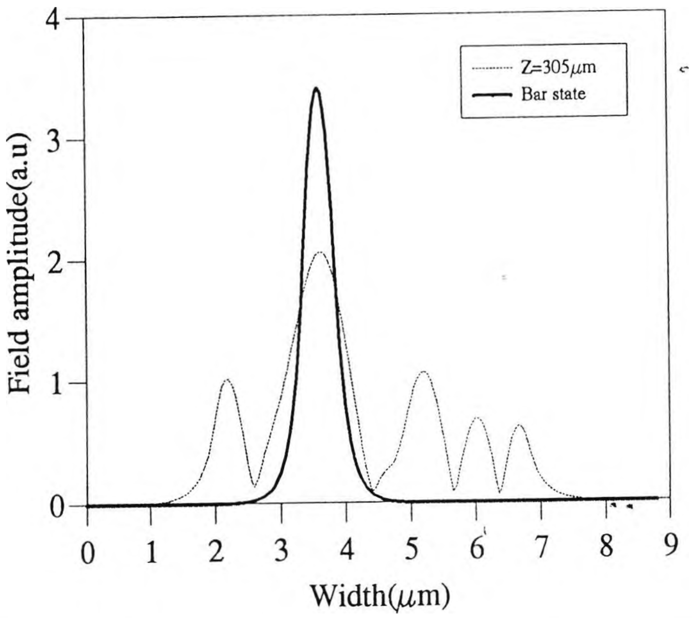

Fig. 5.38 Composite field profile at z=305μm for λ=980nm

Using Eq. 5.16 the coupler length , $L_c = 6L_{\pi}^{980} = 9L_{\pi}^{1550}$. In the design, it was observed that if *W*=4.8μm, then six times L_π at 980nm would be equal to nine times L_π at 1550nm. Fig. 5.39 shows the composite field for λ=1550nm at 305μm which is nine times the coupling length of L_π. At this wavelength most of the power is in the cross state at around 305μm.

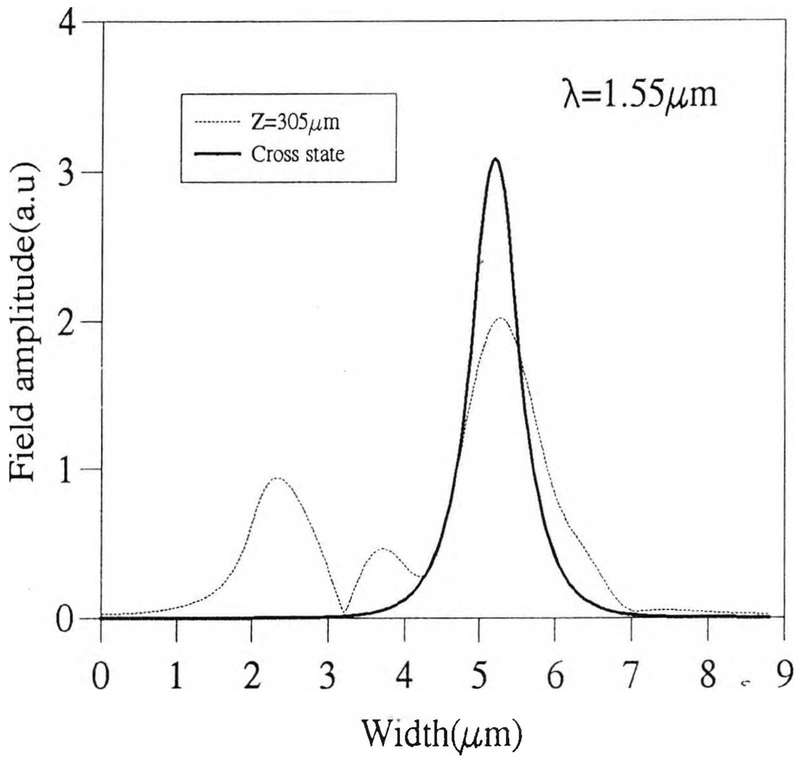

Fig. 5.39 Composite field profile at *z*=305μm for λ=1550nm

So from Fig. 5.38 and Fig. 5.39 it can be seen that at around 305μm, both the wavelengths are emerging out from the bar and the cross states.

Fig. 5.40 shows the power coupling efficiency of the MMI for both the wavelengths considered.

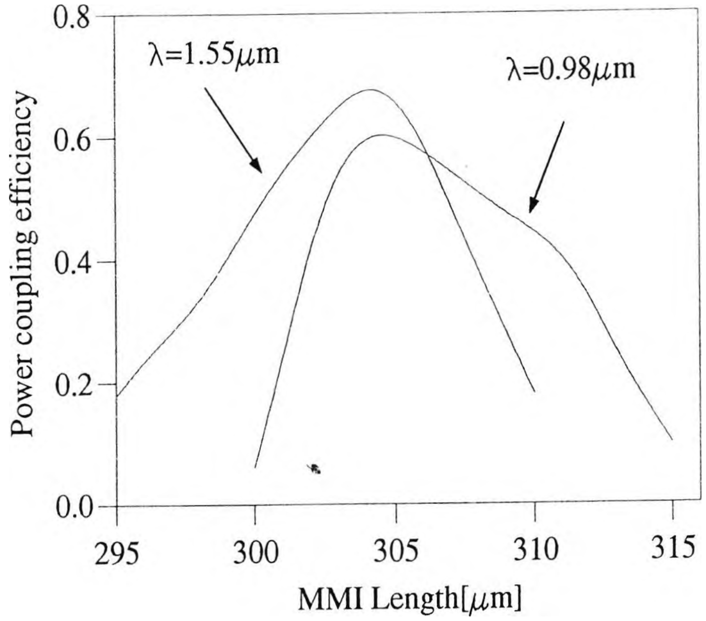

Fig. 5.40 Power coupling efficiency versus MMI length

It can be seen from Fig. 5.40 that around 305μm both the wavelengths have a maximum output power but in two different states.

5.9.3 Results of the 2-D duplexer simulation

Next a two dimensional structure is considered. The schematic of the two-dimensional MMI for a fully-integrated erbium-doped optical amplifier, considered is shown in Fig. 5.41. In this case the width of the single-mode input section was assumed to be d=6μm and that of the MMI section was taken as 21μm.

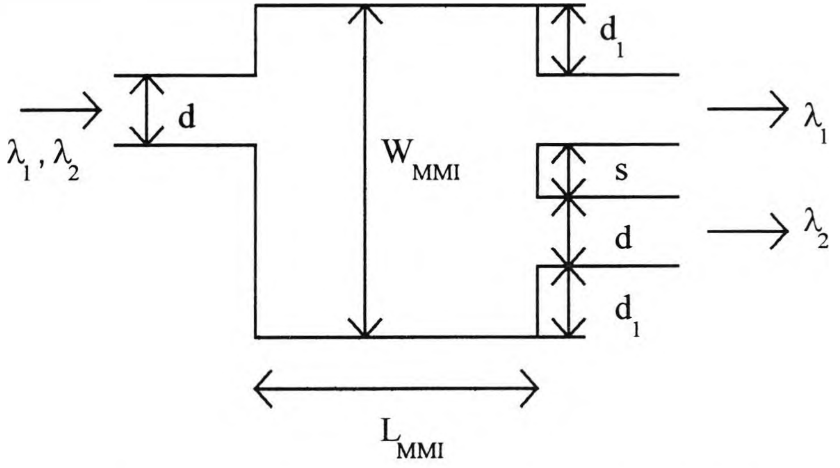

Fig. 5.41 Schematic of the 2-D MMI based duplexer

The output guides were placed at 7µm and at 14µm for the case of '*restricted resonance*'. The output guides were of the same dimensions as the input guide. The output guide directly opposite the input is termed the '*bar state*' and the other output guide is termed the '*cross state*'. The refractive index of the guide was 1.502 and that of the substrate was 1.4507 at an operating wavelength of 980nm and at 1550nm the waveguide index was 1.4982 and that of the substrate was 1.444. Figure 5.42 shows the odd or even multiples of L_C versus the active layer thickness, plotted on a logarithmic scale.

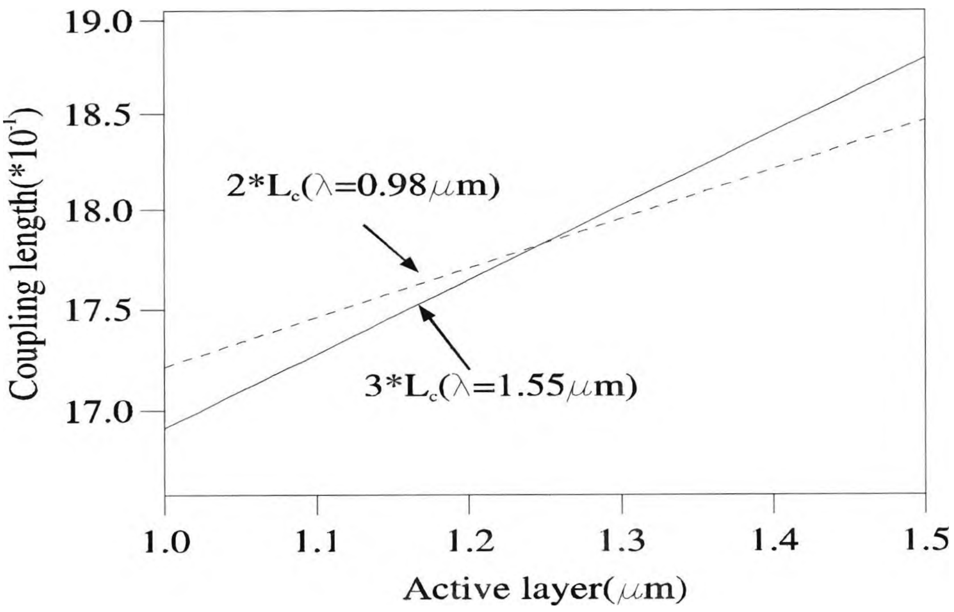

Fig. 5.42 Odd or even multiples of L_c versus active layer thickness

From Fig.5.42 it can be seen that the two wavelengths intersect at an active layer thickness of 1.25µm, and this value was taken for further simulation. The effect of material dispersion is also considered. Figure 5.43 shows the power coupling efficiency to the output guide of the MMI for both the wavelengths considered.

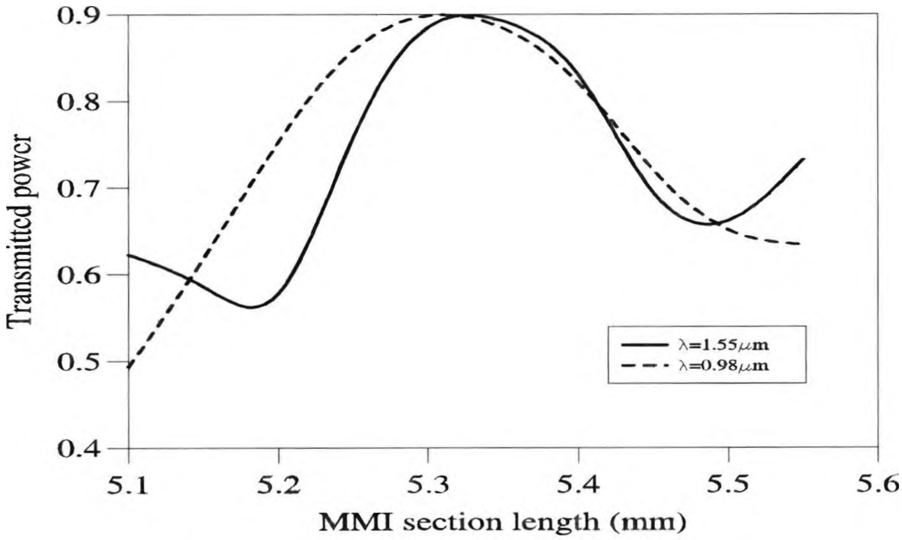

Fig.5.43 Power coupling efficiency of the duplexer

It can be observed from Fig. 5.43 that around 88% of the power is in the bar state for λ =1550nm. The little less efficiency of the 1550nm wavelength is due to the bad imaging of the input field which is caused due to the deviation from the quadrature relationship. However, from the power transfer curve it can be observed that even at losses about 1dB around 70% of power transfer is possible. It can also be observed that this design is less sensitive to the length as can be seen for an axial variation of around 200μm both the wavelengths seems to transmit about 70% of the power. Figure 5.44 shows the composite field profile at *z*=5.2mm for the 1550nm wavelength.

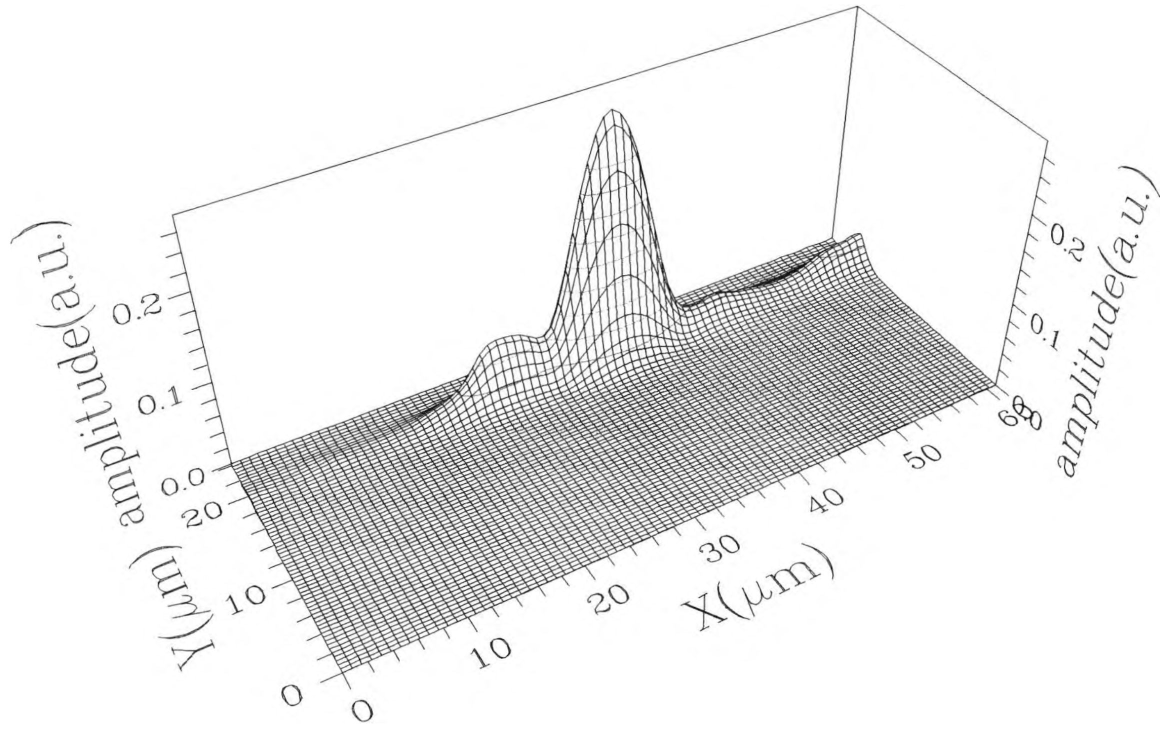

Fig. 5.44 Composite field profile at *z*=5.2mm for λ=1550nm

As can be seen from this plot most of the power is confined in the cross state. However, there is still some power left in the bar state. This is due to the incomplete cancellation of the input field. The higher deviation from the quadrature relationship can be improved by making the rib section slightly curved. This could improve the imaging slightly and hence a better coupling can be achieved. Fig.5.45 shows the field in the bar state for the 980nm wavelength. This wavelength is becoming very popular after the invention of the erbium-doped fibre amplifiers. As it is used as the pump wavelength in the erbium-doped integrated systems. It can be noticed from Fig. 5.45 that most of the power is in the bar state.

It can also be noticed that the quality of the image is better here compared to Figure 5.44. This shows that the quadrature relationship agree better. This is due to the number of guided modes are higher at this wavelength and hence a better performance. Fig. 5.46 shows the power coupling efficiency for the 980nm. The output power in the bar and the cross states is estimated by recalculating the field of the output guides and then reapplying the LSBR technique at the output again.

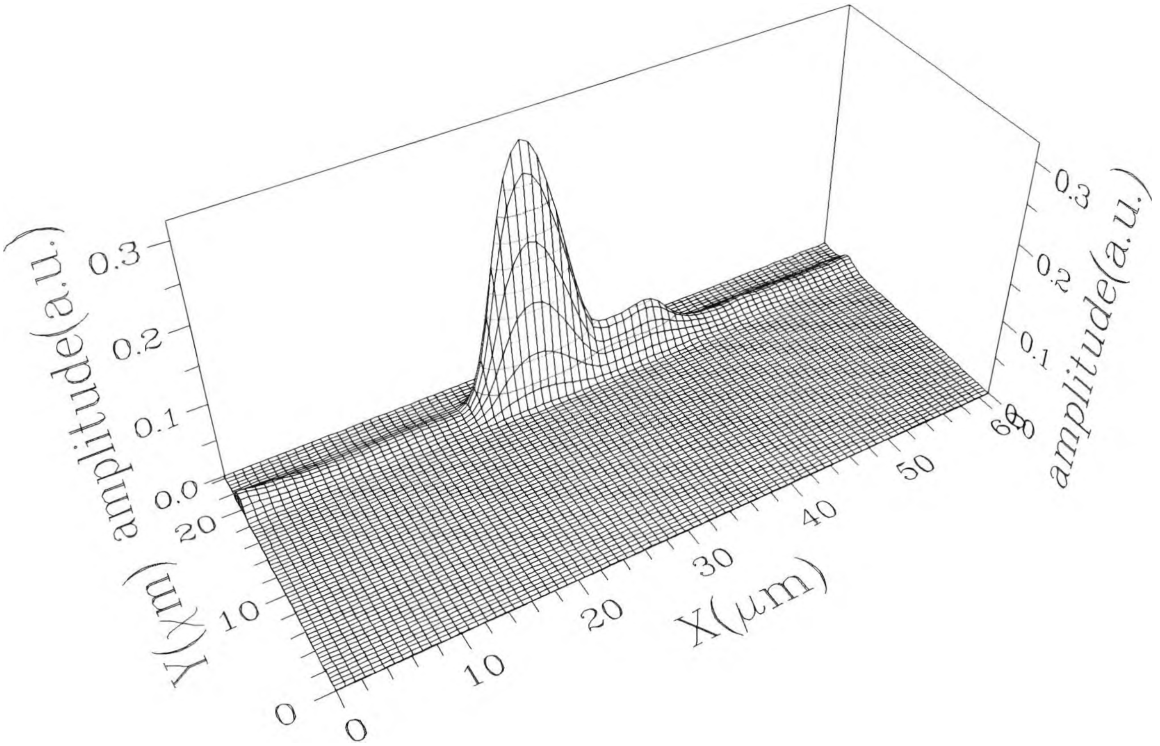

Fig. 5.45 Composite field profile at z=5.2mm for λ=980nm

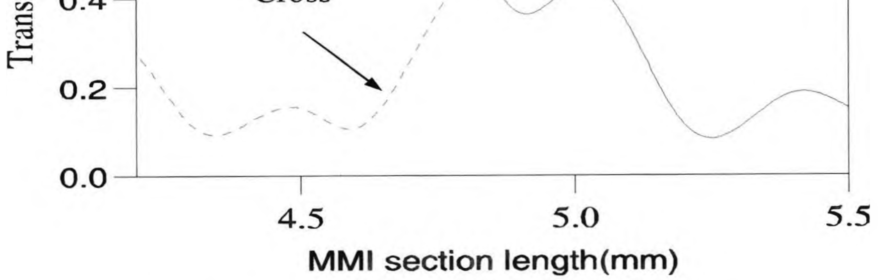

Fig. 5.46 Power coupling efficiency for λ=980nm

As can be seen from this curve the power transfer is maximum at around 5.2mm in the bar state and minimum in the cross state. Next the polarization stability of the duplexer is studied. Figure 5.47 shows the polarization property of the MMI for 980nm wavelength. It can be noticed that the power coupling efficiency for the TM case is slightly better than the TE case.

Since there was around 17µm difference between the TE and the TM wave beat lengths it can be noticed that there is an axial variation of 100µm between the points where the maximum power transfer occur. From this simulation the length of the device is around 5.3mm where as the same *sol-gel* technique employing the same dimensions as the MMI but employing the directional coupler technique resulted in a device length of 10.1mm (Forastiere *et al.*, 1996).

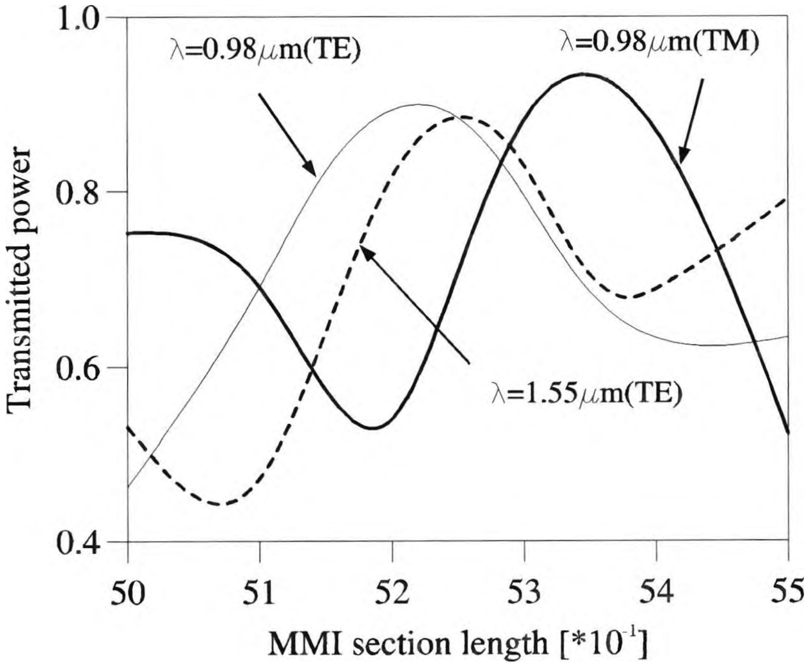

Fig. 5.47 Power coupling efficiency for the TM polarization

5.10 Comparison of the performance of directional couplers with that of MMI

With the maturity of a range of photonic devices, the emphasis on development is now in the design of compact optoelectronic integrated circuits, to exploit the full potential of available low-loss and high-band width optical fibers. Even though directional couplers have proved to be efficient power routing devices, however, the development of multimode interference (MMI) -based devices has proceeded rapidly due to their having attractive properties such as compactness, tolerance to a range of fabrication parameters, an inherent balance, and low optical loss and because they are particularly well suited to use with a moderate number of ports.

In this section a rigorous numerical comparison of the performance of a directional coupler with that of a MMI-based device is studied. To my knowledge this is the first time such a direct comparison is made on the important properties such as cross-talk, polarization sensitivity, device length and fabrication tolerances.

5.10.1 Theoretical background

Directional coupler-based devices are important components in a wide range of integrated optic devices. When light is launched into one of the input guides, at the coupling length most of the power is coupled to the adjacent output guide. However, there may be a small amount of power remaining out the incident output port due to the incomplete cancellation of the modes, and this is responsible for the presence of cross-talk (Chen, 1984). This may be due to the unequal coefficients of the excited even and odd supermodes, structural asymmetry, or the device length not being equal to the coupling length. Shorter coupling length can be obtained for strongly coupled waveguides, however the cross-talk gets worse, since the supermode coefficients become unequal due to the strong coupling between the guides.

The coupling length, L_C, of a directional coupler may be defined as

$$L_C = \frac{\pi}{\beta_e - \beta_o} \tag{5.17}$$

where β_e and β_o are the propagation constants of the even and odd supermodes.

The performance characteristics of MMI-based devices are also evaluated in this study. The MMI devices consist of a large multimode waveguide where the interference between the modes leads to well defined images of the exciting field at specific imaging lengths. In this simulation study, '*restricted resonance*' MMI couplers are used. In these restricted interference devices, the access waveguides are positioned at points $W/3$ and $2W/3$, where W is the width of the MMI, in order not to excite some specific modes in the device. By using the restricted resonance condition, the device length can be reduced by some threefold.

The beat length (L_π) of a MMI may also be defined as

$$L_\pi = \frac{\pi}{\beta_o - \beta_1} \tag{5.18}$$

where β_0 and β_1 are the propagation constants of the first and the second modes in the MMI section. Since the quadrature relationship of the propagation constants for the higher order modes approximately holds (Soldano 1995), at one beat length, most of the input power appears in the *cross state* and produces a *mirror-image* of the input. At twice the beat length, the power couples back into the *bar state* and gives a *self-image*. Here, at the output end, the bar and the cross states are defined as those ports which are directly opposite the input port and at equal distance from the symmetry plane respectively.

The FEM is used to calculate the propagation constants and the LSBR is used to calculate the excited modal coefficients. Once these excited modal coefficients are calculated, the composite field profile, **H** (x,y,z), at any axial position can be calculated using the expression 5.2. By coupling this field to the output access waveguides, the power in the bar and the cross states can be evaluated. For a specific device, the cross-talk, being the ratio of the desired to the unwanted outputs, can be calculated using the expression below :

$$\text{crosstalk (dB)}=10\log_{10}(P_b/P_c) \qquad (5.19)$$

where P_b and P_c are the power in the *bar* and the *cross* states respectively (In this case it is assumed that in ideal case all the power couples to cross state and no output is desired in bar state) .

5.10.2 Results of the Simulation

Figure 5.48 shows a schematic of an individual waveguide of a directional coupler section which can be fabricated using the *sol-gel* technique.

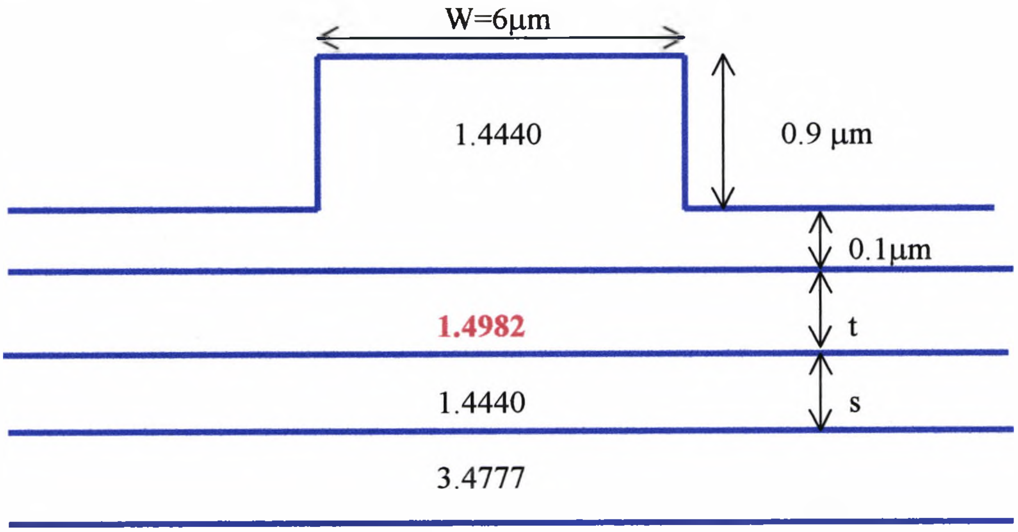

Fig. 5.48 Schematic of an individual guide as used in the directional coupler

The widths of the two identical coupled guides are 3μm and the separation, *S*, between them may be varied. The MMI structure simulated in this study is shown below in Fig.5.49,

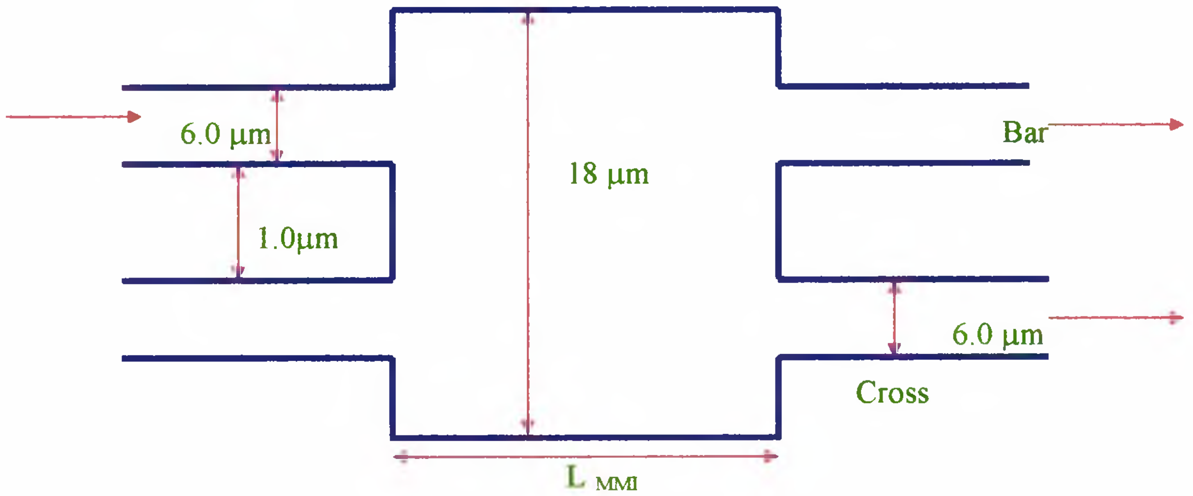

Fig. 5.49 Schematic of the MMI structure (top view)

consists of a large multimode waveguide section of width *W*, and input and output access waveguides which are of the same dimensions as the isolated waveguides of the directional couplers. The material index for the guide and substrate were taken as 1.4982 and 1.4440 respectively, at an operating wavelength of 1.55μm.

When the separation between the waveguides is increased, the coupling length (L_c) increases in the case of the directional coupler, whereas for the MMI, the beat length L_π (the length at which the power transfers to the cross-state) increases with the width of the multimode section. Fig. 5.50 shows the variation of the device length with the width of the MMI and the separation for the directional coupler. It can be seen that when the separation between the guides, *S*, is increased from 1 to 2.5μm, the coupling length ($L=L_c$) changed from 285μm to 637μm. In the design of compact photonic devices, the device length is an important parameter, and it can be seen that it is not only large but also more sensitive to the waveguide parameters for a directional coupler. It was shown in Fig. 5.50 that the device length can be reduced by reducing *S* or *W* for directional coupler or MMI-based devices, but however, in both the cases, the crosstalk is expected to increase.

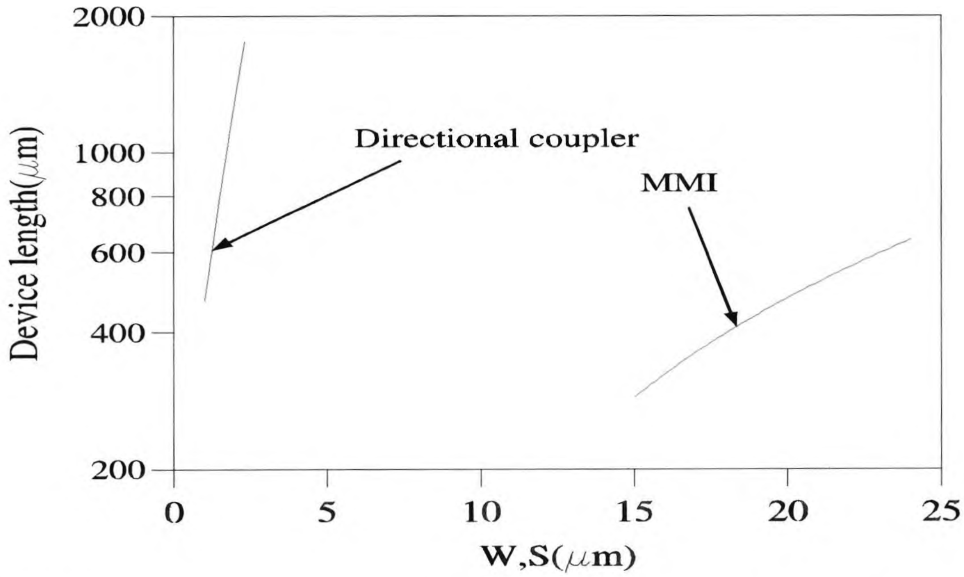

Fig. 5.50 The device length against the width of the MMI and the separation of the directional coupler.

The crosstalk in optical devices may be calculated using the power in the bar and the cross states, as defined by Eq. 5.18. To calculate this, first all the modes in the MMI section or the supermodes in the directional coupler section may be determined by using the FEM. Then the LSBR method is applied to calculate the excited modal coefficients at the waveguide interface. Once the modal propagation constants and the excited modal coefficients are calculated, the field profile along the axial direction can be evaluated by using Eq.5.2. Subsequently the power coupled to the bar and the cross states can be evaluated by reapplying the LSBR technique to find power coupled to a particular output waveguide. Figure 5.51 shows the variation of the crosstalk with the device length (*L*) for the MMI and the directional couplers.

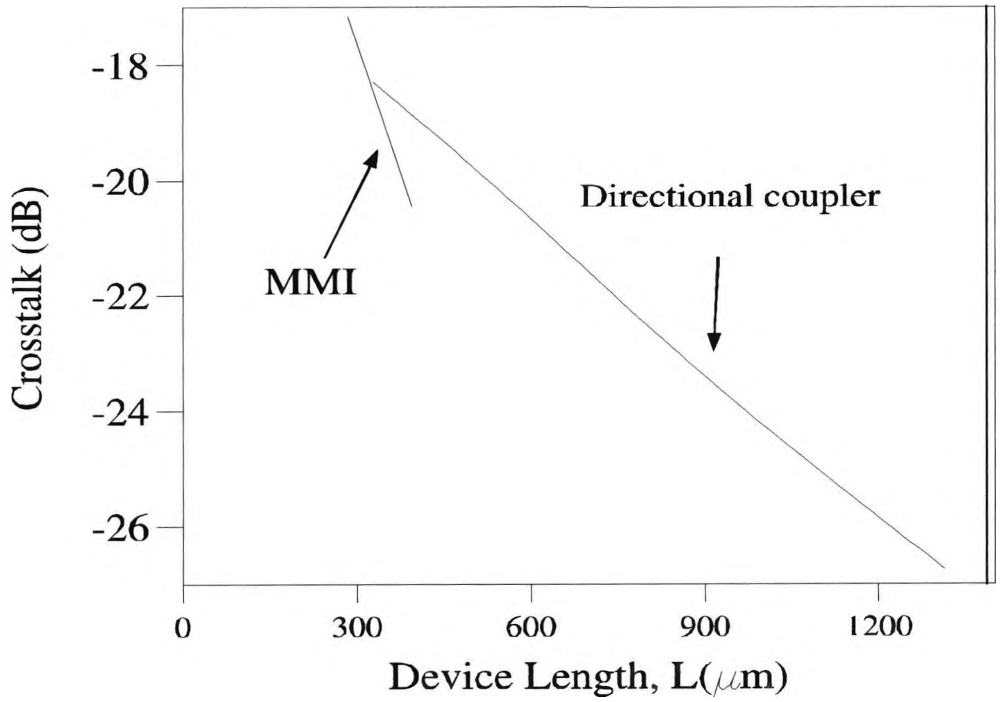

Fig. 5.51 The variation of the crosstalk against the device length for the MMI and the directional coupler.

It can be observed that for both approaches, the crosstalk can be reduced by considering a longer device length. However, for a specific crosstalk requirement, the device length will be shorter if the MMI approach is used, as compared to the use of directional coupler-based devices. It can be noticed from this figure that using the MMI approach, at half the device length as that of the directional coupler, the same crosstalk performance can be achieved. This is a very crucial issue, since it not only proves the value of the shorter device length but also it shows that the same crosstalk can be achieved at a much shorter device length, by using the MMI-based approach. This suggests that the MMI-based devices have a better cross-talk performance when compared to directional coupler-based devices.

In the optical fibre a fixed state polarization cannot be maintained. A knowledge of the polarization performance of these devices is important as most of the optical systems considered are strongly polarization dependent and do not recognize the polarization state of the incoming signal. The variation of the power transfer efficiency along the axial direction for the directional coupler, with a separation of 1.0μm, is shown in Figure 5.52.

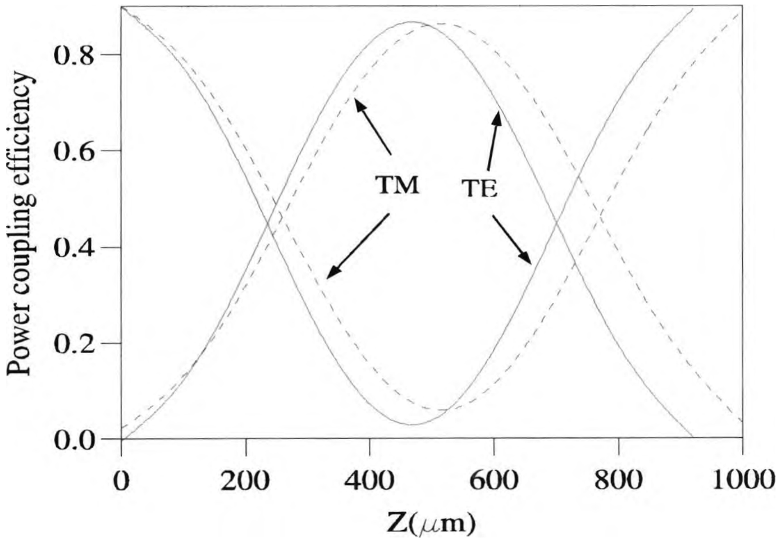

Fig. 5.52 The variation of the power transfer efficiency against the axial distance for both polarizations for a directional coupler with separation, S=1.0μm

Results are shown for both the polarizations, where solid and dashed lines indicate the TE and the TM polarizations respectively, whose coupling lengths were 467μm and 514μm respectively. At low separations between the guides, the excited coefficients of the two supermodes were slightly unbalanced and hence at the coupling length, a maximum of 86% of the input power transfer was coupled to cross-state for the TE polarization. However, at larger separations, the values of the excited coefficients become nearly equal and hence the maximum power transfer efficiency also increases, but however, the coupling lengths also increase. Even though the maximum power transfer is almost identical for both the polarizations, there is a difference of around 47μm in their coupling lengths. The power transfer efficiency is not very sensitive to the axial displacement, as it has been estimated that at an axial variation of ±140μm, the additional loss is only about 1 dB below its maximum value. At the TE coupling length, the TM power transfer is only 82% of the maximum for the TM polarization. When the device length equals to the coupling length for the TE polarization, *i.e.* at 467μm, the cross-talk for TE and TM polarizations are -16dB and -12dB respectively.

Similarly, the polarization dependence of MMI-based devices is also studied. Figure 5.53 shows the TE and TM power transfer curves for the MMI structure considered here. In this case there is only about 1μm difference between the beat lengths for these two polarizations, which represents only a 0.25% difference, whereas for a directional coupler, around 11% difference was observed.

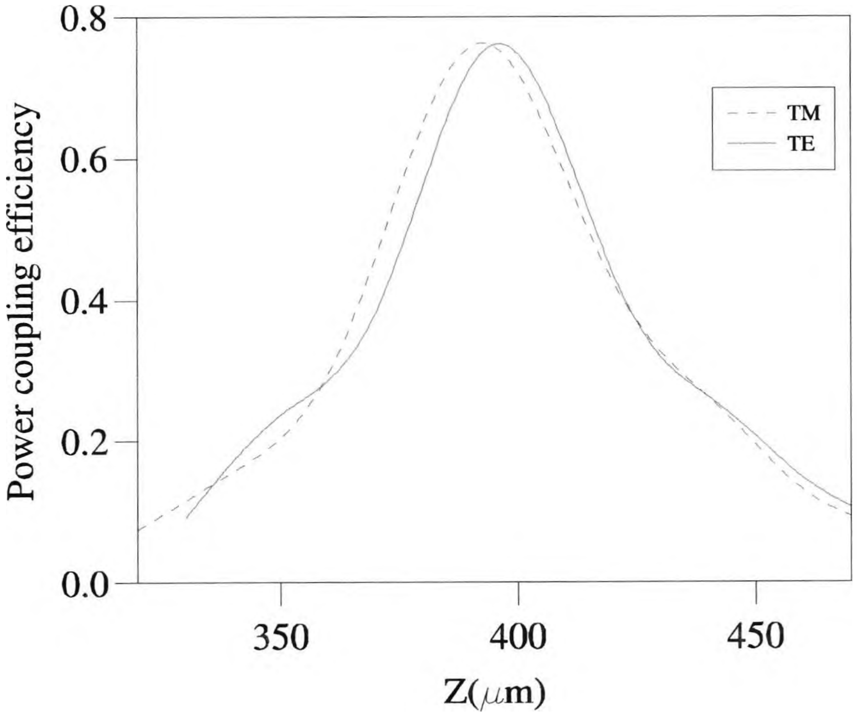

Fig. 5.53 Graph showing the power transfer efficiency for both the TE and the TM polarizations for the MMI.

In the case of the MMI device, again, at maximum, around 77% of the input power transfer is possible. Here the lower power transfer is due to a strong discontinuity at the beginning of the MMI section. It can be seen that the axial distance tolerance is about ±15 μm for the power transfer to be within 1dB of the maximum. Although the power transfer efficiency of an MMI-based design is more sensitive along the axial direction, when compared to the directional coupler-based design, however it is clearly shown for both the cases that tolerance in the device length is not an important issue. The extra loss for the TM polarization at the TE coupling length is only around 1%. This study shows that the MMI approach is almost polarization-insensitive whereas, by contrast, the directional coupler is highly polarization sensitive.

Since it may not be possible to fabricate exactly an ideally designed guided-wave structure due to fabrication tolerances, it is also important to study its performance degradation with any unwanted variation of the waveguide parameters.

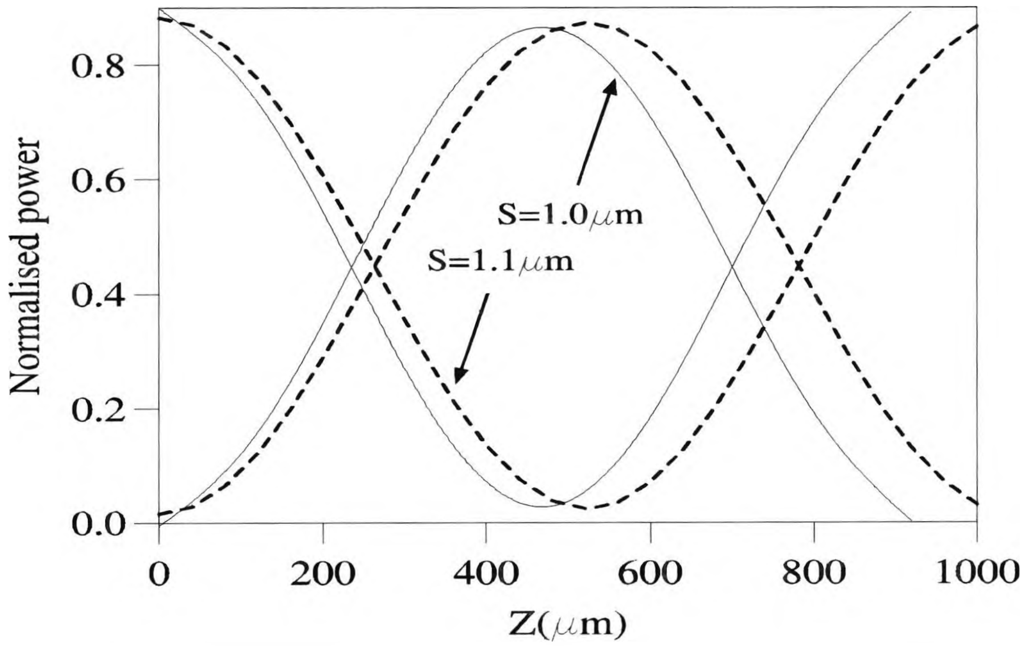

Fig 5.54 Graph showing the power transfer efficiency against the axial distance for S=1.0μm and S=1.1μm.

First the performance of the directional coupler with the change of separation between the waveguides is studied. The solid line in Figure 5.54 shows the performance of an ideal directional coupler section, with the separation between the guides, *S*, being 1.0μm for TE polarization. However, if during the fabrication process, this parameter is changed by only 0.1μm, it can be seen that the value of L_C increases from 467μm to 515μm (in percentage terms 11%).

The dashed line in Figure 5.54 shows the power transfer characteristics for directional coupler case when the waveguide separation, *S*, is increased to 1.1μm. Even though the increase in the coupling length is considerable the power coupling efficiency is almost similar for both the cases, due to the flatness of the output curve.

Similarly, Fig. 5.55 shows the power transfer characteristics for a MMI-based device when the width, *W*, is changed from its design width of 18μm. If the width is increased by 0.1μ m, which could occur unintentionally in the course of the fabrication process, only about a 5μm difference is seen in the beat length. The performance of the power transfer characteristics is almost identical for both the cases. This shows the fabrication tolerance of the MMI-based device could also be relaxed when compared to that of the directional coupler.

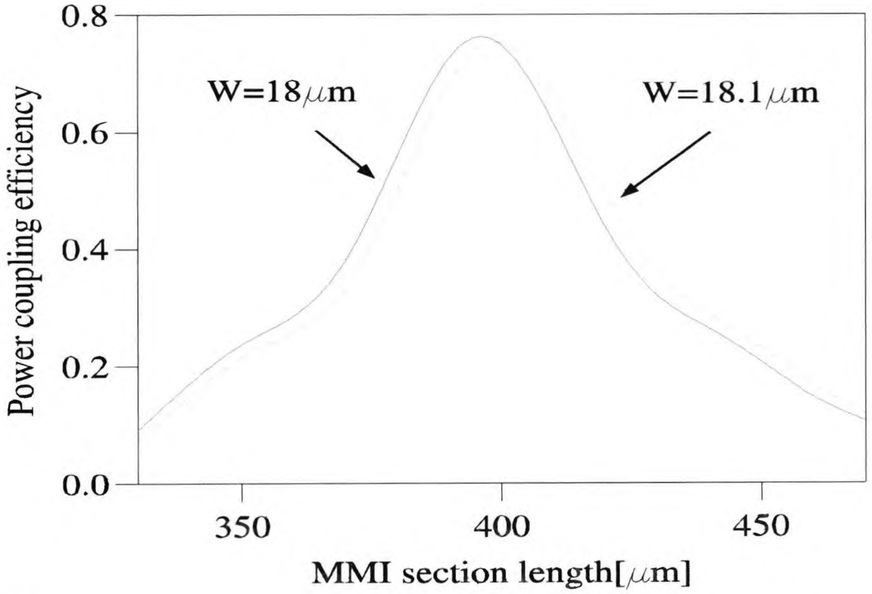

Fig. 5.55 The power transfer efficiency against the MMI widths of *W*=18μm and *W*=18.1μm

On the other hand, during the fabrication of a directional coupler section, the guide width can also be changed. If the widths of both the guides are increased or decreased, the overall effect may not be as detrimental to performance compared to the situation when only one of the guide widths is changed. This type of fabrication error will make the two guides non-synchronous and this effect has been studied.

The power transfer efficiency for this case, with non-identical waveguides, has been calculated. Fig. 5.56 shows the power coupling efficiency for different separations and for the case when the guides are non-identical.

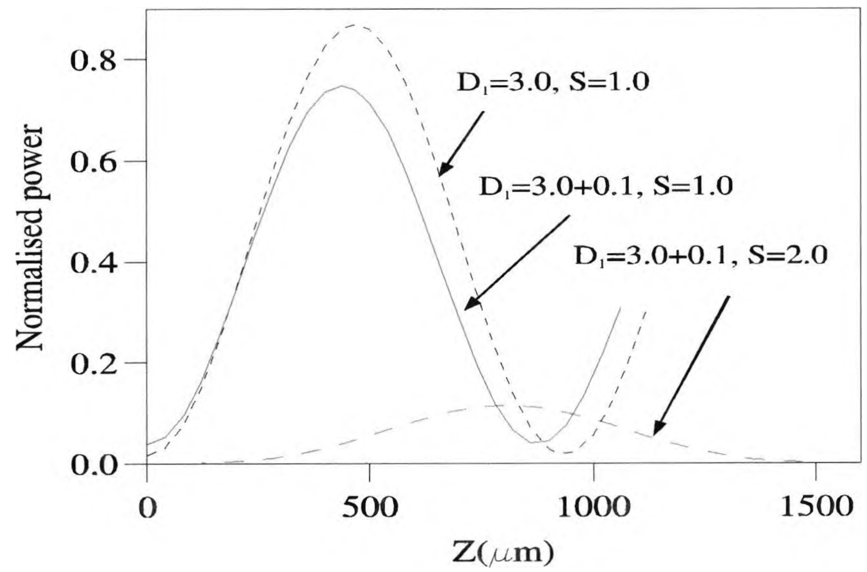

Fig. 5.56 The power transfer efficiency against the axial distance for a non-identical directional coupler.

The small dashed line in Figure 5.56 shows the variation of the power transfer along the axial direction, Z, when the guides are identical, as in case of an ideal design, with S=1.0μm. The coupling length was calculated as 467μm for the TE polarization, and it can be noticed from Fig. 5.56 that the maximum power transfer occurs at that position. However, due to fabrication tolerances, if one of them is made such that it is not identical, by a margin as low as 0.1μm, then the power coupling efficiency deteriorates by 10% due to the phase mismatching. However, the effect of phase mismatching is severe in the case of weakly coupled waveguides. The solid dashed line in Fig. 5.56 shows the power transfer when the guides are non-identical and when their separation, *S*, is 2μm. At this separation, the coupling length is 1309μm for the synchronous coupler, but however, a slight (0.1μm change) introduction of non synchronicity reduces this to a value of 885μm. However, as the guides are no longer phase matched, the coupling length is 68% of the ideal case and the maximum power transfer is now only about 10%, due to this lack of the phase mismatching. Figures 5.57a and 5.57b shows the even and the odd supermodes for a non-identical guide of separation 2μm.

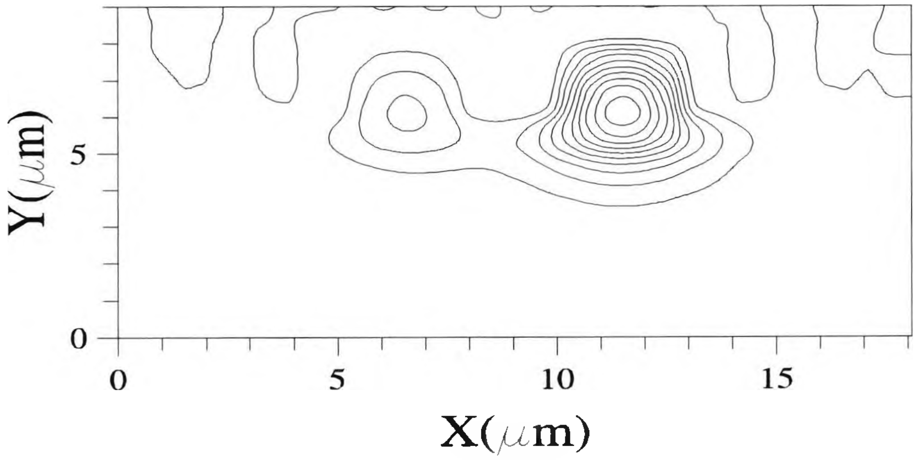

Fig. 5.57a Illustration of an even-like supermode of the coupled non-identical waveguides

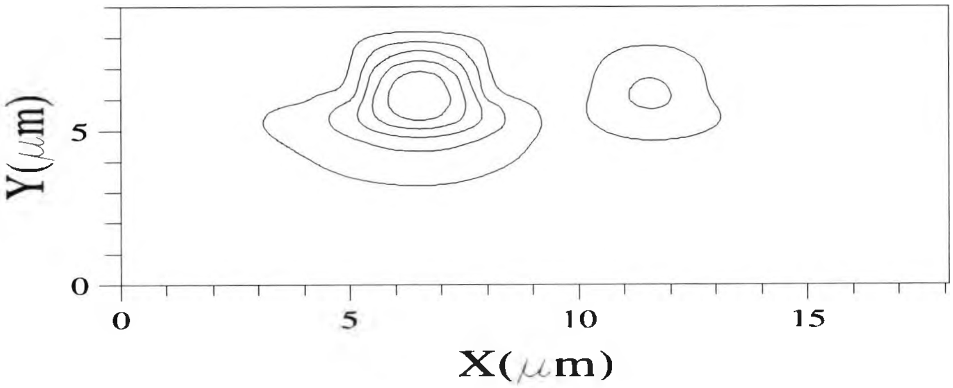

Fig. 5.57b Illustration of an odd-like supermode of the coupled non-identical waveguides

In this case, guide *b* is made non-identical by an increment of only 0.1μm in its width, so the widths of the left and right-hand guides are 3.0μm and 3.1μm, respectively. It can clearly be seen that for the even-like supermode (Fig. 5.57a), most of the power is confined in the right-hand side guide and for the odd-like supermode (Fig. 5.57b) most of the power is in the left-hand guide. These figures show the power imbalance in both guides. Hence the input wave will couple to the even and odd eigenmodes unequally in the coupling region, which would also lead to a high cross-talk value in the device. Although crosstalk for a directional coupler-based devices can be reduced by increasing the separation between the guides, however, this increases the overall length of the device. More importantly, the effect of fabrication tolerance can significantly deteriorates its performance for weakly coupled structures, particularly if the guides lose their phase synchronism.

5.11 Summary

In Chapter 5 the most important photonic device for optical routing/combining was discussed. The multimode interference couplers which is a special case of the directional coupler was shown in this chapter as a 3 dB power splitter, 1x4 was splitter and as a duplexer. The excited coefficients of the modes were calculated by using the LSBR and the overlap integral methods and the accuracy of the LSBR method has been demonstrated. The important design properties such as excess loss, imbalance, crosstalk, fabrication tolerance and polarization dependence have also been discussed for this structure. Finally a direct comparison was made on the important properties such as device length, crosstalk, fabrication tolerance and polarization dependence of directional coupler and MMI. This is the first time such a rigorous direct comparison is made on the performance of these two important devices. The directional coupler which is a very popular component in the photonic integrated circuits is very sensitive to the separation between the guides. However, the MMI is less sensitive to the width variation and can give a similar performance at a very shorter device length. The MMI is less sensitive to the fabrication tolerances compared to the directional coupler and is suitable for more compact photonic integrated circuits.

Chapter 6

Laser-Fibre-Coupling

6.1 Introduction

Tightly confined spot-sizes are generally required for the optimal performance of lasers, amplifiers, modulators, switches and transreceivers and the optical field profiles of these photonic devices are usually elliptical and small in size compared to larger and more circular field profile of a single mode fibre (SMF). This mismatch can cause 80% or more of the power loss if they are butt-coupled directly. As a result, a key issue in bringing optical '**fibre-to-the-home**' is low cost, efficient and reliable coupling for photonic devices to fibre-optic systems.

At the moment the most commonly employed technique is the use of slightly lensed fibres, however, this approach suffers from the need for tight alignment tolerances. Recently, monolithically-integrated tapered structures to expand the mode size of the photonic devices used, are increasingly being considered (Zengerle *et. al.*, 1996, Inaba *et al.*, 1997, Kawano *et al.*, 1997 and Lee *et al.*, 1997) to overcome this problem. In this work, the modal field profiles at the beginning and at the end of the taper are rigorously studied, to enable the development of optimized tapers. An expanded field profile at the end of the taper may be achieved by reducing the waveguide dimensions to operate near cut-off. The coupling efficiency of a spot size expander to a SMF is a critical function of device parameters as it operates near the cut-off regime, and herein the vector **H**-field based finite element method is used to study important design parameters of such devices. The Least Squares Boundary Residual method is also used to determine the coupling efficiency, alignment tolerances, and also the reflection coefficients in such systems.

This chapter covers the three most important techniques of interfacing: butt-coupling using a directional coupler section, mode conversion by a taper and also mode expansion by using a Multimode Interference based device.

6.2 Results from Tapered modal solutions

Mode shape expanders are being studied by various researchers (Brenner *et al.*,1993, Ghirardi *et al.*, 1994 and Hashimoto *et al.*, 1996).

Initially, the change of spot-size, with the waveguide dimensions, of a simple rectangular dielectric waveguide was studied. In this case it was assumed that the height of the guide was the same as the width. The guide and the substrate indices were 3.24 and 3.16 at an operating wavelength of 1.55μm. Figure 6.1 shows the variation of the spot size, defined as the e^{-1} values of the maximum field intensity (Buus *et al.*, 1994), with changing guide width.

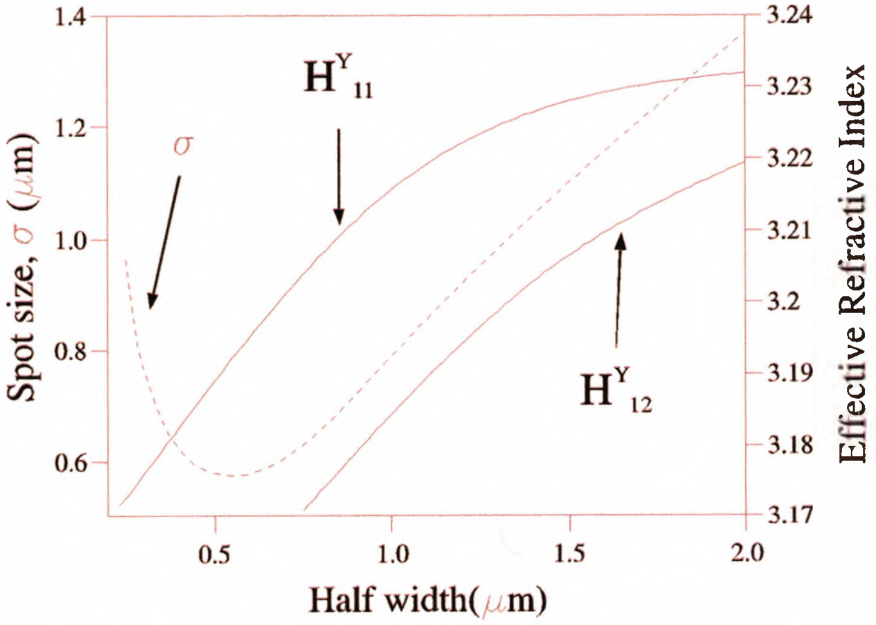

Fig. 6.1 Variation of the spot-size with the guide width

This figure also shows the effective refractive indices change with the core width for the fundamental and the second modes. It can be seen from Figure 6.1 that as the core width is reduced from 4μm to 1μm, the spot size (half-width) from the semiconductor laser gradually decreases but however, over the range from 1μm to 0.26μm, the spot size increases sharply as the fundamental mode approaches the cut-off. It can be seen that the effective index (β/k_0) of the fundamental quasi-TE (H^y_{11}) mode decreases monotonically with the reduction of the waveguide dimensions. It can also be noted that the second quasi-TE (H^y_{12}) mode can only be guided when the waveguide dimensions are larger than 1.6μm.

In the next example, a InGaAsP rib structure is considered, which is similar to the device studied by Motomi *et al.* (Motomi *et al.*, 1994)

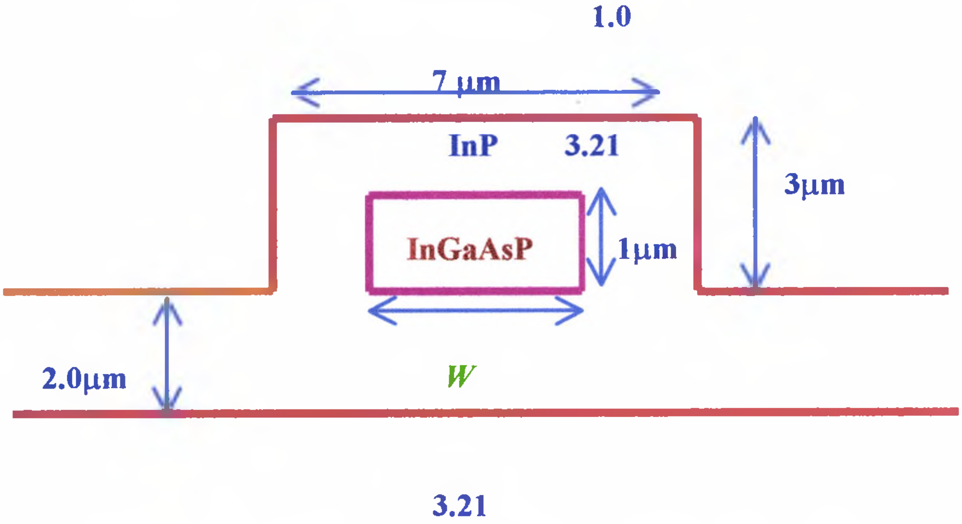

Fig. 6.2 Schematic of the rib structure simulated in this study

Fig. 6.2 shows the rib structure simulated in this study, of height 1μm with the width being varied. The active rib region is surrounded by InP of refractive index 3.21 and further surrounded by air. The refractive index of the guide and the substrate were 3.34 and 3.21 respectively. An operating wavelength of 1.31μm was used for this simulation. For a larger width of the rib, the modal field profile is predominantly confined in the rib region, but however with the further reduction of the width, as the fundamental mode approaches the cut-off, the field expands into the lower InP region just below the guide.

The H_y field profile for the fundamental H^y_{11} mode is shown in Fig. 6.3, when the rib width is 3.0μm.

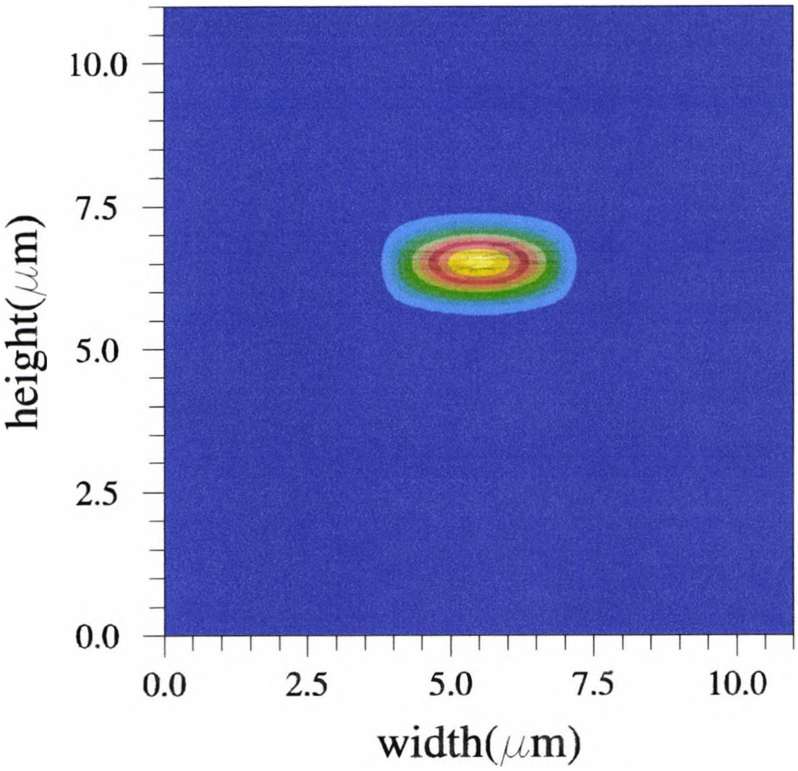

Fig. 6.3 Field profile of the fundamental H^y_{11} mode at W=3μm

From this figure it can be clearly noticed that the mode is highly confined in the rectangular InGaAsP core area. The elliptical shape of the mode shows the position of the waveguide core, due to the 3:1 aspect ratio of the core. Figure 6.4 shows the fundamental H^y_{11} mode field profile at a rib width of 1μm.

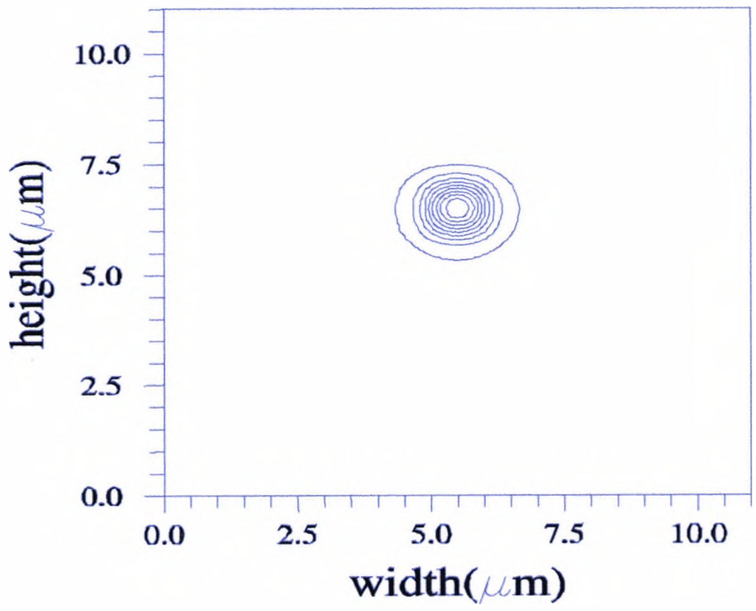

Fig. 6.4 Field profile of the fundamental $H^y{}_{11}$ mode at W=1μm

It can be seen that the elliptical mode shape has changed to a circular shape due to the 1:1 aspect ratio of the core. However, the spot size has reduced further and unsuitable to couple to a single mode fibre. A further reduction of the rib width can cause the mode to contract further. However, as the rib width is reduced even further the mode starts to expand. Fig.6.5 shows the H_y field profile for the fundamental $H^y{}_{11}$ mode at a rib width of 0.15μm. It can be clearly seen from Fig.6.5 that the field profile extends into the InP upper and lower cladding region and confined in the rib-shaped structure.

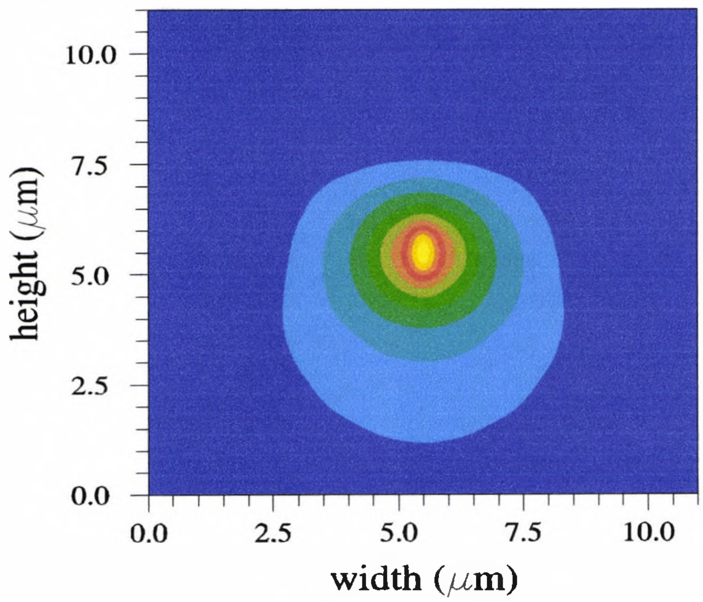

Fig. 6.5 Field profile of the fundamental H^y_{11} mode at W=0.15μm

The coupling loss between such a waveguide termination to a SMF is also calculated. In this case it is assumed that the full-width spot size of SMF is 8μm. The coupling loss between such rectangular or rib waveguides to a SMF is shown in Fig. 6.6 below.

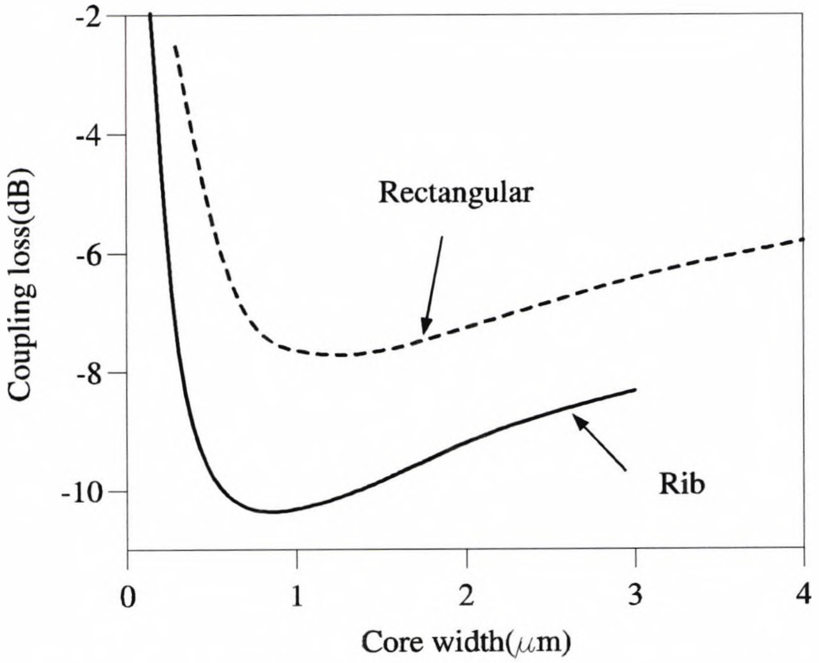

Fig. 6.6 Variation of the coupling loss with the core width

It can be observed that as the waveguide dimension is reduced, initially the coupling loss increases, but however, for smaller dimensions, the coupling losses decrease sharply as the spot size increases. At this point it should be noted that although the design approach using the simple method can predict an enhanced coupling efficiency, however, for a more accurate estimate of the coupling efficiency and the waveguide parameters, a rigorous numerical method based on a vectorial approach is necessary.

In the design of such devices, often the reflection of optical power has been ignored in the analysis presented by many workers. In a properly designed adiabatic taper, reflection along the tapered section may be negligible, but however, there will be a large reflected power at the final interface with the SMF. For many devices such as lasers or amplifiers, it is important to estimate the reflected power, however, many approximate approaches will fail to estimate correctly this important parameter.

The LSBR method can be used to estimate the reflected power of the input fundamental mode, and the variation of the reflection coefficient with waveguide dimensions is shown in Fig. 6.7

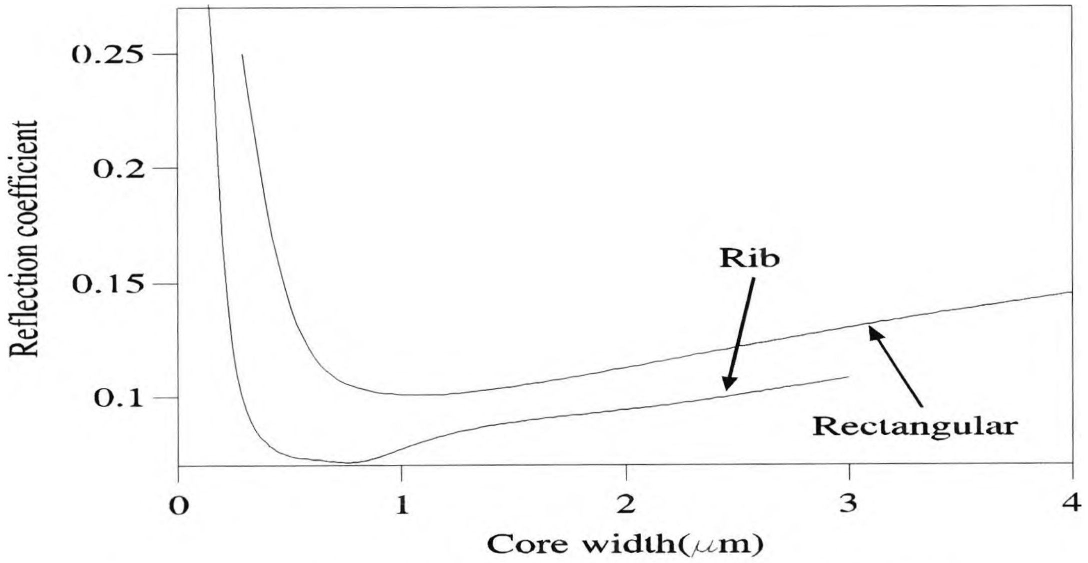

Fig. 6.7 Variation of the reflection coefficient with changing core width

It can be observed that with the reduction of core dimensions, initially the reflection coefficient reduces, but however, near modal cut-off, it actually increases, and this may be a feature which needs more studies, particularly in the simulations of lasers and amplifiers.

The effect of vertical misalignment is crucial in designing laser fibre couplers (Leaver and Pagiatakis, 1994). The effect of vertical alignment of the fibre can also be estimated, using the present approach and which is shown below in Fig. 6.8.

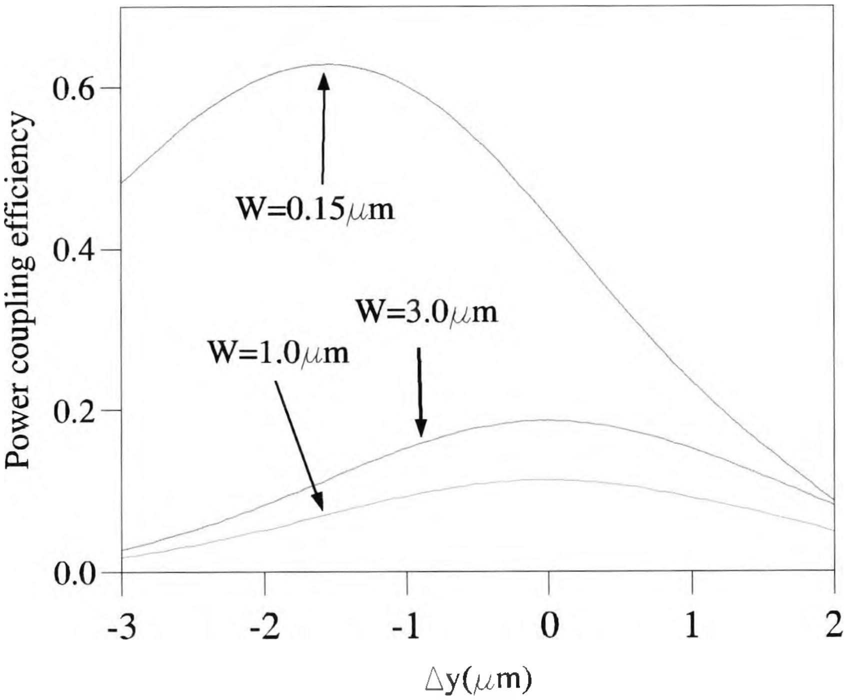

Fig. 6.8 Power coupling efficiency as a function of the vertical misalignment

It is assumed at the position Δy=0, the centre of the fibre is aligned to the centre of the upper inner guide core.

It can be seen from Fig.6.8 that for a guide width W=3μm, the maximum coupling efficiency is 20% when Δy=0, and this efficiency reduces monotonically as the fibre centre shifts from the centre of the rib waveguide core. It can be noticed that for a rib width, *W*=0.15μm, the spot-size increases as does the coupling efficiency. However, as the field profile of the rib waveguide expands in the lower substrate region, the fibre centre also needs to be shifted downward to achieve maximum coupling efficiency. At this rib width, the maximum coupling efficiency is around 61% compared to 20% when the width is 3μm. It can also be seen that by shifting the Guassian field profile by 2.0μm in the positive lateral direction reduces the maximum coupling efficiency as low as 12%. For the case when *W*=0.15μm the maximum coupling efficiency is around 49% for 1dB below the maximum. When *W* =3μm the coupling efficiency is around 15% for a 1dB range. When *W*=1.0μm there is around 9% power coupling over an axial displacement of 2μm at 1dB below the maximum value.

Thirdly, the modal solution of a twin guide structure is also considered, a schematic of which is shown in Fig. 6.9.

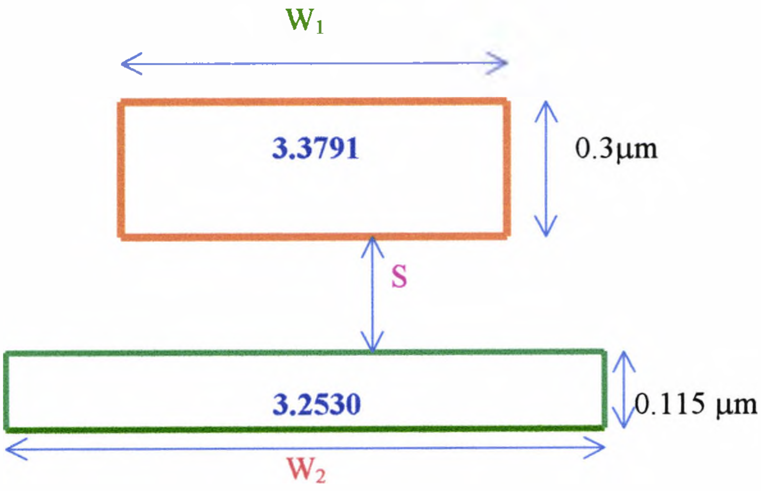

Fig. 6.9 Schematic of the twin guide structure

In this case the width of the lower guide (W_2) and the separation between the guides, *S*, can be adjusted to allow the spot size to expand vertically to optimise the coupling efficiency. In this structure the top and the lower guide indices were 3.3791, 3.2530 and the substrate index of 3.1416 was used at an operating wavelength of 1.55μm. The height of the upper waveguide was 0.3μm and the width (W_1) was varied. The height of the lower guide was 0.115μm and its width (W_2) was varied between 6-10μm to study the mode expansion. The separation, *S*, between the guides was taken as 1 μm. The H_y field profile for the fundamental H^y_{11} mode is shown in Fig, 6.10 for W_2=6μm.

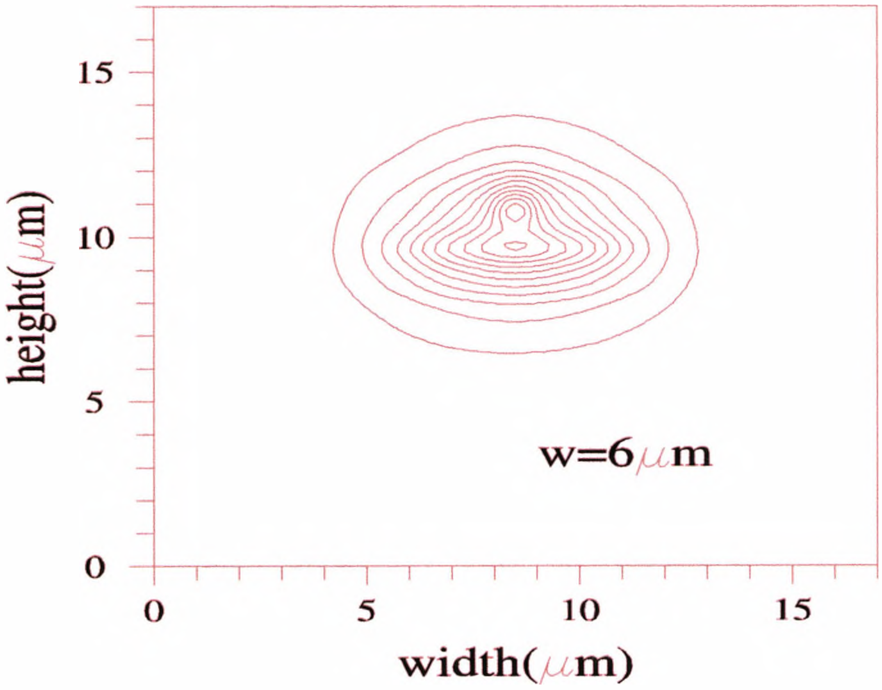

Fig. 6.10 Field profile of the coupled structure at W_1=0.25μm and W_2=6μm

This can also be described as a strongly coupled even-like supermode. For this type of design, the odd-like supermode is usually below the cut-off and will not be guided. With a smaller upper waveguide width, the width of the modal profile is essentially dictated by the width of the lower waveguide. Fig. 6.11 shows the expanded modal field profile of the coupled structure at W_1=0.25µm and W_2=8µm. It can be noticed from Fig. 6.11 that the field has expanded more in the horizontal direction. This could give a better coupling efficiency when coupled to a single mode fibre. Fig. 6.12 shows the field profile at W_1=0.25µm and W_2=10µm. Compared to Figure 6.11, Figure 6.12 shows further expansion. However, the rate of expansion here is very small compared to that between Figures 6.10 and 6.11.

Finally, the variation of the coupling efficiency with the vertical alignment to a SMF is also estimated and this is shown in Fig. 6.13. When the width of the upper guide is 1.2 µm and that of the lower guide is 6µm, the field is well confined. Thus by coupling that field to a SMF with 8µm spot size results in 6 dB coupling loss. However, our simulations shows that if the width of the upper guide is reduced to 0.25µm, then the field would have expanded considerably as the operating region is near cut-off and the coupling loss is only around 1.5dB. By increasing the lower guide width from 6µm to 10µm, the coupling loss can be improved by another 0.2dB.

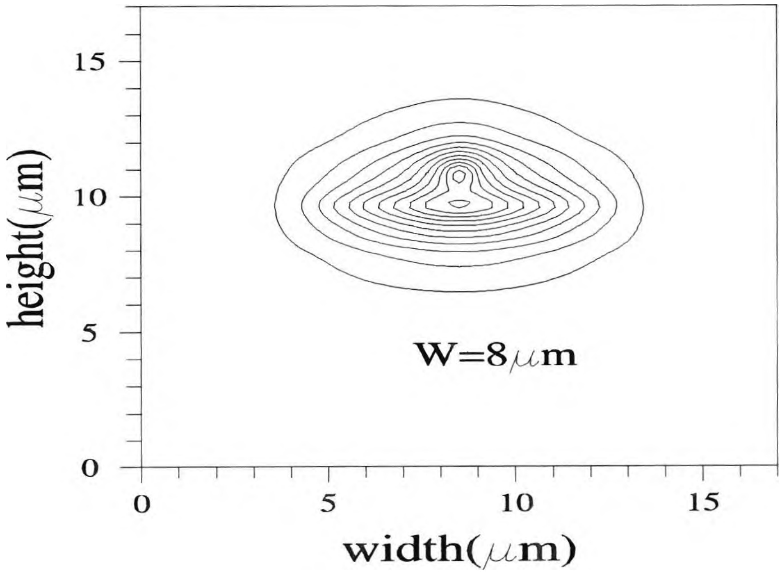

Fig. 6.11 Field profile of the coupled structure at W_1=0.25µm and W_2=8µm

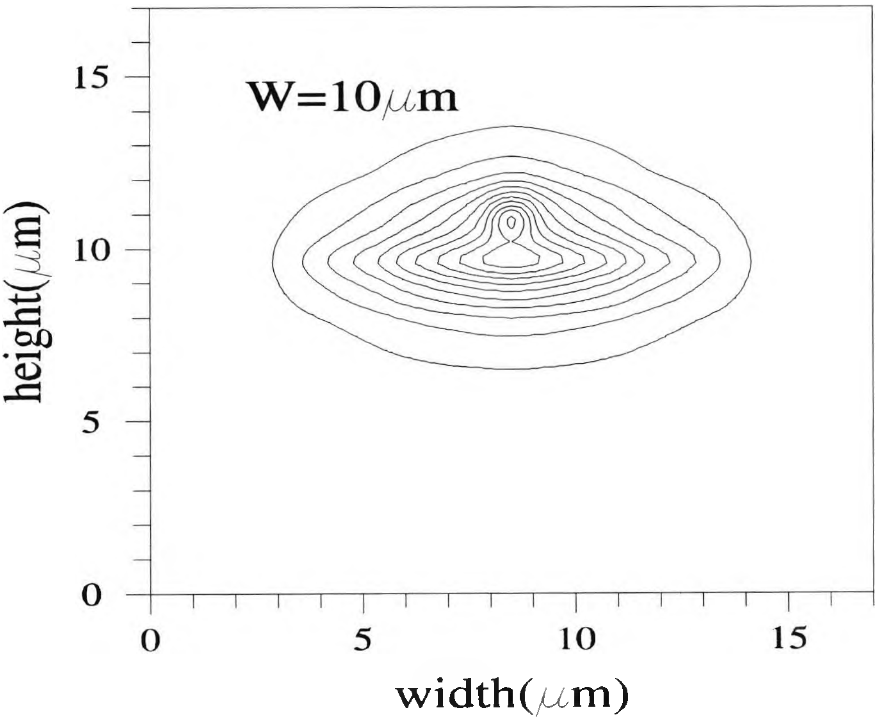

Fig. 6.12 Field profile of the coupled structure at W_1=0.25μm and W_2=10μm

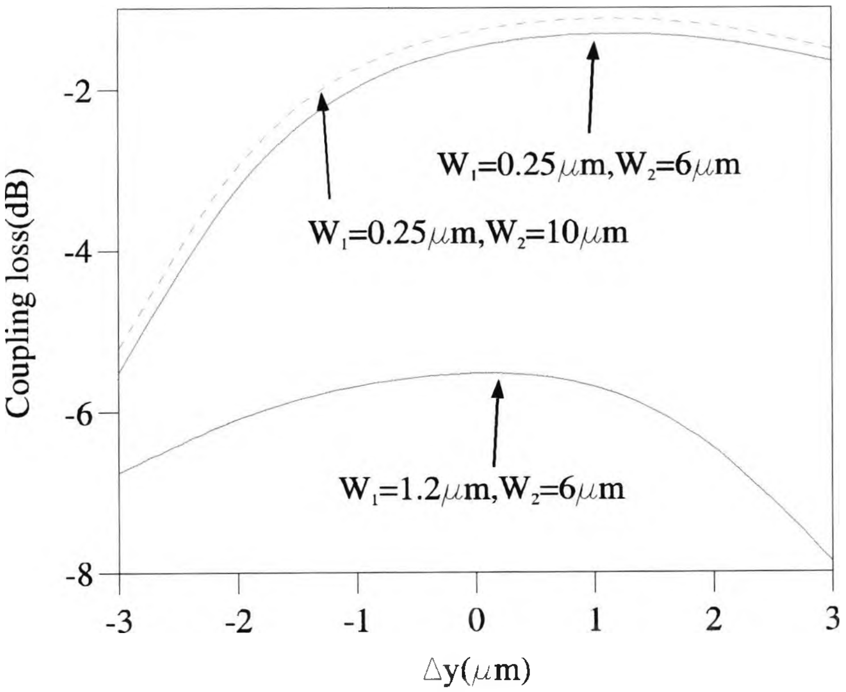

Fig 6.13 Graph showing the coupling loss as a function of the vertical misalignment

From Fig. 6.13 it can be noticed that as the guide width of the top guide is 1.2μm then the coupling loss is quite high. However as the width of the top guide is reduced to 0.25μm the coupling loss is reduced since the spot size has expanded. It can also be noticed that the effect of the lower guide on the coupling efficiency is small.

The field profile in the vertical direction can be adjusted with the separation between the waveguides, *S*, but however it should be noted that a weakly coupled nonidentical waveguide is very sensitive to the fabrication parameters.

6.3 Spot size transformation using synchronous directional couplers

Next, a novel approach to laser-fibre coupling is proposed, by introducing a synchronous directional coupler section between the laser and the fibre to change the spot-size for improved butt-coupling. If a directional coupler is phase matched then most of the power can be coupled from one waveguide to the other (Wongcharoen *et al.*, 1997). By using two nonidentical coupled waveguides which support spot-sizes similar to a laser and a fibre respectively which are at the same time phase matched, overall better laser-to-fibre coupling may be possible.

6.3.1 Results of the synchronous directional coupler spot-size transformers

Fig. 6.14 shows a schematic for the proposed enhanced butt-coupling between a laser and a fibre. Section I on the left-hand side represents a simplified strip loaded InGaAsP laser operating at 1.55μm wavelength.

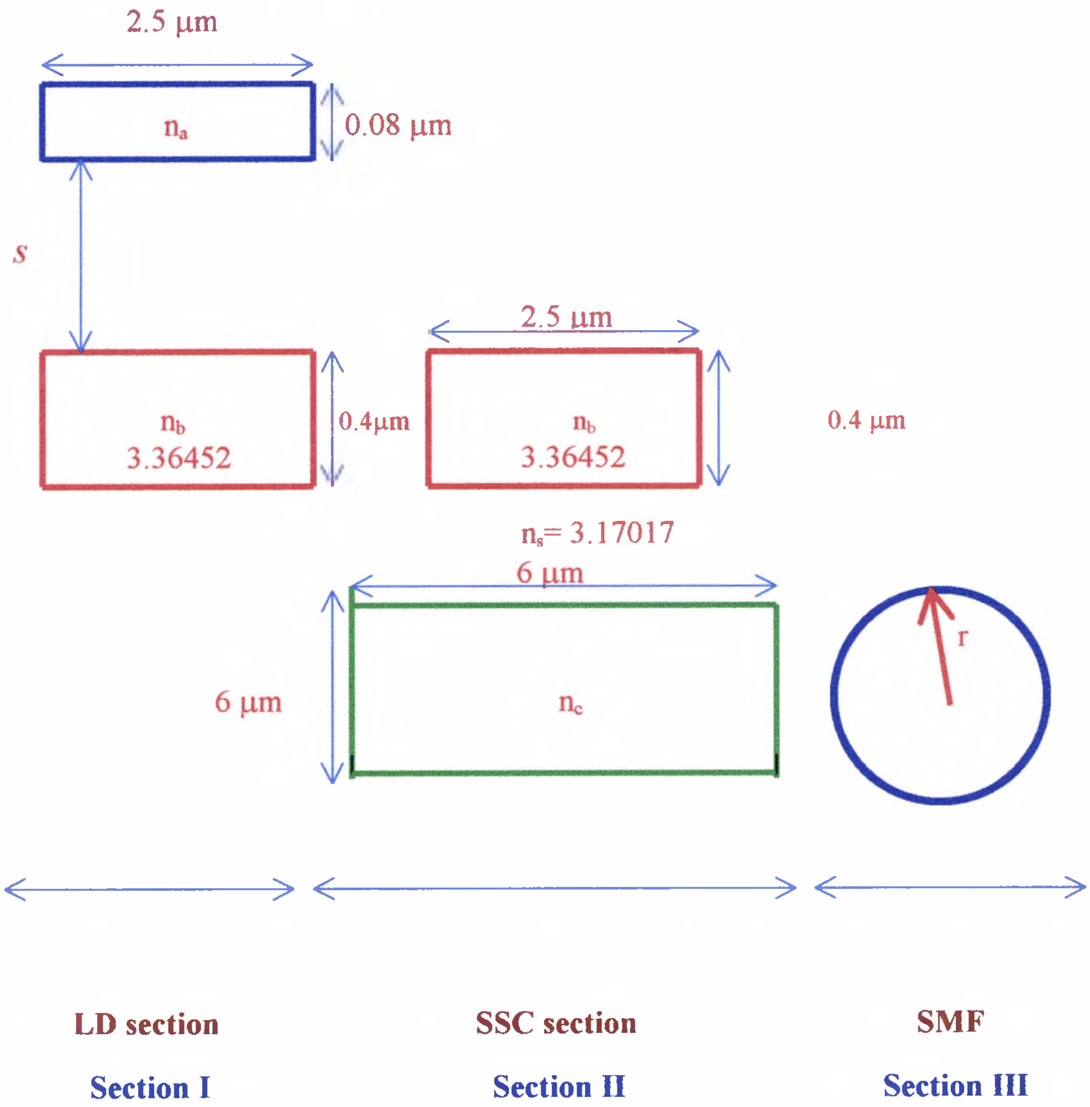

Fig.6.14 Schematic cross-section for a laser-to-directional coupler-to-fibre coupling

The height and width of the active region are 0.08µm and 2.5µm, respectively, close to a loading strip 0.4µm by 2.5µm, which is included in the structure for improved modal confinement. Section *II*, in the middle, represents a directional coupler incorporating nonidentical waveguides. The top guide is identical to the loading strip, to allow most of the power to be butt-coupled to this waveguide, but without the thin active region. In this example its refractive index, n_b, of 3.36452 was used. The smaller spot-size of this waveguide with higher asymmetry is not suitable for direct butt-coupling to an optical fibre with a much larger and circularly symmetric spot-size. However, if the top guide can be phased matched to a lower waveguide then most of the optical power butt-coupled to top waveguide at the beginning of Section *II* will couple to the lower waveguide. If the length of this directional coupler section is equal to the coupling length and the optical fibre aligned with the lower waveguide with a larger spot-size, then the overall power coupling can be improved. To show the validity of this approach for simulation purposes, a 6μm by 6μm square shaped lower guide was considered. In this example the phase matching is achieved by varying the refractive index of the lattice matched $In_{1-x}Ga_xAs_yP_{1-y}$ lower guide (n_c) by adjusting x and y (The calculation of the refractive indices are shown in section 5.4.1).

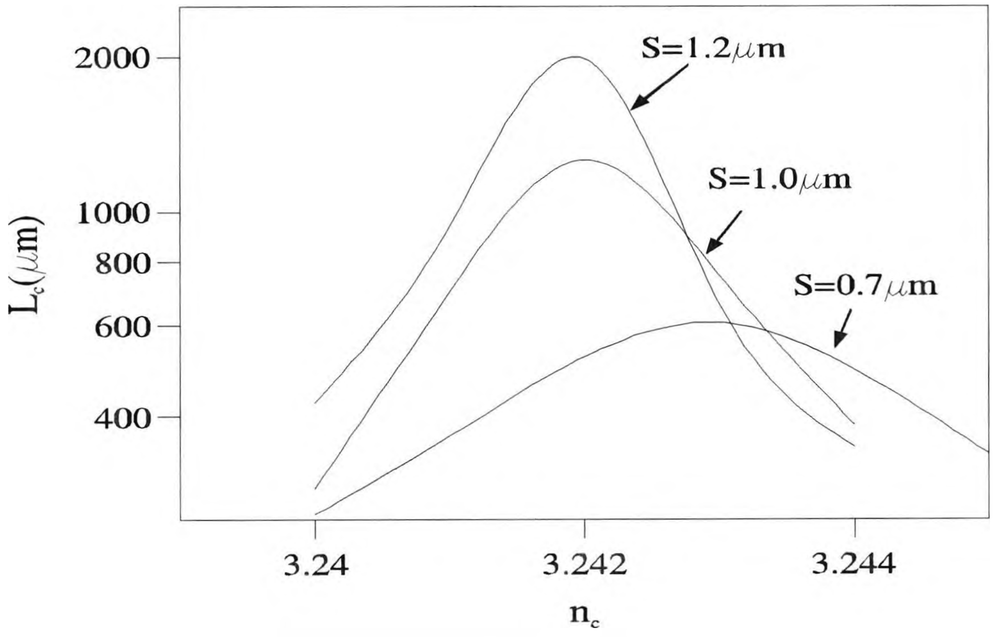

Fig. 6.15 Variation of the coupling length, L_c, with the lower waveguide index (n_c) for different separation distances, S.

The coupling length of the structure consisting of two nonidentical coupled waveguides is calculated by using the vector **H**-field finite element method. In this simulation study 3840 first order triangular elements were used. Since the structure is symmetric the two fold symmetry was exploited to increase the computational efficiency and the accuracy of the results. Figure 6.15 shows the variation of the coupling length, L_C, with n_C. When the guides are phased matched then the difference between the propagation constants of the two supermodes is a minimum, yielding the maximum coupling length. However, when they are not phased matched, although the coupling lengths are smaller, maximum power transfer will not be possible. The increased separation between the guides, *s*, will reduce the cross-talk but will also increase the overall device length.

Figure 6.16 Shows H_y field contours for the first and second supermodes in the transverse *x-y* plane of the directional coupler section by using the vector finite element method. when the separation distance, *s*=0.7μm. It can be observed from Fig. 6.16 (a) when n_C=3.244, as the guides are not phased matched, $\beta_b >> \beta_a$ and hence the first and second supermodes are mostly confined in the top waveguide or in the lower waveguide respectively. Similarly, it can also be noticed from Fig. 6.16 (c) when n_C=3.246, that the first and second supermodes are mostly confined in the lower waveguide or in the upper waveguide, respectively. For, *s*=0.7μm, the best phase matching is when $n_C \approx 3.2452$.

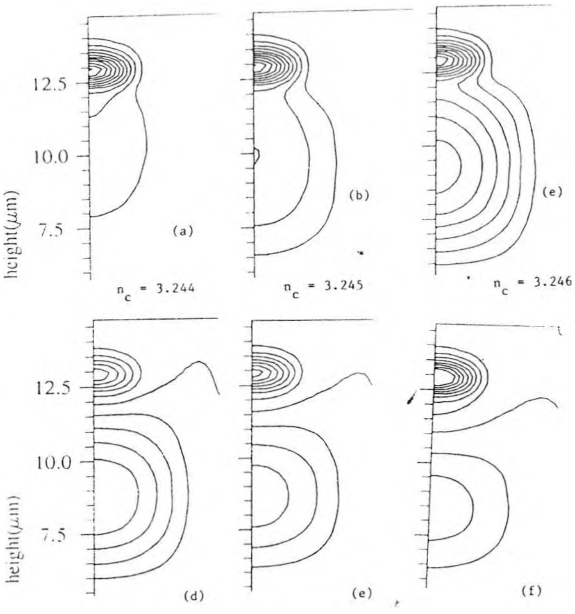

Fig. 6.16 The first and second supermodes field profiles for n_C, (a) 3.244, (b) 3.245 and (c) 3.246 respectively

From Fig.6.16 (b), for n_C=3.245 when the phase matching is better, it can be observed that for both the first and second supermodes, the power division between the two waveguides is nearly equal.

Next, the LSBR method is applied to find the coefficients of the first and second supermodes when the directional coupler section is butt coupled to the laser section. *B*1 and *B*2 are the modal coefficients of the two supermodes excited at the discontinuity plane.

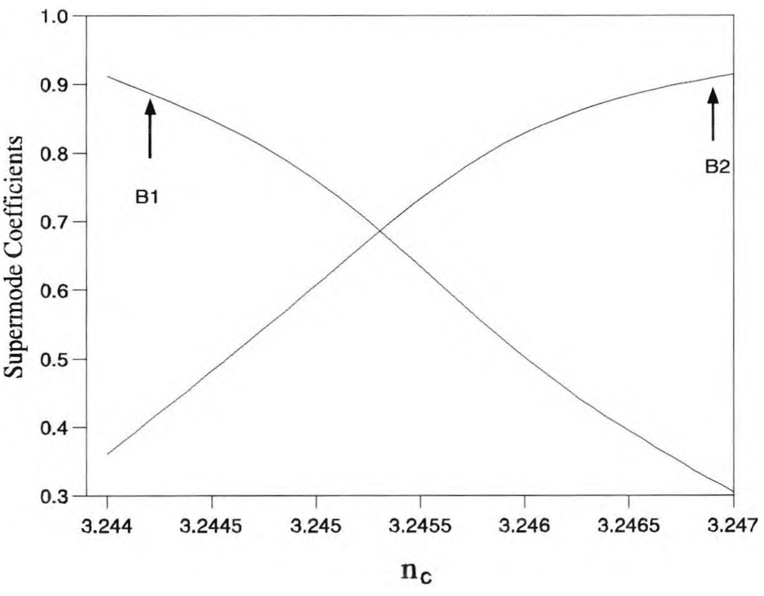

Fig 6.17 The supermode coefficients B1 and B2 with the guide index

Figure 6.17 shows the coefficients of the two supermodes with n_c, the lower guide index. B_1 and B_2 are the modal coefficients of the excited even-like and odd-like supermodes, respectively. It can be observed that when $n_c = 3.2434$, $B1$ and $B2$ are nearly equal to 0.7, and nearly a half of the power is carried by each of the supermode. At this index, when the incident power is launched into waveguide *b*, it excites two supermodes, with equal amplitudes, so at the beginning of the directional coupler section, the overall field amplitude adds in the waveguide *b*, but cancels out in waveguide *a*. However, as the refractive index moves away from the phase matching index, the power carried by each supermodes become unbalanced. For more weakly coupled waveguides, when *s* is increased, the coefficients of the two supermodes become unbalanced more rapidly with the index.

Figure 6.18 shows the H_y field profiles in the transverse planes at differential axial positions (*z*), when n_c=3.245. The modal field profile in the laser section is shown in Figure 6.18 (a). The optical field profile butt-coupled at the beginning of the directional coupler section is shown in Fig. 6.18 (b). The optical field profile coupled laterally to the lower waveguide at the end of the directional coupler, when $L=L_c$, is shown in Fig.6.18 (c).

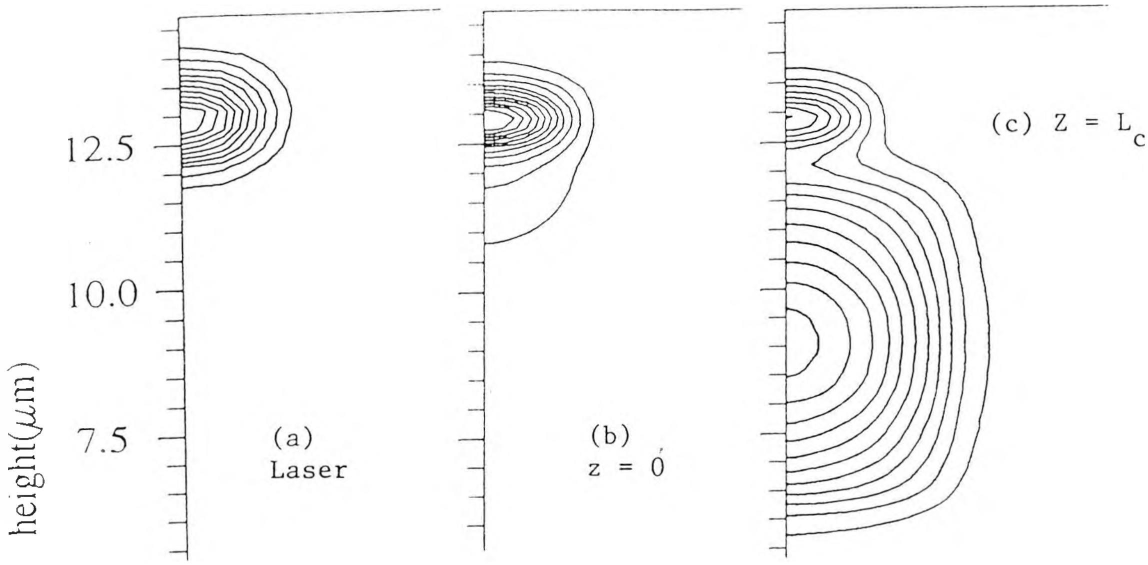

Fig. 6.18 The field profile at (a) laser section (b) at the beginning and (c) at the end of the directional coupler

It can be seen that at this stage most of the power is confined in the lower waveguide with a larger spot-size. The small amount of residual power left in the top guide can be reduced by adjusting the value of n_c more accurately and also by increasing the separation between the waveguides to reduce the cross-talk: however, in this case, the device length will also be longer. The overall transmission (τ) for direct laser-to-fibre (L-F) and for laser-to-directional coupler-to-fibre (L-D-F) section are given in Table 6.1.

n_c	L_c	B_1	B_2	$B_1^2+B_2^2$	τ(L-F)	τ(L-D-F)
3.244	453.99	0.90826	0.36178	0.9558	0.51892	0.6085
3.245	637.24	0.76704	0.60039	0.9488	0.51892	0.8258
3.246	573.28	0.49436	0.83333	0.9388	0.51892	0.7193

Table 6.1 : Transmission coefficients for direct laser-to-fibre couplings and laser-to-directional coupler-fibre.

In this example the combined laser-to-directional coupler-to-fibre transmission loss is only 1.7dB compared to 7.8dB for direct laser-to-fibre coupling. Since the spot size expander section has expanded the field it matches better with the circular fibre field profile. Even though it is possible to expand the laser field by using a taper, the taper approach suffers from tight alignment tolerances.

6.4 Multi-guide directional couplers for spot size expansion

In optical fibre applications, the use of a multi-guide directional coupler as a spot-size expander is studied in this section. Initially a one dimensional three guide structure is studied to validate our numerical tools. The technique is further developed to study two dimensional three and five guide directional coupler based spot size expanders. In this study their coupling efficiency and vertical misalignment tolerances are also studied.

6.4.1 Simulation results for the 1-D waveguide

In this section the laser-fibre coupling principle is explained in more detail. Initially a planar structure as shown in Fig. 6.19 is taken into consideration. The refractive index of the guide is 3.5 and that of the substrate is 3.17 at an operating wavelength of 1.55μm. Fig 6.19 (b) shows the planar equivalent of the optical fibre.

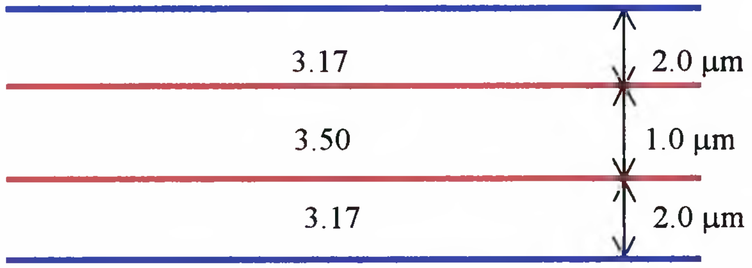

Fig. 6.19 (a) Schematic of the planar waveguide

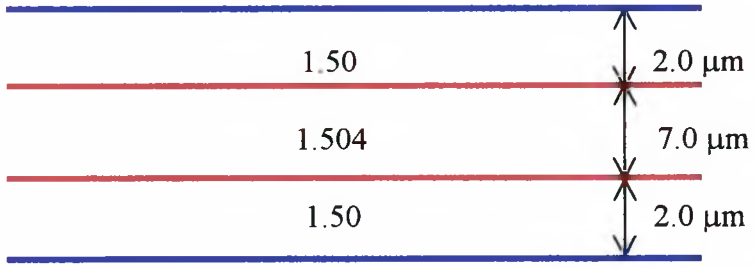

Fig. 6.19 (b) Schematic of the planar equivalent of a optical fibre

The refractive index of the guide was 1.504 and that of the substrate was 1.5 at an operating wavelength of 1.55μm for the fibre case. The equivalent width of the fibre was 7μm. Figs. 6.20 (a) and 6.20 (b) show the fundamental field profiles of the planar guide and the fibre equivalent. It can be seen from these figures that the field profile of the planar structure is very narrow compared to the field profile of the fibre. Since the diameter of the fibre is reasonably large the spot size of the fibre is large. Therefore if a direct coupling is performed then the coupling efficiency will be very low.

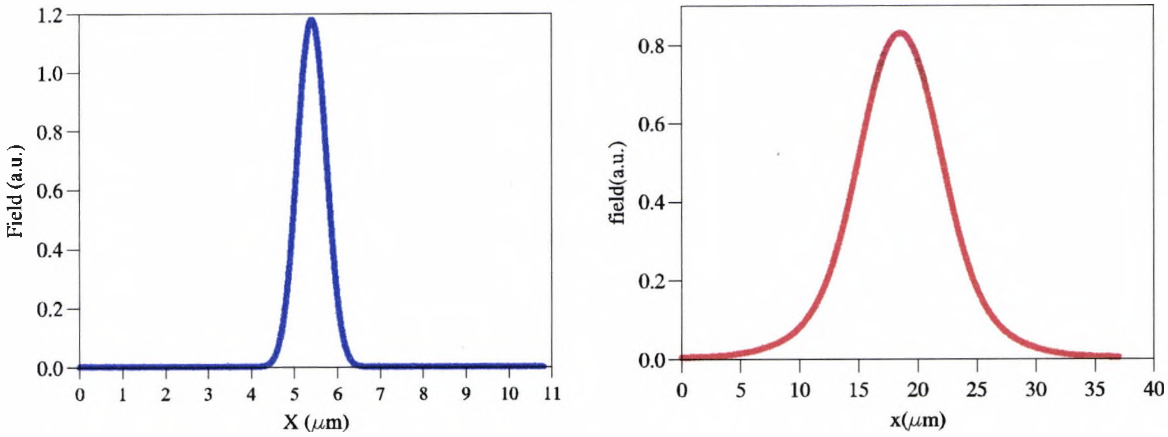

Fig. 6.20 (a) H_y field profile of the planar guide (b) H_y field profile of the fibre equivalent

Next, a three guide planar directional coupler is studied. The schematic of the structure is shown in Fig. 6.21 below. Here a semiconductor laser, at the input of a multimode waveguide, with a guide index, n_g=3.5, a cladding index, n_s=3.17, and a guide thickness of 0.15μm, operating at a wavelength of 1.55μm, was considered in this simulation.

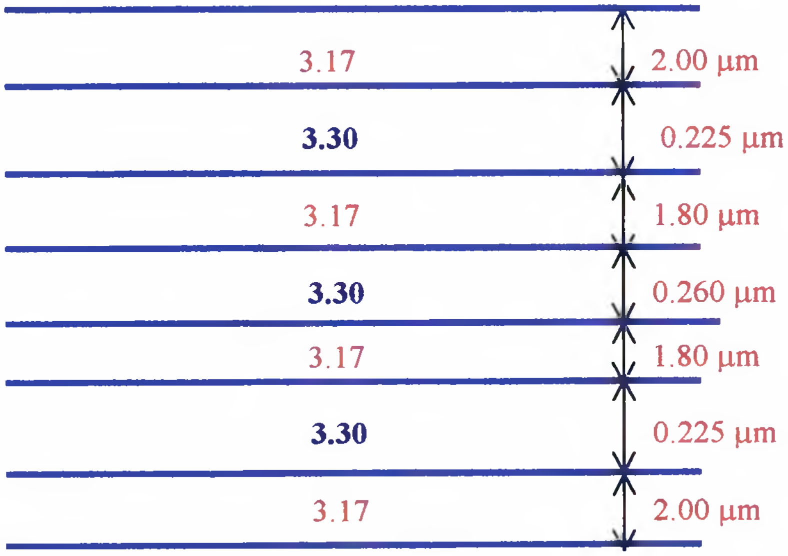

Fig. 6.21 Schematic of the planar three-guide directional coupler

The finite element method was employed to calculate the propagation constant and the field profile of this waveguide section. In this work, the half-width spot-size (HWSS) is defined as the distance from the field maximum position to the position where the field strength is 60.65%. The HWSS of the input laser is calculated to be 0.25μm.

A typical circular fibre is approximated to a symmetrical one-dimensional slab waveguide, with its core and the cladding indices of 1.504 and 1.5 respectively, and its equivalent width being 7.0μm. The HWSS for this equivalent fibre is 3.625μm, much larger than the laser profile, resulting in a significant signal loss, if they are simply butt-coupled.

In order to overcome this power loss, a directional coupler using a three-core-waveguide in close proximity is introduced (Buus *et al.*, 1994 between the laser and the fibre to expand the spot size for better power coupling. In order to obtain spot size conversion with maximum power transfer, a structure is required which transforms the input field, confined in the central waveguide, to a field at the output position, which has the correct amplitudes and phases over all the three waveguides. The spot-size converter considered here is composed of three guides, in which two of the outer guides are of the same dimensions and the middle guide is of different size. The refractive index of the guide, was given by n_g=3.3, and it was surrounded by a cladding of index 3.17. The thickness of the two outer guides was set to be 0.225μm and that of the centre guide was 0.26μm. The separation, *S*, between them was considered to be 1.80μm.

The finite element method was used to calculate the propagation constants and the field profiles of the supermodes of this three-guide structure and also of the input and output waveguides. In this case, the first and the third supermodes, TE_0 and TE_2, are symmetric, whereas the second supermode, the TE_1, is antisymmetric. The corresponding field profiles are shown in Fig. 6.22. Following that the LSBR technique was used to calculate the coefficients of the supermodes generated at *z*=0μ m, the laser-to-directional coupler junction.

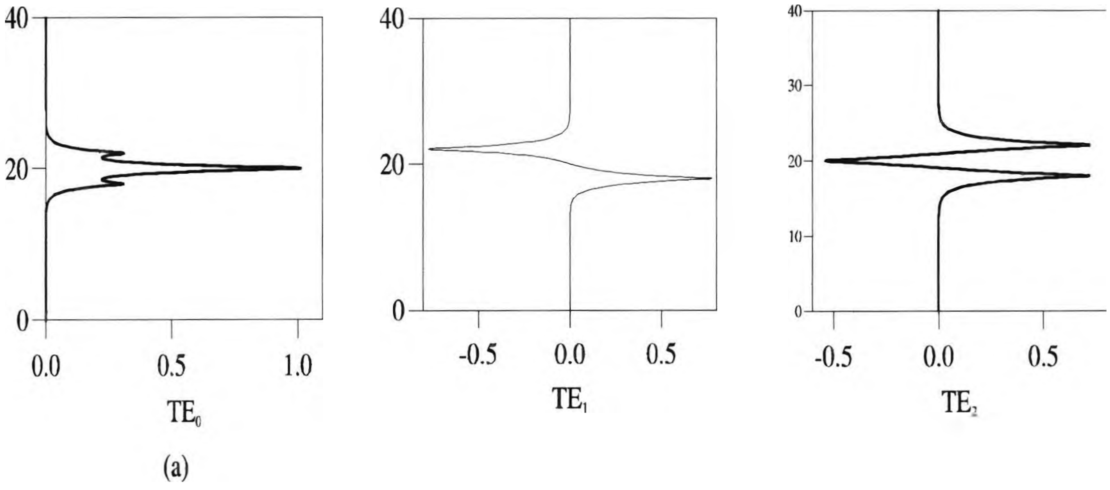

Fig. 6.22 (a) The field profiles of (a) TE_0 mode (b) TE_1 mode and (c) TE_2 mode

In this case the coefficients of the TE_0, TE_1 and TE_2 supermodes are 0.88546, 0.37962E-7 and 0.39256 respectively. Since the complete structure is symmetric and also the incident field profile, so no antisymmetric modes are expected to be excited and a small coefficient for the TE_1 mode proves this point numerically.

At the beginning of the directional coupler section (DC), at *z*=0μm, the superposition of the three supermodes, all in phase, generates a field profile similar to that of the laser section, to satisfy the necessary boundary conditions. However, since the propagation constants of the supermodes are different, due to the relative phase differences between the supermodes, the overall field profile along the axial distance will not be constant. Figures 6.23 (a) and 6.23(b) shows the evolution of the lateral field profile along the axial direction.

As the two symmetric supermodes propagate along the directional coupler section, the fields in the two outside guides start to increase due to their relative phase difference. This clearly demonstrate that as the side lobes start increasing, the amplitude of the field in the central guide is decreasing in the same proportion, showing the overall field

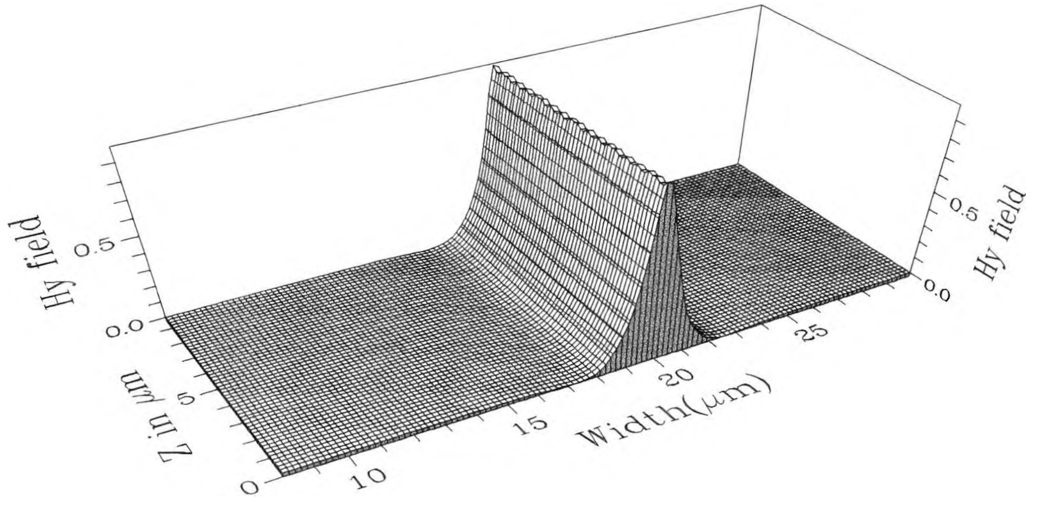

Fig. 6.23 (a) Plot showing the evolution of the lateral field profile along the axial direction from z =0 –10 μm

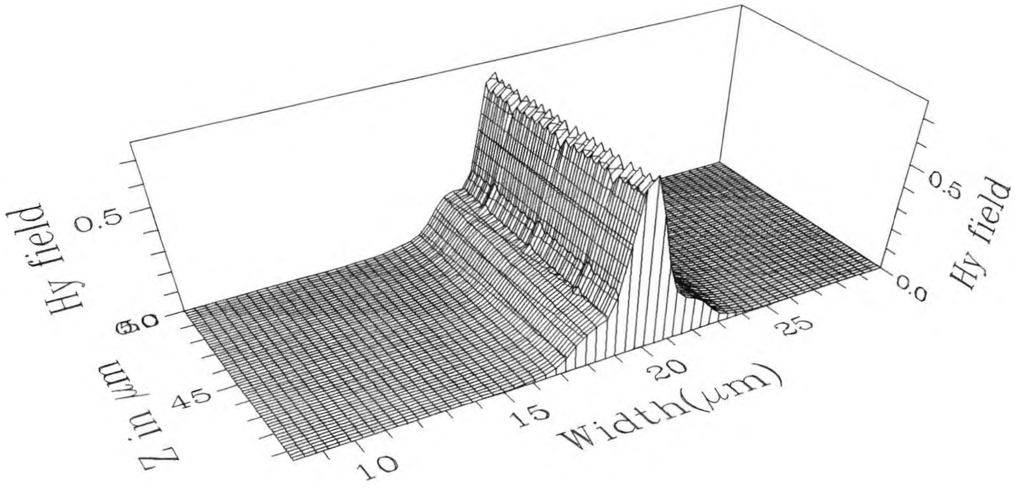

Fig. 6.23 (b) Plot showing the evolution of the lateral field profile along the axial direction from z =40 –50 μm

distribution is spreading to increase the spot-size. Since the coefficient of the TE_1 mode was negligible, the two dominant supermodes, the TE_0 and TE_2, attain a 180 degree phase difference at a beat length, L_b=99.1μm ($L_b = \dfrac{\pi}{\beta_0 - \beta_2}$).

The composite field profile at this location is shown in Figure 6.24 below. It can be seen from Fig. 6.24 that the composite field profile is almost similar to the fundamental mode of the directional coupler section (Fig. 6.22 (a) apart from a slight increase in the side lobes due to the contribution from the third mode.

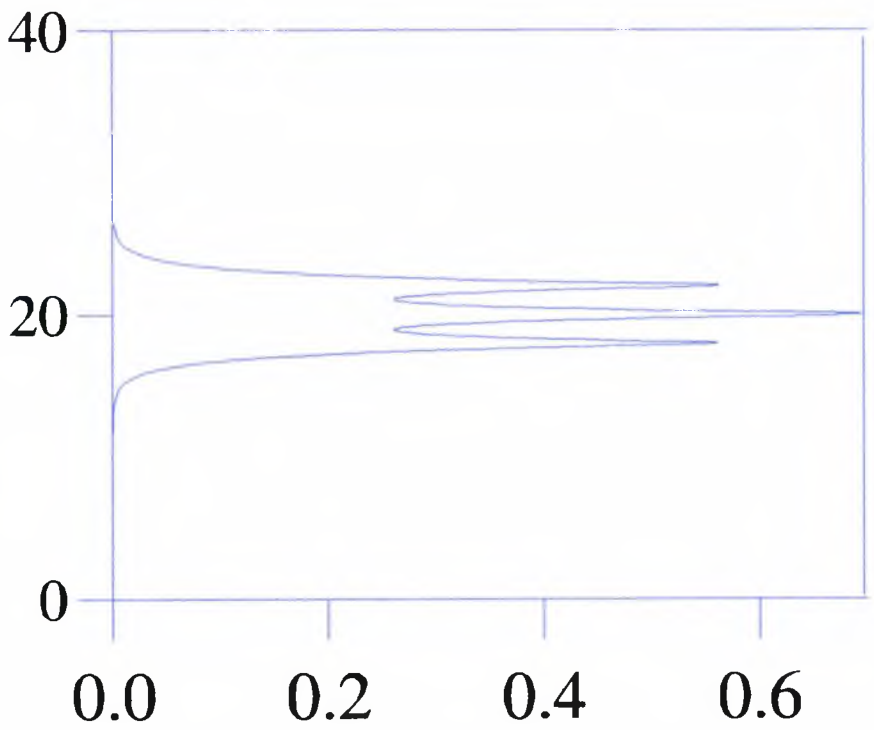

Fig. 6.24 Composite field profile at *z*=99.1μm

Around this axial distance the field has expanded considerably compared to the input field at *z*=0μm, which can be more effectively coupled to a SMF.

Figure 6.25 shows the variation of the power coupling of the composite field along the axial distance.

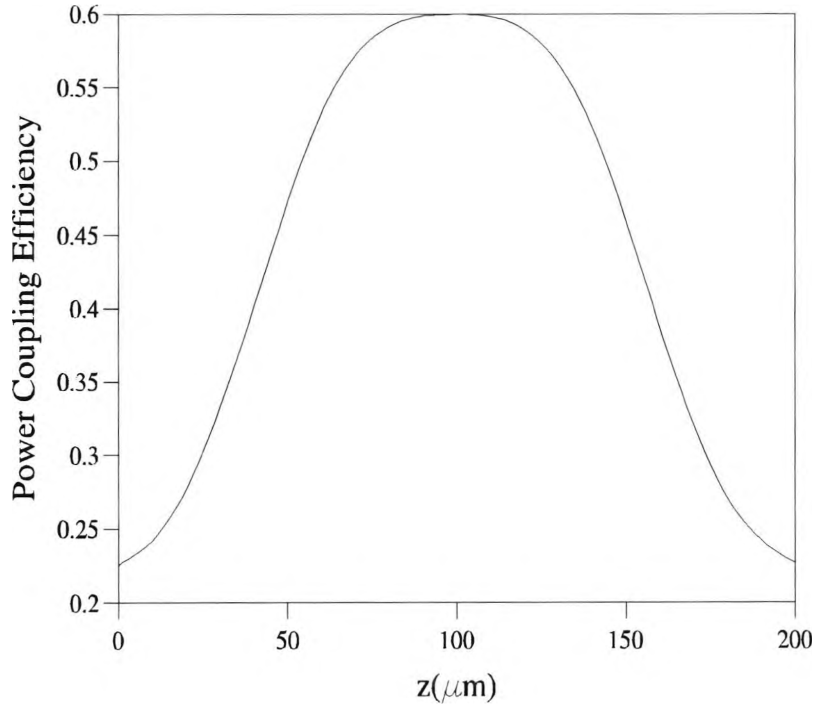

Fig. 6.25 Variation of the coupling efficiency with axial distance (*z*)

It can be seen from this curve that the direct laser-to-fibre power coupling is around 23%, shown at *z*=0μm. The power coupling efficiency can also be calculated analytically using the expression below (Haibara *et al.*, 1983) :

$$\text{Power coupling efficiency} = \frac{4(W_2^2)(W_2^2)}{(W_1^2 + W_2^2)^2} \qquad (6.1)$$

where W_1 and W_2 are the spot sizes of the semiconductor laser and the SMF respectively. A coupling efficiency of 19%, obtained by using the simple analytical expression above Eq.6.1, under estimates the more rigorous calculation by 20%. The analytical expression may be valid for the Guassian field profile, however, the actual field profile is not Guassian most of the time. And this may be the reason for the slight difference in the results. Besides the inaccuracy, the analytical expression cannot be used to estimate the coupling efficiency for the composite field profile along the directional coupler section. As the field propagates further along the length of the directional coupler, at around 100μm, its three peaks nearly follows a Gaussian profile. At this axial position a coupling efficiency of 60% can be achieved. This is nearly three times that achieved when compared to the direct laser-fibre coupling. The location of the maximum power coupling also nearly agrees with the beat length for the first two symmetric supermodes. The result indicates that the use of an intermediate directional coupler section can improve the power coupling efficiency by 5dB, which is a considerable advantage. Figure 6.25 also demonstrates that around 200μm (*i.e.* twice the beat length) the efficiency is similar to that at z=0μm. At this distance, two symmetric supermodes are again in phase and the overall field will be similar to the input field profile. In this one-dimensional simulation 1100 mesh points were used and the CPU time is around 3 minutes to generate all the field values on a SUN Classic workstation.

6.4.2 Simulation results for 2-D three-guide directional coupler based spot-size expander

Next, a directional coupler with two-dimensional confinement is considered and the schematic of the structure is shown in Figure 6.26

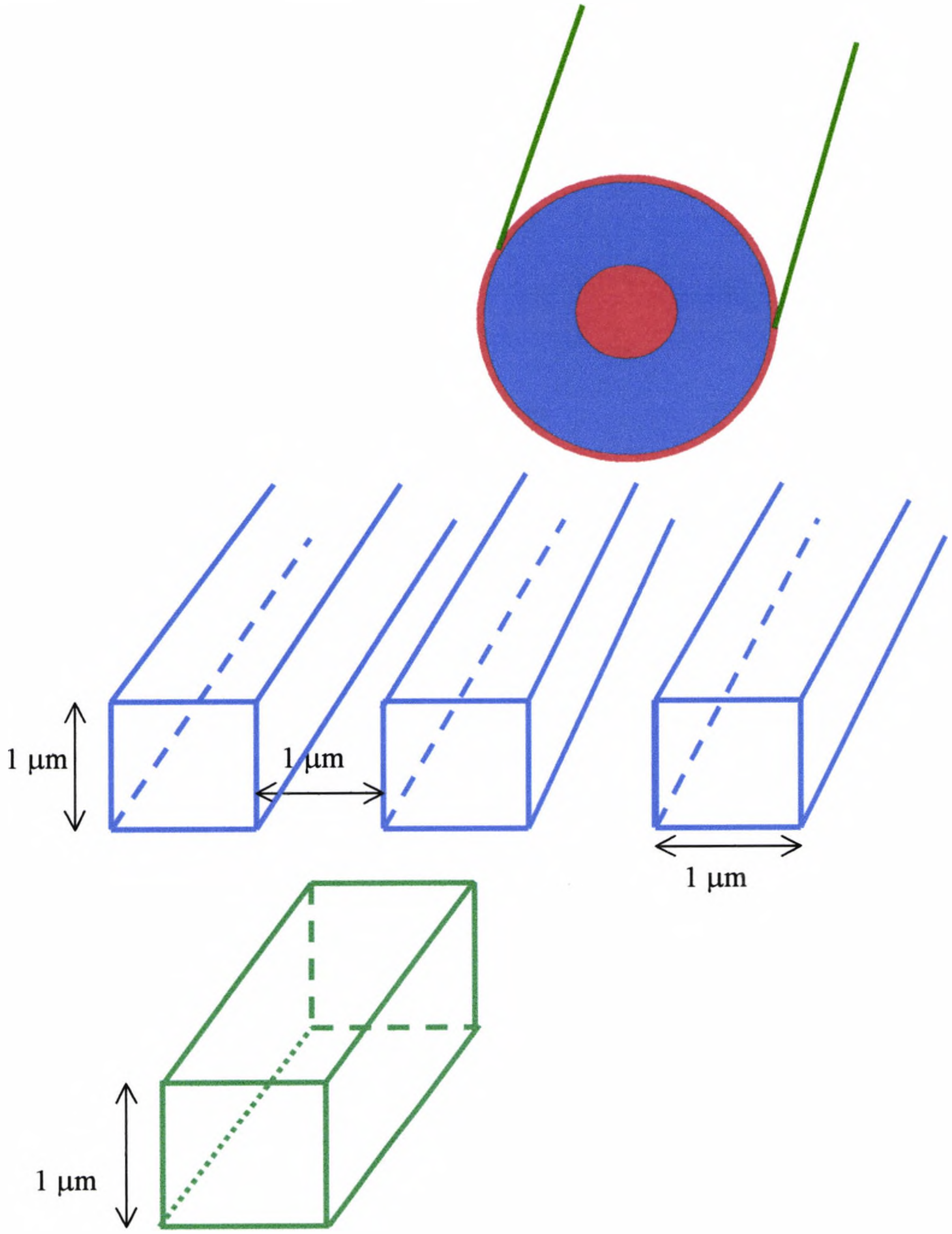

Fig. 6.26 Schematic of the three-guide directional coupler

A simplified single input waveguide of dimensions 1μm x 1μm is connected to a directional coupler section, comprising three identical 1.0μm x 1.0μm waveguides, placed in close proximity with a separation of 1.0μm. The refractive indices of the core and cladding regions are 3.3 and 3.17 respectively and an operating wavelength of 1.55μm is chosen for this simulation study.

In this example, it is assumed that the input waveguide is aligned with the centre waveguide of the three-guide structure. In the FEM simulations and the subsequent LSBR calculations, 4800 first order triangular elements are used. The CPU time for the calculation of all the field values in the input section and the directional coupler section was 30 minutes.

Figure 6.27 (a) shows the H_y field profile of the H^y_{11} supermode in the three-core directional coupler section. The three peaks in the three guide-cores are of identical sign but of unequal amplitudes. On the other hand, Figure 6.27 (b) shows the two side peaks are of opposite sign of the centre core field profile for the H^y_{31} supermode.

The H^y_{21} supermode is anti-symmetric and is not expected to be excited by the symmetric incident field. The values of the excited modal coefficients of the H^y_{11}, H^y_{21}, and H^y_{31} supermodes are calculated to be 0.87696, 0.12036E-6 and 0.46319 respectively. Figure 6.28 (a) shows the snap shot of the field profiles within the directional coupler and the fibre profile.

Figure 6.28 (b) shows the field evolution in the directional coupler section. To illustrate the field propagation clearly, only the evolution of the lateral field profile along the centre of the waveguide is shown. It can be observed that at the beginning of the directional

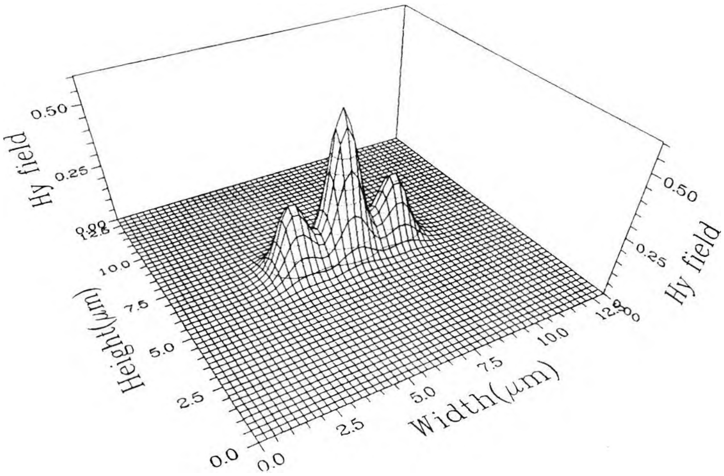

Fig. 6.27 (a) Field profile of the H^y_{11} mode

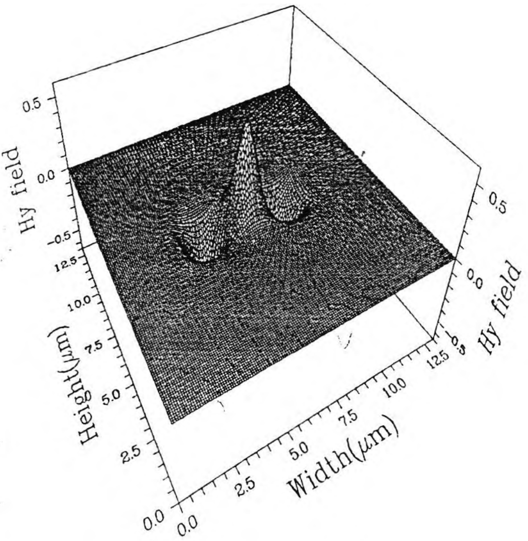

Fig. 6.27 (b) Field profile of the H^y_{13} mode

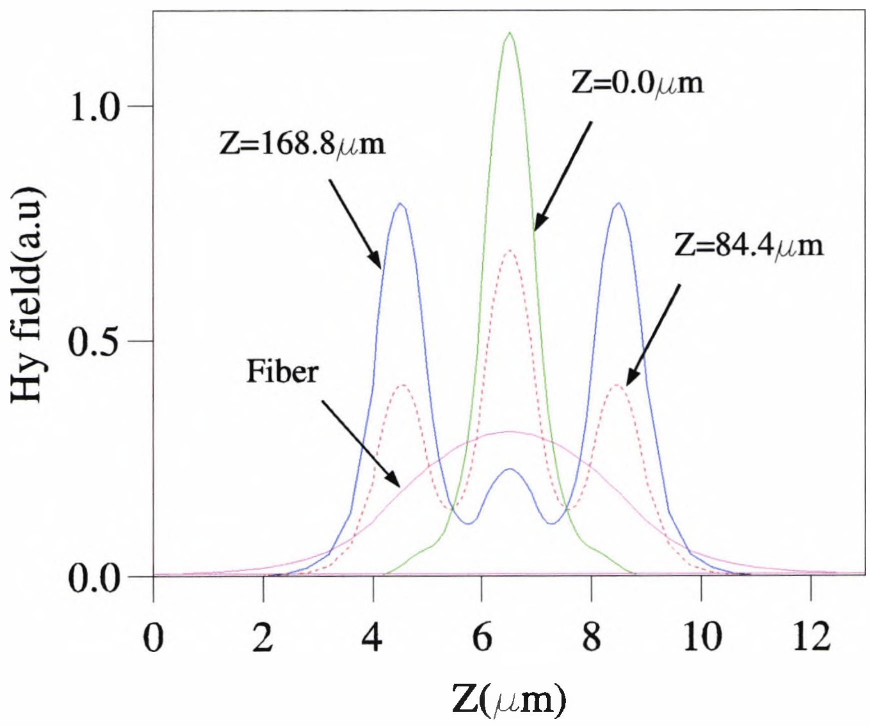

Fig. 6.28 (a) Field profiles at a snap shot for the fibre and at different *z* locations within the directional coupler

coupler section, at *z*=0μm, field profile is similar to the input field profile of the OEIC section and without any energy in the two output guides. However, as light propagates along the length of the coupler, the side lobes start to develop with the peak at the central guide slowly decreasing. The beat length (L_b) for the first two symmetric supermodes was 169μm, where the field is maximum in the two outer guides. However, by adjusting the waveguide dimensions it is possible to obtain 100% power in the two outer guides. Finally as the field propagates further, the middle peak starts to increase with the power in the outer guides slowly decrease and finally vanishing around 300μm, leaving a field profile similar to that of the field, at *z*=0μm.

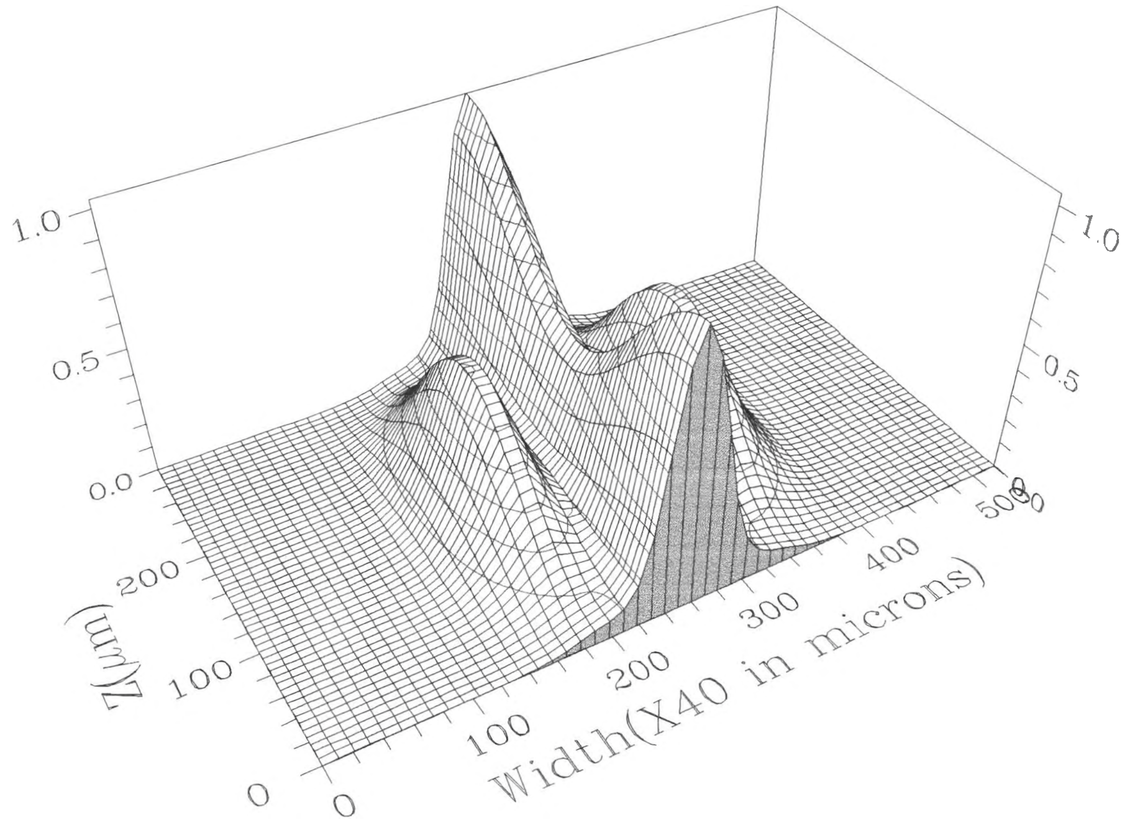

Fig. 6.28 (b) Field profile along the directional coupler

Figure 6.29 shows the power coupling efficiency with respect to the axial distance for the two dimensional, three-core directional coupler-based spot size expander.

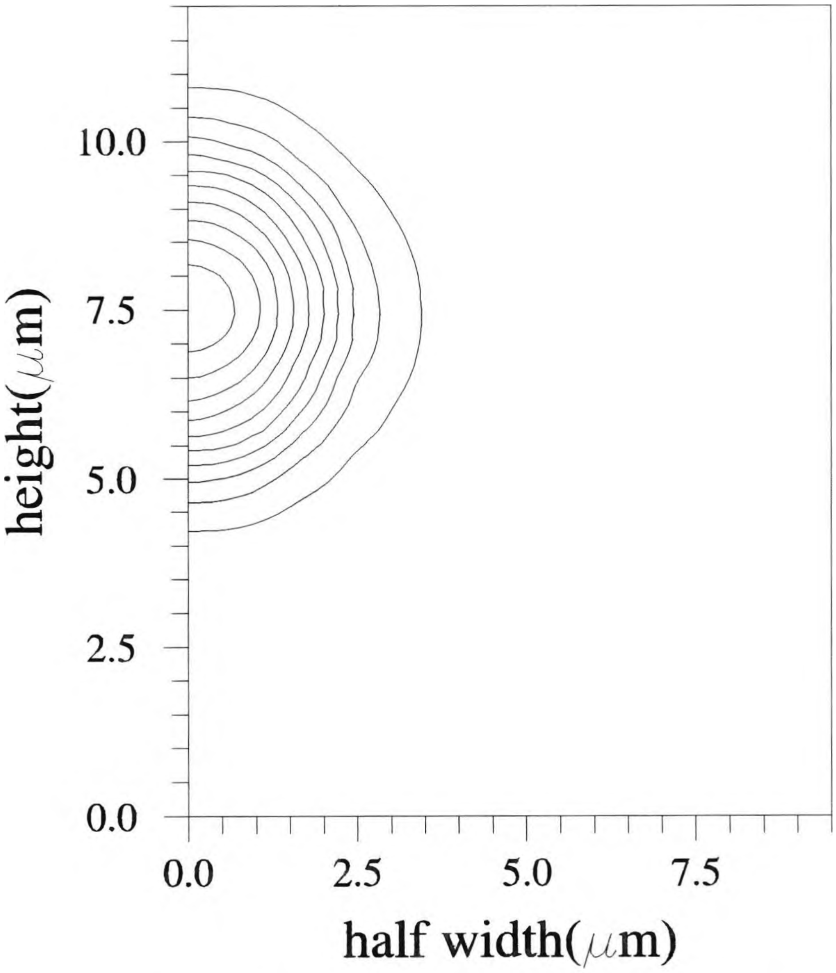

Fig. 6.28 (c) H_y field profile of the single mode fibre

Here the overall field along various axial locations can be butt-coupled to a SMF. The field profile of the SMF is shown in Fig. 6.28*c* above. The structural symmetry is exploited to increase the computational efficiency. The SMF with guide and cladding indices 1.469 and 1.444 respectively and a 2.5µm radius had a HWSS of 1.91µm. The

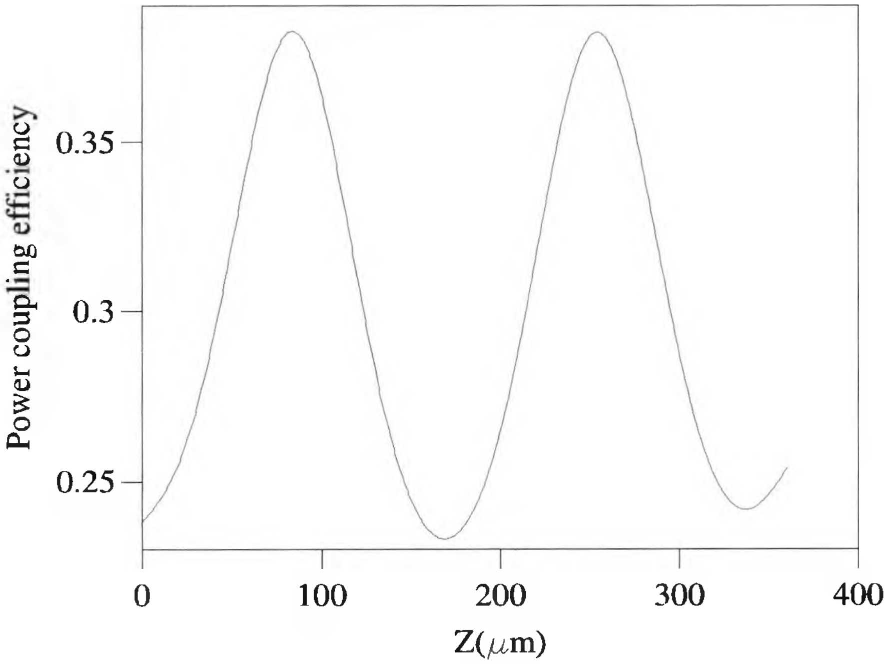

Fig. 6.29 Power coupling efficiency with the axial distance

HWSS of the input OEIC waveguide was 0.46μm. Using the simpler expression given by Eq. 6.1, the power coupling efficiency for direct laser-to-fibre coupling was calculated to be 0.2073, compared to the more rigorous result of the numerical method of 0.2453. This proves, that although the simple analytical expressions can be useful, however, a more rigorous numerical method is necessary, particularly when the field profiles deviate from the Gaussian profile. From Figure 6.29, it can be observed that the maximum coupling efficiency can be achieved at around 80μm which is slightly lower than half beat length. This figure also illustrates that the same phenomenon is happening again around 250μm which corresponds approximately to 3/2 L_b. In this design example, the results obtained predict that 6.10 dB loss for the direct laser-to-fibre coupling can be reduced to 4.15 dB by using an intermediate directional coupler section.

Next a novel design scheme is discussed incorporating a five-core directional coupler, to expand the spot size in both the transverse directions. In this design a single square-shaped input waveguide of 1.0 μm x 1.0 μm is connected to a five-guide directional coupler, where each guide is of 1.0 μm x 1.0μm dimension and separated by 1.0 μm. The schematic of the directional coupler is shown below in Fig. 6.30

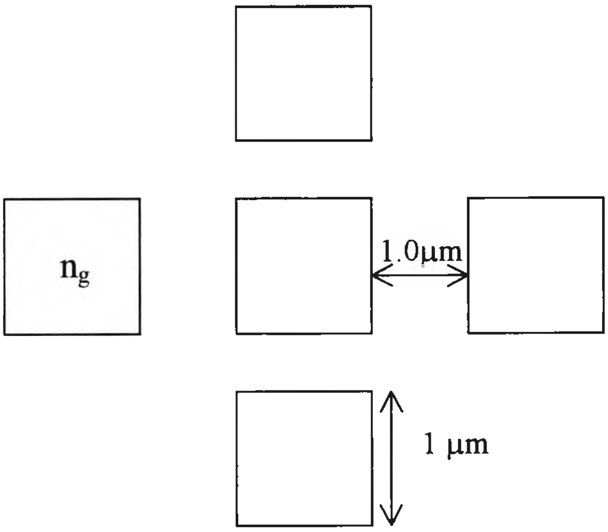

Fig. 6.30 Schematic of the five- guide directional coupler

The refractive indices are 3.3 and 3.17, respectively, for both the waveguide core and the substrate. The operating wavelength was taken as 1.55μm for this simulation study. The laser with a full-width spot size (FWSS) of 1.28 μm and a single mode fibre (SMF) with a slightly smaller FWSS of 4.62 μm compared to the earlier fibre has been considered in this example.

Figs 6.31 (*a*) and (*b*) show the first two supermodes that are present in the directional coupler section. As can be seen from Fig. 6.31 (*a*), there are five peaks for the fundamental supermode, all with positive amplitudes, inside the five waveguide cores of the directional coupler section. Fig 6.31 *(b)* shows the next dominant mode. As can be seen, the central peak is positive, surrounded by small negative peaks. The supermodes of the directional coupler section are excited at the laser-directional coupler junction forming a composite field profile similar to the input field at the beginning of the directional coupler.

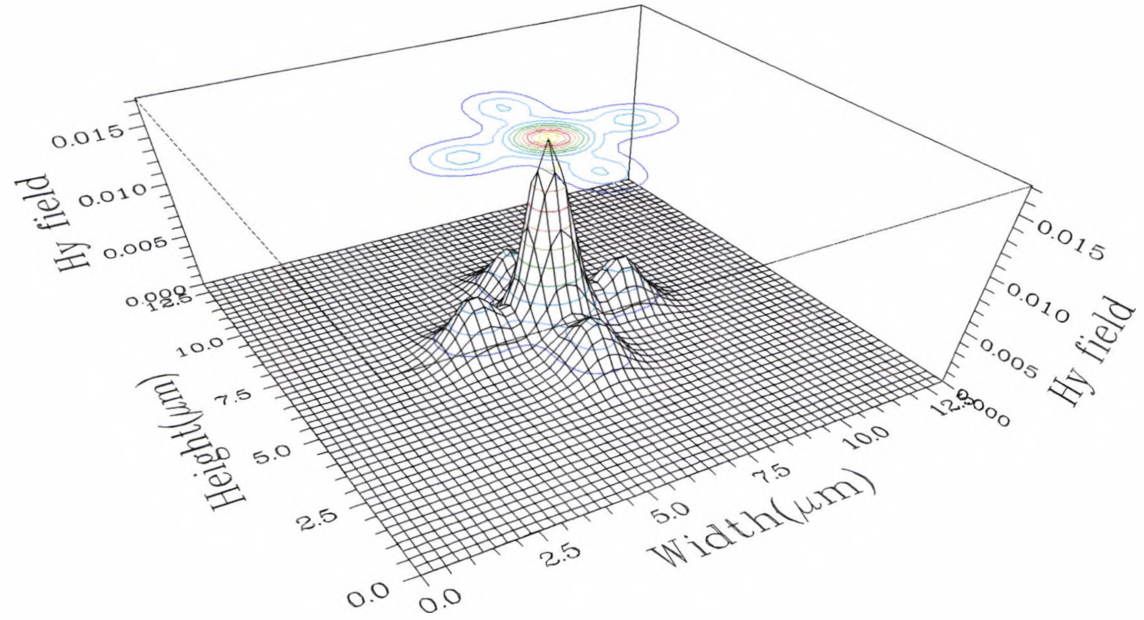

Fig. 6.31 ***a*** H_y field profile of the first supermode

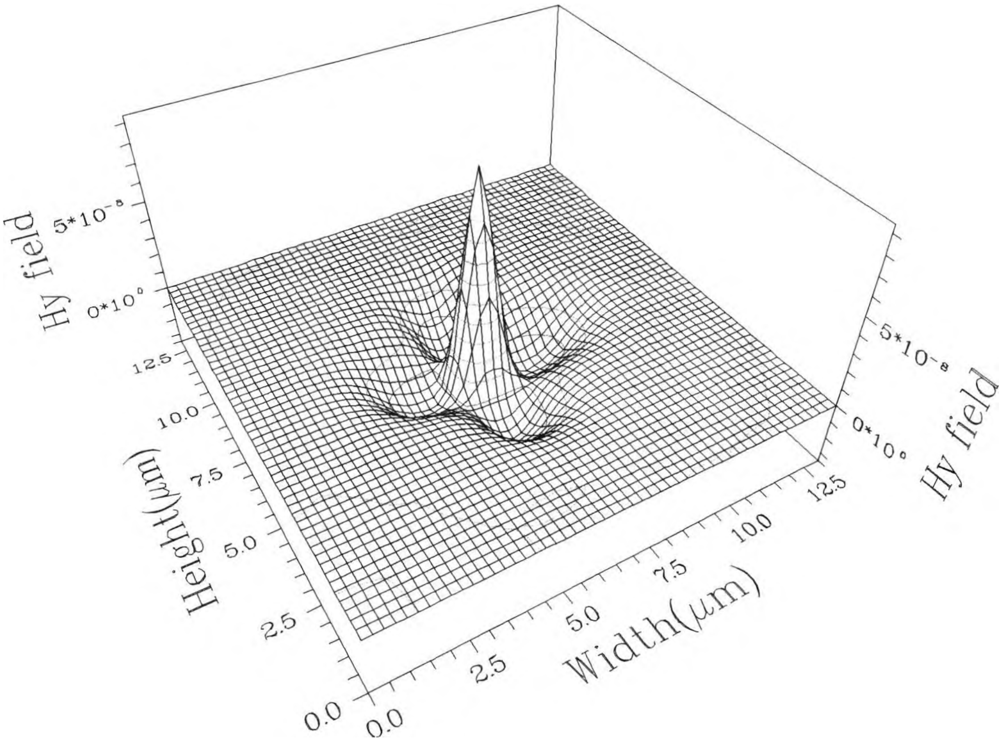

Fig. 6.31*b* H_y field profile of the second supermode

The excited coefficients of the four symmetric supermodes are 0.83717, 0.17902, 0.38867, and 0.26979, respectively. The available structural symmetry was exploited in this case to obtain accurate propagation constants and also to reduce the overall computational time.

Finally, the expanded field from the output of the directional coupler is butt-coupled to a single mode fibre. Fig. 6.32 shows the power coupling of the five-guide directional coupler to a fibre of 4.62 μm spot-size at different axial positions along the directional coupler.

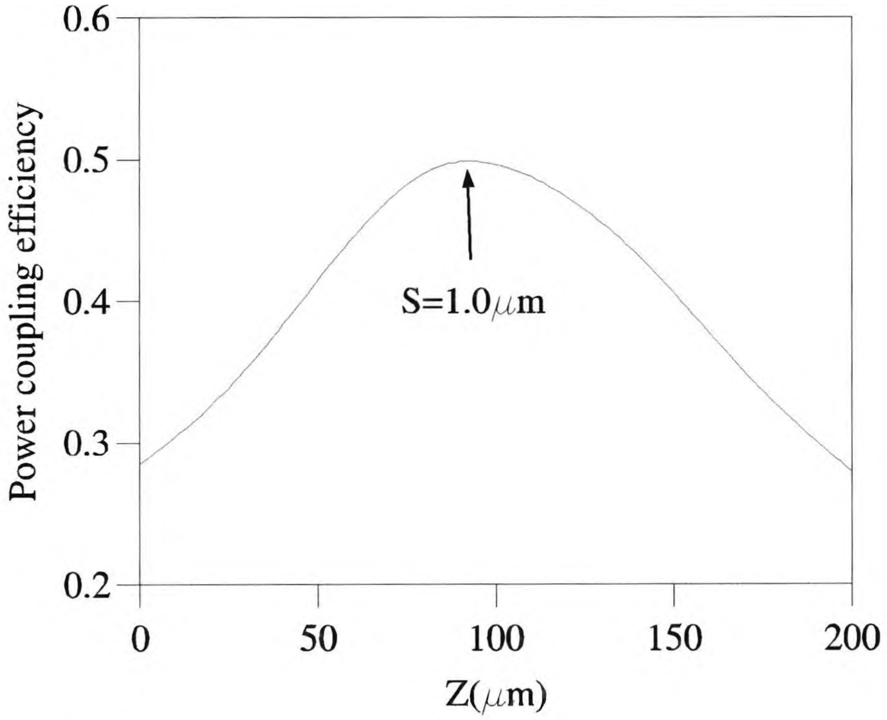

Fig. 6.32 Power coupling efficiency using a five-core directional coupler

The direct laser-to-SMF coupling efficiency may be calculated by using the simpler equation(6.1) as 0.2648, whereas the rigorous numerical simulation gives a value of 0.2919. Here again the importance of the LSBR method is demonstrated in calculating the coupling coefficients for butt-coupled waveguides. The 5.7 dB coupling loss for direct laser-to-fibre coupling can be reduced to 3.1dB by using the five-core directional coupler sandwiched between them. In the five-core design, the overall gain can be 1dB higher than that for the three-core design described earlier, although the later may be easier to fabricate. For the five-guide directional coupler, the beat lengths of the second, third and the forth supermodes were 270 μm, 183 μm, and 103μm, respectively. It can be seen from Fig. 6.32 for direct laser-to-fibre coupling, the coupling efficiency is only 29%. However, by using an intermediate spot-size transformer, this efficiency could be improved to about 52%. The maximum coupling occurs at around 90 μm. In the five-core directional coupler design, the overall power coupling efficiency could be around 41% (-1dB of the maximum) for an axial variation of ± 50 μm. Another important optical parameter is the study of vertical misalignment. Figure 6.33 shows the power coupling efficiency when the semiconductor laser is butt-coupled to a SMF, directly (L-F) and using a five-core directional coupler (L-DC-F).

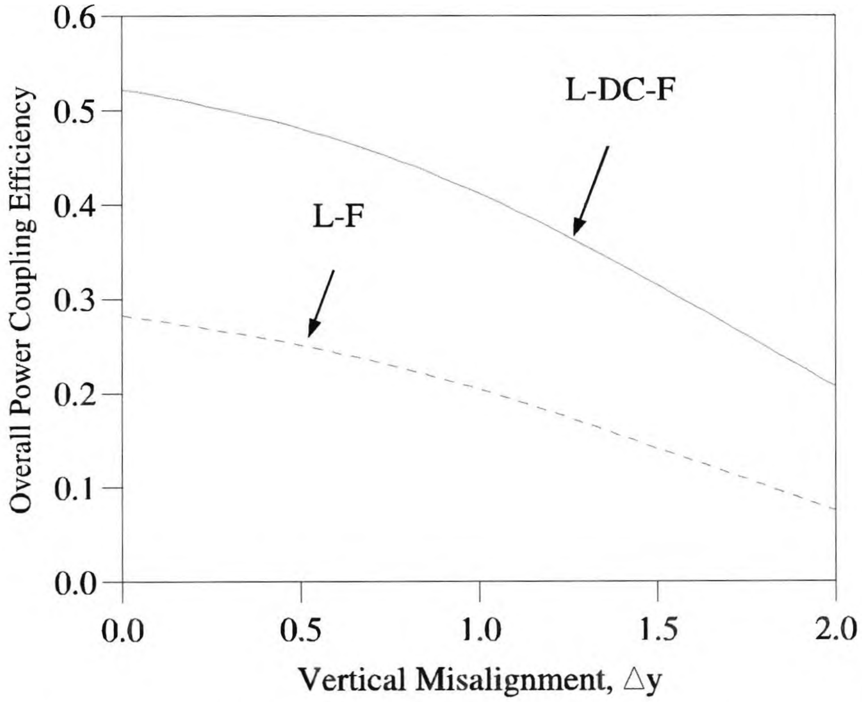

Fig. 6.33 Variation of power coupling efficiency with vertical misalignment

Here the centre of the fibre is shifted in the vertical direction at steps of 0.5 μm, to study the effect of misalignment. It can be observed that both the power coupling curves decrease monotonically. Since the modal field profile of the fibre is reasonably large, the coupling to the smaller laser field profile, after shifting a small distance has less effect on the coupling value, but in both cases the coupling is badly affected when the fibre is shifted by 1.5 μm. If the shift is more than 2 μm, then the coupling efficiency could be as small as 5% compared to about 50% when it is accurately assigned. This confirms the importance of accurate vertical alignment for good power transfer.

6.5 Spot size expanders using Multimode Interference (MMI) couplers

Finally a multimode interference based spot size expander is studied. This is the first time such an approach is discussed for the purpose of mode expansion.

The schematic of the structure is shown in Fig. 6.34.

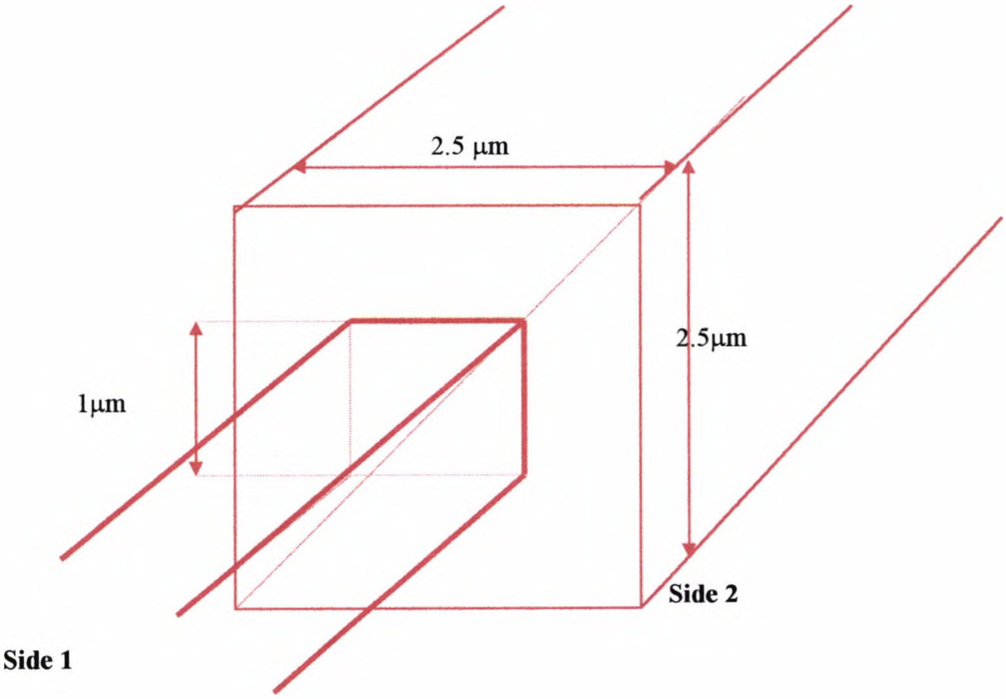

Fig. 6.34 Schematic of the MMI based spot-size expander

A single mode square waveguide with 1μm dimensions is butt-coupled to a MMI section of square cross-section. The guide and cladding indices are 3.3989 and 3.1645, respectively, for both the guides and the operating wavelength was 1.55μm.

In this example, it is assumed that both the waveguides are aligned at the centre, so two-fold structural symmetry does exist. When the fundamental quasi-$TE_{11}(H^y_{11})$ mode is incident from side 1, the available total symmetry condition is exploited to reduce the computational time. In the FE simulations and the subsequent LSBR calculations, 7200 first-order triangular elements are used for a quarter of the structure and it takes about 5 min. CPU time for each modal solution.

The variation of the modal coefficients (τ_{mn}) of the transmitted H_{mn}^y modes in side 2 with the dimension of the square guide (W_{MMI}) in side 2 is shown in Fig. 6.35.

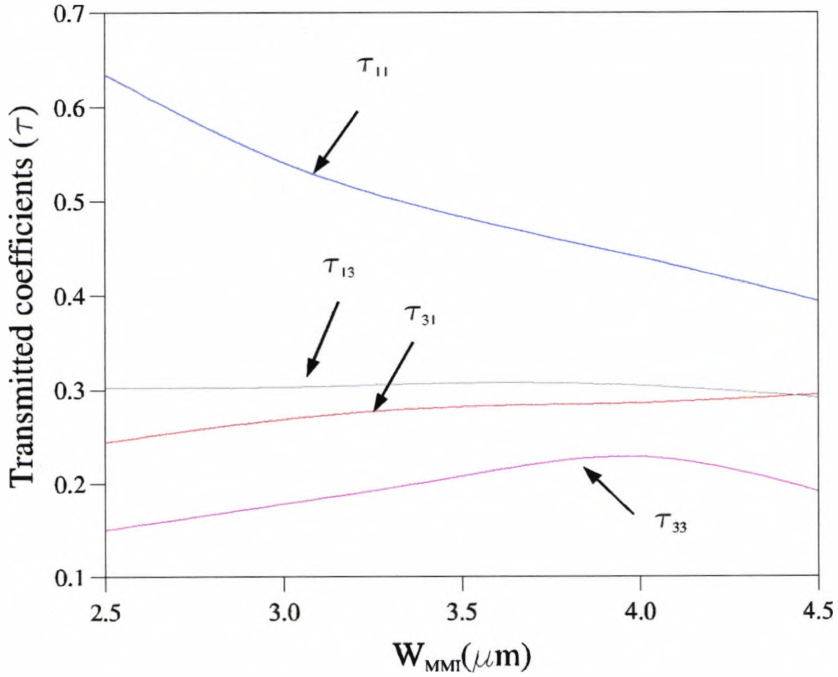

Fig. 6.35 Variation of the transmission coefficients of the guided modes in the MMI section with its width.

It can be seen that as the dimension is increasing, the coefficient of the fundamental mode is decreasing, whereas the coefficients for other higher order modes are increasing. The dominant H_y field profile for the fundamental quasi-TE mode, H^y_{11}, in the narrow input waveguide at $z = 0_-$, is shown in Fig. 6.36 (a). The field profile at the beginning (z=0_+) of the MMI section is shown in Fig. 6.36 (b) (also shown in Fig.5.31).

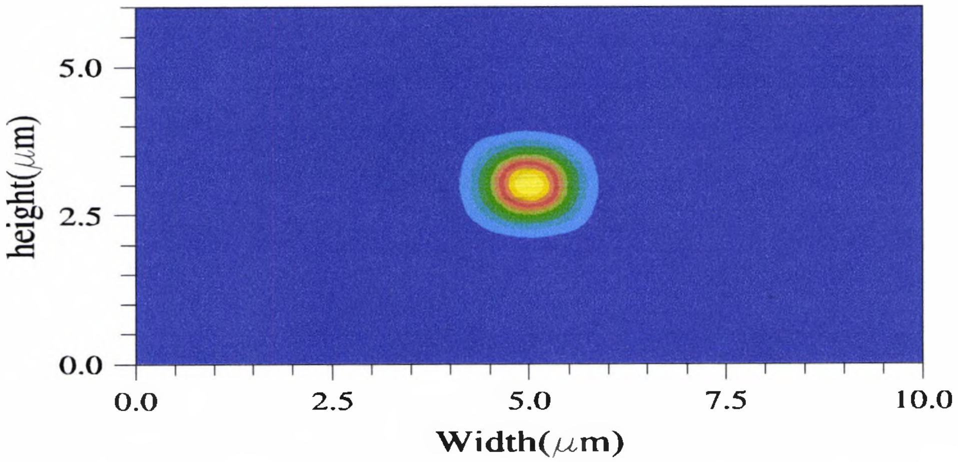

Fig. 6.36 (a) Field profile in the narrow input waveguide section ($z = 0_-$)

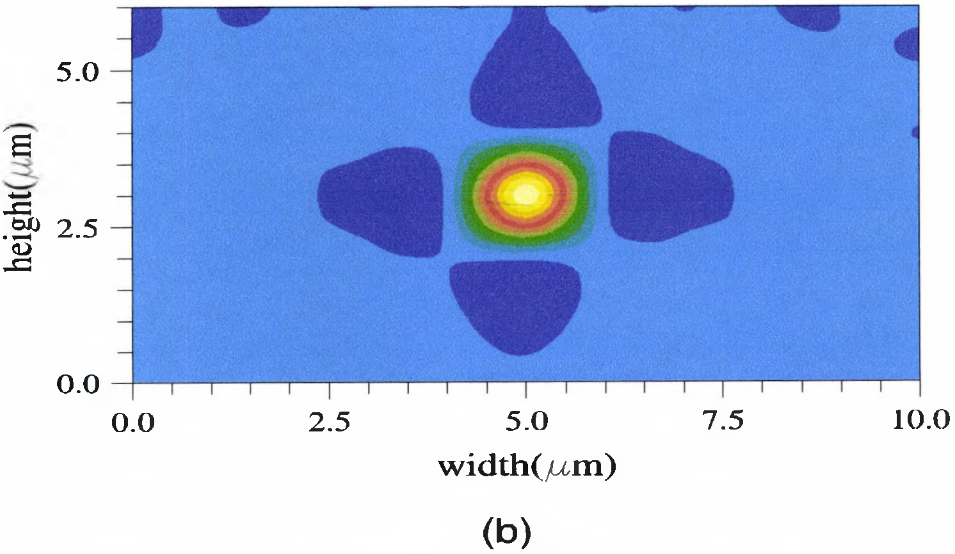

Fig. 6.36 (b) Field profile at the beginning of the MMI section

This profile is obtained by a superposition of all the four modes with their appropriate excitation coefficients. It can be observed that the resultant field profile is very close to the incident field profile shown in Fig. 6.36 (a), except for a slight aberration around the edges of the MMI guide-core. This combined profile is due to all the four modes generated in the MMI section and propagated through the waveguide. However, as the individual modes propagate with different propagation constants, their relative phase difference will change the overall field profile along the axial direction.

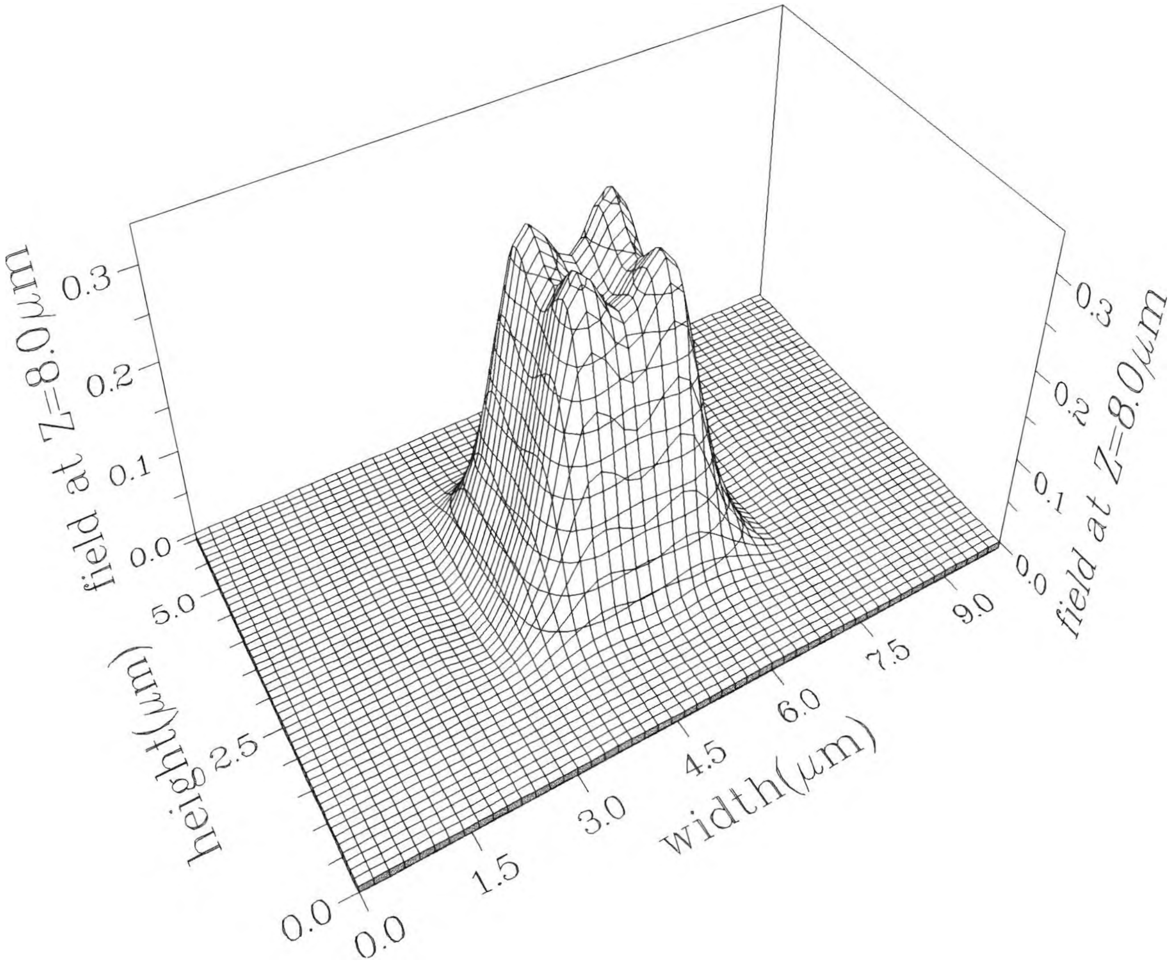

Fig.6.37 Field profile in the MMI section at z = 8.0μm

Fig. 6.37 shows the transverse (*x*-*y*) profile of the resultant H_y field at a distance $z = 8.0\mu m$, which has a much more expanded profile than the input guide and can be used to achieve better coupling between a PIC (photonic integrated circuit) and a fibre. The vertical axis is in arbitrary units for the dominant *y*-component of the resultant expanded field profile to an optical fibre with spot-size radius 2.06μm. In this work the spot size radius is defined as the radial distance where the intensity profile falls to e^{-1} of its maximum value. The variation of the overall power coupling, from the PIC to the fibre mode with the intermediate MMI section, with the MMI section's length and lateral dimension, is shown in Fig. 6.38.

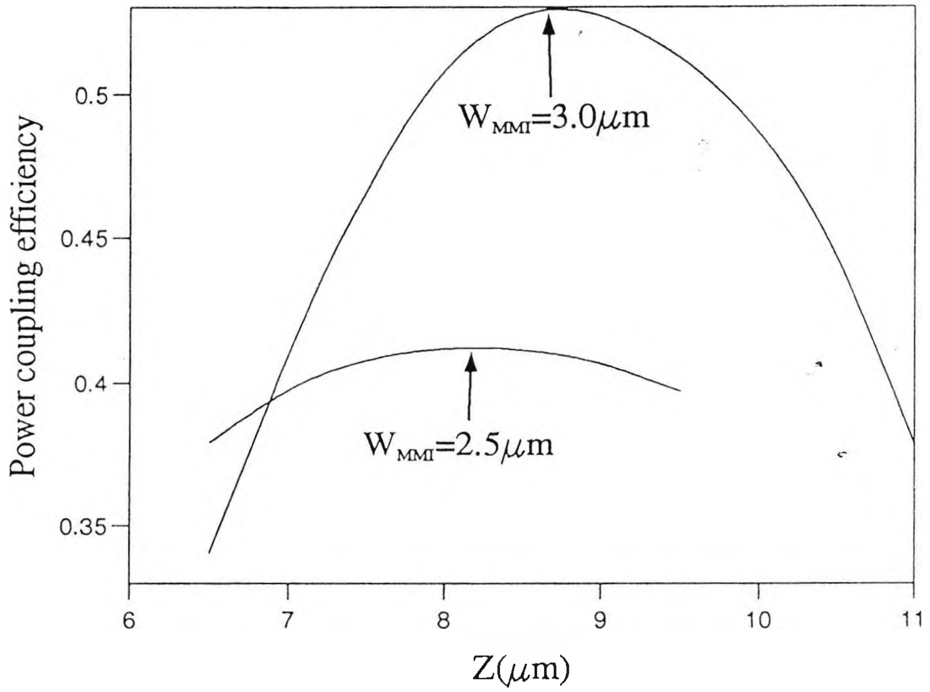

Fig. 6.38 Variation of the overall power coupling with the dimensions of an intermediate MMI section

It can be observed that for a MMI with larger cross section, the maximum power coupling is increased, but however, the optimum longitudinal (*z*) position is also displaced further. It can also be noted that the overall power coupling factor is reasonably stable with the fabrication tolerance of the MMI section. Without the use of such an MMI section, the power coupling factor is only 8% for the direct coupling between the PIC and the optical fibre considered here. However, in any practical situation the difficulty of accurate positioning of the fibre from the etched or cleaved facets also has to be considered. So, an overall 8 dB gain, by using the intermediate MMI section of 3.0μm square, is predicted. For the optical system integration, the dimensions of the MMI section can be optimised, to maximise the coupling with acceptable fabrication tolerance, between a specific PIC and an optical fibre. Alternatively 3 coupled MMIs can be used to expand the mode in the lateral direction and if they are coupled can be expanded in the vertical direction.

6.6 Summary

In this chapter the most promising area in photonic engineering, the use of spot-size expanders was discussed. Initially the taper based mode expanders were studied. Their coupling efficiency tends to increase with the reduction of the guide dimension. The reflection coefficients of some of the structures were also identified for the first time. Although the coupling efficiency increases with guide dimension the reflection also increases at the same rate. This is really a disturbing design factor. Next a synchronous directional coupler based SSE was studied. By phase matching both the guides of the directional coupler and by using non-identical guides the input laser power is expanded considerably. This can be easily coupled to a single mode fibre. Even though the power transfer is not 100% at the coupling length, L_C it can be achieved by perfectly adjusting the waveguide parameters in the directional coupler design. Some multi-guide directional coupler structures were also analysed. Finally a MMI based spot size expander was discussed. This is the first time such an approach is discussed for the spot size expansion application. The MMI is an attractive alternative to the directional coupler due to its compact size and good fabrication tolerance.

Chapter 7

Discussions and suggestions for future work

7.1 Discussions of aims and objectives of this thesis

The main aim in this research work has been to characterize compact photonics devices for optical communication systems using the finite element and the Least Squares Boundary Residual methods. The set of tasks that have been outlined in Chapter 1 have been undertaken successfully, results considered and analyzed and the majority of the work has been published. Most of the results obtained from this research work have been compared with experimental and other numerical results and the validity of the present approach has thus been demonstrated.

A principal objective in this work has been to study the directional coupler and its special form, the multimode coupler, for various optoelectronics applications. Although various numerical approaches are available to study a range of optical waveguide problems, to date the finite element method has proved to be the most accurate and versatile numerical approach for analysing such waveguide problems. This method is capable of handling problems with arbitrary cross section, arbitrary index profile, anisotropy and nonlinearity and in this research work this has been verified for a range of different structures.

The power transfer efficiency has been mostly calculated by using the simple overlap or coupled mode approaches. However, the overlap approach can handle only one mode at a time, whereas in the LSBR method all the modes present in a waveguide can be analysed together. The LSBR method has also been shown capable of calculating the reflection coefficients, and a knowledge of these coefficients is important for the analysis of some of the feedback devices such as optical amplifiers and ring lasers, considered in this work, where initially a planar structure was considered to obtain a rough estimate of the propagation constants and hence the coupling lengths. Following that a two dimensional structure was considered, which is more realistic, and the characteristics of several photonic devices have been studied.

7.2 Application of the numerical techniques in problem solving

For the effective analysis of multimode based devices, it was necessary to find the modal solutions of the associated uniform multimode interferometric (MMI) and the single-mode access or output waveguides. However, in the analysis of MMI devices, often the same transverse behaviour in one of the lateral directions (y) was assumed and a practical, two-dimensional, waveguide problem may in effect be approximated by a simple one-dimensional planar waveguide. Most frequently the effective index method was used to find the modal propagation constants (β_i) and field profiles of such simple planar structures. There are also other available numerical techniques such as the Finite difference (FD) and the Discrete Spectral Index (DSI) methods. However, in this thesis, it has been shown that the use of the finite element method (FEM) for the analysis of optical waveguides offers more accurate results than the other available techniques. The FEM has been used to calculate the propagation constants and the field profiles. From a knowledge of the propagation constants, the coupling lengths, L_C, can be determined, and the coupling efficiency of the coupler can be calculated by using the LSBR technique.

The FEM has been shown to be a powerful technique to analyse optical waveguide problems. Most of the available numerical and analytical techniques cannot handle situations where the waveguide structures are complex with complex material properties, unlike the FEM. Another advantage seen is that its index distribution can be arbitrary, which is important for many practical waveguides.

In this thesis the vector-**H** field finite element was used, which for many purposes has the advantage over all other approaches (e.g. **E**-field). In this formulation, the natural boundary condition is that of an electric wall, so that for arbitrary conducting guide walls it can be left free. In this formulation, the chosen field is continuous at the dielectric interfaces, and so it is very convenient for the finite element solution of dielectric waveguide problems. In this formulation, general anisotropic problems can also be analysed, and as the natural boundary condition is that of an electric wall, boundary conditions need not be forced on conducting guide walls. For regularly shaped waveguides, and at the symmetric walls, the boundary conditions can be enforced to reduce the problem size.

In the FEM analysis discussed in this thesis in most cases, first order shape functions have been used. Where possible, accurate modal solutions have been obtained using the maximum possible mesh divisions and the accuracy of the results obtained is shown in Table 5.3, for two different mesh sizes.

The LSBR method, which is an alternative to the coupled mode and the point-matching method, is more accurate where the boundary condition is satisfied in the usual least squares sense over the interface. The method is rigorously convergent and the error minimisation is global rather than sampled, having also the flexibility of introducing an electric/magnetic weighting factor for error minimisation. This method is used to calculate the power transfer from the input to the output guides.

In this work existing finite element codes were modified to incorporate multimode waveguide analysis and a Least Squares Boundary Residual program was modified to calculate the composite field values at various axial (z) locations. A computer program was also written to calculate the excited coefficients of the individual modes using the overlap integral and a computer code was also developed to calculate the refractive index values for different x and y concentrations of InGaAsP/InP based systems.

7.3 Discussion of the results

Three important areas have been studied in this research work. Initially an optical polarizer based on a metal clad directional coupler has been considered. Even though the idea of such a metal clad polarizer is not novel, the calculation of the isolated mode and coupled mode modal loss has been studied for the first time and shown to have a considerable effect on the coupling efficiency. Secondly a multiple quantum well (MQW) based polarizer was analyzed. In this study using two-dimensional simulation, the equivalent index has been calculated by using both the analytical expressions and the finite element method. It has also been shown that the equivalent index values calculated by using the finite element approach are slightly higher than those using an analytical approach.

In Chapter 5, some of important photonic devices based on multimode interference phenomena have been analysed. Initially a planar 3 dB coupler was considered where the propagation constants and field values were calculated by using the finite element method and the power coupling efficiency is determined by using the Least Squares Boundary Residual method. The accuracy of the finite element method can be seen from the results shown in Table 5.1. The same structure with two-dimensional confinement is also considered and the propagation constants and the field values involved were obtained.

The principle of '*restricted resonance*' has been used to minimise the number of modes and the computational time needed. The excited modal coefficients obtained using the Least Squares Boundary Residual method have been compared with the results of using the overlap integral method to show the accuracy of the present technique. The LSBR method gives on average around 5% higher than the OI values. The quadrature relationship has also been calculated and compared with the finite element solutions. The quadrature error seems to be more for the higher order modes and this can cause unsharp images at particular lengths. Important properties such as excess loss, fabrication tolerance, polarization dependence and crosstalk have been discussed in detail for the multimode interference- based 3 dB coupler.

In further work, a two-dimensional 1x4 power splitter has been analysed, where the structural symmetry was exploited to increase the computational efficiency. This idea can be extended to design 1xN way power splitter and the excess loss for this coupler design has also been calculated.

Finally in Chapter 5, a multimode based duplexer has been studied and initially a planar raised rib structure followed by a two dimensional rib has been considered. The planar coupling lengths were small compared to the two-dimensional results. In Table 5.6 the percentage of deviation from the quadrature relationship is shown where it can be seen that this error increases for higher order modes.

From a knowledge of the characteristics of multimode interference based devices it can be concluded that varying the device parameters such as the refractive index and length are less critical. However, the study shows the width of the MMI section must be controlled to within a certain defined limit.

Further, a rigorous comparison has been made of the performance of directional couplers, compared with that of a multimode interference couplers. Important properties such as the device length, crosstalk, polarization dependence and fabrication tolerances are compared for the first time for both type of device. It has also been shown in the work that for the same crosstalk limit using a multimode section, the device length can be shortened to less than that of the directional coupler based system. The work has also confirmed that MMI-based devices are less polarization dependent, and that fabrication tolerances can deteriorate the device performance, particularly for weakly coupled directional coupler based devices, when they lose their phase synchronism. These attractive properties make multimode interference based systems viable alternatives for future compact, all-optical communication systems.

Finally, in Chapter 6, different techniques to couple the laser field to the fiber field were discussed. Initially the validity of the present approach was tested by reproducing known structures and results. For one particular case, the reflection coefficients were calculated and it was shown that as the coupling efficiency increases for larger spot sizes, when the guide width is reduced, the reflection coefficient is also increased. This is a disturbing phenomenon which has been identified for the first time for such devices. As single mode operation is desired in spot-size transformers, initially the region of appearance of the second mode is also identified.

In this study the infinite element approach has been used, as the mode expands near the cut-off region the field decay is very slow and only by using the infinite elements this problem can be solved. The effect of vertical misalignment has also been studied and it has been shown that by shifting 3.6μm away from the centre, the coupling efficiency could be as low as 18% compared to 61% when aligned correctly. Even though the taper design is very attractive, it requires complex fabrication processes and therefore a novel approach using asynchronous directional couplers has been developed. In this approach, by using non-identical guides, the input laser field can be coupled to a guide of larger dimension by phase matching the guides of the directional coupler which will give a larger spot size and this can be easily and effectively coupled to a single mode fiber.

The above approach has been extended further to the case of three- and five-guide couplers. Planar three-guide couplers were initially studied and the knowledge obtained was extended to waveguides with two-dimensional confinement.

The three-guide directional coupler had three modes, of which the second is anti-symmetric and hence not excited by the input field. To increase the computational speed this mode has been excluded from two-dimensional simulations.

In this work it is shown that various photonic devices based-on directional coupler or multimode interference devices, which involves several butt-coupled uniform sections can be analyzed by the use of the finite element and the least squares boundary residual methods.

In the two-dimensional simulations of a five-guide directional coupler, there were five modes present and thus it can be concluded from the study that the number of modes depends on the number of active guides in a directional coupler

7.4 Future Work

In this thesis the most popular and well established finite element method has been extended to study multimode interference (MMI) based devices. The finite element method (FEM) with the combination of the Least Squares Boundary Residual (LSBR) method has been used to solve guided-wave photonic devices. The only drawback of using the LSBR is it being computationally very costly in analysing tapered structures, which can be overcome by using a beam propagation method. By using the input field generated by the FEM as the input to the taper, an accurate analysis can be carried out where the field profile at the beginning and at the end of the taper can be calculated by using the FEM, but however by using the LSBR, the coupling efficiency can be calculated at the end of the taper to a single mode fibre where the discontinuity is quite large. The FEM solutions can then be compared with those from the beam propagation method and a benchmark can be established for the BPM.

In MMI based devices, the input guide has been assumed straight in most of the simulations reported. However, it is desirable to use input guides with bends so that they can be easily coupled to other components and a compact device can be designed, where the analysis of bends can be done by using the conformal transformation and the propagation of the field inside the bend can be studied by using the BPM. The polarization properties of these bends is an important issue and the vector BPM is an essential tool for such analysis.

The lateral offset is an another important issue that has to be addressed in the study of MMI based devices where as the position of the input guide is a crucial design parameter, careful considerations have to be given for the study of these lateral offsets.

Components which combine both functions of focusing and dispersive elements are also important in compact photonic devices. They are of special interest for the spatial separation of signals with different wavelengths, as are occurring in wavelength demultiplexers and wavelength filters. They may also be used for polarization splitting if the waveguides employed exhibit polarization dispersion.

Arrayed waveguide MMI-based multiplexers are also becoming very important due to their compact size and flexibility. The LSBR method could be modified to include the effect of reflection coefficients as well so that the individual reflections at discontinuity interfaces can be analysed. Further in the LSBR composite field calculations, the phase term can be included to see the phase contribution. This method can also be adjusted to minimise the energy functional, J, by changing the value of the penalty term till a minimum is reached.

The development of the vector BPM could serve as a useful numerical tool in modelling taper-based devices, bends, corners, waveguide grattings and vertical cavity surface emitting lasers. All these devices are becoming important in the field of photonics engineering and a development of such a code would greatly benefit the photonic systems designer.

Most of the modelling work in this thesis has been carried out for passive devices. However, a suitable semiconductor electronic model could be developed to analyse active devices. So that a realistic photonic system can be modelled.

There is thus a wide variety of potential future work, and with the expansion of optical communications, considerable scope exists for the implementation, development and wider use of the numerical methods which have shown a number of successful implementations in this thesis. This will be aided by the anticipated developments in both computer power and memory and the reductions in cost expected. The field of numerical modelling of photonics systems devices is ripe for considerable expansion and development.

APPENDIX A

Vector H-field Formulation

The basic Maxwell's equations are given as :

$$\nabla \times \mathbf{E} = -\frac{\partial \mathbf{B}}{\partial t} \tag{A1.1}$$

$$\nabla \times \mathbf{H} = \mathbf{J} + \frac{\partial \mathbf{D}}{\partial t} \tag{A1.2}$$

Where **E** is the electric field intensity, Volt/Metre
H is the magnetic field intensity, Ampere/Metre
B is the magnetic flux density, Tesla
D is the electric flux density, Coulomb/Metre^2

and the constitutive relations

$$\mathbf{D}=\varepsilon\mathbf{E} \tag{A1.3}$$

$$\mathbf{B}=\mu\mathbf{H} \tag{A1.4}$$

For a source free region, J=0, and equation (A1.2) reduces to :

$$\nabla \times \mathbf{H} = \frac{\partial \mathbf{D}}{\partial t} \tag{A1.5}$$

Taking the curl of equation (A1.5) and using (A1.3)

$$\nabla \times (\nabla \times \mathbf{H}) = \varepsilon \nabla \times \frac{\partial \mathbf{E}}{\partial t} \tag{A1.6}$$

since the fields are time dependent

$$\frac{\partial}{\partial t} = j\omega$$
$$\frac{\partial}{\partial t^2} = -\omega^2$$

From the Maxwell's equations (A1.1 and A1.2) can be written as

$$\nabla\times\mathbf{E} = -j\omega\mu\mathbf{H} \tag{A1.7}$$

$$\nabla\times\mathbf{H} = j\omega\varepsilon\mathbf{E} \tag{A1.8}$$

Rearranging A1.8 gives

$$\frac{1}{\varepsilon}[\nabla\times\mathbf{H}] = j\omega\mathbf{E} \tag{A1.9}$$

Multiplying both the sides of A1.9 by ∇ operator

$$\nabla\times\left\{\frac{1}{\varepsilon}(\nabla\times\mathbf{H})\right\} = j\omega.-j\omega\mu\mathbf{H} \tag{A1.10}$$

$$\nabla\times\left\{\frac{1}{\varepsilon}(\nabla\times\mathbf{H})\right\} = \omega^2\mu\mathbf{H} \tag{A1.11}$$

If ε is a scalar, then it can be taken out of the brackets, { }, before the ∇ operator, however if the material is a tensor then it has to be treated as a matrix inside the brackets, { }.

Multiplying by $\mathbf{H}^*$ and integrating over the whole *xy* domain gives

$$\int_\Omega \mathbf{H}^*\cdot\left[\nabla\times\left\{\frac{1}{\varepsilon}(\nabla\times\mathbf{H})\right\}\right]d\Omega = \omega^2\int \mathbf{H}^*\mu\mathbf{H}\,d\Omega \tag{A1.12}$$

Using Green's theory given by

$$\int_\Omega \mathbf{F}.(\nabla\cdot\mathbf{G})d\Omega = -\int(\nabla\times\mathbf{F})\cdot\mathbf{G}\cdot d\Omega + \oint_\Gamma \mathbf{F}\cdot\mathbf{G}\,d\Omega \tag{A1.13}$$

The second term on the right hand side of A1.13 is zero since there are zero fields in the boundary. Applying A1.13, A1.12 can be written as

$$\omega^2 = \frac{\int(\nabla\times\mathbf{H}^*)\cdot\frac{1}{\varepsilon}(\nabla\times\mathbf{H})d\Omega}{\int\mathbf{H}^*\mu\mathbf{H}\,d\Omega} \tag{A1.14}$$

is the solution to the wave equation given by (A1.6)

APPENDIX B

Calculation of the inverse of ε

It was shown in chapter 2 that the tensor has to be described as a 3x3 matrix
The general ε matrix is defined as

$$\varepsilon = \begin{vmatrix} \varepsilon_{11} & \varepsilon_{12} & \varepsilon_{13} \\ \varepsilon_{21} & \varepsilon_{22} & \varepsilon_{23} \\ \varepsilon_{31} & \varepsilon_{32} & \varepsilon_{33} \end{vmatrix} \qquad \text{(A2.1)}$$

For waveguides with modal loss or gain the H_z field has 90° phase difference with the other two transverse components namely, H_x and H_y. In this case if we consider a transformation the overall element matrix will be real, *i.e* $H_z = jH_z$. However, the permittivity tensor can be modified as

$$\varepsilon = \begin{vmatrix} \varepsilon_{11} & \varepsilon_{12} & j\varepsilon_{13} \\ \varepsilon_{21} & \varepsilon_{22} & j\varepsilon_{23} \\ j\varepsilon_{31} & j\varepsilon_{32} & \varepsilon_{33} \end{vmatrix} \qquad \text{(A2.2)}$$

Since $\hat{\varepsilon}^{-1}$ is required in the vector **H**-field formulation

$$\omega^2 = \frac{\int (\nabla \times \mathbf{H}^*) \cdot \frac{1}{\varepsilon} (\nabla \times \mathbf{H}) \, d\Omega}{\int \mathbf{H}^* \hat{\mu} \mathbf{H} \, d\Omega} \qquad \text{(A2.3)}$$

However for the tensor case $\hat{\varepsilon}^{-1} = P$ which is written as

$$P = \begin{vmatrix} P_{11} & P_{12} & P_{13} \\ P_{21} & P_{22} & P_{23} \\ P_{31} & P_{32} & P_{33} \end{vmatrix} \qquad \text{(A2.4)}$$

where

$P_{11} = (\varepsilon_{22}\varepsilon_{33}+\varepsilon_{23}\varepsilon_{32})/\ det\ \varepsilon$
$P_{12} = -(\varepsilon_{12}\varepsilon_{33}+\varepsilon_{13}\varepsilon_{32})/det\ \varepsilon$
$P_{13} = j(\varepsilon_{12}\varepsilon_{23}-\varepsilon_{13}\varepsilon_{22})/det\ \varepsilon$
$P_{21} = -(\varepsilon_{21}\varepsilon_{33}+\varepsilon_{23}\varepsilon_{31})/det\ \varepsilon$
$P_{22} = (\varepsilon_{11}\varepsilon_{33}+\varepsilon_{13}\varepsilon_{31})/det\ \varepsilon$
$P_{23} = -j(\varepsilon_{11}\varepsilon_{23}-\varepsilon_{13}\varepsilon_{21})/det\ \varepsilon$
$P_{31} = j(\varepsilon_{21}\varepsilon_{32}-\varepsilon_{22}\varepsilon_{31})/det\ \varepsilon$
$P_{32} = -j(\varepsilon_{11}\varepsilon_{32}-\varepsilon_{12}\varepsilon_{31})/det\ \varepsilon$
$P_{33} = -(\varepsilon_{11}\varepsilon_{22}-\varepsilon_{12}\varepsilon_{21})/det\ \varepsilon$

and the *det* ε is given as

$$det\ \varepsilon = \varepsilon_{11}(\varepsilon_{22}\varepsilon_{33}-j\varepsilon_{23}j\varepsilon_{32})-\varepsilon_{12}(\varepsilon_{21}\varepsilon_{33}-j\varepsilon_{23}\varepsilon_{31})+j\varepsilon_{13}(\varepsilon_{21}j\varepsilon_{32}-\varepsilon_{22}j\varepsilon_{31}) \quad (A2.5)$$

Appendix C

List of Publications by the author relevant to the thesis

1. Rahman, B.M.A., Rajarajan, M., Wongcharoen, T., and Grattan, K.T.V (1996). Accurate Analysis of Multimode Interference Devices. In : IEEE Photonics Technology Letters 8 (6) : 809-811.

2. Rahman, B.M.A, Rajarajan, M., Wongcharoen, T., and Grattan K.T.V (1996). Improved Laser-Fiber Coupling by Using Spot-Size Transformers. In: IEEE Photonics Technology Letters 8 (4) : 557-559.

3. Rajarajan, M., Rahamn, B.M.A., wongcharoen, T., and Grattan, K.T.V (1996). Accurate characterization of MMI-based devices In : EOS/SPIE Conference in Networks and Systems, Berlin 2954 22 : 50-61.

4. Rajarajan, M., Rahman, B.M.A., Wongcharoen, T., and Grattan, K.T.V(1996). Accurate Analysis of MMI Devices with 2-dimensional Confinements. In : Lournal of Lightwave Technology LT-14 (9) : 2078-2084.

5. Rahman, B.M.A., Rajarajan, M., Wongcharoen, T., Buah, P.A., Grattan, K.T.V., Perrone, G., and Ivo Montrosset (1996). Computer modelling of photonic devices for optical measurements. In : Colloquium IEE software in measurements.

6. Rajarajan, M., Buah, P.A., Wongcharoen, T., Rahman, B.M.A., Grattan, K.T.V., Schulz, D., Glingener, C., and Kopka, P (1996). Modelling of Multimode Interference -Based Power Dividers Using different Numerical Approaches. In : Applied Optics Conference, Applid Optics and Optoelectronics, ISBN : 0-7503-0382-4, Reading, UK, 429-434.

7. Rajarajan, M., Themistos, C., Rahman, B.M.A., and Grattan, K.T.V (1997). Characterization of metal-clad TE/TM mode splitters using the finite element method. In : Journal of Lightwave Technology LT-15 (12) : 2264-2269.

8. Rahman, B.M.A, Wongcharoen, T., Rajarajan, M., Buah, P.A., Mahmood, N., and Grattan, K.T.V (1997). Rigorous Numerical Analysis of Non-Uniform Optical Guided-Wave Devices. In : Progress in Electromagnetic Research Symposium (PIERS), City University, Kowloon Hong Kong.

9. Rahman, B.M.A., Rajarajan, M., Wongcharoen, T., Katsriku, F., Buah, P.A., Meyer, M., and Grattan, K.T.V., (1998) (Invited). Rigorous characterisation of photonic devices using the finit element method. In : Photonics- 98. IIT. Delhi. India. December 14-18: 497-502.

10. Wongcharoen, T., Rajarajan, M. Rahman, B.M.A., and Grattan, K.T.V., Spot-size conversion using uniform waveguide sections for efficient laser-fibre coupling. In: Photonics- 98. IIT. Delhi. India. December 14-18 : 639-642

11. Rajarajan, M., Rahman, B.M.A., and Grattan, K.T.V (1998). Accurate numerical analysis of multimode interference based 3 dB couplers. In : OSA/IEEE Applied Optics (37). 5672-5678.

12. Rajarajan, M, Rahman, B.M.A, Grattan, K.T.V, (1998). Numerical study of spot-size expanders for an efficient OEIC to SMF coupling. In: IEEE Photon Technol. Lett. (10). 1082-1084.

13. Rajarajan, M., Rahman, B.M.A, and Grattan, K.T.V (1998). Design and Analysis of Optical Polarizers Incorporating MQW Waveguides. In : OSA/IEEE Integrated Photonics Research : IME-6 : 71-73.

14. Rajarajan, M., Rahman, B.M.A., Wongcharoen, T., and Grattan, K.T.V (1998) Rigorous Characterization of MMI-based photonic devices. In : Integrated Optic Devices II. San Jose. California USA 3278 (40) : 13-24.

15. Rahman, B.M.A., Rajarajan,M., Wongcharoen, T., and Grattan, K.T.V (1998). Spot-Size Transformations for Laser-to-Fiber Integrations. In : Integrated Optic Devices II. San Jose. California USA 3278 (40) : 196-206.

16. Rajarajan, M., Rahman, B.M.A, and Grattan, K.T.V (1998). Spot-Size Expansionfor Improved OEIC-to-Fiber Coupling Using Directional Couplers with 2-D Confinement. In : IEE Proceedings Optoelectronics (145) :71-76.

17. Rajarajan, M. Rahman, B.M.A., and Grattan, K.T.V., (1999). Novel approach for passive duplexers using the multimode interference devices. In: Photonics West. 23-29. January 1999. Sanjose. California. USA.

18 Rajarajan, M., Obayya, S.S.A., Rahman, B.M.A., and Grattan, K.T.V., (1999). Rigorous study of leaky modes in optical waveguides. In: Photonics West. 23-29. January 1999. Sanjose. California. USA.

19 Rajarajan, M., Wongcharoen, T., Rahman, B.M.A., and Grattan, K.T.V., (1999).Design and characterization of spot-size expanders for improved laser-fiber coupling. In: Photonics West. 23-29. January 1999. Sanjose. California. USA.

20 Rajarajan, M., Rahman, B.M.A., and Grattan, K.T.V (1999). A Rigorous Comparison of the Performance of Directional Couplers with Multimode Interference Devices. : In: Journal of Lightwave Technol LT-17 (2) : 243-248

References

- Abid, Z.E., Johnson K.L. and Gopinath A. (1993). Analysis of dielectric guides by vector transverse magnetic field finite elements. Journal of Lightwave Technology 11 (10): 1545-1548.
- Ahmed S.(1968). Finite element method for waveguide problems. Electronic Letters 4 : 387-389
- Albrecht, P., Hamacher, M., Heidrich, H., Hoffmann, D., Nolting H.P., and Weinert, C.M. (1990). TE/TM Mode splitters on InGaAsP/InP. IEEE Photonics Technology Letters 2 (2) : 114-115.
- Alferness, R.C., and Schmidt, R.V. (1978). Tunable optical waveguide directional coupler filter. Appl. Phys. Lett. 33 (2) : 161-163.
- Alferness, R.C., Schmidt, R.V., and Turner, E.H (1979). characteristics of Ti-diffused lithium niobate optical directional couplers. Applied Optics, 18 (23) : 4012-4016.
- Alferness, R.C. (1982). Waveguide electrooptic modulators. IEEE Transactions on Microwave Theory and Techniques. MTT-30 (8) : 1121-1137.
- Alman, G. M., Molter, L. A., Shen, H., and Dutta, M., (1992). Refractive index approximation from linear perturbation theory for planar MQW waveguides. IEEE Journal of Quantum Electronics QE-28 (3) : 650-657.
- Berk, A.D.(1956). Variational principles for electromagnetic resonators and waveguides. IRE Transactions on Antennas and Propagations AP-4 : 104-111.
- Berry, G.M., Burke, S.V. (1995). Analysis of optical rib self-imaging multimode interference (MMI) waveguide devices using the discrete spectral index method. Optical and Quantum Electronics 27 : 921-934.
- Besse, P.A., Bachmann, M., Melchior, H., Soldano, L.B., and Smit, M.K. (1994). Optical bandwidth and fabrication tolerances of multimode interference couplers. Journal of Lightwave Technology LT-12 (6) : 1004-1009.

- Besse, P.A., Gini, E., Bachmann, M., and Melchior, H. (1996). New 2X2 and 1X3 multimode interference couplers with free selection of power splitting ratios. Journal of Lightwave Technolgy LT-14 (10) : 2286-2293.

- Bierwirth K. Schulz N. and Arndt F. (1986). Finite-difference analysis of rectangular dielectric waveguide structures. IEEE Transactions on Microwave Theory and Techniques MTT-34 (11): 1104-1114

- Bossavit, A., and Mayergoyz, I. (1989). Edge-elements for scattering problems. IEEE Transactions on Magnetics 25 (4) : 2816-2821.

- Brenner, T., and Melchior, H. (1993). Integrated optical modeshape adapters in InGaAsP/InP for efficient fibre-to waveguide coupling. IEEE Photonics Technology Letters 5 (9) : 1053-1056.
- Broberg, B. and Lindgren, S. (1984). Refractive index of $In_{1-x} Ga_x As_y P_{1-y}$ layers and InP in the transparent wavelength region. Journal of Applied Physics 55 (9) : 3376-3381.

- Bryngdahl, O. (1973). Image formation using self-imaging techniques. Journal of the Optical Society of America 64 (4) : 416-418.

- Buah, P.A., Rahman B.M.A. and Grattan K.T.V. (1997). Numerical study of soliton switching in active three-core non-linear fiber couplers. Journal of Quantum Electronics 33 (5): 874-878.
- Burke, S.V. (1990). Spectral index method applied to rib and strip-loaded directional couplers. IEE Proceedings-J 137 (1): 7-10.

- Buus, J., Stewart, W.J., Haes, J., Willems, J., and Baets, R.G. (1993). Spot size expansion for laser-to-fiber coupling using an integrated multimode coupler. Journal of Lightwave Technology LT-11 (4) : 582-588.

- Chang, D.C., Kuester, E.F. (1981). A hybrid method for paraxial beam propagation in multimode optical-waveguides. IEEE Transactions on Microwave theory and Techniques 29 (9) : 923-933.
- Cheng, Y.H., Lin, W.G. (1990). Investigation of rectangular dielectric wave-guides an iteratively equivalent index method. IEE Proceedings-J Optoelectronics 137 (5) : 323-329.
- Chiang, K.S., Lo K.M., Kwok K.S. (1996). Effective-index method with built-in perturbation correction for integrated optical waveguides. Journal of Lightwave Technology 14 (2): 223-228.
- Chiang, K.S. (1996). Analysis of the effective-index method for the vector modes of rectangular-core dielectric waveguides. IEEE Transactions on Microwave Theory and Techniques 44 (5):692-700.
- Chung, Y., Yi, J.C., Kim, S.H., Choi, S.S. (1989). Analysis of a tunable multichannel two-mode-interference wavelength division multiplexer/demultiplexer. Journal of Lightwave Technology LT-7 (5) : 766-777.
- Davies, J.B. (1989). The finite element method. In: Numerical techniques for microwave and millimeter-wave passive structures, ed. by T. Itoh. (New York: Wiley), pp. 33-132.
- De Ridder, R. M., Sander, A.F.M., Driessen, A., and Fluitman, J.H.J. (1993) An integrated optic adiabatic TE/TM mode splitter on silicon. Journal of Lightwave Technology LT-11 (11) : 1806-1811.
- Donnelly, J.P. (1986). Limitations on power-transfer efficiency in three-guide optical couplers. IEEE Journal of Quantum Electronics QE-22 (5) : 610-616.
- Donnelly, J.P., DeMeo, N.L., Ferrante, G.A. (1983). Three-guide optical couplers in GaAs. Journal of Lightwave Technology, LT-1 (2) : 417-423.
- English, W.J, Young F.J. (1971). An E vector variational formulation of the Maxwell's equations for cylindrical waveguide problems. IEEE Transactions on Microwave Theory and Techniques MTT-19: 40-46.

- Feit, M.D. and Fleck, J.A. (1980) Computation of mode properties in optical fiber waveguides by a propagating beam method. Applied Optics 19 (7): 1154-1164.
- Fernandez, F.A., and Li, Y. (1990). Variational finite element analysis of dielectric waveguides with no spurious solutions, Electronics Letters 26 (25) : 2125-2126.
- Forastiere, M.A., Righini, G.C., and Verciani, A. (1997). Design and numerical analysis of a "silica-on-silicon" integrated optical duplexer. Proceedings of the society of Photo-Optical Instrumentation engineers (SPIE) 2954 (22) :88-98.
- Ghirardi, F., Mersali, B., Brandon. J., Herve-Gruyer, G., and Carenco A. (1994). Quasi planar spot-size tranformer for efficient coupling between a cleaved fibre and an InP/InGaAsP rib waveguide. IEEE Photonics Technology Letters 6 (4) : 522-524.
- Goto, N., Yip, G.L. (1989). A TE-TM Mode Splitter in $LiNbO_3$ by proton exchange and Ti diffusion. Journal of Lightwave Technology 7 (10) : 1567-1574.
- Hardy, A., and Streifer, W. (1986). Coupled modes of multiwaveguide systems. IEEE Journal of Quantum electronics QE-22 (4) : 528-534.
- Hashimoto, T., Nakasuga, Y., Yamada, Y., Terui, H., Yanagisawa, M., Moriwaki, K., Suzaki, Y., Tohmori, Y., Sakai, Y., and Okamoto., H.(1996). Hybrid integration of spot-size converted laser diode on planar lightwave circuit plarform by passive alignment technique. IEEE Photonics Technology Letters 8 (11) : 1504-1506.
- Hayata, K., Koshiba M., Eguchi M. and Suzuki M. (1986b). Vectorial finite-element method without any spurious solutions for dielectric waveguiding problems using transverse magnetic-field component. IEEE Transactions on Microwave Theory and Techniques MTT-34 (11): 1120-1124.
- Huang, W.P., Xu, C.L. (1992).A wide-angle vector beam propagation method. IEEE Photonics Technology Letters 4 (10) : 1118-1120.
- Huang, W.P., Xu, C.L., and Yokoyama, K. (1996). The perfectly matched layer boundary condition for modal analysis of optical waveguides : leaky mode calculations. IEEE Photonics Technology Letters 8 (5) : 652-654.
- Inaba, Y., Kito, M., Nishikawa, T., Ishino, M., and Matsui, Y.S. (1997). Multiquantum-well lasers with tapered active stripe for direct coupling to single-mode fiber. IEEE Photonics Technology Letters 9 (6) : 722-724.

- Jenkins, R.M., Heaton, J.M., Wight, D.R., Parker, J.T., Birbeck, J.C.H., Smith, G.W., and Hilton K.P. (1994). Novel 1XN and NXN integrated optical switches using self-imaging multimode GaAs/AlGaAs waveguides. Applied Physics Letter 64 (6) : 684-686.
- Kao, K.C. and Hockham G.A. (1966). Dielectric-fibre surface waveguides for optical frequencies. Proceedings IEE 113: 1151-1158.
- Kawano, K., Kohtoku, M., Okamoto, H., Itaya, Y., and Naganuma, M. (1997). Comparison of coupling characterisitcs for several spotsize-converter-integrated laser diodes in the 1.3-μm-wavelength region. IEEE Photonics Technology Letters 9 (4) : 428-430.
- Kendall, P.C., McIlroy, P.W.A. and Stern, M.S. (1989). Spectral index method for rib waveguide analysis. Electronics Letters 25 (2): 107-108.
- Kim, H.S, and Ramaswamy, R.V. (1993). Tapered, both in dimension and in index, velocity coupler : theory and experiment. IEEE Journal of Quantum electronics QE-29 (4) : 1158-1167.
- Kim, H.S., Kwon, Y.S., Hong, S. (1997). Square ring laser diode with MMI coupler cavity. IEEE Photonics Technology Letters 9 (5) : 584-586.
- Knox, R.M. and Toulios P.P. (1970). In: Proceedings of MRI Symposium on submillimeter waves, ed. by Fox. J. (Brooklyn: Polytechnic Press), pp. 497-516.
- Koch, T.L., Koren, U. (1990) Semiconductor-lasers for coherent optical fibre communications. Journal of lightwave Technology LT-8 (3) : 274-293.
- Kogelnik, H., and Schmidt, R.V. (1976). Switched directional couplers with alternating Δβ. IEEE Journal of Quantum Electron QE-12 (7) : 396-401.
- Koshiba, M. and Suzuki, M. (1985). Vectorial wave analysis of optical waveguides with rectangular cross-section using equivalent network approach. Electronics Letters 21 (22): 1026-1027.
- Koshiba, M. (1992a). Optical waveguide analysis. (New York: McGraw-Hill).

- Krauss, T.F., De La Rue, R.M., and Laybourn, P.J.R. (1995). Impact of output coupler configuration on operating characteristics of semiconductor ring lasers. Journal of Lightwave Technology LT-13 (7) : 1500-1507.
- Kumar, A., Thyangarajan, K. and Ghatak, A.K. (1983). Analysis of rectangular-core waveguides: An accurate perturbation approach. Optics Letters 8 (1): 63-65.
- Kumar, A., Shenoy, M. R., Thyagarajan, K. (1984). Modes in anisotropic rectangular waveguides – an accurate and simple perturbation approach. IEEE Transactions of Microwave Theory and Techniques MTT-32 (10) : 1415-1418.
- Leaver, K.D., and Pagiatakis, G. (1994). Fabrication tolerances in fibre directional couplers designed to maximise coupling between fibres and diode lasers. IEE Proceedings Optoelectronics 141 (1) : 69-74.
- Lee, C., Wu, M., Sheu, L., Fan, P., Hsu, J. (1997). Design and analysis of completely adiabatic tapered waveguides by conformal mapping. Journal of Lightwave Technology LT-15 (2) : 403-410.
- Liao, Y.P, Lu, R.-C, Yang, C.-H, and Wang W.-S. (1996). Passive Ni:LiNbO$_3$ polarisation splitter at 1.3μm wavelength. Electronics Letters 32 (11) : 1005-1007.
- Lu, Y. and Fernandez ,F.A. (1994). Vector finite element analysis of integrated optical waveguides. IEEE Transactions on Magnetics 30 (5): 3116-3119.
- Mabaya, N.. Lagasse, P.E. and Vandenbulcke P. (1981). Finite Element Analysis of optical waveguides. IEEE Transactions on Microwave Theory and Techiques MTT-29 (6): 600-605.
- Marcatili E.A.J. (1969). Dielectric rectangular waveguide and directional coupler for integrated optics. Bell Systems Technical Journal 48: 2071-2102.
- Marcuse, D. (1972). Loss analysis of single-mode fiber splices. The Bell System Technical Journal 56 (5) : 703-718.
- Maruyama, H., Haruna, M., Nishihara, H. (1995). TE-TM mode splitter using directional coupling between hetrogeneous waveguides in LiNbO$_3$. Journal of Lightwave Technology LT-13 (7) : 1550-1554.

- Meshulach, D., and Ruschin, S. (1994). Active N coupled waveguide switch and power splitter. IEEE Journal of Quantum Electronics QE-30 (6) : 1427-1434.
- Miller, S.E (1969), "Integrated optics: An introduction," Bell Syst. Tech. J 48 : 948-964.
- Mishra, P.K., Sharma, A., Labroo, S., Ghatak, A.K. (1985). Scalar Variational analysis of single-mode wave-guides with rectangular cross-section. IEEE Transactions on Microwave Theory and Techniques MTT-33 (3) : 282-286.
- Mitomi, O., Kasaya, K., Suzaki, Y., Fukano, H., Sakai, Y., Okamoto, M., and Matsumoto, S. (1996). Optical spot-size converters for low-loss coupling between fibers and optoelectronic semiconductor devices. Journal of Lightwave Technology LT-14 (7) : 1714-1720.
- Miyamoto, Y., Hagimoto, K., Kagawa, T. (1991). A 10 Gb/s High-sensitivity optical receiver using an InGaAs-InAlAs superlattice APD at 1.3-μm and 1.55 μm. IEEE Photonics Technology Letters 3 (4) : 372-374.
- Morishita, K., Inagaki, S., and Kumagai, N. (1979). Analysis of discontinuities in dielectric waveguides by means of the least squares boundary residual method. IEEE Transactions on Microwave Theory and Techniques MTT-27 (4) : 310-315.
- Morishita, K and Kumagai, N. (1977). Unified approach to the derivation of variational expression for electromagnetic fields. IEEE Transactions on Microwave Theory and Techniques MTT-25 (4) : 34-40.
- Nahory, R.E., Pollock, M.A., Johnston, W.D., and Barns, R.L. (1978). Refractive index calculations of InGaAs/InP. Applied Physics Letters 33 : 660-664.
- Paim, M.R., Janz, C.F., MacDonald, R.I., and Broughton, J.N. (1995). Compact planar 980/1550-nm wavelength multi/demultiplexer based on multimode interference. IEEE Photonics Technology Letters 7 (10) : 1180-1182.
- Papuchon, M, Combernale, Y., Mathieu, X, Ostrowsky, D.B., Reiber, L., Roy, A.M., Sejourne, B., and Werner, M. (1975) Electrically switched optical directional coupler :Cobra. Applied Phys. Lett., 27 (5) : 289-291.

- Pantic, Z. and Mittra R. (1986). Quasi-TEM analysis of microwave transmission lines by the finite-element method. IEEE Transactions on Microwave Theory and Techniques MTT-34 (11): 1096-1103.
- Peng, S.T. and Oliner, A.A. (1981). Guidance and leakage properties of a class of open dielectric waveguides: Part I-Mathematical formulations. IEEE Transactions on Microwave Theory and Techniques MTT-29 (9): 843-855.
- Pola, J.R.P., Biehlig, W. and Lederer, F. (1996). A generalization of the spectral index method toward multiple rib waveguides. Journal of Lightwave Technology 14 (3): 454-461.
- Qiao, L. and Wang, J. (1992). A modified Ray-Optic method for arbitrary dielectric waveguides. IEEE Journal of Quantum Electronics 28 (12): 2721-2727.
- Rahman, B.M.A., and Davies, J.B. (1984). Finite-element solution of integrated optical waveguides. Journal of Lightwave Technology LT-2 (5) : 682-687.
- Rahman, B.M.A., Davies, J.B. (1984a). Finite element analysis of optical and microwave waveguide problems. IEEE Transactions on Microwave Theory and Techniques MTT-32 (1) : 20-28.
- Rahman, B.M.A, Davies, J.B. (1984b). Penalty function improvement of waveguide solution by finite elements. IEEE Transactions on Microwave theory and Techniques. MTT-32 (8) : 922-928.
- Rahman, B.M.A., and Davies, J.B. (1988). Analysis of optical waveguide discontinuities. Journal of Lightwave Technology 6 (1) : 52-57.
- Rahman, B.M.A., Liu, Y., and Grattan, K.T.V. (1993). Finite-element modelling of one- and two- dimensional MQW semiconductor optical waveguides. IEEE Photonics Technology Letters 5 (8) : 928-931.
- Rasmussen, T., Rasmussen, J. K., and Povlsen, J.H.(1995). Design and performance evaluation of 1-by-64 multimode interference power splitter for optical communication. Journal of Lightwave Technology LT-13 (10) : 2069-2074.

- Saad, M.S. (1985). Review of numerical methods for the analysis of arbitrarily-shaped microwave and optical dielectric waveguides. IEEE Transactions on Microwave Theory and Techniques MTT-33 (10): 894-899.

- Saini, M., and Sharma, E.K. (1995). Equivalent refractive index of multiple-quantum-well waveguides by variational analysis. Optics Letters 20 (20) : 2081-2083.
- Silvester, P.P. and Ferrari, R.L. (1991). Finite elements for electrical engineers. 2nd Ed. (Cambridge: Cambridge University Press).
- Snyder, A.W. and Love J.D. (1991). Optical waveguide theory. 2nd Ed. (London: Chapman and Hall).
- Soldano, L.B., and Pennings, E.C.M. (1995). Optical multimode interference devices based on self-imaging: principles and applications. Journal of Lightwave Technology LT- 13 (4) : 615-626.
- Soldano, L.B., de Vreede, A.H, Smit, M.K., Verbeek, B.H., Metaal, E.G., and Groen, F.H. (1994). Mach-Zehnder interferometer polarization splitter in InGaAsP/InP. IEEE Photonics Technology Letters 6 (3) : 402-405.
- Soldano, L.B., Veerman, F.B., Smit, M.K., Verbeek, B.H., Dubost, A.H., and Pennings, E.C.M. (1992). Planar monomode optical couplers based on multimode interference effects. Journal of Lightwave Technology LT-10 (12) : 1843-1849.
- Soole, J.B.D., Amersfoort, M.R., LeBlanc, H.P., Andreadakis, N.C., Rajhel, A., Casneau, C., Bhat, R., Koza, M.A., Youtsey, C., and I. Adesida. (1996). Use of multimode interference couplers to broaden the passband of wavelength-dispersive integrated WDM filters. IEEE Photonics Technology Letters 8 (10) : 1340-1342.

- Spiekman, L.H., Oei, Y.S., Metaal, E.G., Groen, F.H., Moerman, I., and Smit, M.K. (1994). Extremely small multimode interference couplers and ultrashort bends on InP by deep etching. IEEE Photonics Technology Letters 6 (8) : 1008-1010.

- Spiekman, L.H. (1996). Compact integrated optical components for telecommunication networks. PhD thesis: Delft University of Technology.

- Srivastava, R., Kao, C.K. and Ramasway, R.V. (1987). WKB analysisi of surface waveguides with truncated index profiles. Journal of Lightwave Technology LT-5 (11): 1605-1609.
- Stern,M.S., Kendall, P.C. and McIlroy, P.W.A. (1990). Analysis of the spectral index method for vector modes of rib waveguides. IEE Proceedings-J 137 (1): 21-26.
- Sudbo, A.S. (1992). Why are accurate computations of mode fields in rectangular dielectric waveguides difficult. Journal of Lightwave Technology 10 (4): 418-419.
- Sun, L., and Yip, G.L., (1994). Analysis of metal-clad optical waveguide polarizers by the vector beam propagation method. Applied Optics. 33 (6) : 1047-1050.
- Tamir, T. (1979). Integrated Optics. 2nd Ed. (New York: Springer-Verlag).
- Tamir, T. (1990). Guided wave optoelectronics. 2nd Ed. (Berlin: Springer-Verlag).
- Themistos, C., Rahman B.M.A., Hadjicharalambous, A., and Grattan, K.T.V. (1995), Loss/gain characterization of optical waveguides. Journal of Lightwave Technology LT-13 (8) : 1760-1765.
- Themistos, C., Rahman, B.M.A., and Grattan, K.T.V. (1995). Finite-element analysis of surface-plasmon modes for lossy optical waveguides by the use of perturbation technique. Applied Optics 34 (33) : 7695-7701.
- Thoen, E.R., Molter, L.A., and Donnelly, J.P.(1997). Exact modal analysis and optimization of NxNx1 cascaded waveguide structures with multimode guiding sections. IEEE Journal of Quantum electronics QE-33 (8) : 1299-1307.
- Tseng S.M., Hsu, K.Y., Wei, H.S., and Chen K.F. (1997). Analysis and experiment of thin metal-clad fiber polarizer with index overlay. IEEE Photonics Technology Letters 9 (5) : 628-630.
- Uehara, S., Izawa, T., and Nakagome, H. (1974). Optical waveguide polarizer 13 : 1753-1757.
- Ulrich, R., and Ankele, G. (1975). Self-imaging in homogeneous planar optical waveguides. Applied Physics Letters 27 (6) : 337-339.

- Ulrich, R., and Kamiya, T. (1978). Resolution of self-images in planar optical waveguides. Journal of Optical Society of America 68 (5) : 583-592.

- Van der Tol, J.J.G.M, Pedersen, J.W., Metaal, E.G., van Gaalen, J.J.-W, Oei, Y.S., and Groen, F.H. (1997). A short polarization splitter without metal overlays on InGaAsP-InP. IEEE Photonics Technology Letters 9 (2) : 209-211.

- Vanroey, J., Vanderdonk, J., Lagasse, P.E. (1981). Beam-propagation method-analysis and assessment. Journal of Optical Society of America 71 (7) : 803-810.

- Varshney, R.K., and Kumar, A. (1988). A simple and accurate modal-analysis of strip-loaded optical wave-guides with various index profiles. Optics Letters 6 (4) : 601-606.

- Wada, M., Okamoto, H., kohtoku, M., Kawano, K., Kadota, Y., Kondo, Y, Kishi, K., Kondo, S., Sakai, Y., Kotaka, I., Noguchi, Y., and Itaya, Y. (1997). Fabrication and coupling-to-fibre characteristics of laser diodes integrated with a spot-size converter having a lateral taper. IEE Proceedings-Optoelectronics 144 (2) : 104-108.

- Wang, Y.H., Vassallo, C. (1988). Circular Fourier-analysis of arbitrarily shaped optical fibres. Optics Letters 14 (24) : 1377-1379.

- Weinert, C.M., Agrawal, N. (1995). Three-dimensional finite difference simulation of coupling behaviour and loss in multimode interference devices. IEEE Photonics Technology Letters 7 (5) : 529-531.

- Wilson, L.O., and Reinhart, F.K., Cross-talk problems in optical waveguides. (1974). Bell System Technical Journal 53 : 717-726.

- Wongcharoen, T., Rahman, B.M.A., and Grattan, K.T.V. (1996). Accurate characterization of optical filters with two-dimensional confinement. Journal of Lightwave Technology LT-14 (11) : 2596-2603.

- Wongcharoen, T., Rahman, B.M.A., and Grattan, K.T.V. (1997). Electro-optic directional coupler switch characterization. Journal of Lightwave Technology LT-15 (2) : 377-382.

- Zengerle, R., Bruckner, H., Olzhausen, H., and Kohl, A. (1996). Low-loss fibre-chip coupling by buried laterally tapered InP/InGaAsP waveguide structure. Electronics Letters 28 (7).

- Zienkiewicz O.C. and Taylor R.L. (1994). The finite element method. 4th ed.(London: McGraw-Hill).